University of Glasgow

Electronic Structural Studies of Transition Metal Complexes with Chelating Sulfur Ligands

Cailean Iain Macleod

Submitted in fulfilment of the requirements for the degree of

Doctor of Philosophy

School of Chemistry

College of Science and Engineering

University of Glasgow

December 2019

Declaration

All work presented in this thesis is original work undertaken by the author, except where specific reference has been made to other sources. No work here has been submitted, in whole or in part, for any other degree at this or any other institution.

Cailean Iain Macleod

Date:

“We meet at a college noted for knowledge, in a city noted for progress, in a State noted for strength, and we stand in need of all three, for we meet in an hour of change and challenge, in a decade of hope and fear, in an age of both knowledge and ignorance. The greater our knowledge increases, the greater our ignorance unfolds.”

John Fitzgerald Kennedy, 12th September 1962

Acknowledgments

There are many people to whom I am grateful, without whom this thesis would not have been possible.

The first person I would like to thank is Dr Stephen Sproules. The past few years have been challenging and rewarding, and I consider myself lucky to have had the opportunity to work under as diligent, enthusiastic, knowledgeable and supportive a mentor. In addition to such broad and deep academic support and guidance, I am also thankful for the encouragement and freedom I received to pursue my own ideas and projects. Furthermore, I would like to thank him for conducting the VSM measurements and analysing the magnetic data, and for running the DFT calculations for the Co complexes in the thesis.

I would like to thank: Associate Professor Kyle Lancaster and his group at Cornell for their measurements of XAS data; Dr Haralampos Miras for the measurement and solution of the X-ray crystal structures in this thesis; and Professor Corinna Hess and her group at TUM for the measurement of the SQUID data discussed in this thesis.

I would also like to thank the administrative, technical and academic staff of the School of Chemistry and the College of Science and Engineering for their assistance in matters scientific and administrative. In this instance, I would especially like to thank Mr Andrew Monaghan and Mr Jim Tweedie for microanalytical and mass spectral measurements.

I am also grateful to the European Union and the Engineering and Physical Sciences Research Council for providing the funding for this research project.

I would like to thank Jake and Ludo for being so amazing over the past few years. Both of you have been incredibly supportive and enjoyable to work with, and I honestly can’t

think of better people to work with. Although I have no doubt you will both excel at whatever you do next, I am going to miss you both a great deal.

I would like to thank all my friends in the Ganin group for being so enjoyable to work alongside – having an office that is such a pleasure to work in is a rare thing. A special shout out goes to Jessica – the second person I talked to and friend I made way back in Undergrad, if you told me then it would end with us writing theses, I wouldn't have believed you! Another shout out goes to Roberta – after all these years, we made it!

I would also like to thank the Farnaby group for accommodating us as various things happened to the office and the Corr group for their support during the early part of my PhD.

Other people I would like to thank include Megan and Adam, for being such a pleasure to work with – hopefully, you enjoyed your time in the Sproules Group as much as we enjoyed having you; Thomas Ashton (spelled correctly) for being so encouraging in First Year – I have missed the whiskies and, I suppose, the conversations too; and Michael Beglan for making me feel so welcome and helping me so much at the start of my PhD, it was a real pleasure working with you and I hope you're enjoying your well-earned retirement!

Whilst the remaining people I would like to thank are too many to mention, I would like to especially thank Colin Dow and Jennifer and Houston Ayre for their huge support, and Yahya Shaikh for sparking my interest in Chemistry – without you, this thesis would not exist.

There are many friends I would like to thank, amongst them James for such good craic and Stephen – "worth it". I'd also like to thank Sian, Christian, Naif, Sharon, Liam and Nicole for being such good friends over the past few years.

I would like to conclude by thanking my family for their continued support and love throughout my PhD. I know it hasn't been easy, but I wouldn't be here without all of you. To that I would like to thank my extended family for love and encouragement; Richard and Geetha for their support and patience – I am glad I can finally tell you my thesis is finished(!); my parents, for their infinite love and support in more ways than I can list – and for the encouragement to keep asking questions that led me here; and my sister, for her love and support throughout all of this.

Finally, I cannot thank my endlessly patient and loving wife Divia enough. Facing demands and challenges on multiple fronts throughout the entirety of this PhD, you have been consistently loving, supportive and encouraging. I know without you this thesis would not have been possible, and I am incredibly grateful for you and excited for the road ahead.

Abstract

The coordination chemistry of transition metals with sulfur-based ligands is of huge importance to our everyday life and with increased demand for data storage and processing, it could become more important still. This is because sulfur-ligated metal complexes, particularly pseudotetrahedral Co^{II} complexes, offer great potential for the developing high-performance single-molecule magnets. However, before such systems can be developed the coordination chemistry of such complexes must be further understood and to this end, three different areas of cobalt-sulfur chemistry were studied.

The first of these examined the effect of modifications to the second-coordination sphere on the electronic and chemical properties of Co^{II} arylthiolate complexes. Using electronic and XAS spectroscopy and magnetic susceptibility measurements it was shown that, even as the chemical behaviour changes dramatically, the electronic structures of the $\{CoS_4\}$ moieties remain relatively stable across the series. In the course of study two $[Co_4(SAr)_{10}]^{2-}$ clusters were isolated which showed similar amounts of antiferromagnetic exchange coupling, with the yield proving contingent on the electron-withdrawing strength of the arylthiolate substituents.

The second area of investigation was into 1,1-dithiolate coordination complexes. Research initially focussed on Co^{II} complexes, to investigate the effect of the tight bite-angle on the electronic and magnetic properties of the complexes. Electronic absorption spectroscopy proved the link between the energy and intensity of the $^4A_2 \rightarrow {}^4T_1(P)$ transitions in each D_{2d} complex and the electron-withdrawing strength of the ligand substituents, but magnetic susceptibility measurements proved inconclusive. In the solid-state results consistent with a $S = {}^1/_2$ were obtained, whilst fluid solution results were consistent with $S = {}^3/_2$. Co K-edge XAS confirmed the square-planar nature in the solid-state, with the difference attributed to the fluxional Co^{II} species changing $\{CoS_4\}$ coordination in solution. S K-edge XAS confirmed the link between substituent electron-withdrawing strength and $\{CoS_4\}$ electronic structure, with transition energies correlating

strongly with the substituent electron-withdrawing strength in both the Co^{II} complexes and the free ligand salt.

To probe this further Ni^{II} and Cu^{II} 1,1-dithiolate complexes were prepared. Electronic absorption spectroscopy confirmed the trend, with the energy and intensity of the ligand field transitions increasing as the electron-withdrawing strength decreased in both cases. EPR of the Cu^{II} species showed *g*- and *A*-values to be broadly similar across the series, however, whilst still revealing that the substituent-facilitated ligand charge dominates the in-plane π-bonding in the complexes. The out-of-plane π-bond covalency was shown to be more influenced by the metal-ligand bite-angle. Cyclic voltammetry confirmed the presence of reversible $Cu^{III/II}$ redox events in each 1,1-dithiolate species, with the analogous $Ni^{III/II}$ oxidation events proving irreversible. Once again the substituent effects were clear, with the redox potentials lowering as the substituent electron-withdrawing strength was reduced. The new Cu^{III} species $[Cu(i\text{-ect})_2]^-$ was successfully isolated, with Cu K-edge of the Cu^{II} and Cu^{III} species confirming oxidation of the parent species. S K-edge XAS revealed the same trend as the Co^{II} complexes and the free ligands, with the C−S π* covalency also increasing as substituent electron-withdrawing strength does.

Transition metal tetrathiotungstate chemistry was the final area investigated. Electronic absorption spectra confirmed the formation and purity of the Co, Ni, Cu and Zn bis(tetrathiotungstate) species, with $[Co(WS_4)_2]^{z-}$ (z = 2, 3) the focal point of the investigation. Magnetic susceptibility measurements showed a reduced magnetic moment in the reduced species, with the introduced electron coupling antiferromagnetically to the S = $^3/_2$ system. Co K-edge XAS showed the Co^{II} to be partially reduced, with the bulk of the reduction taking place on the tetrathiotungstate ligands. S K-edge showed the impact of the reduction, with the 1s → 4p transition energy of $[Co(WS_4)_2]^{3-}$ higher than both $[Co(WS_4)_2]^{2-}$ and $[Zn(WS_4)_2]^{2-}$.

Contents

List of Abbreviations and Symbols

A	Hyperfine coupling parameter
acbdt^{2-}	1-benzyl-1-formyl-2,2-ethenedithiolate
acdt^{2-}	1-formyl-2,2-ethenedithiolate
baddt^{2-}	1-benzaldehyde-2,2-ethenedithiolate
bcdt^{2-}	1-cyano-1-butyl-2,2-ethenedithiolate
bicdt^{2-}	1-cyano-1(1*H*-benzimidazole)-2,2-ethenedithiolate
Biq	2,2′-biquinoline
bmim	1-benzyl-2-methylimidazole
bzaadt^{2-}	3,3-dithiolate-2-[(phenylmethylene)amino]-2-propenenitrile
bzedt^{2-}	1-benzoyl-1-ethoxycarbonyl-2,2-ethenedithiolate
C	Celsius
c2cbmadt^{2-}	2-cyano-*N*-(2-chloro-benzenemethanimine)-3,3-dithiolate-2-propenamide
c2cppad^{2-}	2-cyano-*N*-(2-chlorophenyl)-3,3-dithiolate-2-propenamide
c2pdt^{2-}	1-cyano-1-(2-pyridyl)-2,2-ethenedithiolate
c2tpad^{2-}	2-cyano-*N*-(2-methylphenyl)-3,3-dithiolate-2-propenamide
c3cppad^{2-}	2-cyano-*N*-(3-chlorophenyl)-3,3-dithiolate-2-propenamide
c3pdt^{2-}	1-cyano-1-(3-pyridyl)-2,2-ethenedithiolate
c3tpad^{2-}	2-cyano-*N*-(3-methylphenyl)-3,3-dithiolate-2-propenamide
c4cbmadt^{2-}	2-cyano-*N*-(4-chloro-benzenemethanimine)-3,3-dithiolate-2-propenamide
c4cppad^{2-}	2-cyano-*N*-(4-chlorophenyl)-3,3-dithiolate-2-propenamide
c4pdt^{2-}	1-cyano-1-(4-pyridyl)-2,2-ethenedithiolate
c4tpad^{2-}	2-cyano-*N*-(4-methylphenyl)-3,3-dithiolate-2-propenamide
caac	cyclic alkyl(amino)carbene
calix	*para*-tert-butylcalix[8]arene
cbmadt^{2-}	2-cyano-*N*-(benzenemethanimine)-3,3-dithiolate-2-propenamide
cbpd^{2-}	1-cyano-1-(2-bromophenyl)-2,2-ethenedithiolate
cbppad^{2-}	2-cyano-*N*-(4-bromophenyl)-3,3-dithiolate-2-propenamide

cclpd^{2-}	1-cyano-1-(2-chlorophenyl)-2,2-ethenedithiolate
ccpd^{2-}	1-cyano-1-(2-cyanophenyl)-2,2-ethenedithiolate
cctd^{2-}	1-cyano-1-(3-chloro-2-thienyl) -2,2-ethenedithiolate
ccypad^{2-}	2-cyano-*N*-cyclohexyl-3,3-dithiolate-2-propenamide
cdmd^{2-}	1,2-di(methylcarbonyl)-1,2-ethenedithiolate
cdt^{2-}	1-cyano-2,2-ethenedithiolate
cecpad^{2-}	2-cyano-*N*-(4-ethoxycarbonyl)-3,3-dithiolate-2-propenamide
cepad^{2-}	2-cyano-*N*-ethyl-3,3-dithiolate-2-propenamide
cepodt^{2-}	1-cyano-1-di(diethyl phosphite)-2,2-ethenedithiolate
cetbma^{2-}	1-cyano-1-(5-ethyl-1,3,4-thiadiazol-2-amide)-2,2-dithiolate
cfdt^{2-}	1-cyano-1-(2-furyl)-2,2-ethenedithiolate
chdt^{2-}	2-oxo-cyclohexanecarbodithiolate
cmbmadt^{2-}	2-cyano-*N*-(4-methyl-benzenemethanimine)-3,3-dithiolate-2-propenamide
cmobmadt^{2-}	2-cyano-*N*-(4-methoxy-benzenemethanimine)-3,3-dithiolate-2-propenamide
cmopad^{2-}	2-cyano-*N*-(4-methoxyphenyl)-3,3-dithiolate-2-propenamide
cmpad^{2-}	2-cyano-*N*-methyl-3,3-dithiolate-2-propenamide
cnbidt^{2-}	1-cyano-1-(methylbenzimidazole)carbonyl-2,2-ethenedithiolate
cnpd^{2-}	1-cyano-1-(2-nitrophenyl)-2,2-ethenedithiolate
cnpsod^{2-}	1-cyano-1-(phenylsulfonyl)-2,2-ethenedithiolate
codpad^{2-}	2-cyano-*N*-octadecyl-3,3-dithiolate-2-propenamide
Cp	cyclopentadiene
Cp*	1,2,3,4,5-pentamethylcyclopentadiene
cpdt^{2-}	2,4-cyclopentadiene-1-methylenedithiolate
cphdt^{2-}	1-cyano-1-phenyl-2,2-ethenedithiolate
Cp$^{i\mathrm{Pr5}}$	1,2,3,4,5-pentaisopropylcyclopentadiene
cppad^{2-}	2-cyano-*N*-phenyl-3,3-dithiolate-2-propenamide
cpydt^{2-}	*α*-(methylenedithiolate)-*β*-oxo-1-pyrrolidinepropanenitrile
cqdt^{2-}	1-cyano-1-(2-quinolyl)-2,2-ethenedithiolate

$ctdt^{2-}$	1-cyano-1-(2-thienyl)-2,2-ethenedithiolate
cw	continuous wave
Cy	cyclohexyl
D	axial anisotropy
D_0	intensity
$dafdt^{2-}$	4,5-diazafluorene-9-methylenedithiolate
$dbmmdt^{2-}$	1,1-di(bis(dimethylamino)methyl)-2,2-ethenedithiolate
dbtu	1,3-dibutylthiourea
$dbzd^{2-}$	1,1-dibenzoyl-2,2-ethenedithiolate
$dddmdt^{2-}$	1,1-di(1-ethoxy-1-dimethylamino-methyl)-2,2-ethenedithiolate
ded^{2-}	1,1-di(ethoxycarbonyl)-2,2-ethenedithiolate
$dipdt^{2-}$	1,1-di(isopropoxycarbonyl)-2,2-ethenedithiolate
$dmcddt^{2-}$	5,5-dimethyl-1,3-cyclohexanedione-2-methylenedithiolate
dmd^{2-}	1,1-di(methylcarbonyl)-2,2-ethenedithiolate
$dmit^{2-}$	1,3-dithione-2-thione-4,5-dithiolate
$dmit^{2-}$	4,5-dimercapto-1,3-dithiole-2-thione
$dmod^{2-}$	1,1-di(methoxycarbonyl)-2,2-ethenedithiolate
$dmsdt^{2-}$	1,1-di(methylthio)-2,2-ethenedithiolate
dnps	5-(dimethylamino)naphthalen-1-ylsulfonyl
$dpmdt^{2-}$	2-(1-(1,1′-biphenyl)-4-yl-3,3-dithiolato-2-propen-1-ylidene)-propanedinitrile
$dpodt^{2-}$	1,1-di(diisopropyl phosphite)-2,2-ethenedithiolate
$dtbod^{2-}$	1,1-di(1,1-dimethylethyloxycarbonyl)-2,2-ethenedithiolate
$dtdt^{2-}$	1,3-dithiane-2-methylenedithiolate
$dtpdt^{2-}$	1,3-dithiepin-2-ylidenemethanedithiolate
$dtpmdt^{2-}$	1,3-dithiolo[4,5-b]pyrazine-2-methylenedithiolate
dts^{2-}	dithiosquarate
E	transverse anisotropy
$eoepodt^{2-}$	1-ethoxycarbonyl-1-di(diethyl phosphite)-2,2-ethenedithiolate

EPR	electron paramagnetic resonance
Et_2dtc^-	diethyldithiocarbamate
eV	electronvolt
EXAFS	extended X-ray absorption fine structure
Fc	ferrocene
Fc^+	ferrocenium
$fydt^{2-}$	1-(9*H*-fluoren-9-ylidene)-methylenedithiolate
G	giga
g_e	electron spin *g*-value
H	magnetic field
h	Planck's constant
H_3bhmp	2,6-bis(hydroxymethyl)-4-methylphenol
H_3mst	*N*,*N*′,*N*″-[2,2′,2″-nitrilotris-(ethane-2,1-diyl)]tris(2,4,6-trimethylbenzenesulfonamide
H_4tmsb	1,2,4,5-tetrakis(methanesulfonamido)benzene
H_C	Coercive magnetic field
$htdt^{2-}$	1-(4,5-dihexyl-1,3-dithiol-2-ylidene)-methylenedithiolate
$\vec{I}$	nuclear spin operator
i-$bpcct^{2-}$	1-cyano-1-(4-bromophenoxy)carbonyl-2,2-ethenedithiolate
i-$bzct^{2-}$	1-cyano-1-benzoyl-2,2-ethenedithiolate
i-$dbndt^{2-}$	1,1-dibenzyl-2,2-ethenedithiolate
i-$doct^{2-}$	1-cyano-1-dodecoxycarbonyl-2,2-ethenedithiolate
i-ect^{2-}	1-cyano-1-ethoxycarbonyl-2,2-ethenedithiolate
i-edt^{2-}	1,1-ethenedithiolate
i-$mant^{2-}$	1-cyano-1-propanamide-2,2-dithiolate
i-mct^{2-}	1-cyano-1-methylcarbonyl-2,2-ethenedithiolate
i-mdt^{2-}	1,2-dimethyl-2,2-ethenedithiolate
i-mnt^{2-}	1,1-dicyano-2,2-ethenedithiolate

i-moct^{2-}	1-cyano-1-methoxycarbonyl-2,2-ethenedithiolate
inddt^{2-}	1*H*-Indene-1,3(2*H*)-dione-2-methylenedithiolate
i-npdt^{2-}	1-methyl-2,2-ethenedithiolate
i-ooct^{2-}	1-cyano-1-octoxycarbonyl-2,2-ethenedithiolate
ipcdt^{2-}	1-cyano-1-isopropyl-2,2-ethenedithiolate
i-pdt^{2-}	1,1-diphenyl-2,2-ethenedithiolate
i-phct^{2-}	1-cyano-1-phenylcarbonyl-2,2-ethenedithiolate
i-poct^{2-}	1-cyano-1-propoxycarbonyl-2,2-ethenedithiolate
IR	infrared
i-tbdt^{2-}	1,1-di(1,1-dimethylethyl)-ethenedithiolate
i-tbuct^{2-}	1-cyano-1-(1,1-dimethylethyl)carbonyl-2,2-ethenedithiolate
i-tdf^{2-}	1,3-di(trifluoromethyl)-1-propene-2,2-dithiolate
K	Kelvin
K	corrected Fermi contact term
k	kilo
k	Fermi contact term
LF	ligand field
Ln	lanthanide
M	magnetisation
m/*z*	mass to charge ratio
mA	milliamp
mbicdt^{2-}	1-cyano-1(1-methyl-1H-benzimidazole)-2,2-ethenedithiolate
mcdt^{2-}	1-cyano-1-methyl-2,2-ethenedithiolate
mds^{2-}	2-hydrazono-3-bornanemethylenedithiolate
medt^{2-}	1-methylcarbonyl-1-ethoxycarbonyl-2,2-ethenedithiolate
Mes	mesityl
mfydt^{2-}	1-(2,7-dimethoxy-9*H*-fluoren-9-ylidene)-methylenedithiolate
mg	milligram

mL	millilitre
MLCT	metal-to-ligand charge transfer
mm	millimetre
mmol	millimole
mncda^{2-}	1-cyano-1(5-methyl-2-(1-methylethyl)-cyclohexanoxycarbonyl)-2,2-ethenedithiolate
mnt^{2-}	1,2-dicyano-1,2-ethenedithiolate
moepodt^{2-}	1-methoxycarbonyl-1-di(diethyl phosphite)-2,2-ethenedithiolate
MOF	metal-organic framework
mompodt^{2-}	1-methoxycarbonyl-1-di(dimethyl phosphite)-2,2-ethenedithiolate
ms	mesitylsulfonyl
mtdt^{2-}	1-(4,5-dimethyl-1,3-dithiol-2-ylidene)-methylenedithiolate
Naph	naphthyl
nbozdt2−	1-(4-(methylthio)-2-azetidin)-1-(p-nitrophenoxycarbonyl)-2,2-ethenedithiolate
NEXAFS	near-edge X-ray absorption fine structure
NIR	near infrared
nmnodt^{2-}	3,3-dithiolate-1-(6-methoxy-5-nitro-2-naphthalenyl)-2-propen-1-one
nmt^{2-}	1-nitro-2,2-ethenedithiolate
npidt^{2-}	6,6-dimethyl-bicyclo[3.1.1]heptan-2-one-3-methylenedithiolate
nps	naphthalen-1-ylsulfonyl
ocdt	1,2-carborane-1,2-dithiolate
optidt^{2-}	5-oxo-1-phenyl-2-thioxo-4-imidazolidinecarbodithiolate
otidt^{2-}	5-oxo-2-thioxo-4-imidazolidinecarbodithiolate
P	dipolar hyperfine coupling parameter
pdms^{2-}	1,2-phenylenedimethanesulfonamido
pepodt^{2-}	1-phenyl-1-di(diethyl phosphite)-2,2-ethenedithiolate
Ph	phenyl

PPh^{4+}	tetraphenylphosphonium
$ptdt^{2-}$	1,3-benzodithiole-2-methylenedithiolate
QTM	quantum tunnelling of magnetisation
$(r^{-3})_{av}$	averaged radial wave functions r^{-3} value
$rcdt^{2-}$	9,12-carborane-1,2-dithiolate
S	electronic spin
$\vec{S}$	electron spin operator
SAr^{-}	arylthiolate
$sded^{2-}$	1-ethoxycarbonyl-1-ethoxysulfonyl-2,2-ethenedithiolate
$shapdt^{2-}$	1-(4-(((1,1-dimethylethyl)dimethylsilyl)oxy)benzaldehyde)-2,2-ethenedithiolate
SIM	single-ion magnet
$smant^{2-}$	1-cyano-1-propanthioamide-2,2-dithiolate
SMM	single-molecule magnet
$STol^{-}$	*para*-tolylthiolate
T	Tesla
T_B	magnetic blocking temperature
$tbcdt^{2-}$	1-cyano-1-(1,1-dimethylethyl)-2,2-ethenedithiolate
$tbfydt^{2-}$	1-(2,7-bis(1,1-dimethylethyl)-9H-fluoren-9-ylidene)-methylenedithiolate
^{t}Buphs	4-tert-butylphenylsulfonyl
$teidt^{2-}$	1-(1,3-dihydro-1,3-diethyl-4,5-dimethyl-2H-imidazol-2-ylidene)-methylenedithiolate
THF	tetrahydrofuran
$tipidt^{2-}$	1-(1,3-dihydro-1,3-diisopropyl-4,5-dimethyl-2H-imidazol-2-ylidene)-methylenedithiolate
TM	transition metal
$tmidt^{2-}$	1-(1,3-dihydro-1,3,4,5-tetramethyl-2H-imidazol-2-ylidene)-methylenedithiolate

tmtu	1,1,3,3-tetramethylthiourea
tos	tosyl
tpa	tris(pyrrolylmethyl)amine
TTF	tetrathiafulvalene
U_{eff}	anisotropy barrier
UV-Vis	ultraviolet visible
XANES	X-ray absorption near-edge structure
XAS	X-ray absorption spectroscopy
ZFS	zero-field splitting
α	σ-bonding parameter
α'	ligand σ-bonding parameter
β	in-plane π-bonding parameter
δ	out-of-plane π-bonding parameter
ε	in-plane π-bonding parameter
μ_B	Bohr magneton
µm	micrometer
μ_N	nuclear magneton
ν	frequency
τ	magnetic relaxation time
φ	configurational excitation energy
χ	magnetic susceptibility
χ_D	diamagnetic susceptibility
χ_P	paramagnetic susceptibility

1 Introduction

Sulfur chemistry is some of the oldest found on Earth, and so influential the origins of life have been tied to iron-sulfur chemistry occurring billions of years ago.[1] Despite this sulfur chemistry has lagged somewhat behind that of carbon and other elements,[2] and whether due to misconceptions around the smell of sulfur-based compounds or for some other reason, it is only in recent years sulfur chemistry has truly flourished. Flourish it has however, with research yielding ever greater understanding of compounds showing fascinating, unusual and useful properties. Use of these properties in coordination chemistry stimulated the research here, which examines a series of homoleptic first-row transition metal species ligated by both mono- and dithiolate ligands along with the fascinating properties they exhibit, with the aim of synthesising new complexes with useful chemical and physical properties.

1.1 The Origins of Magnetism

A material is magnetised when its atomic dipoles (electrons) remain aligned, with χ defining the ease of alignment. When a material is placed in a homogeneous magnetic field, H, the atomic dipoles (electrons) in a material align and the sample acquires magnetisation, M. The response of M to H is magnetic susceptibility, χ, defined by Equation 1.1.[3]

$$\chi = \frac{dM}{dH} \tag{1.1}$$

Equation 1.1 holds until the magnetic field decreases such that χ becomes independent of H; at this point Equation 1.2 can be used.[3]

$$\chi = \frac{M}{H} \tag{1.2}$$

χ is the sum of the diamagnetic, χ_D, and paramagnetic, χ_P, susceptibilities, with net χ defined by Equation 1.3.[4]

$$\chi = \chi_D + \chi_P \tag{1.3}$$

χ_P arises a material has unpaired electrons that align in the direction of the magnetic field, causing a magnetic susceptibility with a positive value. χ_D arises when the electrons bound to the nucleus create a magnetic field in opposition to the external field. χ_D is thus negative[5] but also generally negligible, with χ typically calculated from χ_P.[4]

Bulk magnetic behaviour arises from long-range interactions between paramagnetic centres, manifest as ferromagnetism or antiferromagnetism (Figure 1.1b and Figure 1.1d). Ferromagnetism occurs when the centres align in parallel, antiferromagnetism when the alignment is anti-parallel.[6] Ferromagnetism gives a large net magnetic moment, antiferromagnetism a net magnetic moment of zero.

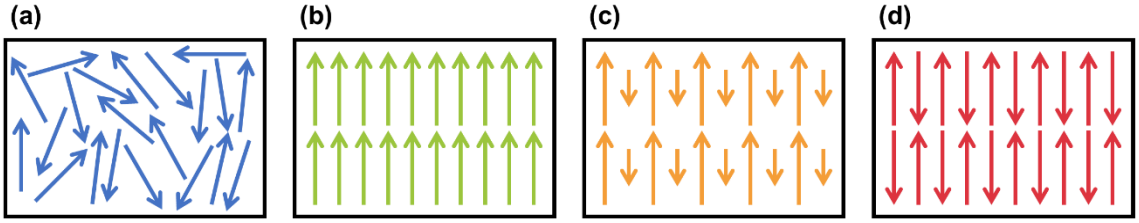

Figure 1.1 Illustration of (a) para-, (b) ferro-, (c) ferri- and (d) antiferromagnetism.

Ferrimagnetism (Figure 1.1c) is coupling with partial cancellation of magnetic moment, resulting in a reduced magnetic response with more complex temperature dependence.[7] For any of these interactions to occur long range coupling is necessary, requiring paramagnetic centres that can easily interact without interference: conventional magnets rely on cooperative interaction of magnetic particles at a macroscopy scale.

Magnetisation is due to an energy barrier (*vide infra*), which the system must overcome if equilibrium (Figure 1.1a) is to be restored. If the barrier is large enough, restoration of equilibrium requires application of a reverse magnetic field. In this case slow

magnetic relaxation causes hysteresis to be observed: a magnetic effect that can be manipulated for data storage.

1.2 The Future of Magnetic Data Storage

Drum memory was the first commercially successful application of magnetic recording principles described by Smith.[8] As drum memory gave way to ever faster and denser data storage methods truly remarkable advances were made,[9] with magnetic data storage now integrated into the fabric of our everyday lives, forming the bedrock on which society rests. The volume of data now used presents new challenges,[10] challenges that single-molecule magnets (SMMs) can help address.

SMMs are molecules that exhibit magnetic properties like hysteresis and slow magnetic relaxation.[11] They offer the possibility both of storing and processing information at far higher densities[12] and speeds[13] presently achievable, and the chance to use quantum mechanics to bypass the difficulties associated with such large volumes.[12] Novel molecular applications in areas such as spintronics[14] and quantum computing[15] are also possible, with SMMs showing potential as generalised qubits known as qudits.[16] They have recently been used in demonstrations of Grover's quantum search algorithm,[17] an algorithm showing the primacy of quantum versus classical computing.

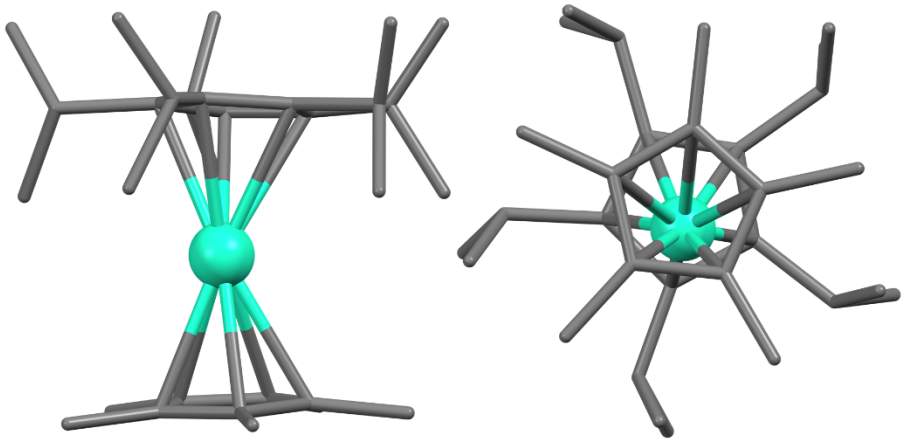

Figure 1.2 Perspectives of $[(Cp^{iPr5})Dy(Cp^{*})]^{+}$ side-on (left) and top-down (right) (dysprosium, teal; carbon, charcoal). Hydrogens atoms omitted for clarity.

The main limitation facing SMMs is the operating temperature, which for most SMMs remains low. Recent research into Ln-based SMMs has given impressive results, with the recent report of $[(Cp^{iPr5})Dy(Cp^{*})]^{+}$ (Cp^{iPr5} = C_5-1,2,3,4,5-$^{i}Pr_5$; Cp* = C_5-1,2,3,4,5-Me_5; Figure 1.2) the first of a "high-temperature" SMM functioning above 77 K.[18] Interest into transition metal (TM) SMMs remains however, as unlike Ln SMMs TM SMMs are known to function in the absence of an applied magnetic field.[19] Furthermore, the ease of 3d orbital manipulation ensures first row TMs remain attractive targets for the rational design of high-performance SMMs.[20] Mononuclear species are easiest to manipulate and as such recent TM SMMs research has focused on 3d single-ion magnets (SIMs).

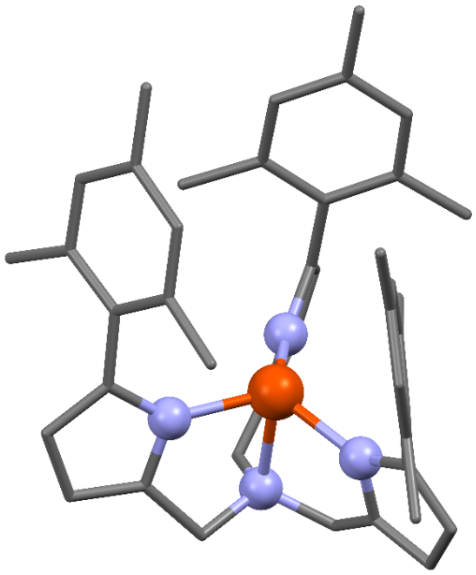

Figure 1.3 Molecular structure of $[(tpa^{Mes})Fe]^{-}$ (iron, orange; nitrogen, cornflower; carbon, charcoal). Hydrogen atoms omitted for clarity.

Specific structural and electronic properties have especially favoured the development of Fe^{II} and Co^{II} SIMs, with $[(tpa^{Mes})Fe]^{-}$ (tpa = tris(pyrrolylmethyl)amine; Mes = mesityl; Figure 1.3) the first recorded 3d SIM.[21] Although generating a great deal of interest, $[(tpa^{Mes})Fe]^{-}$ does not show slow magnetic relaxation in the absence of an applied field; such behaviour was first observed in $[Co(SPh)_4]^{2-}$.[19] With typical values of S = 2 and S = $^{3}/_{2}$ respectively, the fundamental difference between Fe^{II} and Co^{II} is the spin state (S). To behave as a magnet a complex must have two stable polar states: as Co^{II} has a half-

integer ground state, it is a Kramers' ion and will be bistable regardless of the ligand field (LF).[22]

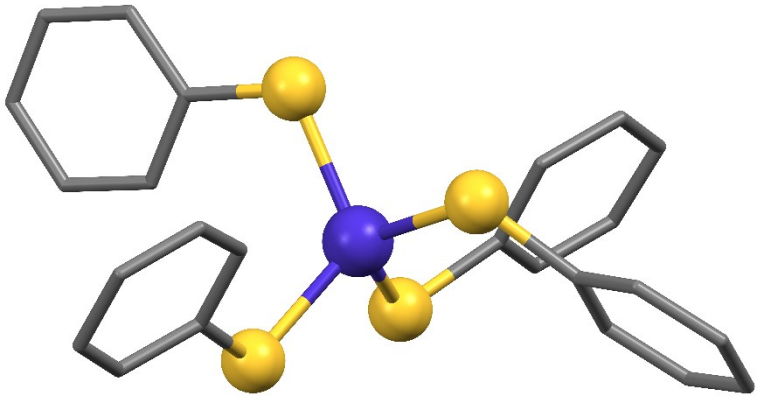

Figure 1.4 Molecular structure of $[Co(SPh)_4]^{2-}$ (cobalt, grape; sulfur, pineapple; carbon, charcoal). Hydrogen atoms omitted for clarity.

The bistability of $[Co(SPh)_4]^{2-}$ (Figure 1.4) means it behaves as an SMM in zero applied field, but the research aimed to improve SIM performance more broadly.[19]

1.3 Single-Molecule Magnet Performance

There are three main metrics of measuring of SMM performance. The first is the effective energy barrier to the reversal of magnetisation (the anisotropy barrier; U_{eff}), the energy needed to convert an SMM back into a paramagnet. This is the most common metric, with a large U_{eff} necessary to observe SMM behaviour at higher temperatures. The second metric is the coercive magnetic field (H_C), the field strength required to drive magnetisation from saturation to zero. The final metric is the magnetic blocking temperature (T_B), the highest temperature an SMM exhibits hysteresis (where magnetisation loss after saturation fails to keep pace with the magnetic field, forming a loop) in the plots of M vs H (Figure 1.5). Lack of standardisation hinders this latter metric, however, as T_B strongly depends on the magnetic field sweep rate. Defining T_B as the temperature where the magnetic relaxation time (τ) is 100 s has been suggested,[23] but not widely adopted.

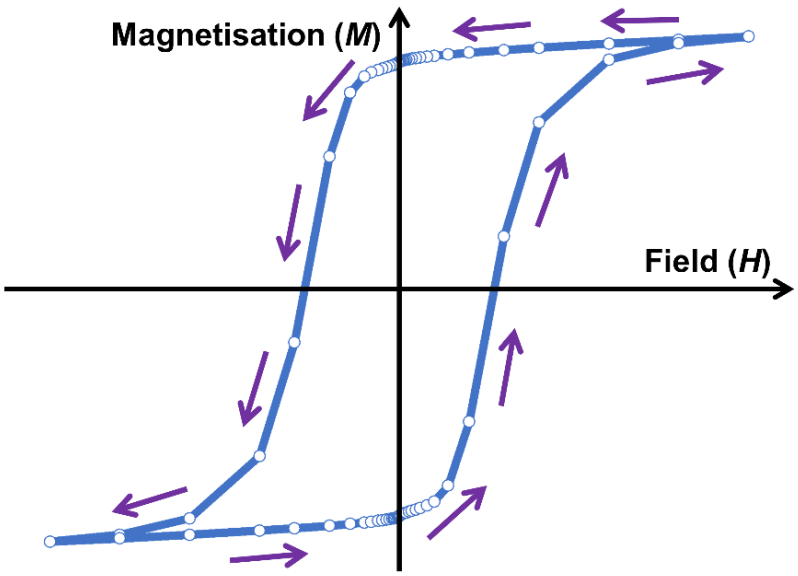

Figure 1.5 Magnetic hysteresis loop.

Some SMMs have been characterised using the latter two measurements but the occurrence of quantum tunnelling of magnetisation (QTM) has limited adoption. As discussed above, magnetisation relies on an energy barrier the system must overcome to restore equilibrium. In SMMs this is the U_{eff}, defined by Equations 1.4 and 1.5, for systems with integer and half-integer S, respectively.[24]

$$U_{\text{eff}} = S^2|D| \tag{1.4}$$

$$U_{\text{eff}} = \left(S^2 - \frac{1}{4}\right)|D| \tag{1.5}$$

The interaction between the electronic spins and their magnetic field is the anisotropy, known as zero-field splitting (ZFS) and parameterised by *D*. Anisotropy is where the coupling of lower lying excited states in a system with $S > {}^1/_2$ with the ground state through spin orbit coupling causes the ground states of a single ion to split into $2S+1$ non-degenerate $\pm m_s$ levels (Figure 1.6).[25]

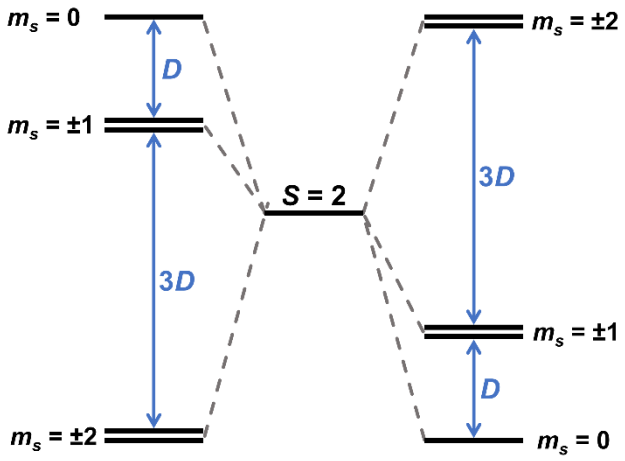

Figure 1.6 Zero-field energy level (m_S) splittings in zero-field for a spin triplet with negative (left) and positive *D* (right).

The preferred orientation has the hard plane of the complex aligned perpendicular to the easy axis, along which the potential energy of the magnetic moment will be lowest; the spin orientation (magnetic moment) potential energy can thus be represented by a double energy well separated by the U_{eff} (Figure 1.7a).[26]

There are several ways a magnetised SMM can relax. Slow magnetic or Orbach-type relaxation is dominant mechanism at higher temperatures, involving thermal activation over the energy barrier until equilibrium is restored (Figure 1.7c).[27] Another process is two-

phonon Raman-type relaxation. More complex than Orbach-type relaxation, it shows a power law dependence on temperature of CT^n, where C and n are variables.[28]

The final process is fast magnetic relaxation, commonly known as quantum tunnelling of magnetisation (QTM), that occurs when spins relax without crossing the anisotropy barrier, resulting in a loss of magnetisation regardless of U_{eff}. QTM occurs when two degenerate spin states are able to spin state mix, allowing spins to move between the $-S$ and $+S$ states without crossing the U_{eff} (Figure 1.7c). Hysteresis in which QTM occurs are not completely smooth, exhibiting small jumps at critical field values where spin states mix.[4] Furthermore, as QTM does not cross the anisotropy barrier, when the spins lack energy to relax conventionally at lower temperatures it dominates magnetic behaviour.[7]

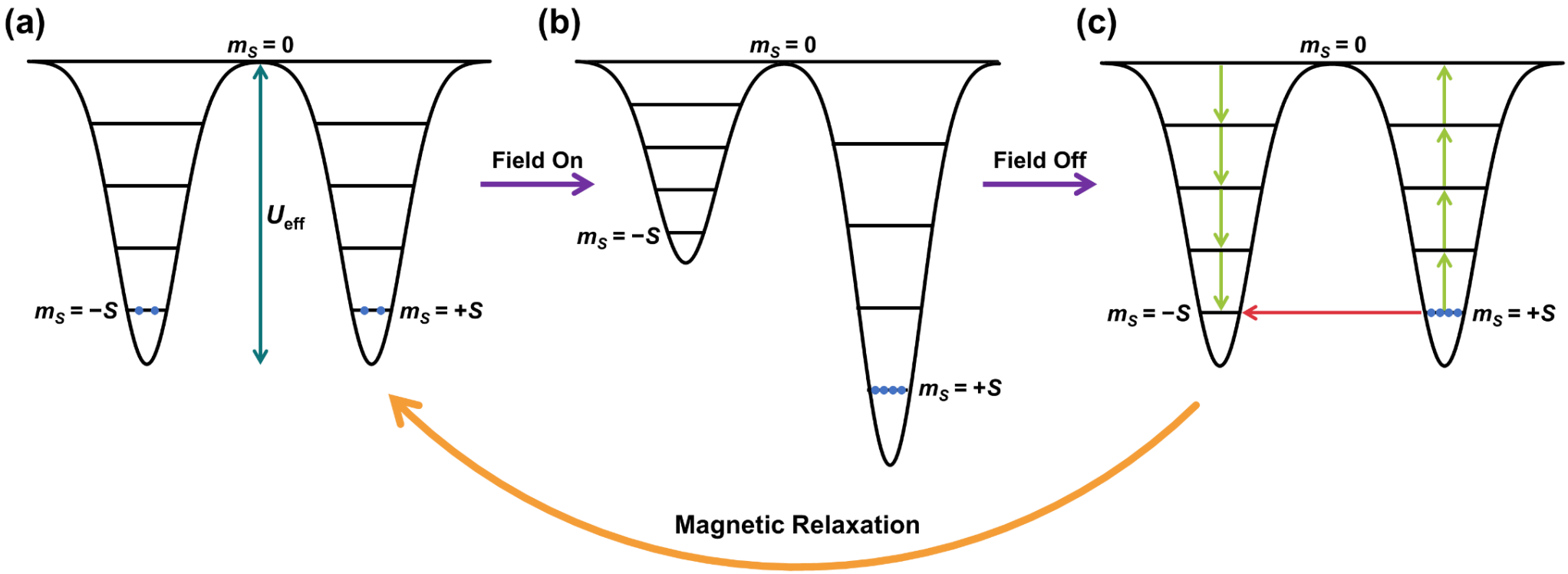

Figure 1.7 Magnetisation and relaxation of a single-molecule magnet: (a) at equilibrium, (b) under an applied field and (c) magnetised. Effective energy barrier (U_{eff}) is indicated in teal, slow magnetic relaxation in green and fast magnetic relaxation (QTM) in red

The different relaxation mechanisms can be manipulated for different purposes. Theoretically, manipulation of U_{eff} allows slow magnetic relaxation to be harnessed to allow magnetic data storage at various temperatures. Although studies of Raman-type relaxation are commonly used to provide insight into vibrational modes of a material, in molecular magnetism it is deleterious, becoming one of the dominant relaxation processes at higher U_{eff} values.[28] Raman-type relaxation has been a focus of recent research, which has shown it to be strongly supressed in exchange-coupled $[\{(H_2tmsb^{2-})Co^{II}\}_2(\mu\text{-}tmsb^{3\bullet-})]^{3\bullet-}$ (H_4(tmsb) = 1,2,4,5-tetrakis(methanesulfonamido)benzene; Figure 1.8).[29]

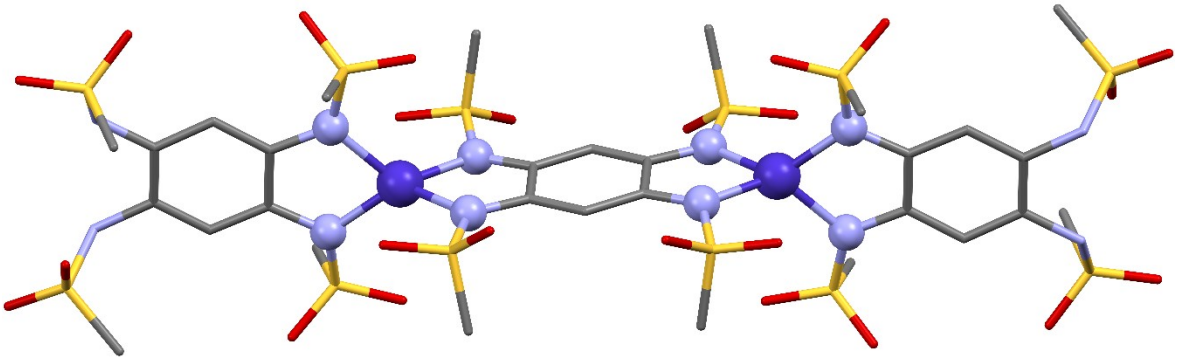

Figure 1.8 Molecular structure of $[\{(H_2tmsb^{2-})Co^{II}\}_2(\mu\text{-}tmsb^{3\bullet-})]^{3\bullet-}$ (cobalt, grape; sulfur, pineapple; nitrogen, cornflower; oxygen, scarlet; carbon, charcoal). Hydrogen atoms omitted for clarity.

QTM stems from mixing of the $\pm m_S$ levels via hyperfine interactions, dipolar interactions or transverse anisotropy (E),[30] and is also inimical to SMM performance. It can be limited through three main ways: applying a magnetic field so the ground states are isolated, ensuring significant separation between molecules or by using a half-integer spin system, for which Kramers' theorem predicts mixing of the ground $\pm m_S$ states by E to be forbidden.[31] The latter reasons were why $(PPh_4)_2[Co(SPh)_4]$ was first investigated: the Kramers' Co^{II} ensured slow magnetic relaxation in the absence of an applied field, whilst Zn^{II} dilution significantly reduce QTM.[19] With QTM attenuated, the large negative D reported[32] for $(PPh_4)_2[Co(SPh)_4]$ was hoped to increase U_{eff}, concomitantly improving SIM performance.

1.4 Single-Ion Magnets

Slow magnetic relaxation in 3d SIMs remains relatively rare, with most species building on the original $[Co(SPh)_4]^{2-}$.[19] With QTM attenuated in Co^{II} SIMs, research turned to increasing U_{eff} to improve SIM performance. Historically the relationship between U_{eff} and S (Equations 1.4 and 1.5) meant research focussed on increasing S. Initially moderately successful, the shortcomings of the approach were illustrated when $[Mn_{19}(\mu_4\text{-}O)_8(\mu_3,\eta_1\text{-}N_3)_8(Hbhmp)_{12}(MeCN)_6]^{2-}$ (H_3bhmp = 2,6-bis(hydroxymethyl)-4-methylphenol; Figure 1.9) was discovered: an $S = {}^{83}/_2$ aggregate with $U_{eff} = 4$ cm^{-1}.[33]

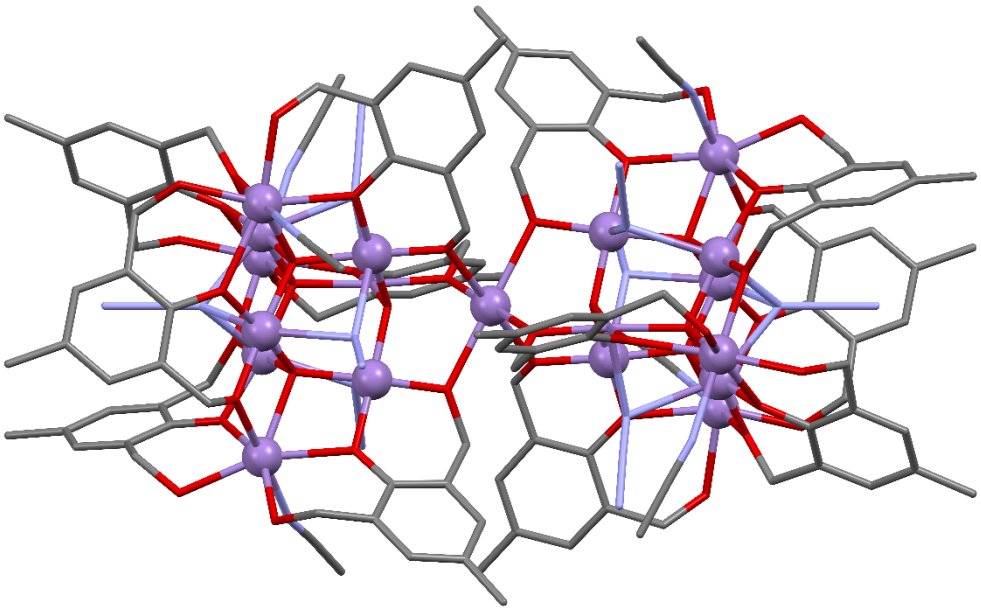

Figure 1.9 Molecular structure of $[Mn_{19}(\mu_4\text{-}O)_8(\mu_3,\eta_1\text{-}N_3)_8(Hbhmp)_{12}(MeCN)_6]^{2-}$(manganese, lavender; nitrogen, cornflower; oxygen, scarlet; carbon, charcoal). Hydrogen atoms omitted for clarity.

S was found to correlate inversely to D,[34] so in line with the broader trend change and with $S = {}^3/_2$ typically fixed, Co^{II} SIM research focussed instead on increasing U_{eff} by increasing D through manipulation of the LF. The stronger the LF, the more mixing of excited and ground states, the larger D. In Co^{II} SIMs this can be achieved by changing either the coordination geometry or donor atoms.

1.4.1 Donor Atom Influence on Axial Anisotropy

The positive correlation between *D* and LF strength was first highlighted by Long *et al.*,[35] with a study of $[Co(EPh)_4]^{2-}$ = (E = O, S, Se) by Zadrozny *et al.* linking donor-atom softness to *D* directly. With the hardest donor-atoms $[Co(OPh)_4]^{2-}$ has $D = -11.1$ cm^{-1}, which increases across the series to $D = -83$ cm^{-1} in $[Co(SePh)_4]^{2-}$;[36] an even larger value was calculated for $[Co(TePh)_4]^{2-}$.[37] Later studies have supported this, with *D* decreasing from +9.2 to −74.7 cm^{-1} and −11.6 to −36.9 cm^{-1} as donor-atom softness increases in $[Co(L_{Pn})_2I_2]$ (L_{Pn} = quinoline, PPh_3, $AsPh_3$) and $[Co(PPh_3)_2X_2]$ (X = Cl, Br, I), respectively.[38] The trend is not universal for halide ligands, with $D = +10.5$, +12.5 and +10.3 cm^{-1} for $[Co(biq)X_2]$ (biq = 2,2′-biquinoline; X = Cl, Br, I) respectively,[39] but appears consistent for chalcogen ligands.

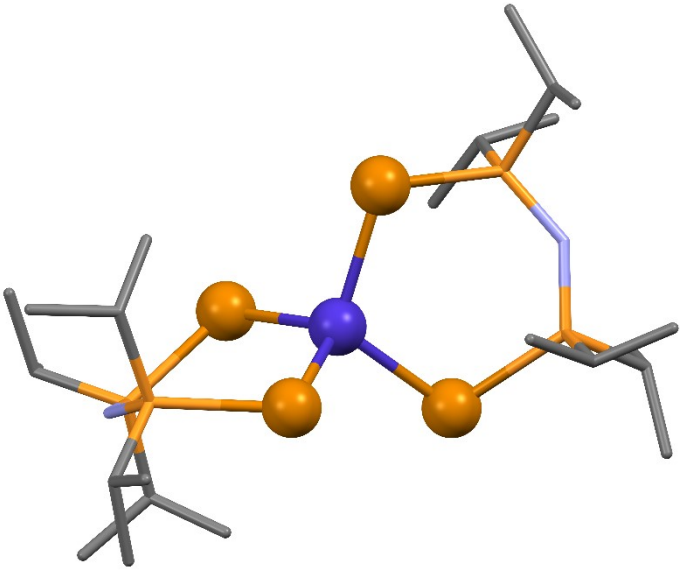

Figure 1.10 Molecular structure of $[Co(\{TeP^iPr_2\}_2N_2)]$ (cobalt, grape; tellurium, bronze; phosphorus, carrot; nitrogen, cornflower; carbon, charcoal). Hydrogen atoms omitted for clarity.

However, although higher anisotropy should be more easily accessible with softer chalcogens, beyond $[Co(SePh)_4]^{2-}$ only one Te-ligated[40] (Figure 1.10) and three Se-[40-42] Co^{II} SIMs are known. Synthetic difficulties associated with the elements has likely stymied research, but the rich vein of S-based Co^{II} SIM research remaining will also have played a

role. Whilst $[Co(SPh)_4]^{2-}$ has been investigated further,[43,44] the field has broadened hugely and given exciting results.

Among the S-based Co^{II} SIMs reported was a series of thiourea complexes with *D* values ranging from −21.3 to −80.7 cm^{-1}. Noting the origin of *D* in first-coordination sphere interactions, the series also proved the importance of the second-coordination sphere such that $[Co(dbtu)_4]^{2+}$ (dbtu = 1,3-dibutylthiourea; Figure 1.11) showed zero-field SMM behaviour with a large U_{eff}, whilst $[Co(tmtu)_4]^{2+}$ (tmtu = 1,1,3,3-tetramethylthiourea) only behaved as an SMM in an applied field.[45]

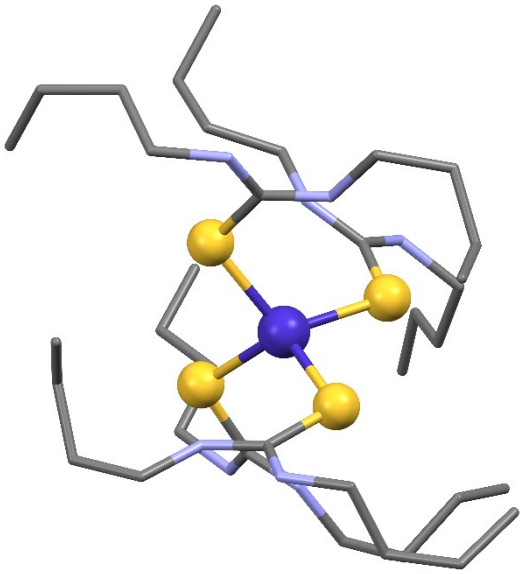

Figure 1.11 Molecular structure $[Co(dbtu)_4]^{2+}$ (cobalt, grape; sulfur, pineapple; nitrogen, cornflower; carbon, charcoal). Hydrogen atoms omitted for clarity.

A follow-up investigation of $[Co(L_{tu})_2X_2]$ (L_{tu} = thiourea, 1,1,3,3-tetramethylthiourea; X = Cl, Br, I) confirmed the importance of the secondary coordination sphere, with slower relaxation times observed for tetramethyl-substituted than the unsubstituted species.[46] Similar trends are observed in $[Co(bmim)_2X_2]$ (bmim = 1-benzyl-2-methylimidazole; X = SCN, NCO, N_3), where *D* correlates with the size of the non-coordinated pseudohalide atoms.[47]

Aware of the importance of donor-atom softness and on LF strength and the need to be aware of factors beyond the first coordination sphere, the possibility of tailoring geometry to maximise *D* was investigated.

1.4.2 Anisotropy and Geometry

The presence of unquenched orbital angular momentum means complexes with lower coordination numbers generally have higher anisotropies. That said, a variety of complex geometries show large magnetic anisotropy, with symmetry determining *D*.[48,49]

1.4.2.1 Two-Coordinate Single-Ion Magnets

Early research into SIM geometries focused on minimising the coordination number, with some success. A series of linear two-coordinated Fe^{II} complexes came first in 2013,[50] followed soon after by linear or near-linear Fe^{I}, Co^{I} and Ni^{I} species.[51-53] The first notable success was $[Fe\{C(SiMe_3)_3\}_2]^-$ (Figure 1.12), an Fe^{I} complex with U_{eff} = 226 cm^{-1} that briefly held the record U_{eff} for a TM SIM.[51]

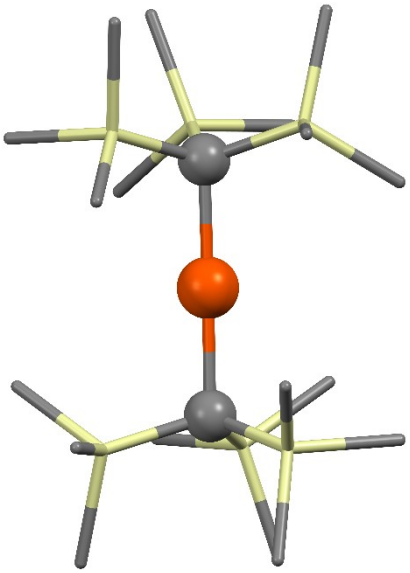

Figure 1.12 Molecular structure $[Fe\{C(SiMe_3)_3\}_2]^-$ (iron, orange; silicon, cream; carbon, charcoal). Hydrogen atoms omitted for clarity.

As in Co^{II}, the $S = {}^3/_2$ ground state minimises QTM in $[Fe\{C(SiMe_3)_3\}_2]^-$, which shows slow magnetic relaxation in the absence of an external magnetic field.[54] Linear Fe^{II} complexes do not show such behaviour,[50] which is also not inherent to linear Fe^{I} species: a strong applied magnetic field is necessary to observed the minute U_{eff} of $[Fe(caac)_2]^+$ (caac = cyclic alkyl(amino)carbene; Figure 1.13).[55]

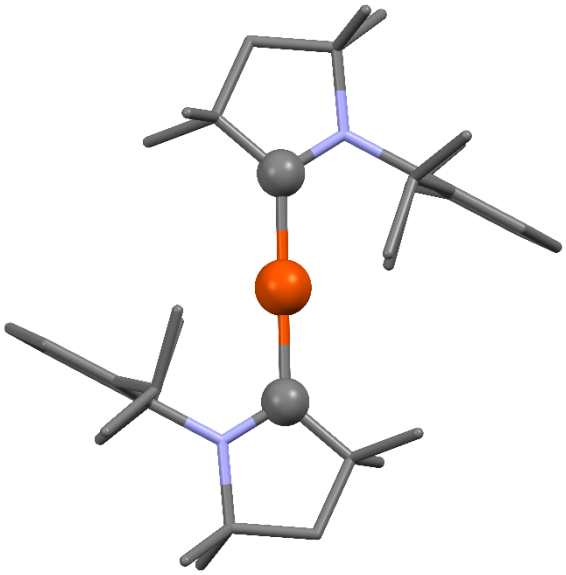

Figure 1.13 Molecular structure $[Fe\{C(SiMe_3)_3\}_2]^-$ (iron, orange; nitrogen, cornflower; carbon, charcoal). Hydrogen atoms omitted for clarity.

Furthermore, minor deviations from ideal $D_{\infty h}$ symmetry severely curtail anisotropy, with orbital angular momentum and anisotropy quenched in complexes such as $[Fe\{N(H)Ar^{\#}\}_2]$ ($Ar^{\#} = C_6H_3$-2,6-(C_6H_2-2,4,6-$Me_3)_2$), with a L−M−L bond angle of 140.9°.[50]

Such behaviour is observed in a series of dioxocobaltate SIMs doped into apatite lattices. Although whether the complexes can be considered true SIMs is ambiguous, the dramatic decrease in U_{eff} as the distortion away from a L−M−L bond angle of 180° is remarkable. The initial species has a O−Co−O angle of 156° and U_{eff} = 387 cm^{-1},[56] which then decreases to 254 cm^{-1} for a O−Co−O angle of 150°[57] and ~63 cm^{-1} for 149°.[58] However, the ambiguity of the SIM status of the complex and the differing host matrices means the trend should be noted, but not over-interpreted. Linear Co^{II} SIM performance is

illustrated more clearly by [Co{C(SiMe$_2$ONaph)$_3$}$_2$] (Naph = naphthyl), which with U_{eff} = 450 cm^{-1} currently has the largest U_{eff} of any TM SMM.[59]

1.4.2.2 Three-Coordinate Single-Ion Magnets

The practicality of linear two-coordinate TM SIMs is hampered by their air-sensitivity and the extreme sensitivity of the coordination environment. Furthermore, the coordination environment reduces LF effects,[49] preventing quenching of the orbital contributions to the magnetic moment: the possible presence of first order orbital angular momentum complicates analysis.[60] Alternative coordination environments can address these issues, with high-anisotropy complexes accessible in a variety of higher coordination number environments.

As the structural formula of [Fe(N{SiMe$_3$}$_2$)$_3$] (Figure 1.14) was first reported in 1969,[61] it is not surprising the first three-coordinate SIM was the related [Fe{N(SiMe$_3$)}$_2$(PCy$_3$)] (Cy = cyclohexyl).[62] Whilst behaving as an SIM under an applied field the precise D and U_{eff} values are uncertain, with two different values reported.[62,63]

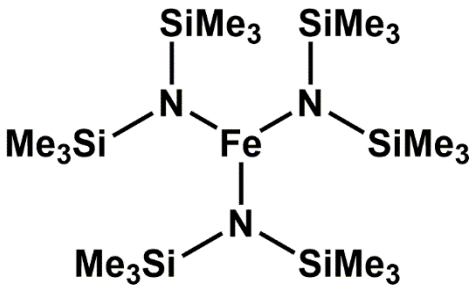

Figure 1.14 Structural formula of [Fe(N{SiMe$_3$}$_2$)$_3$]

The first trigonal-planar Co^{II} SIMs were [Co{N(SiMe$_3$)}$_2$L] (L = PMe$_3$, THF, pyridine and N(SiMe$_3$)$_2$), reported by Phil Power *et al.*; although U_{eff} data was absent, D values between −62 and −82 cm^{-1} were reported.[64] U_{eff} values for [Co{N(SiMe$_3$)}$_2$L] (L = PCy$_3$ and THF) were provided by Eichhöfer *et al.*, alongside data for [Co{N(SiMe$_3$)}$_3$]. Although the reported U_{eff} values are modest, large negative D values between −57 and −82 cm^{-1} were

confirmed.[63] Large negative *D* values of −85.4 and −80.6 cm^{-1} are also observed in the two trigonal-planar Co^{II} SIMs reported since.[65]

Non Fe^{II} or Co^{II} three-coordinate SIMs are rare, but Fe^{III} and Ni^{I} species have been reported,[66,67] although with poorer performance than comparable Co^{II} species.

1.4.2.3 Four-Coordinate Single-Ion Magnets

Although some three-coordinate SIMs have reasonable *D* values, such species suffer from the same stability issues as two-coordinates systems. Dovetailing with $[Co(SPh)_4]^{2-}$ research (*vide supra*), focus turned to four-coordinate and higher systems. Although higher-coordinate SIMs with large anisotropies and U_{eff} values have been reported, principles derived from four-coordinate species informed the research here. Four-coordinate SIMs will thus be covered before discussing these principles rather than higher-coordinate SIM performance.

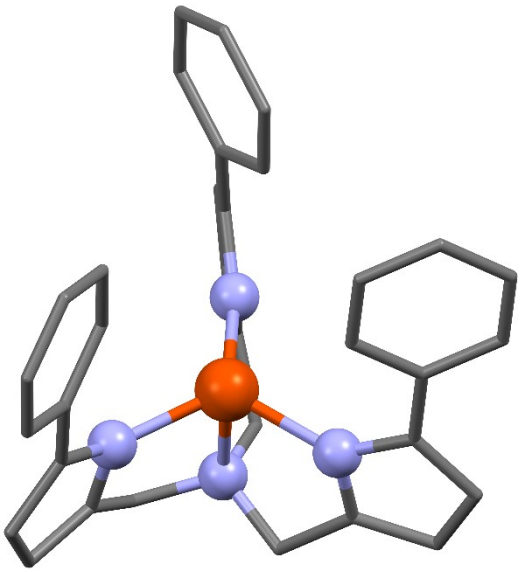

Figure 1.15 Molecular structure of $[(tpa^{Ph})Fe]^-$ (iron, orange; nitrogen, cornflower; carbon, charcoal). Hydrogen atoms omitted for clarity.

The geometries of four-coordinate SIMs range the trigonal pyramidal geometry of $[(tpa^{Mes})Fe]^-$ (see above) to tetrahedral and square planar environments. The variety of coordination environments allows access to an array of high-anisotropy TM SIMs

geometries; as a result, compared to two- and three-coordinate SIMs, four-coordinate species are super-abundant. As noted, Long *et al.* first highlighted the link between LF strength and *D*.[35] Proof came from a series of trigonal pyramidal Fe^{II} complexes, where it was shown the lower *D* of $[(tpa^{Ph})Fe]^-$ (Figure 1.15) compared $[(tpa^{t\text{-}Bu})Fe]^-$ meant that despite possessing crystallographically imposed three-fold symmetry, $[(tpa^{Ph})Fe]^-$ has the smaller U_{eff}.[35]

Although trigonal pyramidal Fe^{II} complexes show large negative *D* values,[48] Co^{II} species do not: the three trigonal pyramidal Co^{II} SIMs all show small positive *D* and modest U_{eff} values under applied fields. The first species reported was $[Co\{N(CH_2CONC(CH_3)_3)_3\}]^+$, with $D = +16\ cm^{-1}$ and $U_{eff} = 8.7\ cm^{-1}$,[48] followed by $[Co\{(Me_3SiNCH_2CH_2)_3N\}Li(THF)]$, with a larger $D = +27\ cm^{-1}$ and a higher anisotropy barrier of $U_{eff} = 18\ cm^{-1}$.[68] Still larger values of $D = +33\ cm^{-1}$ and $U_{eff} = 33\ cm^{-1}$ were reported for the mst^{3-} (H_3mst = N,N′,N″-[2,2′,2″-nitrilotris-(ethane-2,1-diyl)]tris(2,4,6-trimethylbenzenesulfonamide; Figure 1.16) ligated Co^{II} species.

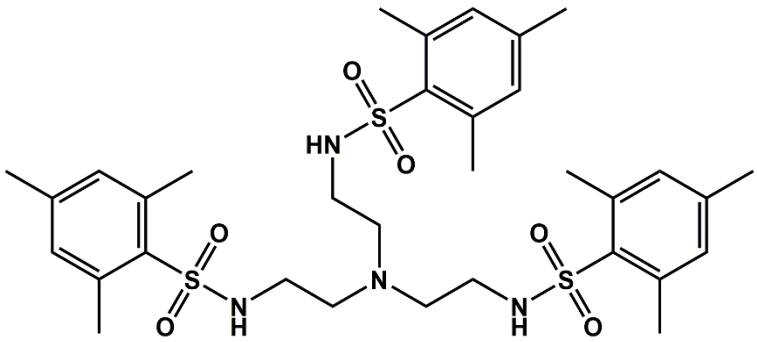

Figure 1.16 Structural formula of the neutral H_3mst ligand

The mst^{3-} species are noteworthy as, although the *D* and U_{eff} values reported for $[Co(mst)]^+$ are modest, a near record negative *D* of $-434\ cm^{-1}$ is reported for $[Ni(mst)]^+$. Despite this, the Ni^{II} species did not show slow magnetic relaxation under any circumstances and so cannot be considered an SIM.[69]

The only square-planar TM SIMs known are the Cr^{II} species $[Cr(N(SiMe_3)_2)_2(L_S)_2]$ (L_S = pyridine, THF; Figure 1.17); SIM performance is poor, with the best performance of $D = -2.54$ cm^{-1} and $U_{eff} = 8.2$ cm^{-1} recorded for $[Cr(N(SiMe_3)_2)_2(THF)_2]$.[70]

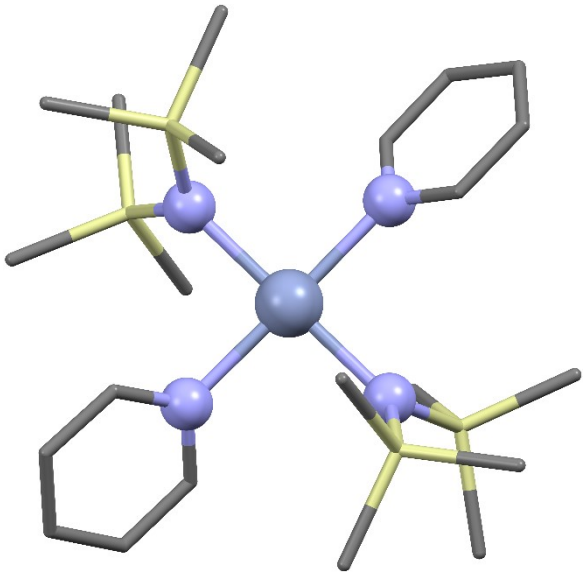

Figure 1.17 Molecular Structure of $[Cr(N(SiMe_3)_2)_2(L_S)_2]$ (chromium, aegean; nitrogen, cornflower; silicon, cream; carbon, charcoal). Hydrogen atoms omitted for clarity.

Building on the studies of $[Co(SPh)_4]^{2-}$ (see above),[19] research into tetrahedral and pseudotetrahedral TM SIMs has given impressive results. Although an air-stable complex showing slow magnetic relaxation in zero field with high anisotropy of $D = -62$ cm^{-1}, at 21.2 cm^{-1} the U_{eff} in $[Co(SPh)_4]^{2-}$ is unexceptional. The large D parameter was found to arise from distortions away from T_d to D_{2d} generating a low lying excited state, boosting anisotropy by increasing the frequency of spin conserving transitions.[19] Attempts to increase D in Co^{II} SIMs by increasing the distortion toward D_{2d} have thus occurred, taking advantage of the control over coordination geometry offered by bidentate ligands.

1.5 Co^{II} Single-Ion Magnets with Bidentate Ligands

Aiming to find a complex with the geometry and electronic structure required for large negative *D*, attention turned to pseudotetrahedral Co^{II} complexes with two small bite-angle bidentate ligands.[71] With distorted D_{2d} geometry caused by metal-ligand bite-angles of ~94° the 1,2-dithiolate complex $[Co(dmit)_2]^{2-}$ ($dmit^{2-}$ = 4,5-dimercapto-1,3-dithiole-2-thione) matched the criteria and proved the worth of the guiding principles. Although at U_{eff} = 33.9 cm^{-1} the effective energy barrier is not huge, the complex has D = −161 cm^{-1} – a remarkably high value for an air-stable species.[71]

The principles were confirmed in a following study of $[Co(pdms)_2]^{2-}$ ($pdms^{2-}$ = 1,2-phenylenedimethanesulfonamido; Figure 1.18). With greater D_{2d} geometry facilitated by the metal-ligand bite-angle of ~81°. Although at D = −115 cm^{-1} the anisotropy is smaller than $[Co(dmit)_2]^{2-}$, with U_{eff} = 118 cm^{-1} the complex has one of the largest anisotropy barriers reported for a Co^{II} SIM to date.[60]

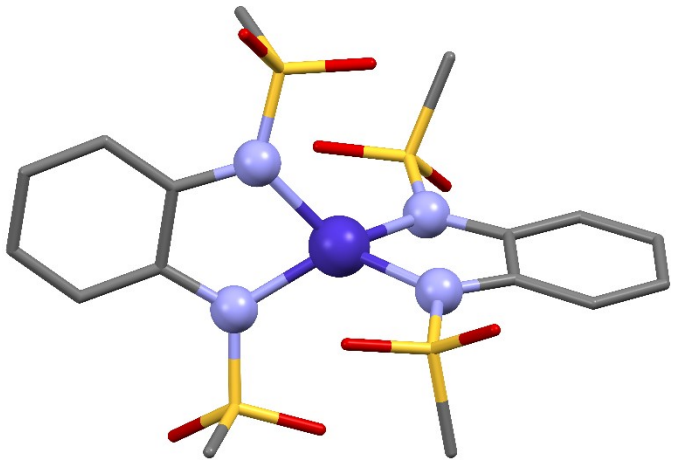

Figure 1.18 Molecular structure of $[Co(pdms)_2]^{2-}$ (cobalt, grape; sulfur, pineapple; nitrogen, cornflower; oxygen, scarlet; carbon, charcoal). Hydrogen atoms omitted for clarity.

The combination of strong axial distortion with the strong LF from the bis(sulfonamido) ligands proves crucial to the energy barrier, with Co^{II} SIMs lacking either showing reduced performance. Ensuring both characteristics has yielded some impressive

results however, with bidentate-ligated Co^{II} SIMs with high axial anisotropy shown in Table 1.1 alongside data for $[Co(SPh)_4]^{2-}$ and $[Co(SePh)_4]^{2-}$.

Table 1.1 High axial anisotropy (> −45 cm^{-1}) pseudotetrahedral Co^{II} SIMs

	U_{eff} / cm^{-1}	D / cm^{-1}	Reference
$[Co(dmit)_2]^{2-}$	33.9	−161	71
$[Co(pdms)_2]^{2-}$	118	−115	60
$[Co(SePh)_4]^{2-}$	19.1	−83	36
$[Co(H\{C_6N_2H_5\}dnps)_2]$	127.7	−91.9	72
$[Co(AsPh_3)_2I_2]$	32.6	−74.7	38
$[Co(ocdt)_2]^{2-}$ [a]	26.8	−71.6	73
$[Co(H\{C_6N_2H_5\}ms)_2]$ [b]	89.7	−64.5	72
$[Co(SPh)_4]^{2-}$	21	−62	19, 36
$[Co(H\{C_6N_2H_5\}^tBuphs)_2]$ [c]	81.3†	−58.5	72
$[Co\{(N^tBu)_3SMe\}_2]$	75	−58	74
$[Co(H\{C_6N_2H_5\}tos)_2]$ [d]	80.2	−57.7	72
$[Co(H\{C_6N_2H_5\}nps)_2]$ [e]	75.2	−54.1	72
$[Co(Me\{C_6N_2H_5\}^tBuphs)_2]$ [c]	70.2	−50.5	72
$[Co\{(TeP^iPr)_2N\}_2]$	16	−45.1	40

† Under an applied magnetic field; [a] ocdt = 1,2-carborane-1,2-dithiolate; [b] ms = mesitylsulfonyl; [c] ^{t}Buphs = 4-*tert*-butylphenylsulfonyl; [d] tos = tosyl; [e] nps = naphthalen-1-ylsulfonyl

Carborane-1,2-dithiolate ligands potentially meet both conditions. So far, the only species synthesised and fully characterised is $[Co(ocdt)_2]^{2-}$ ($ocdt^{2-}$ = 1,2-carborane-1,2-dithiolate), with anisotropy of D = −71.6 cm^{-1} and U_{eff} = 26.8 cm^{-1}.[73] Computational studies note the importance of coordination geometries however, predicting a far larger axial anisotropy of −147.2 cm^{-1} for the most distorted D_{2d} $[Co(ocdt)(rcdt)]^{2-}$ ($rcdt^{2-}$ = 9,12-carborane-1,2-dithiolate); D = −43.5 cm^{-1} is calculated for the least distorted bis(9,12-carborane-1,2-dithiolate) species.[75] Similar results are reported in a broader computational study of twenty icosahedral and octahedral Co^{II} carborane complexes.[76]

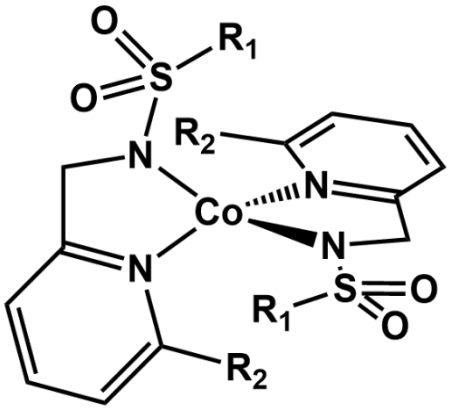

Figure 1.19 The parental Co^{II} bis(N-(pyridine-2-ylmethyl)-sulfonamide) framework.

Better results centre around the monoanionic N-(pyridine-2-ylmethyl)-sulfonamide ligand framework, with several $[Co(R_1\{C_6N_2H_5\}R_2)_2]$ (Figure 1.19) SIMs showing high anisotropy. With D = −91.9 cm^{-1}, the best performing species was $[Co(H\{C_6N_2H_5\}dnps)_2]$ (dnps = 5-(dimethylamino)naphthalen-1-ylsulfonyl), which with U_{eff} = 127.7 cm^{-1} has the current record anisotropy barrier for a pseudotetrahedral TM SIM.[72]

A unique approach to maximising D was taken in $[Co\{(N^tBu)_3SMe\}_2]$,[74] where the acute N−Co^{II}−N ligand bite-angles offered by triimidosulfonates were used to maximise distortion away from T_d toward D_{2d} and C_{2v}. Although giving reasonably successful results of D = −58 cm^{-1} and U_{eff} = 75 cm^{-1}, the monoanionic ligands limited charge-density on the metal centre, despite metal-ligand bite-angles of ~71°.[74]

1.6 Rational Design of Co^{II} Single-Ion Magnets

The examination of the SIMs performed above establishes a set of principles for rationally designing Co^{II} SIMs. As Co^{II} SIMs in D_{2d} coordination environments provide the most stable platform for constructing high-anisotropy species, ligand choice must centre around maximising distortion towards D_{2d}. Furthermore, as the approach relies on maximising the charge density on the Co^{II}, where possible dianionic ligands must be used. The final synthetic principle notes the influence of donor atom softness on axial anisotropy, requiring that the softest possible ligands be used. Frequent use of Te or Se based ligands is impractical, but S-based ligands show promise: they are easier to work with whilst outperforming O-based systems (see above). Furthermore, with larger 3p orbitals they should outperform N-based ligands. An ideal ligand system would therefore be a dianionic S-based system, with acute metal-ligand bite-angles.

1.6.1 Sulfur Ligands for Co^{II} Single-Ion Magnets

Although sulfur chemistry is well-established, the electronic properties of S ligand systems are less understood meaning that despite the variety of ligands available, rational employment in SIMs is challenging. The thiourea complexes discussed above neatly illustrate the challenges, with the substituents profoundly impacting the SIM properties in hard-to-predict ways. Thus, whilst attempting to create the ideal ligand system Co^{II} SIM research should examine platforms offering the control over metal-ligand bite-angles, it is also important to look at properties beyond the first coordination sphere.

As mentioned, the most desirable ligand systems maximise S charge density. Considering this, fully reduced arylthiolates (Figure 1.20a) present an attractive platform for studying changes to the second coordination sphere. As the archetypal TM SIM, the unsubstituted $[Co(SPh)_4]^{2-}$ is well studied,[19,36,43] whilst modified arylthiolates should retain D_{2d} coordination environments, with the only differences being the changed substituents. Many areas of research note the impact of changes to the second coordination sphere, and

$[Co(SAr)_4]^{2-}$ systems will allow their impact on the electronic structure of a Co^{II} SIM to be assessed.

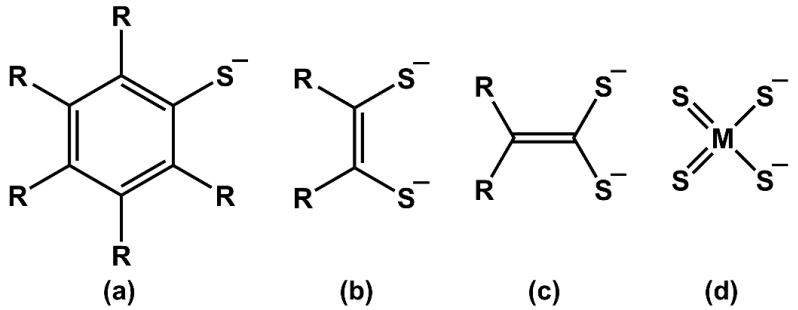

Figure 1.20 General structures of ligand systems investigated here: (a) arythiolates, (b) 1,2-dithiolates, (c) 1,1-dithiolates and (d) tetrathiometallates.

After assessing the impact of the second coordination sphere on Co^{II} SIM performance, the effect of reducing metal-ligand bite-angles will be investigated. To do this dianionic bidentate sulfur ligands will be used. As noted, high anisotropy Co^{II} SIMs have been successfully prepared using 1,2-dithiolate ligands (Figure 1.20b), with large anisotropy SIMs possibly accessible if the S−Co−S angles are reduced. One way of doing this by shifting from a five- to four-membered coordination ring by reducing the number of atoms in the chelating ligand as in $[Co\{(N^tBu)_3SMe\}_2]$.[74] Examination of prior research revealed two ligand systems matching the criteria: 1,1-dithiolates (Figure 1.20c) and tetrathiometallates (Figure 1.20d).

Examination of tetrathiotungstate complexes proved reducing the coordination ring size does not always lead to concomitantly reduced metal-ligand bite-angles. The resulting complexes offer other advantages however, which will be examined fully in Chapter 4.

The reduced bite-angle is more certain in 1,1-dithiolate complexes, with crystallography confirming the consistently smaller bite-angles relative to comparable 1,2-dithiolate complexes (*vide infra*). 1,1-Dithiolate chemistry will be discussed more below, but before doing so it is important to note other possible effects of changing ligand systems.

Whilst offering advantages in terms of the coordination geometry, changing ligand systems can affect the physical properties of the final compound in unpredictable ways. Whilst these may be advantageous and improve the stability, crystallinity or solubility of the product, the effects may also be deleterious, or counteracted by the substituents or counterions.

Although some general strategies[77] have given promising results, no consistent and effective methods of SMM device integration and fabrication are available. The most promising results use the physical properties of SMMs to aid device manufacture: sublimation can be used with appropriate neutral SMMs,[78] whilst appropriate modification of charged SMMs can aid surface deposition.[79] Considering this, the physical properties of the systems examined here may affect future devices uses, as well as the ease of handling and examination in laboratory conditions.

1.6.2 1,1-Dithiolate Coordination Chemistry

1,1-Dithiolates form when bifunctional C−H acids with the general formula $H_2CR_1R_2$ react with carbon disulfide in the presence of a base.[80] The reaction proceeds via the mechanism shown in Scheme 1.1, with the formation of 1,1-dithiolates contingent on the electron-withdrawing strength of the R_1 and R_2 groups and the base used.

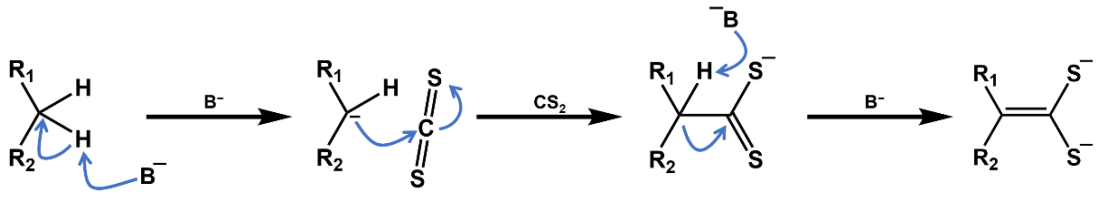

Scheme 1.1 General reaction scheme for 1,1-dithiolate ligands.

Weakly basic nucleophiles such as $C(NO_2)_3^-$ and $C(CN)_3^-$ do not react with carbon disulfide, whilst weak bases will not perform the second deprotonation, forming monoanionic dithioacids. In certain cases, typically where R_1 and R_2 are alkyl groups, it is possible to use a strong base to reduce dithioacid salts to give 1,1-dithiolates.Contrasting

with the multiple 1,2-dithiolene $\{S_2C_2\}$ configurations (Figure 1.21), in 1,1-dithiolates the C−C bond in the elementary $\{S_2C_2\}$ moiety only exists in one form: that of an alkene dithiolate with olefinic double bond and two geminal thiolate substituents.

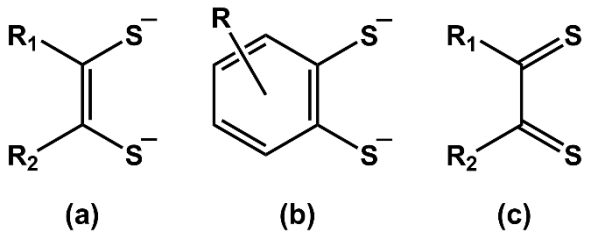

Figure 1.21 General classes of 1,2-dithiolene ligands: (a) alkene dithiolates, (b) arene dithiolates and (c) neutral dithiones.

Although more limiting, the simple synthetic pathway still allows access to a large variety of 1,1-dithiolates, with the basic motif adapted to yield ligand salts with an assortment of properties (Figure 1.22). Ligand formation is dependent on the substituents ensuring the starting material is nucleophilic enough to be doubly deprotonated and stabilising the geminal two sulfur anions: as such the bulk of 1,1-dithiolates have strongly electron-withdrawing cyano, ketone or ester substituents.

The former is most common, with the electron-withdrawing strength of the cyano group often compensating for the weakness of the other substituent. 1,1-Dithiolates with weaker electron-withdrawing substituents are known, but require delicate reaction conditions; the few known are extremely unstable are typically prepared and reacted in situ.[81] The ligand most widely encountered in 1,1-dithiolate chemistry is 1,1-dicyano-2,2-ethenedithiolate, abbreviated *i*-mnt^{2-} as it is the 1,1-dithiolate isomer of mnt^{2-}, in turn named from the *cis*-orientation of the cyanide substituents found in maleonitrile. The two cyano substituents makes synthesis trivial and stabilises the ligand salt.

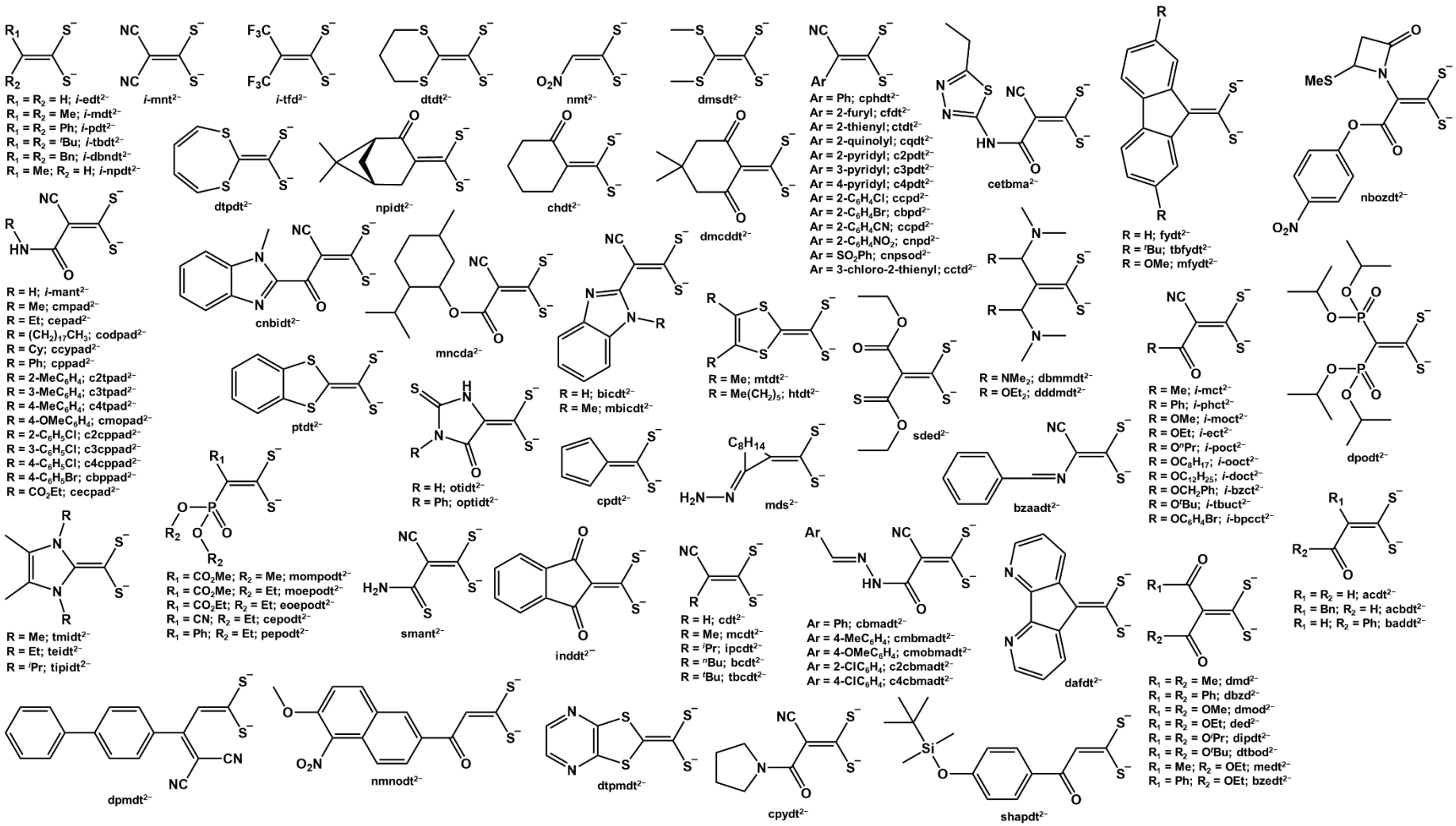

Figure 1.22 Conventionally synthesised 1,1-dithiolate ligands and their abbreviations. (See list of abbreviations for ligand identification.)

A suite of *i*-mnt^{2-} complexes were the first reported 1,1-dithiolate species, and were used to provide insight into the role of the ligand structure in stabilising lower oxidation states.[82] Comparison with 1,2-dithiolene complexes was explicitly made, with the interesting properties of the latter ligand systems highlighted. However, although 1,1-dithiolate and 1,2-dithiolate chemistry began and developed concurrently (vide infra), the novel chemical and electronic properties of 1,2-dithiolenes rapidly eclipsed 1,1-dithiolate research, with the differing ligand redox chemistries especially responsible.

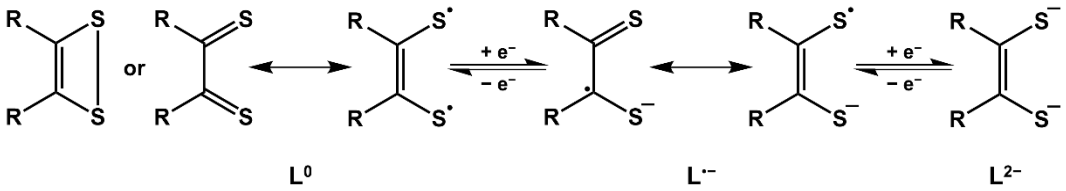

Scheme 1.2 The three oxidation states of 1,2-dithiolene ligands (L = 1,2-dithiolene).

The square-planar nature of bis(dithiolenes)[83] can only arise with ligand participation in frontier molecular orbitals,[84] which combined with the multiple accessible 1,2-dithiolene oxidation states (Scheme 1.2) can result in ambiguity, or “non-innocence” of oxidation states.[85]

The lack of comparable redox activity in the strictly “innocent” 1,1-dithiolates[86] meant that 1,1-dithiolate coordination chemistry languished as interest in 1,2-dithiolene complexes surged.[84,85] Although the structural resemblance of 1,1-dithiolates to tetrathiafulvalene (TTF) generated some later interest,[87] attention moved away from ligand coordination chemistry to their use in organic molecules[88] where, with a few exceptions discussed in the proceeding chapters, research has since remained broadly focussed.

Although limited, research into 1,1-dithiolate coordination complexes illustrates the remarkable properties of the ligands: they are shown to stabilise high-oxidation state Fe^{IV} and Cu^{III} ions[89,90] and heavily influence the Mo$^{V/IV}$ redox couple.[86] The latter effect is notable as it is the 1,1-dithiolate innocence that allows definite assignment of the redox couple.

Comparable monoanionic ligands (Figure 1.23) do not influence the redox behaviour as profoundly, illustrating the unique utility of the 1,1-dithiolate ligand framework.

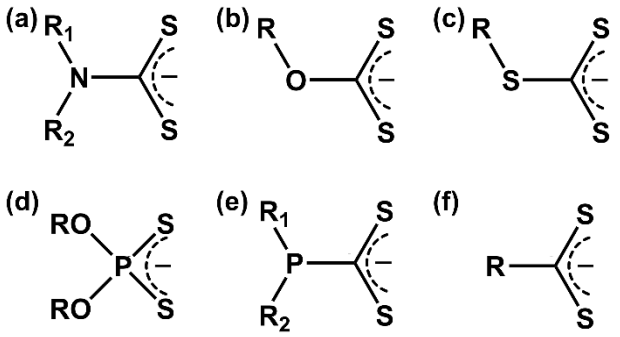

Figure 1.23 Monoanionic, small bite-angle, bidentate disulfide ligands: (a) dithiocarbamate, (b) xanthate, (c) thioxanthate (d) dithiophosphate, (e) phosphino-dithioformate[91] and (f) dithiocarboxylate (dithioacid) ligands.

Interest in monoanionic small bite-angle ligand systems remains however, as synthesis of $[Co\{(N^tBu)_3SMe\}_2]$[74] illustrates. Their appeal is two-fold: ligand synthesis is trivial, and the resulting complexes offer the tantalising combination of small bite-angle and short M−S bond lengths. Examination of the average Ni−S lengths and S−Ni−S bite-angles given in Table 1.2 demonstrates this, where at 2.201(1) Å, the diethyldithiocarbamate (Et_2dtc^-) complex has the shortest Ni−S lengths; the monoanionic ligand systems also offer bite-angles comparable to those in $[Ni(i\text{-}mnt)_2]^{2-}$.

Table 1.2 Average Bond Distances (Å) and Angles (°) in a suite of $\{NiS_4\}$ complexes.

	Ni−S	S−Ni−S	Reference
$[Ni(mnt)_2]^{2-}$	2.175(1)	92.18(1)	92
$[Ni(i\text{-}mnt)_2]^{2-}$	2.209(1)	78.78(1)	93
$[Ni(Et_2dtc)_2]$	2.201(2)	79.19(4)	94
$[Ni(S_2P(OEt)_2)_2]$	2.211(3)	88.33(3)	95
$[Ni(S_2COEt)_2]$	2.211(2)	79.4(6)	96

However, although the geometry is alluring and a greater array of ligands are accessible at ambient conditions,[97] there are two major shortcomings stemming from the monoanionic nature of the ligands. The first is that using geometry to enhance *D* in Co^{II}

SIMs relies on maximising the Co^{II} charge density, something limited by the reduced ligand charge. Examination of comparable $\{Zn^{II}S_4\}$ species demonstrates the second shortcoming. Whilst as for Ni^{II}, on moving from $[Zn(dmit)_2]^{2-}$ to $[Zn(i\text{-}mnt)_2]^{2-}$ the S−Zn−S bite-angles decrease from 95.15(3)° to 77.87(1)° and Zn−S lengths increase from 2.335(1) to 2.348(1) Å[98,99], Zn^{II} dithiocarbamate species are only isolable as dimers.[100,101] This is due to the weaker binding strength of the monoanionic ligands, suggesting that whilst 1,1-dithiolates may not bind as closely to metal centres, the increased charge strengthens the bond and increases the monomer stability.

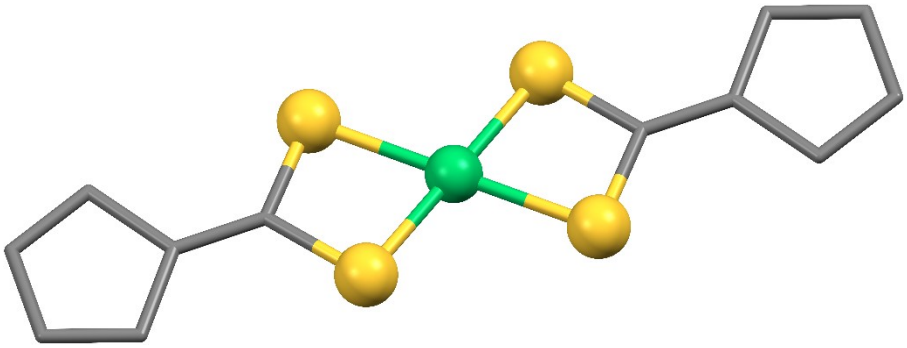

Figure 1.24 Molecular structure of the $[Ni(cpdt)_2]^{2-}$ (nickel, seafoam; sulfur, pineapple; carbon, charcoal). Hydrogen atoms omitted for clarity.

It should be noted that in contrast to 1,2-dithiolenes[85] and despite their stability, synthesis of 1,1-dithiolate metal complexes can be more complex than synthesis of the ligand. Although many 1,1-dithiolates species can be prepared by combining the correct stoichiometric ratio of free dithiolate with an appropriate metal reagent, this metathetical approach is not always possible. Two comprehensive reviews provide detailed information about 1,1-dithiolate coordination chemistry pre-1977,[80,102] but it is research since that best highlights the associated challenges. Although metal complexes of 1,3-di(trifluoromethyl)-1-propene-2,2-dithiolate (i-tdf^{2-})[103] and 2,4-cyclopentadiene-1-methylenedithiolate ($cpdt^{2-}$; Figure 1.24)[104,105] were prepared, only the alkali salts and organic derivatives of 1,3-dithiane-2-methylenedithiolate ($dtdt^{2-}$)[106] could be isolated, something attributed to the lack of resonance stabilisation in the ligand system. The role of resonance stabilisation in 1,1-

dithiolate complexes is fascinating, suggesting a degree of system non-innocence as electron density shifts to the ligand periphery. Although no redox activity is facilitated by this it is likely responsible for the remarkable electronic properties of 1,1-dithiolate complexes, with a systematic study of ligand effects offering an appealing avenue of investigation.

In summary, whilst the tight bite-angle, stability and high {MS_4} charge density makes Co^{II} 1,1-dithiolate complexes appealing high axial anisotropy SIM candidates, a broader study of the electronic and chemical properties of 1,1-dithiolate complexes is also attractive.

2 Co^{II} Arylthiolate Second Coordination Sphere Effects

2.1 Introduction

Coordination complexes have two coordination spheres: a first coordination sphere consisting of atoms bound directly to the metal centre and a second coordination sphere consisting of molecules attached to the first coordination sphere, but not bound to the metal.[107] This consists of everything from solvent molecules[108] to ligand parts not directly coordinated to the metal. There has been no comprehensive investigation into the effect of modifications to the second coordination sphere on SIM performance, despite the fact that alterations can have profound effects on electronic and chemical properties (*vide infra*); cobalt arylthiolates provide an attractive platform for such research.

The first mononuclear Co^{II} arylthiolate was discovered by Beck, who in a series of ground-breaking publications reported the synthesis and analysis of $[Co(SC_6F_5)_4]^{2-}$.[109-111] Exciting as this was Beck focussed on more explosive research,[112] with the unadorned $[Co(SPh)_4]^{2-}$ remaining unavailable until 1971.[113]

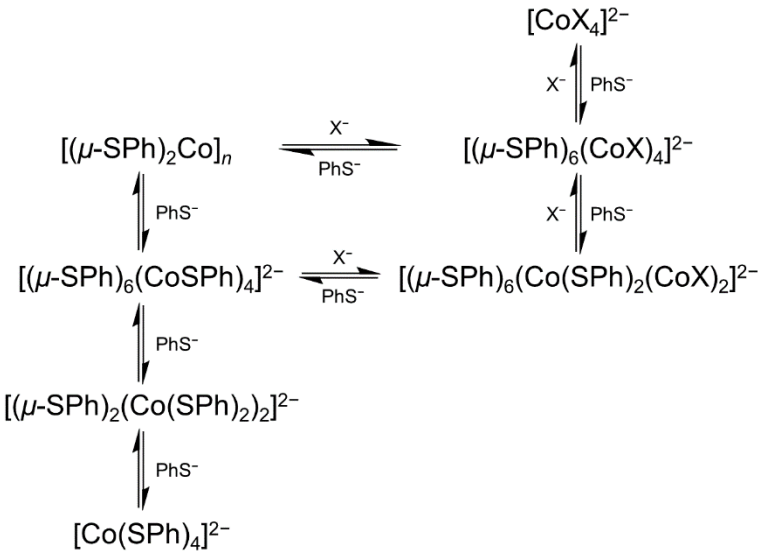

Scheme 2.1 Equilibrium scheme reported by Dance and co-workers (X = Cl, Br).

The lethality of the TlSPh used in the initial synthesis slowed research until a simpler method was developed by Dance and co-workers.[114] In doing so they made large scale

synthesis practical, sparking a revolution that ensured interest in Co^{II}/thiolate systems endures to the present day. Whilst isolating $[Co(SPh)_4]^{2-}$ it also proved possible to isolate Co^{II} clusters (Scheme 2.1) through adjustments of the ligand/metal ratio,[114,115] a discovery that fortuitously occurred shortly after the first report of a synthetic analogue of an Fe-S protein active site. The variety of biochemical processes the natural protein takes part in[117,118] generated huge interest in the development of synthetic analogues of this and related proteins (Figure 2.1).[119] The cluster nature of the active sites could have diminished interest in $[M(SR)_4]^{z-}$ complexes were it not for Richard Holm. Whilst writing the book on biologically relevant Fe-S clusters,[120] Holm led research that kept interest in monometallic monothiolate species alive. Although Christou and Garner that showed that Fe clusters could be isolated from elemental sulfur and Fe^{II} or Fe^{III} salts in the presence of sufficient thiolate reductant,[121] building on work by Coucouvanis it was Holm who drove the field forward.

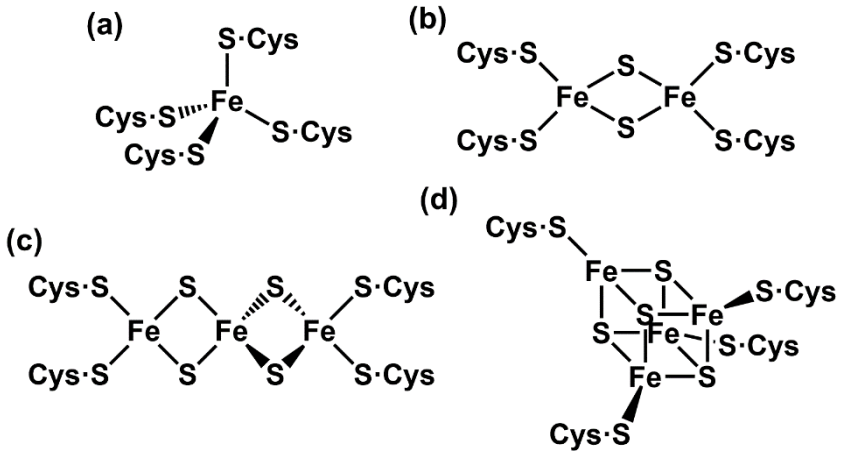

Figure 2.1 Schematic representations of some Fe−S protein sites: (a) oxidised rubredoxin, (b) Fe_2S_2 ferredoxin, (c) pig heart aconitase and (d) Fe_4S_4 ferredoxin.

Pipped to the post for $[Co(SPh)_4]^{2-}$, Coucouvanis conducted the first comprehensive study of $[Fe(SPh)_4]^{2-}$, proving it to be a good candidate for the active site of reduced rubredoxin.[122] The reaction of $[Fe(SPh)_4]^{2-}$ with organic trisulfides was thus remarkable, indicating that in the presence of sufficient reducing reagent, organic linear and cyclic sulfides could be sources of inorganic sulfides such as ferredoxins.[123] Building on this, Holm

made the discovery that laid the groundwork for an explosion in research: that of $[Fe_4(SPh)_{10}]^{2-}$,[124] the Fe^{II} analogue of the Co^{II} cluster discovered by Dance.[114] The discovery led Holm to propose development of a rational framework of reaction sequences with the aim of replacing the unpredictable spontaneous self-assembly method. This proved a stunning success, resulting in a scheme allowing the rational targeting of a desired product (Scheme 2.2).[125]

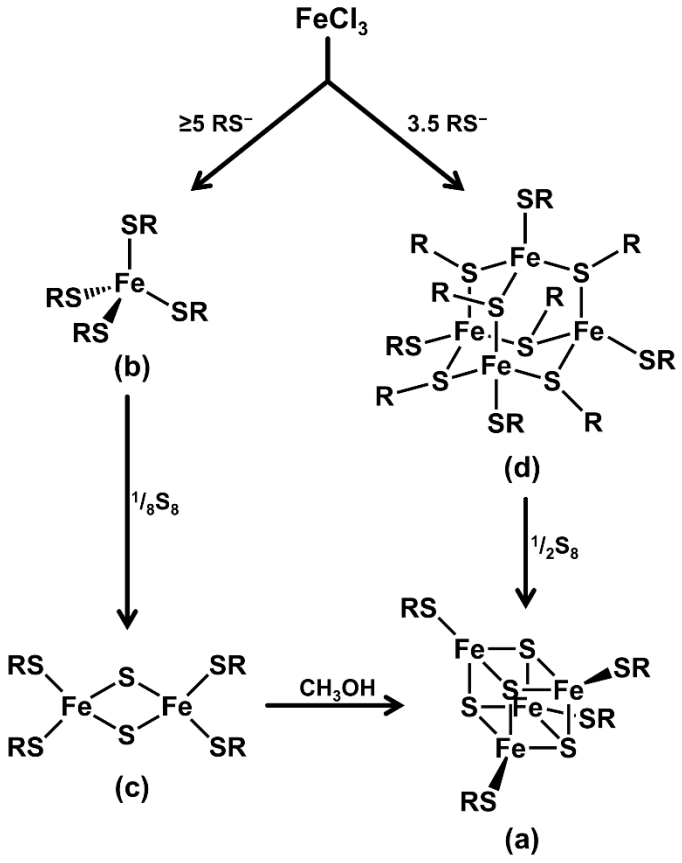

Scheme 2.2 Reaction pathways for the assembly of (a) $[Fe_4S_4(SR)_4]^{2-}$ clusters via intermediates (b) $[Fe(SR)_4]^{2-}$, (c) $[Fe_2S_2(SR)_4]^{2-}$ and (d) $[Fe_4(SPh)_{10}]^{2-}$.

The framework developed, four avenues of research remained: changing the metal centre, the ligand substituents (second-coordination sphere), the reaction conditions and developing Fe-S chemistry further to give new polynuclear systems. The latter avenue has proven immensely profitable,[126,127] but is less relevant than the others, whilst as altering the reaction conditions provides information about the interactions between the metal centres,

ligands and reaction media, that avenue it dovetails neatly with the remaining areas of research.

Fe-S research continued, but the field rapidly broadened to other elements; initial focus remained on Fe analogues, with $[Co^{II}(SAr)_4]^{2-}$ systems being used for $[Fe^{III}(SCys)_4]^-$ oxidised rubredoxin.[32] Research into other metal-thiolate systems rapidly developed independently however, as the essential nature of other elements became clear[128,129] just as metal-exchange was being used to develop spectroscopic aids for metalloproteins.[130,131]

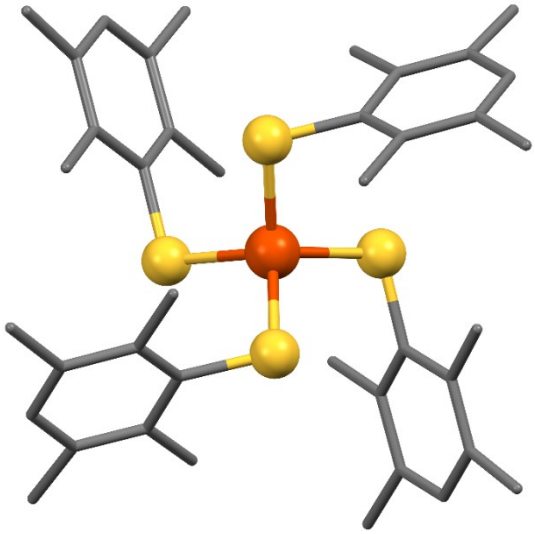

Figure 2.2 Molecular structure of $[Fe(SC_6HMe_4)_4]^-$ (iron, orange; sulfur, pineapple; carbon, pewter). Hydrogen atoms omitted for clarity.

Interest in second-coordination sphere pre-dates the bulk of M-S research, being grounded in the well-known reactions between Fe^{III} salts and thiols that prove to be auto-redox processes yielding Fe^{II} compounds and disulfides.[132] As modern Fe-S cluster research was beginning Koch *et al.* investigated the effect of changing ligand substituents. The reaction proved to slow as the thiophenolate steric bulk increased, such that stable Fe^{III} complexes of 2,3,5,6-tetramethylthiolate (Figure 2.2)[133] and 2,4,6-triisopropylthiolate[132] could be isolated.

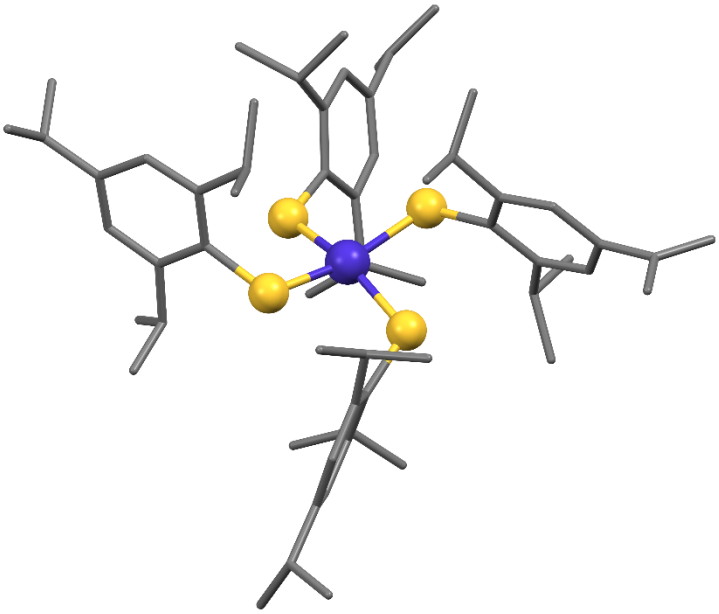

Figure 2.3 Molecular structure of $[Co(SC_6H_2{}^iPr_3)_4]^-$ (cobalt, grape; sulfur, pineapple; carbon, charcoal). Hydrogen atoms omitted for clarity.

The sole square planar homoleptic Co^{III} thiolate complex was isolated using the latter ligand (Figure 2.3).[134] The homologous Fe^{III} and isoelectronic Fe^{II} species are known to possess distorted T_d geometry,[135,136] illustrating the effect of the higher LF splitting in Co^{III}.[134] The Co^{II} complex is the dinuclear $[Co_2(SC_6H_2{}^iPr_3)_5]^-$,[137] with coordination geometry between the edge-sharing trigonal planar $\{CoS_3\}$ moieties of $[Co_2(SC_6H_2{}^tBu_3)_4]$[138] and the mononuclear T_d $[Co(SC_6HMe_4)_4]^{2-}$;[139] comparisons across the series showed the bleaching reaction rate to remain tied to steric hindrance,[132,133] illustrating the consistent importance of the second coordination sphere.

Bulky aryl ligands have since been used to isolate a host of low-coordinate TM complexes,[140] in the process illustrating the electronic effects of changing phenyl substituents: the more electron-donating the substituents, the shorter the metal-ligand bond lengths. Co−S bond lengths are 0.022 Å shorter[137] in $[Co_2(SC_6H_2{}^iPr_3)_5]^-$ than the unadorned species, [43] with Co−S lengths decreasing 0.108 Å further in $[Co(SAr^*)_2]$ ($Ar^* = C_6H_3$-2,6-(C_6H_2-2,4,6-$^iPr_3)_2$).[141] Although the molecular- and macro-scale importance of the second-coordination sphere is well-documented in other areas of chalcogenate coordination chemistry, the change in bond lengths is the first time the impact of the second coordination

sphere on the LF in such complexes has been reported, beyond simple changes to coordination geometry. Given $[Co(SPh)_4]^{2-}$ is the archetypal 3d SIM and the link between magnetic and electronic properties, the remaining knowledge gap is stunning.

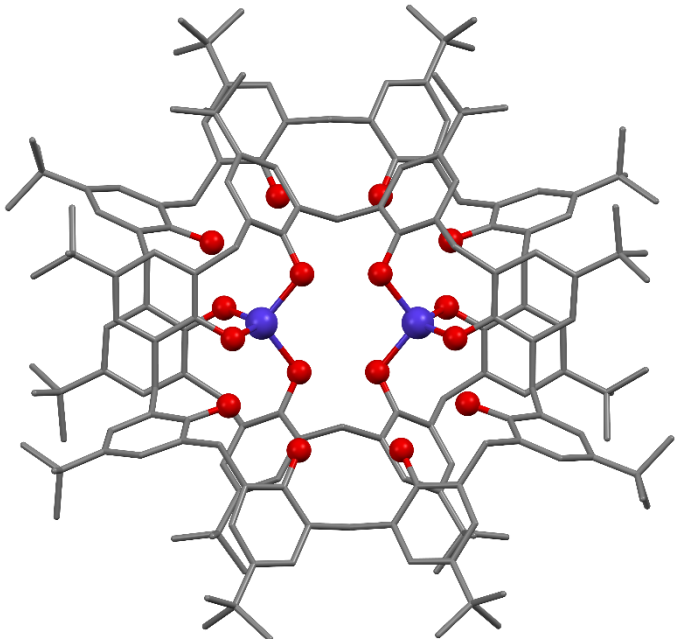

Figure 2.4 Molecular structure of $[Co_2(calix)_2]^{2-}$(cobalt, grape; oxygen, scarlet; carbon, charcoal). Hydrogen atoms omitted for clarity.

Despite being first noted over a decade ago,[142] a similar gap exists in knowledge of the broader impact of the second-coordination sphere on SMM performance. Luneau *et al.* reported larger than predicted energy level splitting in $[Co_2(calix)_2]^{2-}$ (calix = *p*-tert-butylcalix[8]arene; Figure 2.4),[142] the cause of which was the lower symmetry of the second-coordination sphere, which interacted with the coordinated oxygens such that the Co^{II} LF symmetry was also lowered; such interactions were not accounted for in simpler analytical models.[143,144] Despite these findings second-coordination sphere effects are examined in just one further study,[145] even as the importance of the second-coordination sphere became apparent in other areas research and SIMs where performance should rest solely on the primary- and secondary-coordination spheres[146] rose to prominence.

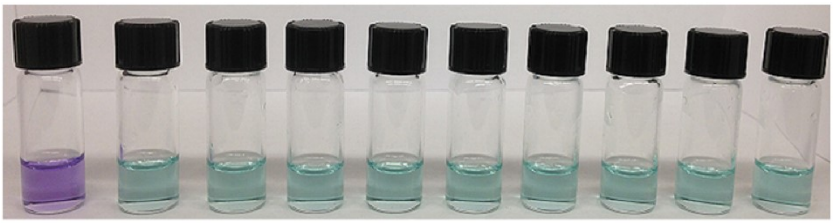

Figure 2.5 Second-coordination sphere assisted colorimetric selectivity in a monometallic Co^{II} complex (a) F^-, (b) Cl^-, (c) Br^-, (d) I^-, (e) HPO_4^{2-}, (f) BH_4^-, (g) OAc^-, (h) NO_2^-, (i) NO_3^- and (j) free solution.

A systematic examination of modifications to the second-coordination sphere is very attractive, offering the opportunity for knowledge that could be used to develop principles that link the second-coordination sphere and SMM performance in a framework similar to that developed by Ruiz *et al.* that tied forecast anisotropy to the electronic configuration and coordination modes.[48] Although challenging, such a framework is plausible given research tying second-coordination sphere to photo-chemical and -physical properties,[147] that led to development of colorimetric sensors with second-coordination sphere determined selectivity (Figure 2.5).[148]

Modifications to the phenyl ring in $[Co(SPh)_4]^{2-}$ present an ideal starting point, providing insight into the effect of such changes on a well-studied Co^{II} SIM. To this end two modified $[Co(SAr)_4]^{2-}$ complexes were prepared and compared against the original species. The first was $[Co(SC_6F_5)_4]^{2-}$, where the hydrogens were substituted for electron-withdrawing fluorines. A complex with electron-donating substituents was also synthesised, although as the initial target $[Co(SMes)_4]^{2-}$ (SMes = SC_6H_3-2,4,6-Me_3; mesitylthiolate) complex could not be isolated the less substituted $[Co(STol)_4]^{2-}$ (STol = SC_6H_5-6-Me, *p*-tolylthiolate) was prepared. The three arylthiolate species were compared alongside $[CoCl_4]^{2-}$ to examine the effect of changes to the second-coordination sphere on electronic and magnetic properties.

2.2 Synthesis

The Co^{II} complexes were synthesised using similar methods: taking one equivalent of a Co^{II} salt, adding the ligand equivalents required to drive formation of the mononuclear T_d species, then isolating the product with an appropriate counterion.

The first T_d Co^{II} species isolated was $[CoCl_4]^{2-}$, which is a useful baseline as it coordinated by pure π-donors with no MLCT bands obscuring the LF transitions.[149] Synthesis was easy, with the product precipitating on mixing a 2:1 ratio of $CoCl_2{\cdot}6H_2O$ and NEt_4Cl in EtOH; IR, ESI-MS and electronic spectroscopy measurement confirmed product formation and purity.

Research has shown that the axial anisotropy of Co^{II} complexes can be tailored through modifications to the geometry and donor atom softness (*vide supra*), but little is known about the impact of the second-coordination sphere on axial anisotropy. The lack of second-coordination sphere in $[CoCl_4]^{2-}$ makes it a useful as a baseline against which $[Co(SPh)_4]^{2-}$ can be compared, with $[Co(SC_6F_5)_4]^{2-}$ and $[Co(STol)_4]^{2-}$ compared against both. The effect of going from halide to arylthiolate ligands can then be traced and compared against the effect of altering the second-coordination sphere: $[Co(SC_6F_5)_4]^{2-}$ and $[Co(STol)_4]^{2-}$ will be affected by both steric and electronic effects, stemming from the change in geometries and ligand π-donor abilities relative to $[Co(SPh)_4]^{2-}$.

The high anisotropy of $[Co(SPh)_4]^{2-}$ is well known, with Fukui *et al.* first promulgating D = 100 ± 30 cm^{-1},[32] a value more recently refined to 110(2) cm^{-1} by Suturina *et al*.[43] Different counterions cause D to vary significantly, however, with measurements by Suturina *et al*. showing $(PPh_4)_2[Co(SPh)_4]$ to possess strong axial anisotropy of D = −55(1) cm^{-1}, whilst $(NEt_4)_2[Co(SPh)_4]$ has rhombic anisotropy, with D = +11(1) cm^{-1}.

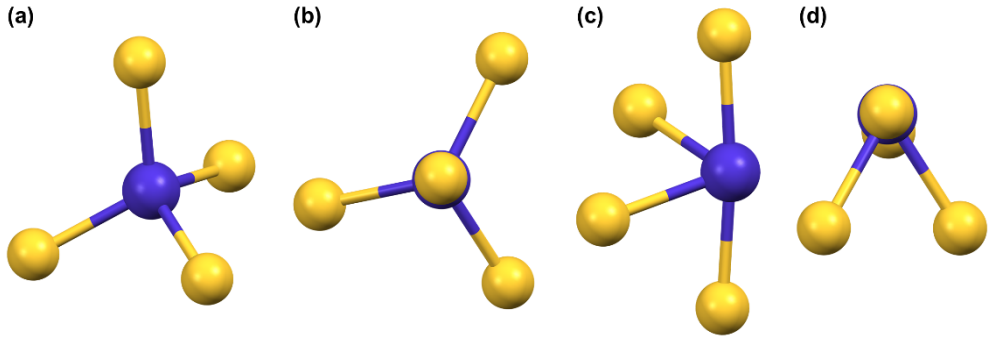

Figure 2.6 Perspectives of the $\{CoS_4\}$ moiety in $(PPh_4)_2[Co(SPh)_4]$, side-on (a) and top-down (b), compared to $(NMe_4)_2[Co(SPh)_4]$, side-on (c) and top-down (d) (cobalt, grape; sulfur, pineapple). Phenyl rings and counterions have been omitted for clarity.

However, both measurements are in the solid-state, introducing packing effects[43] dramatically changing the complex structures (Figure 2.6):[150,151] changes not occurring in solution. Counterions do not impact[152] XAS, which gives consistent results in solid and solution-states,[153] so only the magnetic susceptibility measurements are in question. These will be discussed below, but for consistency where possible tetraphenylphosphonium was used as a counterion; this was not possible for $[Co(STol)_4]^{2-}$ (*vide infra*).

A large scale synthetic method for $[Co(SPh)_4]^{2-}$ has been available since 1979 (*vide supra*),[114] which formed the basis for the synthesis used here.[43] The complex was prepared in good yield (72%) by adding one equivalent of Co^{II} in dry MeCN to a stirring solution of 5.6 equivalents NaSPh under nitrogen. A counterion was added and the reaction mixture stirred briefly, before cannula filtering the reaction mixture and sealing the filtrate under nitrogen in a Schlenk flask at −35 °C for 72 h, inducing precipitation of the product as vivid emerald crystals.

The formation of tetranuclear Co^{II} clusters are known,[114] with ligand equivalencies < 5.6 favouring thiophenolate cluster formation. The first electronic spectra of $[Co(SPh)_4]^{2-}$ were recorded in CH_2Cl_2, which proved unsuitable with the colour changing rapidly from green to brown. The spectra of the brown solution matched $[Co_4(SPh)_{10}]^{2-}$ (Figure 2.7),[114] which the presence of trace EtOH stabiliser had caused to form. Recent research into Co^{II}

polynuclear systems[154] sparked further interest, with $(PPh_4)_2[Co_4(SPh)_{10}]$ prepared and compared with the mononuclear species (see below).

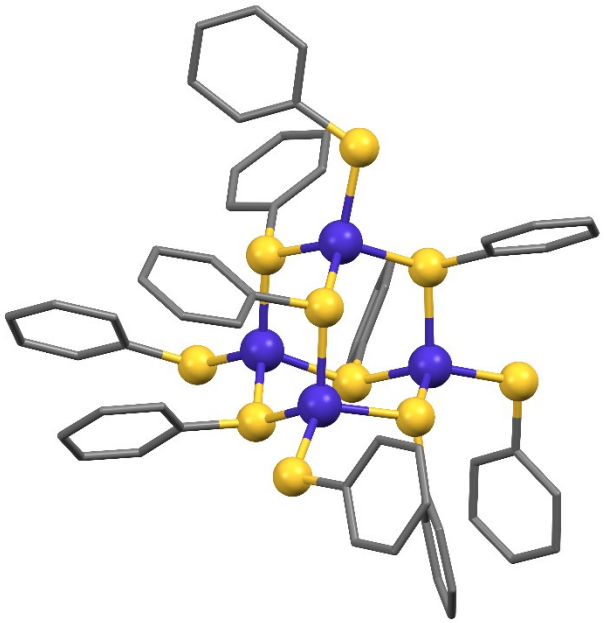

Figure 2.7 Molecular structure of $[Co_4(SPh)_{10}]^{2-}$ (cobalt, grape; sulfur, pineapple; carbon, charcoal). Hydrogen atoms omitted for clarity.

The tetranuclear species was isolated on reacting one equivalent of Co^{II} with three of thiophenolate, adding an appropriate counterion, then storing at −35 °C for 18 h. After this time the dark microcrystalline product could be filtered off.

The first modified species synthesised was the fluorine-substituted $[Co(SC_6F_5)_4]^{2-}$. The electron-withdrawing fluorine substituents should attenuate the ligand π-donor abilities, changing *D*. The larger size of and lack of hydrogen bonding in the fluorinated ligand could affect *D*, but the effects should be minor.

The ease of preparation of $[Co(SC_6F_5)_4]^{2-}$ reflected the changed chemical behaviour on fluorination, changes tied to correspondingly changed electronic properties.

Substitution of hydrogen for fluorine reduces the pK_a of alcohols, with pK_a = 10.0 for phenol[155] and pK_a = 6.0 for pentafluorophenol.[156] There has been comparatively little research into the chemistry of fluorinated thiols, but enough the acidities of thiophenol and its fluorinated analogue are available, with reported values of pK_a = 6.49[157] and pK_a =

2.68,[158] respectively. Thiols are more acidic than alcohols, with fluorination also increasing acidity.

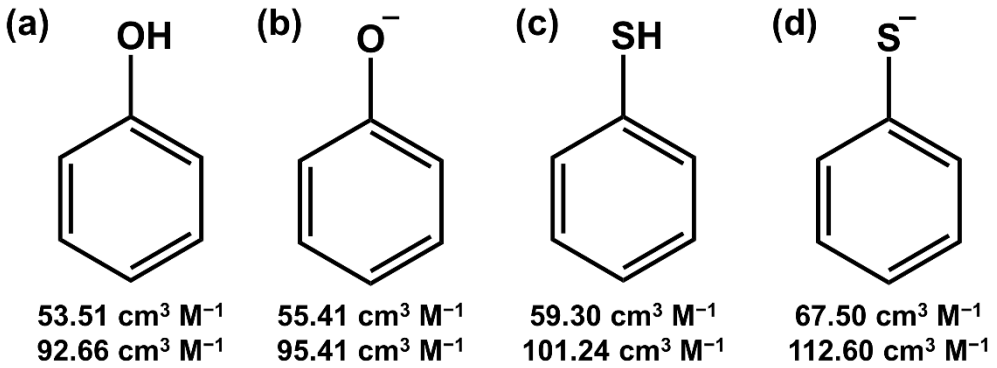

Figure 2.8 The van der Waals radii (top row) and molecular cavity volumes (bottom row) for (a) phenol, (b) phenolate, (c) thiophenol and (d) thiophenolate.

The cause of the increased acidity is well-studied, moving from examinations of the phenol/thiophenol size difference (Figure 2.8),[159] to models accounting for the increased electron delocalisation facilitated by the less electronegative sulfur atom.[160] F substituents ease thiol deprotonation further,[157] with the resulting Lewis base strong enough thiolate alkali metal salts can be prepared in aqueous solutions. This was done, with the resulting pentafluorothiophenolate salt reacted with aqueous $Co^{II}SO_4$ to give $[Co(SC_6F_5)_4]^{2-}$. The crude product precipitated on addition of an appropriate counterion in the same medium, with recrystallisation from acetone and Et_2O used to purify the product. At ambient conditions the pure product was stable for short period, degrading to an insoluble yellow material if left longer or heated; long term storage required lowered temperatures.

The extreme insolubility of the decomposed product rendered characterisation impossible, but it is likely a sulfur oligomer formed by the nucleophilic attack of a $SC_6F_5^-$ on the *para* F-substituent on another $SC_6F_5^-$.[161] Fascinatingly, this behaviour is unique to pentaflurothiophenolate: the lack of *para* F-substituent in 2,3,5,6−tetrafluorothiophenol retarding the reaction,[162] whilst both pentachlorothiophenol[163] and pentafluorophenol[164] require special conditions if the reaction is to occur. The unique ligand behaviour has been

harnessed in novel ways, but no methodical study of the F-substituent LF effect has been performed.

To allow comparison with the unadorned species, $[Co_4(SC_6F_5)_{10}]^{2-}$ was prepared through reacting of one equivalent of Co^{II} with three of ligand, with the product precipitating om storing at −35 °C for 24 h after addition of a counterion. The electron-poorer ligands reduced product yield (2%).

The trimethyl-substituted $[Co(SMes)_4]^{2-}$ (SMes = 2,4,6-trimethylthiophenolate or mesitylthiolate) was selected as an initial target complex. The electron-donating CH_3-groups should increase ligand π-donor abilities and so change the LF and *D*, with *ortho* methyl groups also shown to impact the coordination geometry relative to $[Co(SPh)_4]^{2-}$.[165] These properties have seen mesitylthiolate used in a variety of areas, including the previously discussed research into Fe-S clusters[166] and model enzyme active sites.[167] The ligand system has also been used to synthesise transition metal $[M(SMes)_2]_\infty$ polymers,[168,169] including with Co^{II}.[170] As related T_d Co^{II} durylthiolate complexes are also known, albeit typically heteroleptic ones with three durylthiolate and either 1-methylimidazole[171] or MeCN,[139] synthesis of $[Co(SMes)_4]^{2-}$ appeared both attractive and feasible.

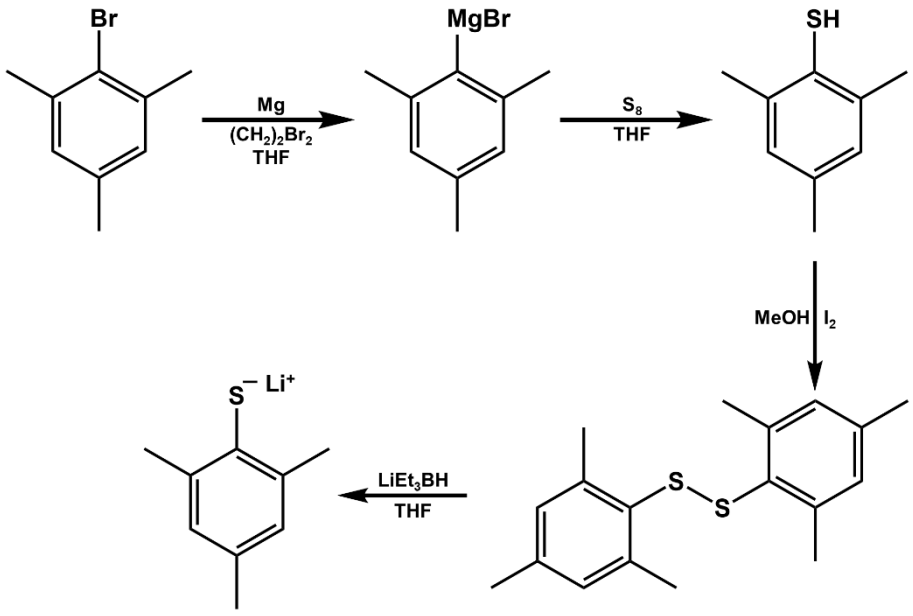

Scheme 2.3 Reaction scheme for lithium mesitylthiolate.

Dimesityl disulfide was synthesised through reacting mesitylmagnesium bromide with elemental sulfur, then oxidising the formed product with I_2; reduction of the disulfide generated mesitylthiolate in solution (Scheme 2.3). Synthesis of $[Co(SMes)_4]^{2-}$ frustratingly proved impossible, although valuable information can still be obtained. The existence of $[Co(SDur)_4]^{2-}$ (SDur = SC_6H_3-2,4,5,6-Me_4; durylthiolate)[139] shows the different chemistry of $SMes^-$ stems from the *p*-CH_3-subsitutent induced changes to the thiolate electronic properties, not steric effects. The three CH_3-subsitutents thus facilitate the formation of $[Co(SMes)_2]_\infty$ polymers,[170] but do not donate enough electron density to allow formation of dimeric Co^{II} or square-planar Co^{III} species like $SC_6H_2{}^iPr_3{}^-$.[134,137]

As an alternative to $[Co(SMes)_2]^{2-}$ the *p*-CH_3-subsituted species $[Co(STol)_4]^{2-}$ was prepared. The complex is known,[32,151] with the CH_3-group producing an electron-rich S atom that should increase ligand π-donor abilities. Furthermore, unlike $[Co(SDur)_4]^{2-}$ and related species, it forms discrete T_d species under the right conditions. Although $(PPh_4)_2[Co(STol)_4]$ could not be isolated, $(NEt_4)_2[Co(STol)_4]$ was prepared in reasonable yield (48%) by stirring eight equivalents of *para*-thiocresol and NEt_3 with one equivalent Co^{II} in thoroughly degassed EtOH, adding two equivalents of NEt_4^+ and chilling at −35 °C to precipitate the product. In spite of prior reports,[115] $[Co_4(STol)_{10}]^{2-}$ proved impossible to prepare.

The difference in syntheses of $[Co(STol)_4]^{2-}$, $[Co(SC_6F_5)_4]^{2-}$ and $[Co(SPh)_4]^{2-}$ illustrate the profound effect changes to the second-coordination sphere can have. Whilst the former complex requires a huge 8:1 ligand to metal ratio, the unsubstituted $[Co(SPh)_4]^{2-}$ can be made using a more moderate 5.6:1 ratio and the F-substituted a ratio as low as 1:1 (Figure 2.9). The changing ratios stem from changing thiolate π-donor strengths: the more π-donating the ligand the more likely Co^{II} clusters (*vide supra*) are to form and the more equivalents are necessary to drive formation of the $[Co(SAr)_4]^{2-}$ species.

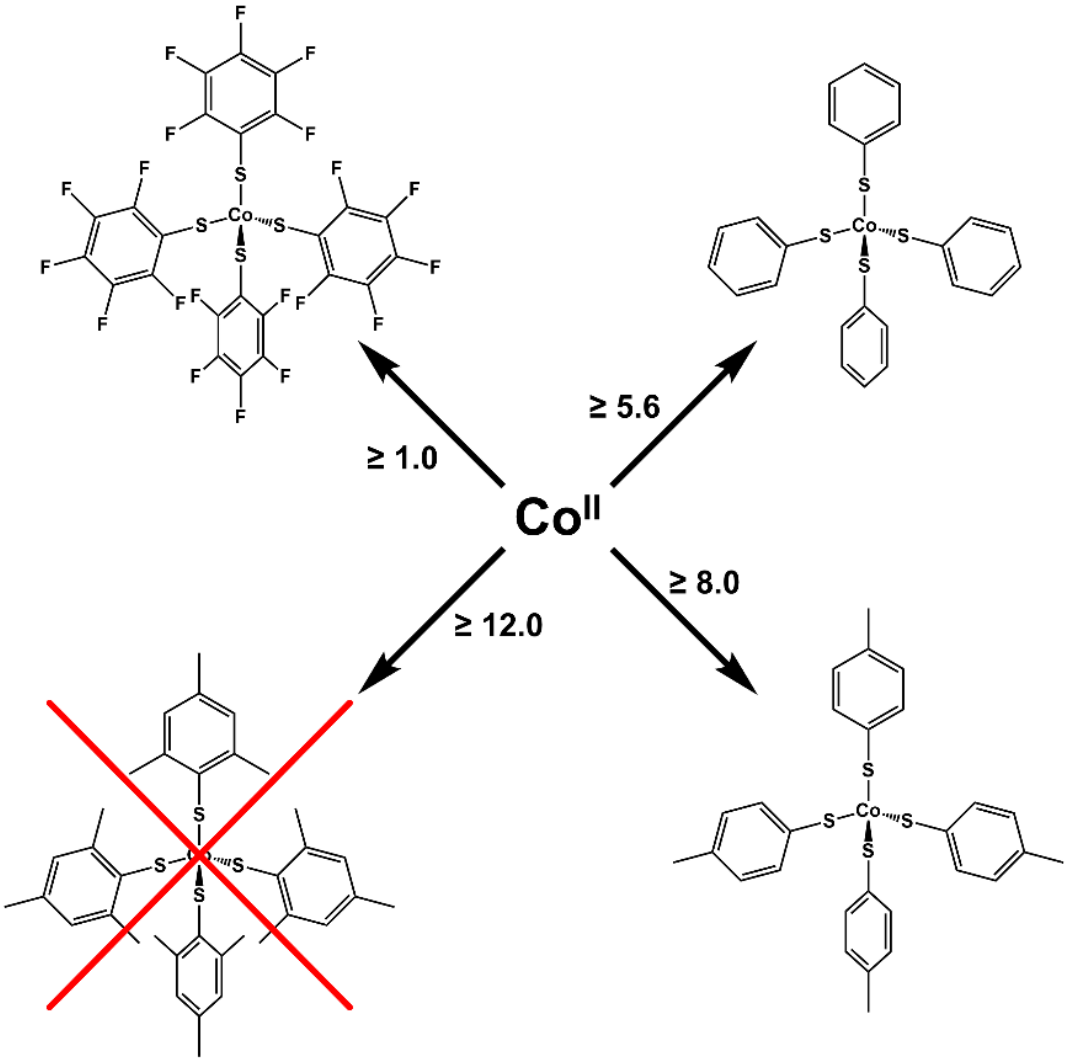

Figure 2.9 Illustration of the number of ligand equivalents necessary to isolate the dianionic Co^{II} arylthiolate complexes shown.

The favoured solvents also change, with synthesis of $[Co(SPh)_4]^{2-}$ most favourable in polar aprotic solvents such as MeCN or CH_2Cl_2; $[Co(SC_6F_5)_4]^{2-}$ can be made in polar aprotic media (H_2O), whilst optimal synthesis of $[Co(STol)_4]^{2-}$, albeit with different counterions, is in EtOH. These differences are due to second-coordination sphere induced changes to the solubility, demonstrating the influence of the second-coordination sphere outside the electronic structure.

2.3 Results and Discussion

2.3.1 Electronic Absorption Spectroscopy

Electronic spectroscopy allows the energy and intensity of electronic transitions to be recorded. As shown in Figure 2.10, three spin allowed LF transitions are visible in the electronic spectra of tetrahedral Co^{II} complexes. The most intense is the highest energy $^4A_2(F) \rightarrow {}^4T_1(P)$ transition, followed by the NIR $^4A_2(F) \rightarrow {}^4T_1(F)$ transition, then the $^4A_2(F) \rightarrow {}^4T_2$ transition at the lowest energy. The electronic spectra range here prevents observation of the lower-energy transitions, but the $^4A_2(F) \rightarrow {}^4T_1(P)$ transitions are visible in the electronic spectra between 550 and 750 nm.

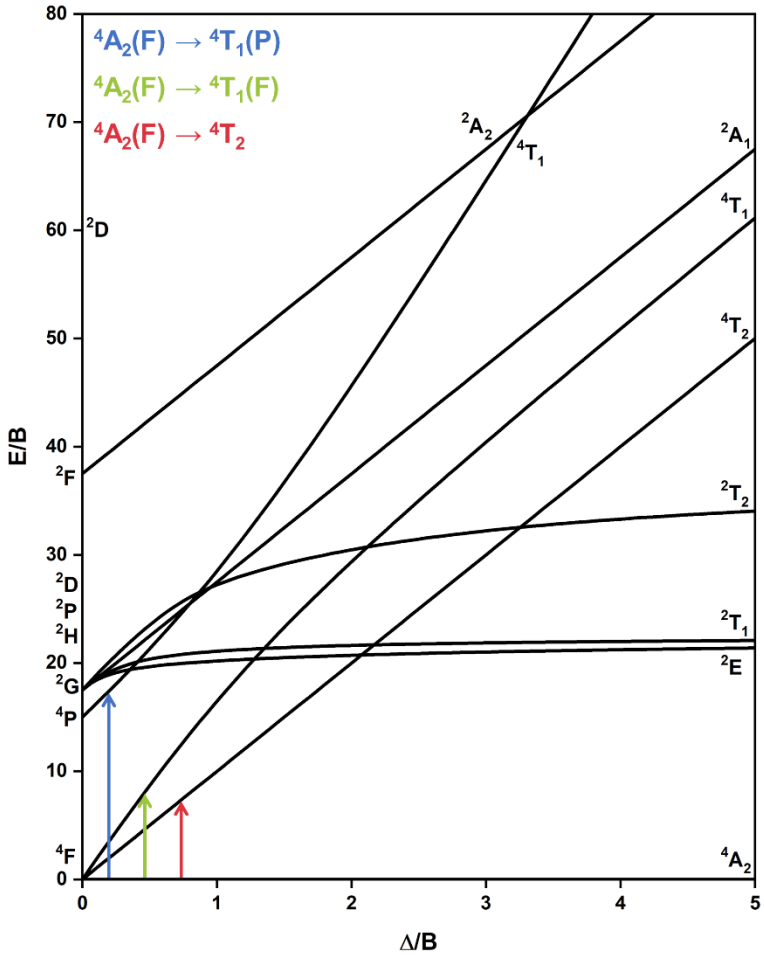

Figure 2.10 Tetrahedral d^7 Tanabe-Sugano Diagram with LF transitions illustrated.

Intraligand π−π* transitions can occur in this region and obscure the LF transitions,[172] but as spectral data is available for the unadorned species[114,173] transition misassignment is not a concern. Ligand properties still influence the spectra however, so the spectrum of $[CoCl_4]^{2-}$ (Figure 2.11) was measured as a baseline of an ideal T_d unadorned system.

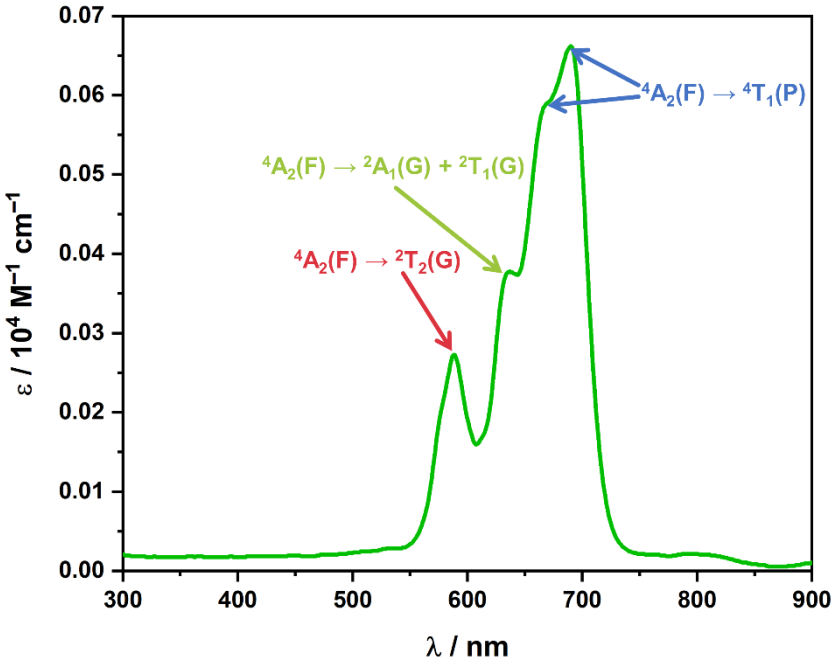

Figure 2.11 The electronic spectra of $[CoCl_4]^{2-}$; transitions responsible for the features are indicated.

As is typical,[174] the spectrum is dominated by $^4A_2(F) \rightarrow {}^4T_1(P)$ occurring at λ_{max} = 690 nm. The pure π-donor chloride ligands limit intraligand or metal-to-ligand CT, allowing the observation of the spin-forbidden $^4A_2(F) \rightarrow {}^2A_1(G) + {}^2T_1(G)$ and $^4A_2(F) \rightarrow {}^2T_2(G)$ transitions at 637 and 589 nm, respectively.

The electronic spectra of the Co^{II} arylthiolates were then measured, with the spectra overlaid in Figure 2.12; individual spectra are available in Appendix 8.1. $[Co(SPh)_4]^{2-}$, $[Co(SC_6F_5)_4]^{2-}$ and $[Co(STol)_4]^{2-}$ have similar profiles, with LF transitions visible between 600 and 650 nm and intense LMCT bands dominating at higher energies.

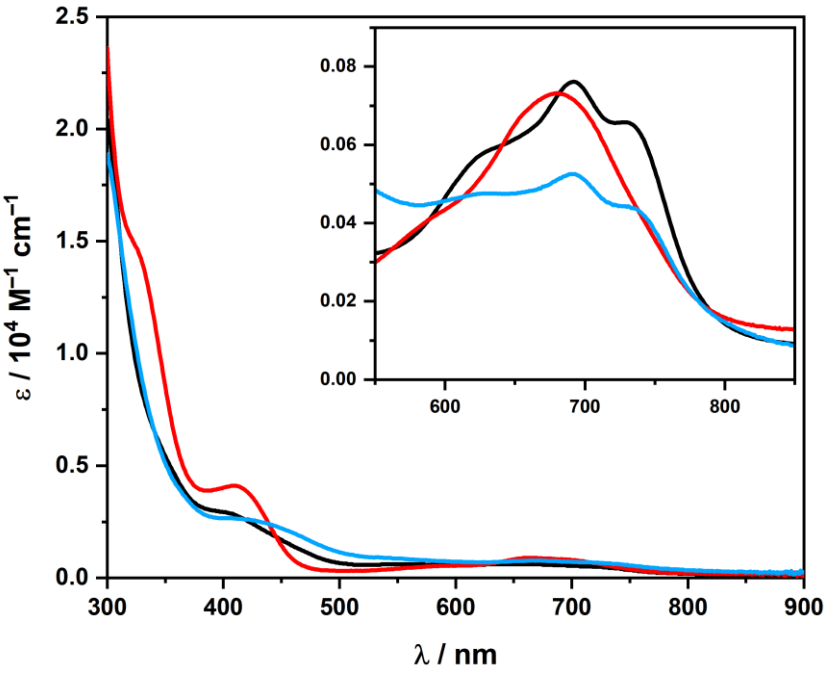

Figure 2.12 Overlay of the electronic spectra of $[Co(SPh)_4]^{2-}$ (black), $[Co(SC_6F_5)_4]^{2-}$ (red) and $[Co(STol)_4]^{2-}$ (blue); the inset shows an expanded view of the LF transitions.

Significant metal-ligand π-bonding and -backbonding occurs in the arylthiolate species,[175,176] with the resulting mixing of excited states reducing the spectral definition of the LF transitions. The $^4A_2(F) \rightarrow {}^4T_1(P)$ transition remains visible however, allowing valuable information to be gleaned. The transition parameters are collated in Table 2.1, with a magnification of the transitions inset in Figure 2.12.

Table 2.1 Spectral Parameters of the $^4A_2 \rightarrow {}^4T_1(P)$

	λ_{max} / nm	ε_{max} / M^{-1} cm^{-1}
$[Co(SPh)_4]^{2-}$	692	761
$[Co(SC_6F_5)_4]^{2-}$	680	732
$[Co(STol)_4]^{2-}$	689	525
$[CoCl_4]^{2-}$	690	662

The $^4A_2(F) \rightarrow {}^4T_1(P)$ shows the impact of alterations to the second coordination sphere on the LF to be minor. Although the lowest energy transition is found in $[Co(SPh)_4]^{2-}$, both modified complexes have similar $^4A_2(F) \rightarrow {}^4T_1(P)$ energies. The transition energy in $[Co(STol)_4]^{2-}$ is ~63 cm^{-1} higher in energy than the unadorned species, with the shift likely

due to the different steric environment in the Me-substituted system; at ca. 255 cm^{-1} the shift the fluorinated species experiences is larger, but overall remains small.

The impact of modifications to the second coordination sphere can be assessed by examining the $^4A_2(F) \rightarrow {}^4T_1(P)$ intensities: the more allowed the transition, the more intense it is.[177] The value of ε_{max} = 662 M^{-1} cm^{-1} recorded for $[CoCl_4]^{2-}$ is typical for LF transitions in T_d Co^{II} complexes, with the increased $^4A_2(F) \rightarrow {}^4T_1(P)$ intensity in $[Co(SPh)_4]^{2-}$ due to the greater SOC-induced anisotropy reported for the complex.[32,43] The intensity is tied to the species non-centrosymmetry, which means LF transitions are symmetry allowed and very intense.[178] The reduced $^4A_2(F) \rightarrow {}^4T_1(P)$ intensity in both modified species suggests the substituents are increasing the $\{CoS_4\}$ centrosymmetry, with the most profound impact from the Me-substituent. The effects remain minor however, suggesting changes in energy and intensity can be tied to substituent-induced changes in $\{CoS_4\}$ geometries rather than LF strength.

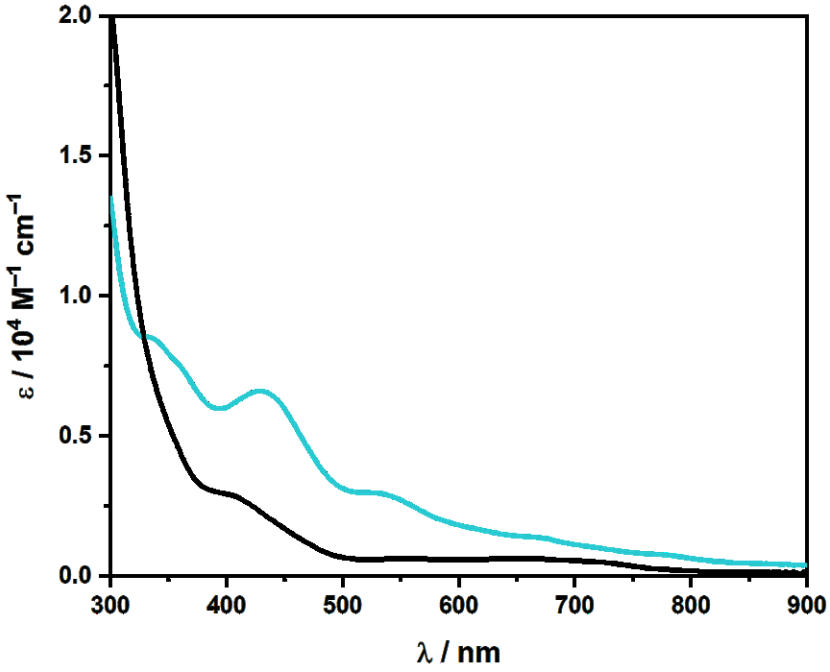

Figure 2.13 Overlay of the electronic spectra of $[Co(SPh)_4]^{2-}$ (black) and $[Co_4(SPh)_{10}]^{2-}$ (cyan).

The electronic spectrum of $[Co_4(SPh)_{10}]^{2-}$ is very different to $[Co(SPh)_4]^{2-}$ (Figure 2.13), although both spectra have identical origins. Matching that reported by Dance *et*

al.,[114] the spectrum of $[Co_4(SPh)_{10}]^{2-}$ is dominated by higher energy MLCT bands, with $^4A_2(F) \rightarrow {}^4T_1(P)$ visible at lower energies. The LF transition overlaps with lower energy MLCT bands however, preventing definite transition assignment and increasing the intensities of the transitions between 550 and 850 nm.

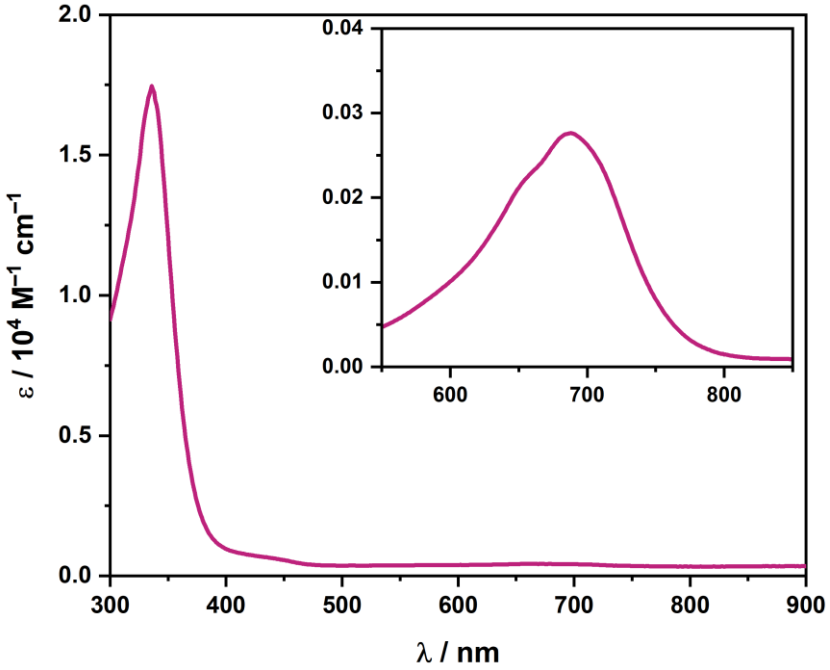

Figure 2.14 Electronic spectrum of $[Co_4(SC_6F_5)_{10}]^{2-}$ recorded in MeCN.

Compared to $[Co_4(SPh)_{10}]^{2-}$, the electronic spectrum of $[Co_4(SC_6F_5)_{10}]^{2-}$ (Figure 2.14) is relatively featureless. With an intense peak at 336 nm followed by a weak shoulder at 440 nm, the spectrum is closer to that of $[Co(SC_6F_5)_4]^{2-}$. In addition, the $^4A_2(F) \rightarrow {}^4T_1(P)$ is clearly observed at λ_{max} = 688 nm. With ε_{max} = 276 M^{-1} cm^{-1} the transition intensity is of the order known for T_d Co^{II} but considerably weaker than in $[Co(SC_6F_5)_4]^{2-}$, possibly due to Co^{II}–Co^{II} exchange coupling reducing LF transitions. Such coupling would be revealed by magnetic susceptibility measurements.

2.3.2 Magnetic Susceptibility Data

Magnetic susceptibility is typically measured using Evan's method,[179] where the NMR shift of a solvent against a known quantity of the compound is used to obtain the moment (*vide infra*), or by using a Gouy balance.[180] Evan's method has several advantages, but the solution-state instability of the complexes required solid-state Gouy measurements to be used instead. The presence of many spin-conserving transitions in T_d Co^{II} complexes causes significant spin-orbit coupling (SOC), significantly increasing *g*.[181] The deviation of *g* from g_e (*g*-shift) provide insight into the electronic structure, and relate to the separation of energy levels through Equation 2.1.[182]

$$\Delta g = \frac{\xi}{\Delta E} \tag{2.1}$$

Where ξ is the SOC constant, ΔE is the energy level separation and Δg is the *g*-shift, defined as $\Delta g = g - g_e$; the smaller ΔE the higher the *g*-shift.

$$g = \frac{\mu_{eff}}{\sqrt{S(S+1)}} \tag{2.2}$$

The *g*-values of the Co^{II} complexes can be obtained from the measured magnetic moments (μ_{eff}) using Equation 2.2, where $S = {}^3/_2$. The collated magnetic susceptibility data is given in Table 2.2.

Table 2.2 Magnetic Susceptibility Data for Co^{II} Complexes

	***g*-value**	**μ_{eff} / B.M.**
$[Co(SPh)_4]^{2-}$	2.55	4.93
$[Co(SC_6F_5)_4]^{2-}$	2.50	4.84
$[Co(STol)_4]^{2-}$	2.35	4.55
$[CoCl_4]^{2-}$	2.37	4.58
$[Co_4(SPh)_{10}]^{2-}$		6.83
$[Co_4(SC_6F_5)_{10}]^{2-}$		7.02

The *g*-values for all the complexes are consistently higher than value of 2.0023 for a free electron[183] for T_d Co^{II} species with large SOC,[36] with Δg for $[Co(SPh)_4]^{2-}$ considerably higher than that of $[CoCl_4]^{2-}$. The greater Δg means ΔE will be smaller in $[Co(SPh)_4]^{2-}$, with concomitantly greater mixing of energy levels in the thiolate species. The mixing is responsible for the large *D* reported for $[Co(SPh)_4]^{2-}$.[32,43] However, the variation in magnetic moments recorded for the arylthiolate species is within experimental error,[184] meaning ΔE has been little impacted by the alterations to the second-coordination sphere.

$$\mu_{SO} = 2.55\sqrt{4 \times S \times (S+1)} \tag{2.3}$$

A magnetic moment of μ_{eff} = 6.83 B.M. was measured for $[Co_4(SPh)_{10}]^{2-}$, confirming the existence of a polymetallic species. The spin-only magnetic moment was calculated using Equation 2.3, where 2.55 is the *g*-value calculated for $[Co(SPh)_4]^{2-}$, used to approximate *g* due to the identical Co^{II} coordination environments, 4 is the number of Co^{II} centres, and $S = {}^3/_2$ for a Co^{II} ion. The value of μ_{SO} = 9.88 B.M. obtained was far higher than the experimental result.

The magnetic moment of the individual Co^{II} ions was then calculated using Equation 2.4, using both effective and spin-only moments of the complex, where 4 is the number of Co^{II} centres.

$$\mu = \sqrt{\frac{{\mu_{eff}}^2}{4}} \tag{2.4}$$

A value of 3.42 B.M per metal ion was measured, compared to value of 4.94 B.M. using μ_{SO}. Consistent with reported data,[115] comparison of the values show each Co^{II} ion in $[Co_4(SPh)_{10}]^{2-}$ to have approximately two unpaired electrons at room temperature, with the third coupled to neighbouring Co^{II} ions.

A magnetic moment of μ_{eff} = 7.02 B.M. was measured for $[Co_4(SC_6F_5)_{10}]^{2-}$, confirming the existence of a polymetallic species. The spin-only magnetic moment was calculated using Equation 2.3, although with the *g*-value of 2.50 for $[Co(SC_6F_5)_4]^{2-}$ instead of 2.55, giving a value of μ_{SO} = 9.68 B.M. – much higher than the experimental result. Using Equation 2.4 a per Co^{II} value of μ_{eff} = 3.51 B.M. was calculated, showing each Co^{II} ion to similarly have approximately two unpaired electrons at room temperature, with the third coupled to other Co^{II} ions. Although the μ_{eff} for individual Co^{II} ions is smaller in $[Co_4(SC_6F_5)_{10}]^{2-}$ than $[Co_4(SPh)_{10}]^{2-}$, both values are within experimental error.

2.3.3 X-ray Absorption Spectroscopy

2.3.3.1 Experimental Background

X-ray Absorbance Spectroscopy yields valuable information about electronic structures of elements in a complex. Simply put (Figure 2.15) K-edge absorbance spectra stem from the excitation of an electron from the 1s core ("K shell") to a vacant orbital on an absorbing atom.

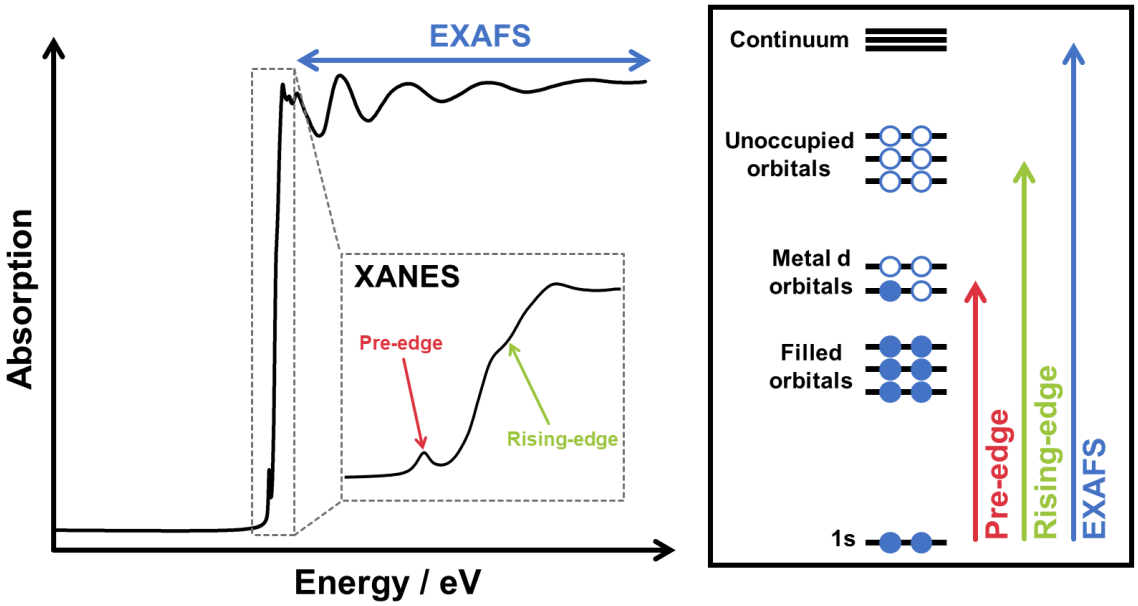

Figure 2.15 A simplified depiction of the components of a metal K-edge XAS experiment. In the XANES section the pre-edge is generated through excitation of a core 1s electron to vacant d orbitals, whilst the rising-edge is dominated by dipole-allowed 1s → *n*p transitions. In the EXAFS region beyond the edge the input energy from the X-ray is enough to expel electrons from the absorbing atom; these emanate as photoelectrons that interact with electrons in the surrounding atoms, giving rise to the oscillations in the spectrum.

The part of the spectrum this occurs is called the X-ray absorption near-edge structure (XANES) and reveals detailed information about the electronic structure of the examined material. As more energy is applied after the edge the absorbed electron is ejected from the absorbing atom, emanating outwards as a photoelectron which interacts with neighbouring electrons. This post-edge spectrum is termed the extended X-ray absorption fine structure (EXAFS), as interference of the photoelectrons with electrons in

the surrounding atoms cause oscillations from which geometric information (mainly distances) can be derived.

The XANES region is divided into pre- and rising-edge sections, with the latter dominated by dipole-allowed 1s → *n*p transitions (Figure 2.15). In metal K-edge the pre-edge region arises from dipole-forbidden, quadrupole-allowed 1s → *n*d transitions that gain intensity through mixing of metal p character caused by departures from centrosymmetry, such as distortions from D_{2h} to T_d. As discussed, such distortion also affects LF splitting, and so the transition energy. As the core 1s orbital will bind more deeply to higher effective nuclear charges (Z_{eff}) (i.e. higher oxidation states), the K-edge can be used to directly measure Z_{eff}. An increase of 1 eV in rising edge is generally accepted as corresponding to an increase of one in the oxidation state.

For the most part the transitions outlined above dominate the XANES region in metal K-edge XAS, but in certain instances multi-electron transitions occur. The first type of transition is simple, occurring when the incoming X-ray has enough energy to excite an extra electron into a higher energy band, giving a doubly excited state. This transition is known as a shake-up transition, reflecting the excess energy "shaking" an additional electron into an excited state.

A second type of multi-electron transition is possible: a multi-step process known as a shakedown transition (see Figure 2.16). Excitation of a core electron 1s electron effectively converts the atom with atomic number Z_{eff} to one with Z_{eff}+1. In certain circumstances, notably Cu^{II}, the increase in nuclear charge lowers the energy of the metal 3d orbitals to the extent they are lower in energy than the ligand orbitals (Figure 2.16b and c). Two transitions are now possible: direct 1s to the lowered energy 4p (Figure 2.16b), and a multielectron transition where a ligand electron transitions to a lower energy metal d orbital (Figure 2.16c). The latter is called a shakedown transition, and results in an excited state with lower energy. Outside Cu^{II} XANES,[185] such transitions are not common.

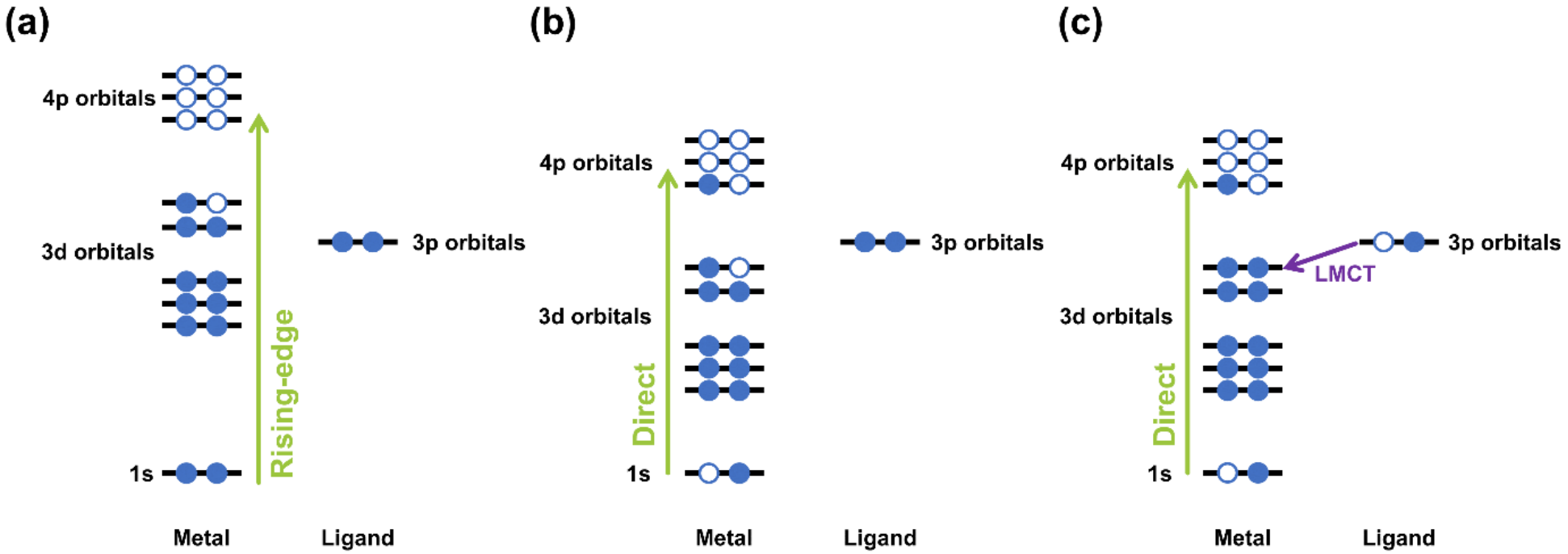

Figure 2.16 An illustration of the energy levels involved in bound-state 3d metal K-edge XANES features. The metal orbitals (1s, 3d, 4p) are on the left and ligand orbitals (3p) are on the right in each diagram. The transitions are as follows: (a) the 1s → 4p rising edge transition; (b) 1s core-hole excited state direct 1s → 4p transition; (c) 1s core-hole excited state showing multielectron 1s → 4p plus LMCT shakedown transition. The higher Z_{eff} of the core-hole excited state means the multi-electron transition in (c) is at a lower energy than the 1s → 4p transition. Transitions are marked in green; filled blue circles indicate electrons; vacant blue circles indicate vacancies in the electron shell.

The compounds studied meant two complimentary XAS measurements were used – metal K-edge and sulfur K-edge XAS spectroscopy. The metal K-edge measurements depended on the metals present in the compound under investigation, but the experimental principles are consistent enough that they are discussed above as a single technique. S K-edge XAS follows the same principles, but differences in the origin of certain spectral features need to be specifically addressed.

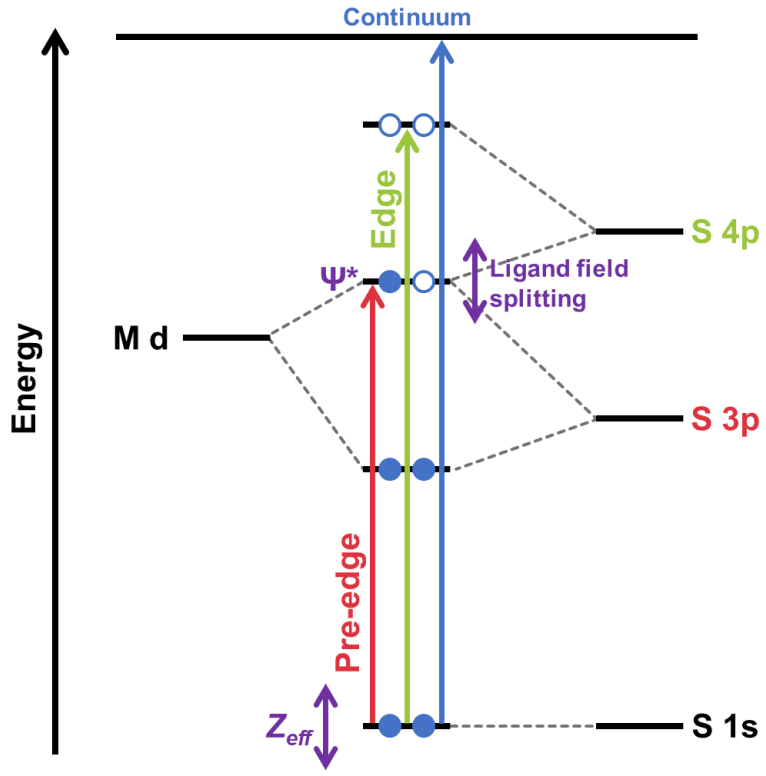

Figure 2.17 A simplified molecular orbital manifold of a M−S coordination complex, with the S K-edge pre-edge and edge transitions indicated.

S K-edge follows the principles outlined above, except pre-edge features stem from dipole-allowed S 1s → 3p transitions (Figure 2.17). Vacancies in the 3p orbitals arise in two circumstances: when electron removal generates a sulfur-based radical and when M−S covalent bonding shifts electrons from full S 3p orbitals to empty metal d orbitals, forming a partial hole. In the latter case S K-edge probes all orbitals of a metal complex with S 3p character and so directly measure M−S bond covalency, with peak intensity correlation with the S 3p content of the absorbing orbital.[186-188] The pre-and rising edge energies will reflect

the oxidation level of the sulfur atoms, but in cases with more than one S atom a shift of ≥1 eV is rarely observed. Moreover, effects from changes to geometry (*vide supra*) can counteract this shift.

As discussed above, intense pre-edge features are often observed in the ligand K-edge of TM complexes;[187,189] in S K-edge these features stem from transitions from the S 1s to the formally filled S 3p orbitals, where bonding causes mixing with metal d orbitals. As the pre-edge transitions are localised on the S atoms, transition intensity correlates with the S character of the M orbitals and thus also M−S bond covalency.[186,190] This principle has been applied to a variety of systems with M−S bonds and successfully used to determine the S character of ground-state wave functions, illustrating the usefulness of S K-edge as spectroscopic technique.[188,191]

S K-edge XAS measurements have thus been used throughout this thesis, complimenting metal K-edge measurements and allowing insight into the effects of changing ligand substituents and oxidation states in comparable systems. Where possible additional insight was gained from further measurements between coordinated and uncoordinated ligands or ligand-equivalents.

2.3.4 X-ray Absorption Spectroscopy Discussion

Co K-edge XAS was used to examine the difference in electronic structures of $[Co(SPh)_4]^{2-}$, $[Co(SC_6F_5)_4]^{2-}$ and $[Co(STol)_4]^{2-}$, with complimentary S K-edge used to probe the substituent influence on the coordinated S atoms.

2.3.4.1 Co K-edge XAS of Co^{II} Arylthiolate Complexes

The Co K-edge spectra of the Co^{II} arylthiolate complexes are shown in Figure 2.18, with the energies of the rising edge positions determined at the first inflection point of the edge summarised alongside the pre-edge energies in Table 2.3; individual spectra are available in Appendix 8.2. The Co K-edge spectra of the Co^{II} arylthiolate species are virtually identical, with pre- and rising-edge features occurring at near-identical energies and intensities.

Table 2.3 Co K-edge XAS pre- and rising-edge energies (eV), and intensities (D_0) for $[Co(SPh)_4]^{2-}$, $[Co(SC_6F_5)_4]^{2-}$ and $[Co(STol)_4]^{2-}$.

Complex	Pre-edge energy	D_0	Rising-edge energy[a]
$[Co(SPh)_4]^{2-}$	7709.6	0.047	7716.7
$[Co(SC_6F_5)_4]^{2-}$	7709.4	0.041	7717.1
$[Co(STol)_4]^{2-}$	7709.5	0.048	7716.8

[a] Determined at the first inflection point.

The pre-edge features are consistent with T_d Co^{II} species,[192,193] occurring at 7709.5 ± 0.1 eV with intensities supporting a non-centrosymmetric D_{2d} coordination environment. More significant changes are observed in the rising edge. Although charge-transfer shakeup processes and multiple scattering effects can complicate assignments,[185,192,194,195] the rising edge region of the spectra (7715 to 7725 eV) reflects changes in Co charge, Z_{eff}. The possibility of shakedown transitions in the rising edges makes assigning specific values to the 1s → 4p transition difficult, but a general trend is observable. The transitions in $[Co(SPh)_4]^{2-}$ and $[Co(STol)_4]^{2-}$ both occur at 7716.7 ± 0.1 eV, whilst in $[Co(SC_6F_5)_4]^{2-}$ the 1s → 4p energy increases to 7717.1 eV.

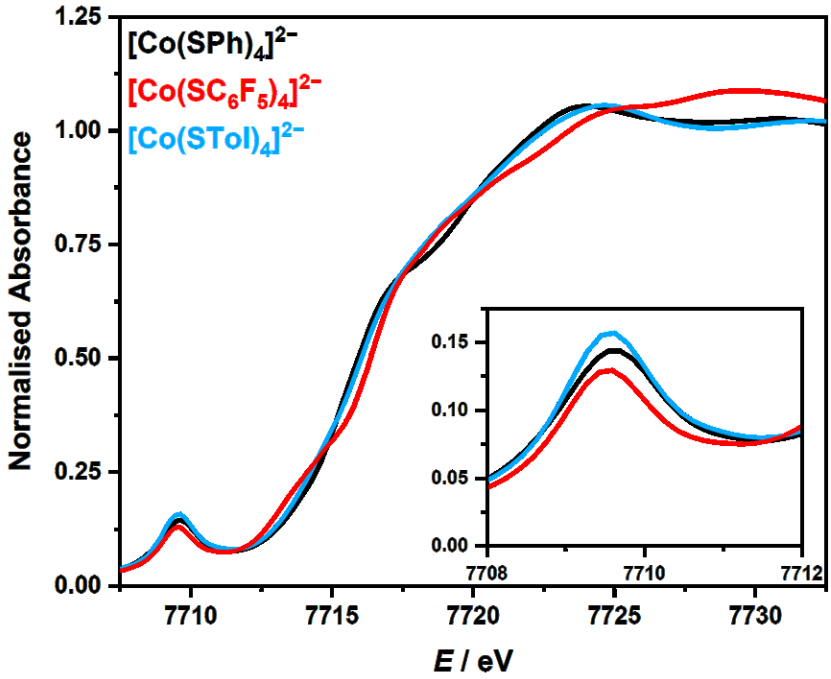

Figure 2.18 Overlay of the normalised Co K-edge XAS spectra of the Co arylthiolate complexes. The inset shows an expanded view of the pre-edge region.

The rising edge transition energies in $[Co(SPh)_4]^{2-}$ and $[Co(STol)_4]^{2-}$ confirm the identical oxidation states of the Co ion in both complexes, with little impact from the electron-donating substituents in the latter species observable. In contrast, the electron-withdrawing F-substituents in $[Co(SC_6F_5)_4]^{2-}$ have a clear effect, increasing the 1s → 4p energy by ~0.4 eV as they siphon electron density from the Co ion. The shift thus stems from the substituents increasing Co Z_{eff}, not direct oxidation of the Co ion. An oxidation state change of ±1 generally corresponds to a shift of ~1 eV,[196] much more than observed.

Overall the Co K-edge shows that although the substituents in $[Co(SC_6F_5)_4]^{2-}$ do slightly impact Co Z_{eff}, the impact on electronic structures across the series is negligible. The pre-edge region illustrates this, with the similar feature energies and intensities showing the LF splitting to be near-identical across the series.

2.3.4.2 S K-edge XAS of Co^{II} Arylthiolate Complexes

The S K-edge spectra of the Co^{II} arylthiolate complexes and their second derivatives are shown in Figure 2.19; individual pseudo-Voigt deconvolutions are displayed in Figure 2.20 with the pre-edge peak energies and intensities listed in Table 2.4. Individual spectra are available in Appendix 8.3.

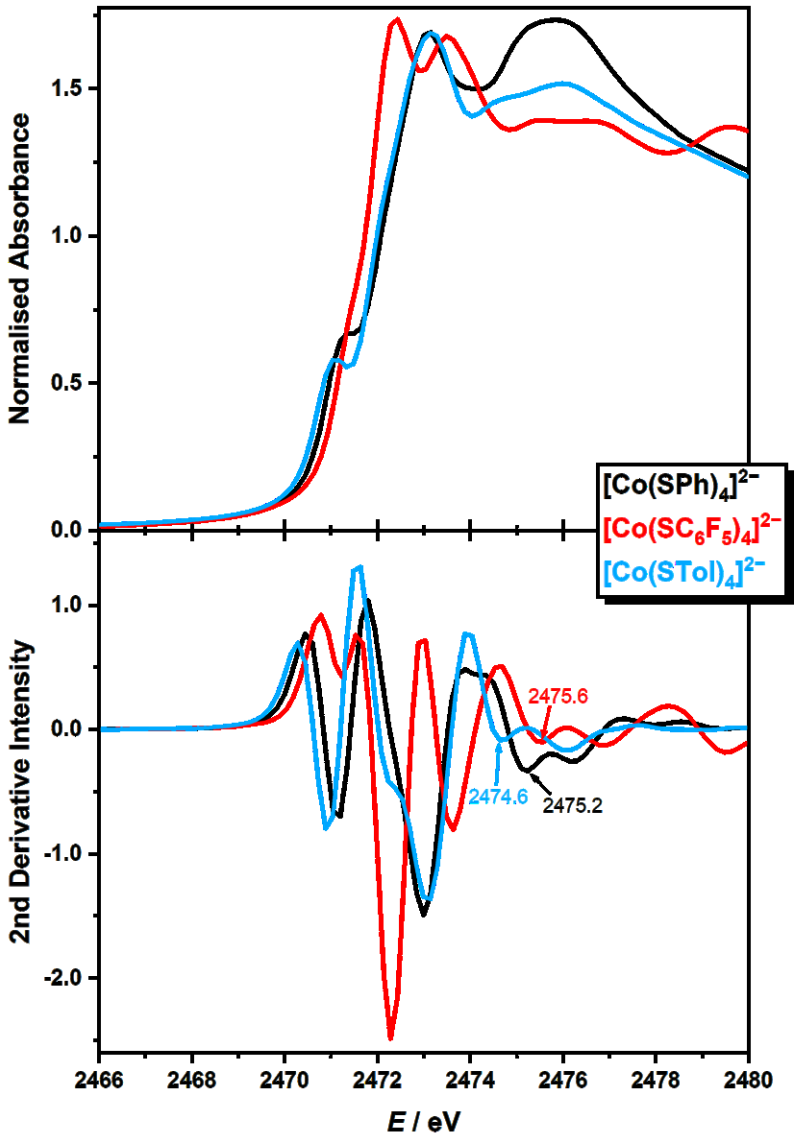

Figure 2.19 Comparison of the normalised S K-edge spectra (top) and their second derivatives (bottom) for $[Co(SPh)_4]^{2-}$, $[Co(SC_6F_5)_4]^{2-}$ and $[Co(STol)_4]^{2-}$. The 1s → 4p edge transitions are indicated in the plots of the second derivatives.

The S K-edge spectra of $[Co(SPh)_4]^{2-}$, $[Co(SC_6F_5)_4]^{2-}$ and $[Co(STol)_4]^{2-}$ contain two well resolved pre-edge features, with lower energy transitions at 2471.25 ± 0.25 eV followed

by higher energy transitions at 2472.24 ± 0.1 eV. Although at ±0.1 eV[190] the resolution of the experiment is not high enough to allow comparison of the energies of both transition across the series, it is enough to allow discussion of the energy gap between them.

Table 2.4 Pre-Edge Peak Energies (eV) and Intensities (D_0) for the Co^{II} arylthiolate complexes.

	Pre-edge energy	D_0	h	α^{2a}
$[Co(SPh)_4]^{2-}$	2471.24	0.11	2	
	2472.22	0.13	2	
$[Co(SC_6F_5)_4]^{2-}$	2471.47	0.09	2	
	2472.29	0.30	2	
$[Co(STol)_4]^{2-}$	2471.06	0.08	2	
	2472.19	0.15	2	

[a] Determined from $\alpha^2 = 12D_0/(H \times I_S)$. I_S = 10.95, 11.85, 12.75, 13.20 (Estimated from the S 1s → 4p transition energies in Figure 3.17 and the correlation plot in reference 191)

At 0.82 eV, the electron-poor $[Co(SC_6F_5)_4]^{2-}$ system has the lowest energy gap, which increases to 0.98 eV in $[Co(SPh)_4]^{2-}$ and 1.13 eV in $[Co(STol)_4]^{2-}$. Most of the shift is due to increases in the lower transition energy, from 2471.06 to 2471.24 to 2471.47 eV in $[Co(STol)_4]^{2-}$, $[Co(SPh)_4]^{2-}$ and $[Co(SC_6F_5)_4]^{2-}$, respectively. The substituent effects mean that although the Co LF splitting remains constant, the S 3p orbitals are more affected by the changing substituents. The electron-donating methyl substituent stabilise the S 3p orbitals most, decreasing the pre-edge transition energy, whilst in $[Co(SC_6F_5)_4]^{2-}$ the S 3p orbital is destabilised, raising the energy of the transition relative to $[Co(SPh)_4]^{2-}$. Unfortunately, although intensity stems from the degree of overlap of the S 3p and Co 3d orbitals, the transitions could not be isolated with enough certainty for discussion of Co−S bond covalency.

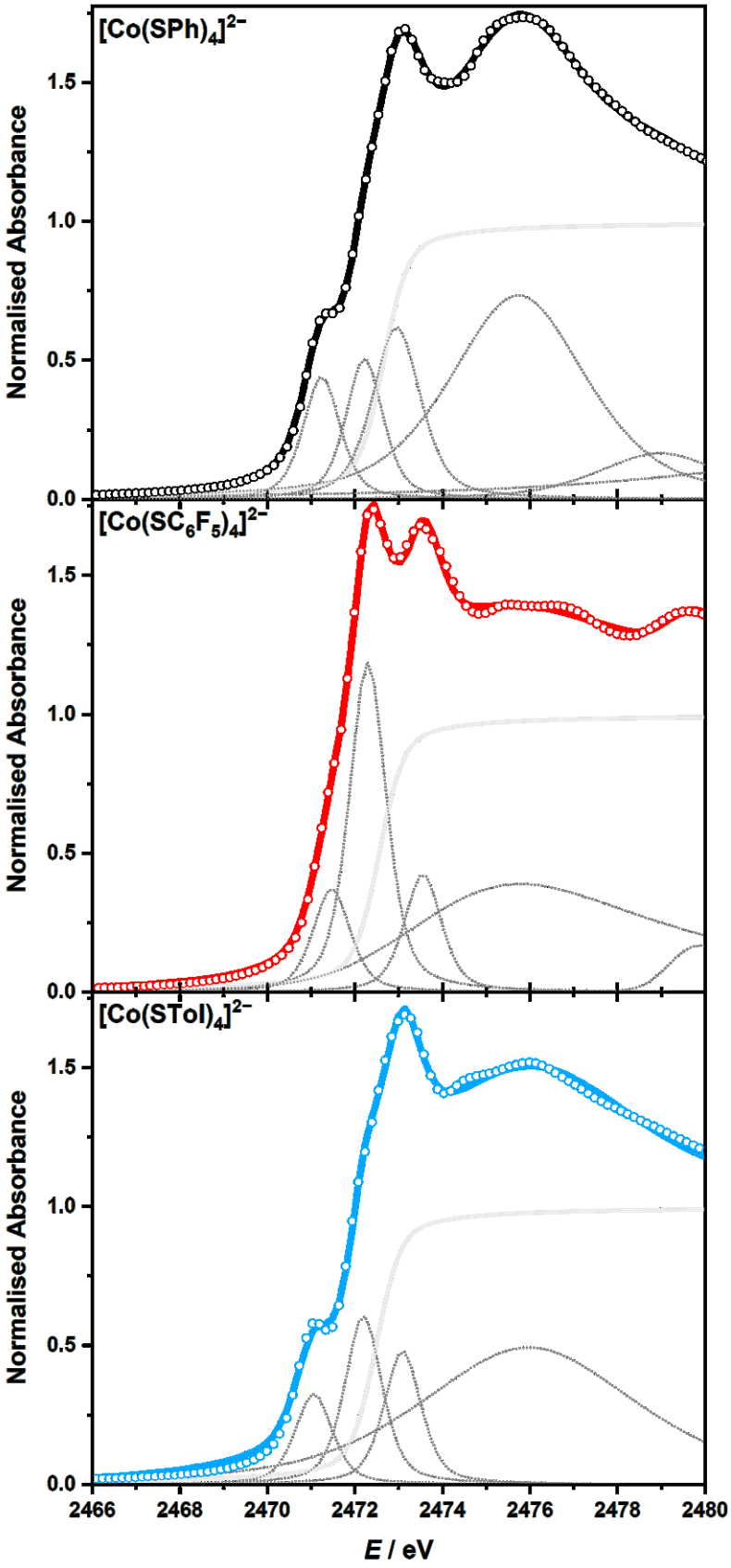

Figure 2.20 Pseudo-Voigt deconvolution of S K-edge spectra of $[Co(SPh)_4]^{2-}$, $[Co(SC_6F_5)_4]^{2-}$ and $[Co(STol)_4]^{2-}$. Circles represent the experimental data; dotted lines represent the pseudo-Voigt; the solid grey line the edge jump; and the solid coloured line is the sum of the fit.

Substituent effects are also observed in the 1s → 4p transition energy: at 2474.6 eV $[Co(STol)_4]^{2-}$ has the lowest energy transition, which occurs at 2475.2 and 2475.6 eV in $[Co(SPh)_4]^{2-}$ and $[Co(SC_6F_5)_4]^{2-}$, respectively. An "oxidation index" for S K-edge transitions developed by Vairavamurthy[197] was supported Frank *et al.*, who confirmed the near-linear relationship between absorption energy and oxidation state in S K-edge features of S compounds.[198] Vairavamurthy showed thiolato S to have transition energies of 2474.1 eV,[197] significantly lower than the 1s → 4p transitions observed here. However, Frank *et al.*, show the absorption energy to increase by 1.6 ± 0.2 eV per oxidation state,[198] so with the exception of $[Co(SC_6F_5)_4]^{2-}$, the shifts in the complexes do not indicate oxidation of the S atoms. The shifts instead stem from ligand coordination to the Co^{II} centres as formation of Co−S bonds delocalises electron density from the S to the Co atom. The substituent influence is clear, as the S in the electron-withdrawing fluorinated system has less electron density, whilst in $[Co(STol)_4]^{2-}$ the methyl substituent donates electron density to the S atom, giving it the lowest formal oxidation state and lowest 1s → 4p energy. The unadorned species falls in the middle.

2.4 Experimental

2.4.1 Physical Measurements

Electronic absorption spectra were recorded using a Shimadzu UV-3600 UV-Vis-NIR spectrophotometer (200 – 1500 nm) in a 1 cm quartz cuvette at a scan rate of 1 nm per second. Infrared data were taken as pressed pellets using a Shimadzu FTIR-8400S spectrophotometer with a diamond anvil cell. ^{1}H and ^{13}C NMR spectra of the complexes were measured at 25 °C on a Bruker AVI 400MHz NMR spectrometer, with chemical shifts referenced to the protonated solvent residual.[199] Magnetic susceptibility measurements were on a Sherwood Scientific Mark 1 Magnetic Susceptibility Balance using an aqueous solution of $Hg[Co(CNS)_4]$ as a calibrant.[200] Mass spectrometry (MS) spectra (electrospray ionization, ESI) were obtained with a Bruker microTOF-Q Quadrupole Time-of-Flight Mass Spectrometer operating in positive- and negative-ion modes Elemental analyses were determined by the departmental microanalysis services using an EA 1110 CHNS, CE-440 Elemental Analyser.

2.4.2 X-ray Absorption Spectroscopy

All X-ray Absorption data were measured at the Stanford Synchrotron Radiation Lightsource (SSRL).

Co K-edge data was measured in a high-magnetic field mode of 20 kG on the 16-pole beamline 9−3 under conditions of 3 GeV and 500 mA. A fully tuned Si(220) double-crystal monochromator was used for energy selection and a Rh-coated mirror set to an energy cut-off of 9 keV used for Harmonic rejection. Internal energy calibration was accomplished by the simultaneous measurement of the absorption of a Co foil placed between two ionisation chambers situated after the sample, with the first inflection point of the foil spectrum fixed at 7709.5 eV.[201] Samples were diluted in BN, pressed into a 1 mm Al spacer and sealed with 37 μm Kapton tape. Data was measured in the transmission mode using an N_2-filled ionisation chamber placed after the sample, which was maintained at 10 K using a liquid He flow cryostat. Data represent the average of 4 scans. Data were

processed using the MAVE and PROCESS modules of the EXAFSPAK software package[202] by fitting a second-order polynomial to the pre-edge region and subtracting this background from the entire spectrum. A three-region cubic spline was used to model the smooth background above the edge. The absorbance was normalised by subtracting the spline and normalising the post-edge absorbance to 1.0.

S K-edge data was collected on the 20-pole wiggler beamline 4−3 in a high-magnetic field mode of 10 kG with a Ni-coated harmonic rejection mirror and a fully tuned Si(111) double-crystal monochromator. Incident intensity was recorded using an ion chamber in a flowing helium flight path, with complete details for the optimisation of the setup for low energy described by Hedman et al.[203] All samples were measured at room temperature as fluorescence spectra using a Lytle detector. Samples were ground finely and dispersed as thinly as possible on Mylar tape to minimise the possibility of fluorescence saturation effects. Data represent 2−3 scan averages. All samples were monitored for photoreduction throughout the course of data collection. The energy was calibrated using the S K-edge spectrum of $Na_2S_2O_3 \cdot 5H_2O$, run at intervals between sample scans. The maximum of the first pre-edge feature in the spectrum was fixed at 2472.02 eV. A step size of 0.08 eV was used over the edge region. Data were averaged, and a smooth background was removed from all spectra by fitting a polynomial to the pre-edge region and subtracting this polynomial from the entire spectrum. Normalisation of the data was accomplished by fitting a flattened polynomial or straight line to the post-edge region and normalizing the post-edge to 1.0.

2.4.3 Syntheses

The compounds $(PPh_4)_2[Co(SPh)_4]$, $(NEt_4)_2[Co(SC_6H_4Me)_4]$, $(PPh_4)_2[Co_4(SPh)_{10}]$ were prepared using methods based on that of Dance *et al*.[114] Dimesityl disulfide was synthesised using an amalgamation of several literature procedures for related compounds,[204] whilst $(PPh_4)_2[Co(SC_6F_5)_4]$[109] and $(NEt_4)_2[CoCl_4]$[205] were prepared following literature methods directly. Except for dimesityl disulfide and sodium thiophenolate, all reagents were purchased from commercial sources and used as received. Dry solvents were either dried with a system of drying columns from the Glass Contour Company or distilled according to standard procedures,[206] before being stored under an inert atmosphere of dinitrogen over 3 Å molecular sieves prior to use. All reactions were conducted under an inert atmosphere of dinitrogen using standard Schlenk techniques, using dry or degassed solvents.

Dimesityl Disulfide. Under a positive flow of dinitrogen Mg turnings (5.77 g; 234 mmol) were added to a solution of dibromoethane (1.00 mL, 2.17 g; 11.6 mmol) in dry THF (150 mL). The resulting mixture was refluxed for 1 h, before the slow addition of 2-bromomesitylene (25.0 mL, 32.5 g; 163 mmol) over 1.5 h. After this time the reaction was refluxed for a further 12 h, before being cannula filtered into a 250 mL Schlenk flask. S_8 (5.23 g; 20.4 mmol) was then added under a positive flow of nitrogen, and the resulting mixture stirred for 72 h. The solution was hydrolysed by slow addition of H_2O (25 mL) followed by 6 M HCl (37 mL), and the organic layer extracted into hexane (4 × 25 mL), before being dried over $MgSO_4$ and reduced under vacuum to give a significant volume of yellow oil. This was reconstituted in MeOH (60 mL), and I_2 (5.86 g; 23.1 mmol) added. After stirring for 1 h, the tan precipitate that formed was collected by vacuum filtration, washed with MeCN (4 × 25 mL) and dried under vacuum for 4 h to yield the final product. Yield = 14.9 g (60%).

^{1}H NMR (400 MHz, $CDCl_3$) δ: 6.84 (s, 4 H); 2.25 (s, 6 H); 2.21 s (s, 12 H). ^{13}C NMR (400 MHz, $CDCl_3$) δ: 143.4; 139.3; 131.5; 129.0; 21.5; 21.2. IR (cm^{-1}): 2918 s, 2849 w, 2731 w,

1751 w, 1599 s, 1456 m, 1435 m, 1371 s, 1294 m, 1246 w, 1175 w, 1032 m, 887 w, 862 s, 853 s, 718 m, 625 m, 557 s, 482 w, 413 w. ESI-MS: *m*/*z* 325.1 $[M+Na]^+$.

Sodium Thiophenolate, NaSPh. A 50 mL Schlenk flask was charged with sodium (103 mg; 4.49 mmol) and dried under vacuum on a Schlenk line for 0.5 h. A cannula was then used to add dry THF (30 mL) under an inert atmosphere of dinitrogen, followed by thiophenol (0.46 mL, 495 mg; 4.49 mmol), added dropwise to the vigorously stirring solution; the mixture was then refluxed under dinitrogen for 4 h. The solution was then left to cool for 45 min after which time degassed diethyl ether (20 mL) was added to induce precipitation. The resulting solid product was collected under suction on a sintered glass funnel, washed with diethyl ether (3 × 5 mL) and dried under vacuum for 18 h. The resulting solid product was collected and weighed before being stored under an inert dinitrogen atmosphere. Yield = 485 mg (90%).

Bis(tetraethylammonium) Tetrakis(chloro)cobaltate, $(NEt_4)_2[CoCl_4]$. To a rapidly stirring solution of $CoCl_2{\cdot}6H_2O$ (1.19 g; 5.00 mmol) in absolute EtOH (10 mL) was added a solution of $NEt_4Cl{\cdot}H_2O$ (1.84 g; 10.0 mmol) in absolute EtOH (10 mL), resulting in the immediate formation of a blue precipitate. The solid was collected under suction, washed with cold EtOH (3 × 5 mL) and Et_2O (3 × 5 mL), and dried under vacuum. Yield = 1.34 g (58%).
IR (cm^{-1}): 3017 w, 2978 m, 2947 m, 1458 s, 1402 m, 1182 s, 1152 w, 1121 w, 1080 m, 1034 s, 1007 s, 897 w, 791 s. μ_{eff} (Gouy balance, 289 K) = 4.58 B.M. ESI-MS: *m*/*z* 330.9 $[M]^-$.

Bis(tetraphenylphosphonium) Tetrakis(thiophenolato)cobaltate, $(PPh_4)_2[Co(SPh)_4]$. The complex was prepared using a method based on that of Suturina *et al*.[43] A solution of $Co(NO_3)_2{\cdot}6H_2O$ (92.6 mg; 0.318 mmol) in dry MeCN (12 mL) was prepared and added dropwise to a solution of vigorously stirring solution of NaSPh (235 mg; 1.78 mmol) in dry MeCN (10 mL) in a 50 mL Schlenk flask. The resulting solution was stirred for a further 5

min, before solid PPh_4Br (445 mg; 1.06 mmol) was added under a positive flow of dinitrogen. The reaction mixture was stirred for a further 1 h before being cannula filtered into a second 50 mL Schlenk flask. The filtrate was concentrated under reduced pressure, sealed under nitrogen and stored in a freezer at −35 °C for 72 h. The resulting bright green solution was filtered yielding a large quantity of emerald crystals; these were washed with hexane (3 × 5 mL) and Et_2O (3 × 5 mL) before being dried under vacuum for 18 h. Yield = 265 mg (72%). IR (cm^{-1}): 3090 w, 3038 w, 1583 m, 1570 m, 1483 w, 1470 m, 1435m, 1315 w, 1263 w, 1213 m, 1184 m, 1165 w, 1105 s, 1078 m, 1022 m, 993 m, 897 w, 847 w, 756 m, 746 m, 719 s, 686 s. μ_{eff} (Gouy balance, 288 K) = 4.93 B.M.

Bis(tetraphenylphosphonium) Tetrakis(pentafluorothiophenolato)cobaltate, $(PPh_4)_2[Co(SC_6F_5)_4]$. Pentafluorothiophenol (1.06 mL, 1.60 g; 8.00 mmol) was added to a solution of NaOH (480 mg; 12.0 mmol) in H_2O (6 mL), and the resulting solution mixed thoroughly. A solution of $CoSO_4{\cdot}7H_2O$ (2.25 g; 8.00 mmol) in H_2O (10 mL) was simultaneously prepared, and the sodium pentafluorothiophenolate solution added severally to it over one minute. A dark green solution rapidly formed, which was filtered and PPh_4Cl (1.50 g; 4.00 mmol) in H_2O (10 mL) added to the filtrate. A vivid green precipitate formed immediately and was collected under suction, washed with a cold 1:1 mixture of EtOH:H_2O (3 × 15 mL) and Et_2O (5 × 15 mL), before being dried under vacuum. The dried crude product was then collected and recrystallised from acetone and Et_2O, yielding bright green crystals of the pure product. Yield = 2.43 g (79%)

IR (cm^{-1}): 3057 w, 1717 w, 1618 w, 1586 m, 1497 s, 1468 s, 1437 s, 1387 m, 1366 w, 1319 w, 1265 m, 1188 m, 1165 w, 1107 s, 1076 m, 997 m, 964 s, 949 w, 854 s, 814 m, 754 m, 722 s, 689 s, 640 w, 619 w. μ_{eff} (Gouy balance, 288 K) = 4.84 B.M.

Bis(tetraethylammonium) Tetrakis(4-methylthiophenolato)cobaltate, $(NEt_4)_2[Co(SC_6H_4Me)_4]$. Under an inert atmosphere of dinitrogen a solution of 4-methylthiophenol (1.98 g; 16.0 mmol) and NEt_3 (2.23 mL, 1.62 g; 16.0 mmol) in degassed

EtOH (5 mL) was prepared and a cannula used to add it to a vigorously stirring solution of $CoCl_2 \cdot 6H_2O$ (474 mg; 2 mmol) in degassed EtOH (3 mL). After 5 min a solution of NEt_4Br (840 mg; 4.00 mmol) in degassed EtOH (5 mL) was added dropwise to the stirring reaction mixture, with the resulting solution stirred for a further 1 h. The solution was then cannula filtered into a 50 mL Schlenk tube, sealed under nitrogen and stored in a freezer at −35 °C for 18 h. After this time a forest green microcrystalline precipitate had formed, which was collected under suction, washed with ^{i}PrOH (6 × 5 mL) and Et_2O (6 × 5 mL), and dried under vacuum for 18 h. Yield = 783 mg (48%).

IR (cm^{-1}): 3057 w, 2980 w, 2856 w, 2334 w, 1681 w, 1585 m, 1497 m, 1468 s, 1435 m, 1267 m, 1107 s, 1076 m, 997 m, 964 s, 854 s, 754 m, 721 s, 689 s, 615 w. μ_{eff} (Gouy balance, 288 K) = 4.55 B.M.

Bis(tetraphenylphosphonium) Deca(thiophenolato)tetracobaltate, $(PPh_4)_2[Co_4(SPh)_{10}]$. A solution of $Co(NO_3)_2 \cdot 6H_2O$ (81.5 mg; 0.280 mmol) in degassed EtOH (3 mL) was prepared and heated to 40 °C, before being added to a solution of thiophenol (93.7 mg, 0.087 mL; 0.84 mmol) and NEt_3 (85.0 mg, 0.117 mL; 0.84 mmol) in degassed MeCN (2 mL), stirring under an inert atmosphere of dinitrogen. Immediately after a boiling solution of PPh_4Br (419 mg; 1.00 mmol) in degassed MeOH (1 mL) was added, and the reaction mixture sealed under nitrogen and was placed in a freezer at −35 °C for 18 h. After this time a dark microcrystalline precipitate had formed which was collected under suction, washed with ^{i}PrOH (4 × 5 mL) and Et_2O (3 × 5 mL) and dried under vacuum for 18 h. Yield = 93 mg (9 %).

IR (cm^{-1}): 3052 w, 1576 m, 1476 m, 1435 m, 1339w, 1316 w, 1221 w, 1186 w, 1107 m, 1080 m, 1070 w, 1024 m, 997 m, 968 w, 901 w, 845 w, 721 s, 689 s, 611 w. μ_{eff} (Gouy balance, 288 K) = 6.83 B.M.

Bis(tetraphenylphosphonium) Deca(pentafluorothiophenolato)tetracobaltate, $(PPh_4)_2[Co_4(SC_6F_5)_{10}]$. Under an inert atmosphere of dinitrogen a solution of

$Co(NO_3)_2 \cdot 6H_2O$ (82 mg; 0.280 mmol) in degassed EtOH (3 mL) was prepared and heated to 40 °C. The hot solution was then added dropwise to a solution of pentafluorothiophenol (0.111 mL, 168 mg; 0.840 mmol) and NEt_3 (0.117 mL, 85.0 mg; 0.84 mmol) in dry MeCN (2 mL), stirring under nitrogen in a Schlenk flask. After stirring for 5 min, a solution of PPh_4Br (419 mg; 1.00 mmol) in boiling degassed MeOH (1 mL) was added, and the resulting dark brown reaction mixture sealed under nitrogen before being stored at −35 °C for 24 h. After this time a small amount of dark crystals had formed, which were collected under suction in air, washed with ^{i}PrOH (4 × 5 mL) and Et_2O (3 × 5 mL) and dried under vacuum for 18 h. Yield = 21 mg (3%).

IR (cm^{-1}): 2460 w, 1499 m, 1470 m, 1437 m, 1246 w, 1188 w, 1107 m, 997 w, 966 m, 856 m, 812 w, 754 w, 721 m, 689 m, 617 w, 525 s, 511 s, 446 s, 415 s, 401 s. ESI-MS: *m*/*z* 2903 $[M]^-$. μ_{eff} (Gouy balance, 289 K) = 7.02 B.M.

3 Co^{II} 1,1-Dithiolate Complexes

3.1 Introduction

Since the 1960s dithiolene systems have been active subjects of study,[80,85] with applications in biological cofactors and other synthetically useful systems driving research forward.[207] In recent years there has been much interest in Co dithiolene complexes, with promise shown in areas ranging from SMM[71,73] and qubit[15] research to novel metal-organic framework (MOF)[208] and catalyst[209] systems. Despite this, Co 1,1-dithiolate systems have been poorly studied, with research focussing almost exclusively on 1,2-dithiolates.

Initial investigations were performed by groups led by Dimitri Coucouvanis and Harry B. Gray, with research conducted alongside early work into 1,2-dithiolate systems. Although Coucouvanis claimed to have synthesised many Co^{II} 1,1-dithiolate systems, including the *i*-mnt^{2-} and nmt^{2-} ligated complexes discussed below,[210] no data on any Co 1,1-dithiolate species was published until the reporting of $[Co^{III}(i\text{-}mnt)_3]^{3-}$ by Gray and co-workers.[82] Coucouvanis reported data for the same species soon after.[211] Further progress has proven slow, as nothing concrete has been reported outside of a Co^{II} bis(cyclopentadienedithiolate) species by Bereman *et al*.[212] The latter complex was prepared in response to a dearth of Co^{II} 1,1-dithiolate species, in the belief that the dianionic ligand would stabilise a Co^{II} species:[212] analogous monoanionic dithiocarbamate complexes are found to spontaneously oxidise even under anhydrous and oxygen-free conditions.[213] The bis(cyclopentadienedithiolate) complex provides some insight into the lack of Co^{II} species, noting that the stability of such species decreased as the number of d-electrons was reduced, showing the importance of the ligand electron-withdrawing strength in complex stability.

This information makes $[Co^{III}(i\text{-}mnt)_3]^{3-}$ interesting and highlights the difference between 1,1-dithiolate and both 1,2-dithiolates and dithiocarbamate complexes. Given the instability of dithiocarbamate species it is unsurprising 1,1-dithiolate complexes are similar, yet the synthesis of $[Co^{III}(i\text{-}mnt)_3]^{3-}$ uses $Na_3Co^{III}(CO_3)_3{\cdot}3H_2O$ as a starting material, rather than relying on in-situ oxidation of a Co^{II} salt.[82] The synthetic procedure relies on extensive

heating, giving a green-gold microcrystalline product with an electronic spectra significantly different to the species examined in this work. Furthermore, in contrast to both the complexes examined here and the bis(cyclopentadienedithiolate) species,[212] magnetic susceptibility measurements confirm the diamagnetic nature of $[Co^{III}(i\text{-mnt})_3]^{3-}$.[82]

No crystal structures have been reported for any Co 1,1-dithiolate complex, something likely attributed to the distorted nature of the Co species combined with the electron-withdrawing nature of the 1,1-dithiolate ligands. The latter property results in the frequent oxidation of the coordinated ligand in the timeframe of crystal growths, preventing diffraction quality crystals of the Co complexes from forming.

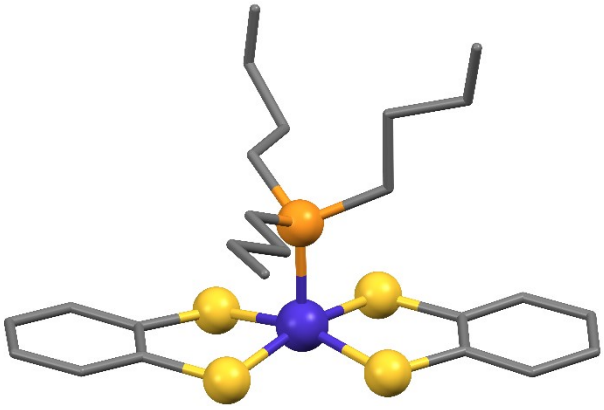

Figure 3.1 Molecular structure of $[Co(bdt)2(^{n}Bu_3P)]-$ (cobalt, grape; sulfur, pineapple; carbon, charcoal; phosphorus, tangerine).

The paucity of data on Co 1,1-dithiolates is not unforeseen given the differences between 1,2- and 1,1-dithiolates. 1,1,-Dithiolate species do not display the redox noninnocence that makes the 1,2-dithiolate species so fascinating, and have a far less reversible $Co^{II/III}$ redox couple: oxidation of Co^{III} 1,2-dithiolates results in either stacked $[\{Co^{III}(L)_2\}_2]^{2-}$ units[214] or heteroleptic $[Co^{III}(L)_2(X)]^{-}$ species[215] if appropriate ligands are introduced (i.e. Figure 3.1).[216] In contrast, $[Co^{III}(i\text{-mnt})_3]^{3-}$ is the only Co^{III} species known, with the coordination of an additional ligand limiting redox reversibility.

Despite the differences, Co^{II} 1,1-dithiolate species still offer an attractive area of investigation, with comparisons between the 1,1- and 1,2-dithiolate complexes of other metals offering insight into the behaviour of Co^{II} 1,1-dithiolate systems. Compared to Co^{II},

a wealth of Ni^{II} species have been reported, with considerable numbers of crystal structures available; one such structure is that of [Ni(*i*-mnt)$_2$]$^{2-}$.[93] This is useful as a direct comparison can be made between the 1,1-dithiolate species and [Ni(mnt)$_2$]$^{2-}$,[92] the analogous 1,2-dithiolate complex.

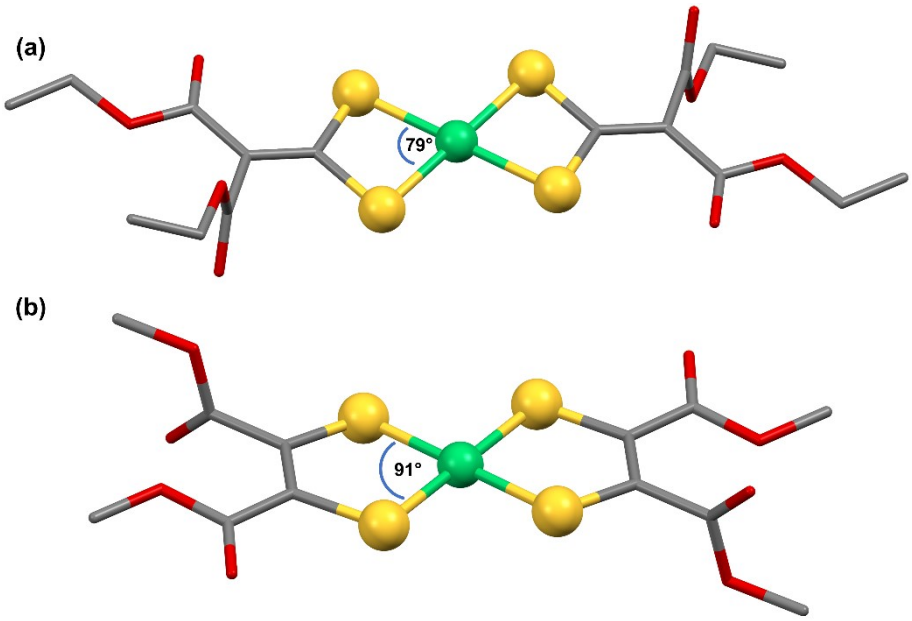

Figure 3.2 Molecular structures of (a) [Ni(ded)$_2$]$^{2-}$ and (b) [Ni(cdmd)$_2$]$^{2-}$ (nickel, mint; sulfur, pineapple; carbon, charcoal; oxygen, scarlet).

The structures show that even as the metal-ligand S−Ni−S bite-angle decreases from 92.2(1)° in [Ni(mnt)$_2$]$^{2-}$ to 86.1(1)° in [Ni(*i*-mnt)$_2$]$^{2-}$, the Ni−S bond length increases from 2.174(1) to 2.209(1) Å. Identical trends are observed in other comparable species, although the degree of changes differs: comparison between the ester-substituted [Ni(ded)$_2$]$^{2-}$ and [Ni(cdmd)$_2$]$^{2-}$ species[90,217] shows that although the S−Ni−S bite-angle undergoes a larger decrease from 91.2(1)° to 78.9(1)°, the difference in bond length is less significant, going from 2.181(1) to 2.195(1) Å. While the ligands are not perfect isomers (Figure 3.2), the importance of substituent-effects is clearly illustrated.

Research into Co^{II} 1,1-dithiolates has much appeal, providing opportunities to study the effects of both altering ligand substituents and going from a 1,2- to a 1,1-dithiolate ligand system. As with 1,2-dithiolate ligands, the geometry of the 1,1-dithiolate complexes is not

guaranteed, but they offer the possibility of synthesising an ideal D_{2d} system that would be an attractive platform for comparing to previously discussed D_{2d} Co^{II} 1,2-dithiolate SIMs. If successfully isolated, the effect of the tighter metal-ligand bite-angle could be compared against the likely increase in Co−S bond length.

3.2 Synthesis

3.2.1 Ligands

All ligands used in this work have been well studied and are either 1,2- or 1,1-dithiolates (Figure 3.3). 1,1-Dithiolate ligands with an array of substituents were chosen to study electronic affects across the series. Published procedures were used to prepare Na_2(mnt), K_2(dts), $(PPh_4)_2$(dts) and the $dmit^{2-}$ species outlined below, with the formation and purity of the products confirmed by IR, NMR and ESI-MS spectroscopy.

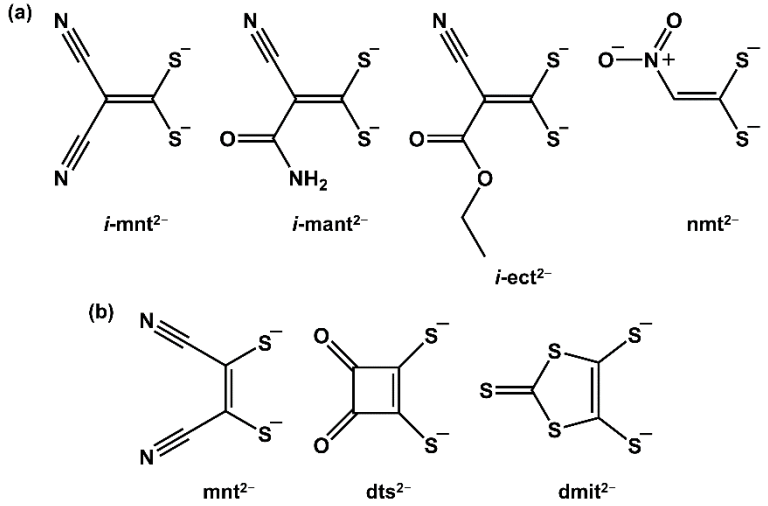

Figure 3.3 The (a) 1,1-dithiolate and (b) 1,2-dithiolate ligands used in this chapter.

Free $dmit^{2-}$ hydrolyses rapidly, so additional steps were taken to isolate the stable $[Zn(dmit)_2]^{2-}$ and benzoyl-protected forms (Scheme 3.1). Although the Zn^{II} complex is stable, cleaner complexation is achieved using benzoyl-protected dmit: as base cleaves the protecting group in situ, free $dmit^{2-}$ is generated on demand. A transition metal salt can then be added to give the desired product in high yield.

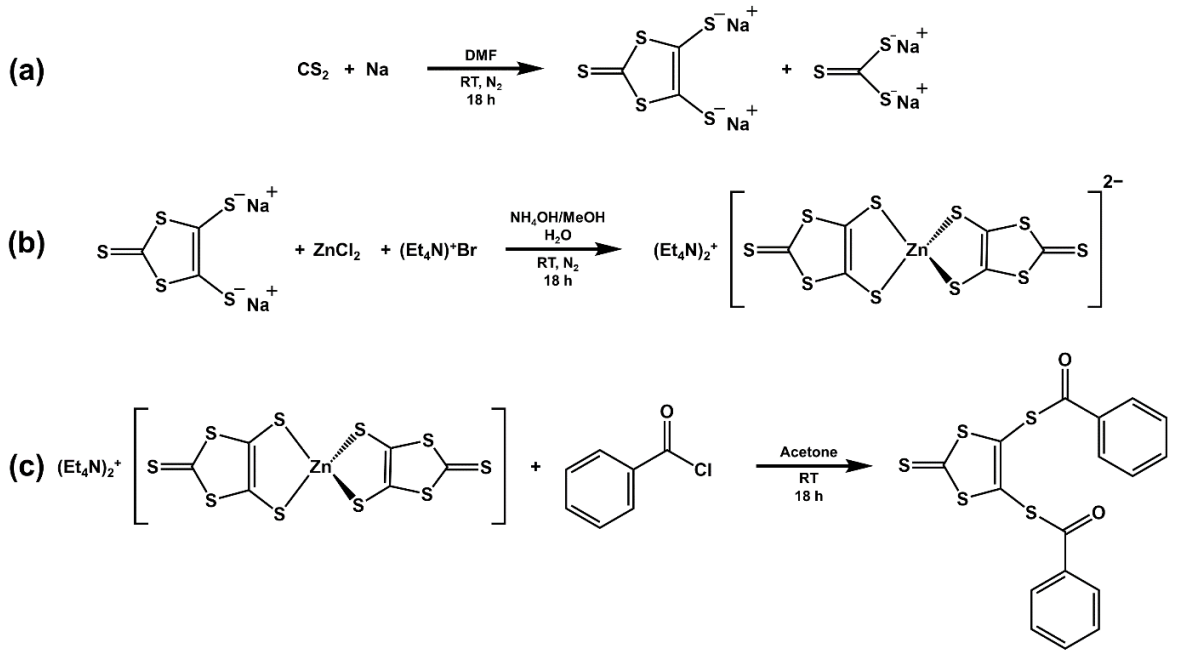

Scheme 3.1 Reaction scheme for (a) Na_2(dmit), and the stable compounds isolated: (b) $(NEt_4)_2[Zn(dmit)_2]$ and (c) Benzoyl dmit.

The synthesis of 1,1-dithiolates was accomplished by reaction of a bifunctional C−H acid with general formula $H_2CR_1R_2$ (where R_1 and R_2 are sufficiently electron withdrawing substituents) and carbon disulfide in the presence of a base at 0 °C (Scheme 3.2). The low reaction temperature limits formation of intractable by-products. EtOH proved the most suitable solvent, as although there was poorer dissolution of KOH, the product precipitated out in good yield as the reaction proceeded.

The IR spectrum of K_2(nmt) was unlike the others, with a strong band at 1414 cm^{-1} corresponding to N=O featured alongside a weak ν(C−H) peak at 3096 cm^{-1}. Features typical of CN are visible in the spectra of Na_2(*i*-mnt), K_2(*i*-mant) and K_2(*i*-ect) at 2174, 2164 and 2151 cm^{-1}, respectively, as the energy decreases with the total inductive effect of the substituents (*vide infra*). The opposite trend is observed in the C=O and C−O stretches: the former increases from 1311 to 1615 then 1618 cm^{-1} for K_2(*i*-mant), K_2(*i*-ect) and K_2(ded), respectively, with the large energy difference of the approximately 305 cm^{-1} between K_2(*i*-mant) and the others stemming from the amide substituent. With respective energies of 1320 and 1369 cm^{-1}, a more modest increase is observed in C−O IR stretch in the ester-

substituted K_2(*i*-ect) and K_2(ded) ligand salts. The C−S asymmetric stretching vibrations lie in the range 1085 − 1341 cm^{-1}.[218]

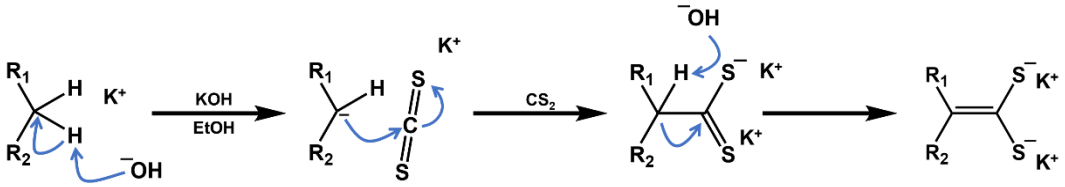

Scheme 3.2 General reaction scheme for 1,1-dithiolate alkali metal salts.

NMR also aided definition of the ligands, with all ^{13}C NMR resonances corresponding to the two olefinic carbons present all spectra. The resonances vary considerably as the ligand substituents change: *i*-mnt^{2-} starts with the lowest resonance at 30 ppm, as the C=C peak shifts to 49, 60 and 62 ppm for *i*-mant^{2-}, *i*-ect^{2-} and ded^{2-}, it continues to reach 71 ppm in the spectra of nmt^{2-}. The overall shift of >40 ppm is acceptable and is in fact smaller than observed in the parent methylene bridging carbons. Malononitrile has a single shift at 8 ppm,[219] compared to 26 ppm for 2-cyanoacetamide,[220] 25 ppm for ethyl cyanoacetate,[221] 42 ppm for diethylmalonate[222] and 63 ppm for nitromethane,[223] resulting in an overall shift of 55 ppm.

NMR shifts corresponding to the CN carbons are visible in the cyano-substituted ligands at 125 ± 2 ppm, and C=O stretches in the amide-[224] and ester-substituted[225] at 170 ± 3 ppm. The ester-substituted ligands K_2(*i*-ect) and K_2(ded) also show features at 94 and 14, and 71 and 14 ppm respectively, corresponding to the -CH_2- and -CH_3 in the ester substituents.[221,222]

The ^{1}H NMR spectra vary considerably: a single resonance at 7.95 ppm is observed for K_2(nmt), whilst K_2(*i*-mant) has a sole doublet at 3.52 ppm. The spectra of K_2(*i*-ect) and K_2(ded) are similar, with features corresponding to the ester ethyl groups visible in both spectra.

3.2.2 Co^{II} Complexes

Three 1,2-dithiolate complexes were synthesised and characterised: $[Co(mnt)_2]^{2-}$, $[Co(dmit)_2]^{2-}$ and $[Co(dts)_2]^{2-}$, to contrast with the 1,1-dithiolates; $[Co(mnt)_2]^{2-}$ was chosen as it is the 1,2-dithiolate isomer of $[Co(i\text{-}mnt)_2]^{2-}$, and is known to have a tight S−Co−S bite-angle with a D_{4h} $\{CoS_4\}$ coordination environment (Figure 3.4a).[226] This contrasts with $[Co(dmit)_2]^{2-}$, which has a slightly larger bite-angle, but a D_{2d} coordination environment (Figure 3.4b).[227] Although $[Co(dmit)_2]^{2-}$ is known to have a large D, the presence of intense π−π* transitions significantly obscure the LF transitions in the electronic spectra;[172] these are not present in $(PPh_4)_2[Co(dts)_2]$, which was easily prepared at ambient conditions in an aqueous medium, with recrystallisation yielding diffraction-quality crystals of the product in the emerald green typical of T_d $\{Co^{II}S_4\}$ species.

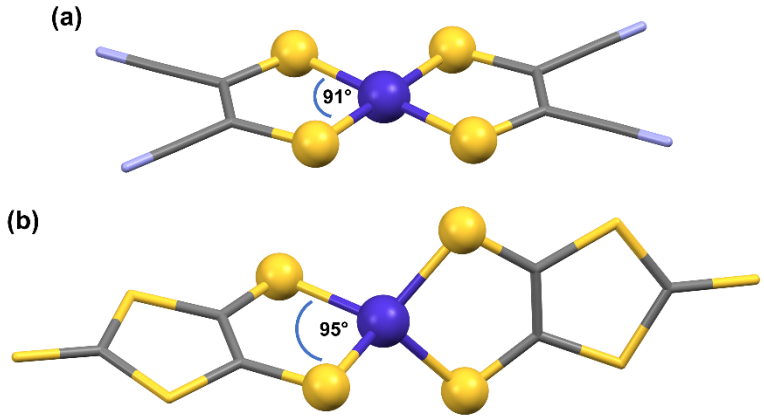

Figure 3.4 Molecular structures of (a) $[Co(mnt)_2]^{2-}$ and (b) $[Co(dmit)_2]^{2-}$ (cobalt, grape; sulfur, pineapple; carbon, charcoal; nitrogen, cornflour).

Synthesis of the other 1,2-dithiolate species proved similarly easy, although anaerobic conditions were maintained to ensure the purity of the final product. K-edge XAS was performed on all three species and used alongside the electronic spectral data to extract information about the LF in the Co^{II} centres. As $[Co(mnt)_2]^{2-}$ is square planar, it gave an EPR signal; this is known and confirms the square-planar $S = {}^1/_2$ nature of the $[Co(mnt)_2]^{2-}$ spin ground state.[228] The D_{4h} $\{CoS_4\}$ coordination environment results in a $2B_{2g}$ (d_{xz}) ground state indicated by $g_{\parallel} > g_{\perp}$. The shift to D_{2h} in $[Co(i\text{-}mnt)_2]^{2-}$ change the SOMO,

resulting instead in a $2A_g$ (d_{z^2}) ground state; this alteration results in different assignments of the S K-edge spectrum (*vide infra*).

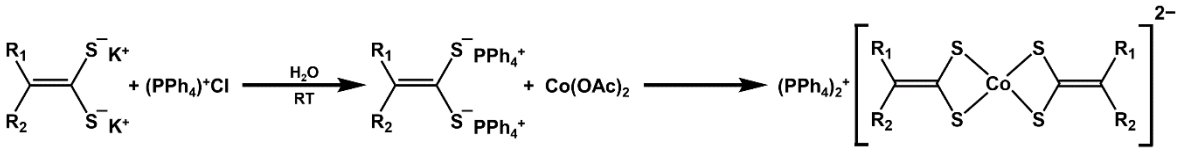

Scheme 3.3 General reaction scheme for Co^{II} bis(1,1-dithiolato) tetraphenylphosphonium salts.

The differences between the 1,2- and 1,1-dithiolates are again reflected in the synthesis of the 1,1-dithiolate Co^{II} species (Scheme 3.3). The tetraphenylphosphonium salts of all species were prepared in good yield in an aqueous medium in ambient conditions, with the desired product precipitating out on adding a solution containing one equivalent of Co^{II} salt to one with two equivalents of 1,1-dithiolate and counterion.

3.3 Results and Discussion

3.3.1 Crystal Structures

Diffraction quality crystals of $(PPh_4)_2[Co(dts)_2]$ were obtained by cooling a saturated acetone solution of the complex to −35 °C, and of $(PPh_4)_2(dts)$ by vapour diffusion of diethyl ether into a concentrated acetonitrile solution.

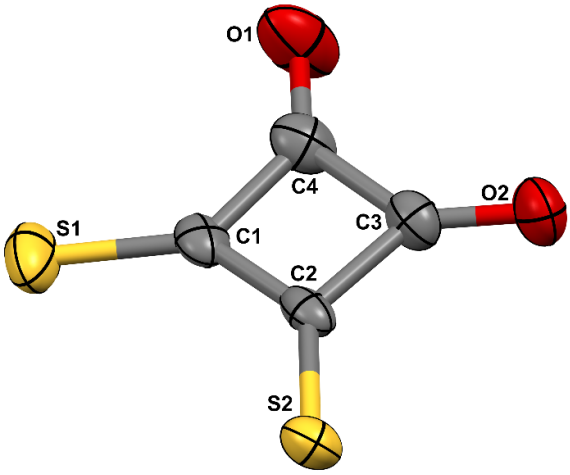

Figure 3.5 Structure of the anion in crystals of $(PPh_4)_2(dts)$·MeCN. Thermal ellipsoids are shown at the 50% probability level.

The molecular structure of $(dts)^{2-}$ is illustrated in Figure 3.5, with selected bond lengths and angles listed in Table 3.1. the structure is that of a square-planar four-membered carbon ring, with two oxygens and two sulfurs in 1,2-positions relative to the each other.

Table 3.1 Selected Bond Distances (Å) and Angles (°) in $(PPh_4)_2(dts)$·MeCN

C1−S1	1.679(5)	C2−S2	1.688(5)
C4−O1	1.237(6)	C3−O2	1.238(6)
C1−C2	1.432(7)	C4−C3	1.498(7)
C1−C4	1.480(7)	C2−C3	1.472(6)
S1−C1−C2	135.3(4)	S2−C2−C1	134.6(3)
O1−C4−C3	135.5(5)	O2−C3−C4	135.7(4)
C1−C2−C3	88.8(4)	C2−C3−C4	88.6(4)
C3−C4−C1	91.7(4)	C4−C1−C2	90.8(4)

Although the C−O bond lengths are significantly shorter than the C−S bonds, the average C−S bond length of ca. 1.684 Å is close to that of ca. 1.70 Å observed in thiourea[229] and thiourea complexes.[230] As the average C−O bond length of ca. 1.238 Å is similarly close to the 1.258 Å observed in the urea,[231] the difference in C−O and C−S bond lengths stem from the larger size of the 3p S relative to the 2p O rather than significantly different bond orders. More information can be derived from the C−C bonds, as the C1−C2 bond is much shorter than C4−C3, with C2−C3 and C1−C4 lengths in between the two. The C−C lengths combined with the multiple C−S and C−O bond character suggests a structure dominated by resonance form (a) in Figure 3.6, with contributions from forms (b) and (c).

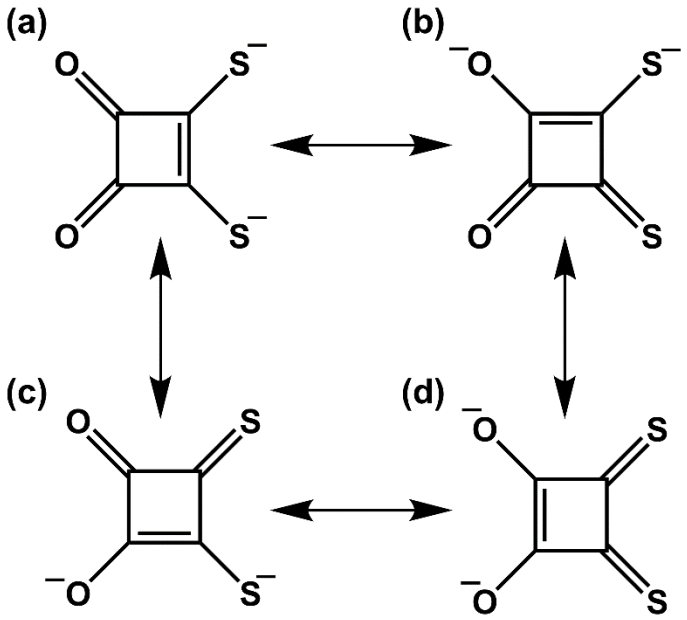

Figure 3.6 Resonance forms of the dithiosquarate dianion.

The dithiosquarate dianion is rigidly square-planar, with the interior angles of the central C_4 ring showing distortions of < 2° away from the ideal of 90° for a square. All bond lengths and angles are comparable to the sole known crystal structure of the free ligand, where the dts^{2-} charge was balanced by one *n*-tetrabutylammonium and one guanidinium counterion and the ligand was described using resonance form (a) in Figure 3.6.[232]

The molecular structure of the $[Co(dts)_2]^{2-}$ is illustrated in Figure 3.7; selected bond lengths and angles are listed in Table 3.2. The complex consists of a discrete monometallic

{CoS_4} moiety where the central Co ion is surrounded by four sulfurs from two bidentate dithiosquarato ligands; the charge of the complex is balanced by two PPh_4^+ counterions.

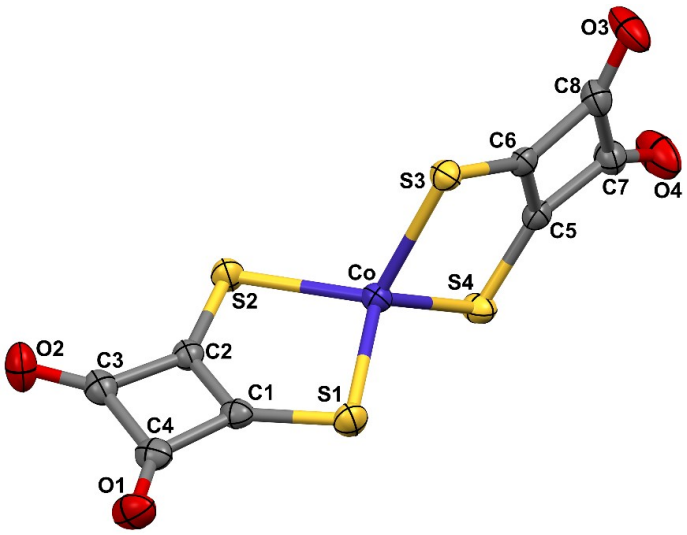

Figure 3.7 Structure of the anion in crystals of $(PPh_4)_2[Co(dts)_2]$. Thermal ellipsoid plots are shown at the 50% probability level.

The mean {CoS_2} planes are orthogonal with distortions of ca. 4° towards planarity, which combined with the ~97° bite-angle of the dts^{2-} ligand results in a tetragonally elongated pseudotetrahedral coordination sphere. The C−S bond lengths remain close to those observed in the free ligand, whilst the C−O bonds decrease; although the decrease is slight, it suggests that resonance form (a) in Figure 3.6 is favoured in the coordinated species. This is corroborated by the reduction in the C1−C2 and C5−C6 and increase in the C3−C4 and C7−C8 bond lengths relative to the free ligand.

With an average length of ca. 2.342 Å, the Co−S bonds in the complex are longer than the M−S bonds in the analogous Ni^{II} and Cu^{II} species which have average lengths of ca. 2.218 Å and 2.318 Å, respectively.[233] The Co−S bonds are also longer than comparable 1,2-dithiolate species, with the equivalent bond lengths in $[Co(dmit)_2]^{2-}$ and $[Co(mnt)_2]^{2-}$ approximately 2.303 and 2.162 Å, respectively;[226,227] and are closer to lengths to the Co−S lengths of ca. 2.323 Å in $[Co(SPh)_4]^{2-}$. When the C−C bonds in the chelating {C_2S_2} moieties are compared: 1.401 Å for $[Co(dts)_2]^{2-}$ compared to 1.355 and 1.339 Å for $[Co(dmit)_2]^{2-}$ and $[Co(mnt)_2]^{2-}$ respectively,[226,227] it is clear the nature of the dts^{2-} ligand removes electron

density away from the $\{CoS_2C_2\}$ coordination pocket towards the rear of the ligand system, increasing Co−S and C−C bond lengths relative to 1,2-dithiolate such that the Co−S lengths are comparable to arylthiolate species.

Table 3.2 Selected Bond Distances (Å) and Angles (°) in $(PPh_4)_2[Co(dts)_2]$

Co−S1	2.352(1)	Co−S2	2.339(1)	Co−S3	2.339(1)
Co−S4	2.336(1)	C1−S1	1.699(2)	C2−S2	1.697(2)
C5−S3	1.697(2)	C6−S4	1.698(2)	C4−O1	1.213(2)
C3−O2	1.212(2)	C7−O4	1.217(2)	C8−O3	1.220(2)
C1−C2	1.400(2)	C3−C4	1.543(3)	C5−C6	1.402(2)
C7−C8	1.537(3)	C1−C4	1.476(2)	C2−C3	1.488(2)
C6−C8	1.473(2)	C5−C7	1.480(2)		
S1−Co−S2	96.64(2)	S3−Co−S4	97.54(2)	S1−C1−C2	128.3(1)
S2−C2−C1	128.3(1)	S3−C5−C6	128.6(1)	S4−C6−C5	128.4(1)
O1−C1−C2	136.0(2)	O2−C3−C4	135.7(2)	O3−C8−C7	135.6(2)
O4−C7−C8	135.3(2)	C1−C2−C3	87.00(1)	C2−C3−C4	92.54(1)
C3−C4−C1	87.45(1)	C4−C1−C2	93.01(1)	C5−C6−C8	87.25(1)
C6−C8−C7	92.42(1)	C7−C5−C6	87.47(1)	C8−C7−C5	92.80(1)

The shorter M−S bonds in the Ni^{II} and Cu^{II} dts^{2-} species stems from the square-planar nature of the complexes. The extended π-system formed facilitates localisation of electron density on the $\{MS_4\}$ moieties, counteracting the electron-withdrawing effect of the dts^{2-} ligand system. The reduction of the C1−C2 and C5−C6 bond lengths (*vide supra*) in $[Co(dts)_2]^{2-}$ relative to dts^{2-} suggests that the effect is ameliorated by coordination in general, but more so in square-planar systems.

The tetragonal elongation of the coordination sphere pushes the geometry of $[Co(dts)_2]^{2-}$ away from T_d towards D_{2d}. As the complex has ligand bite-angles of 96.64(2)° and 97.5(2)°, the distortion is between that of $[Co(SPh)_4]^{2-}$, with angles of 97.36(5)° and 98.33(6)°, and those of 94.05(1)° and 94.13(1)° recorded for $[Co(dmit)_2]^{2-}$.

3.3.2 Electronic Absorption Spectroscopy

3.3.2.1 Electronic Spectra of 1,1-Dithiolate Ligand Salts

Electronic spectral data and parameters are available in Appendix X. The spectra of Na_2(*i*-mnt), K_2(*i*-mant), K_2*i*-ect) and K_2(ded) are broadly similar, with two intense bands between 300 and 350 nm that stem from S based π → π* transitions. The different ligand substituents give a significantly different spectrum for K_2(nmt), as the nitro group facilitates charge delocalisation throughout the molecule. Analysis of the spectrum of nitromethane has shown that in the molecule the nonbonding oxygen 2p orbitals mix with the σ-electron system;[234] in K_2(nmt) the extended σ- and π-systems in the nitro substituent will facilitate stronger mixing than the cyano-substituent species, increasing charge distribution throughout the molecule. This will be responsible for the unique low energy feature, with the two higher energy transitions corresponding to the same transitions discussed above.

3.3.2.2 Electronic Spectra of Co^{II} 1,1-Dithiolate Complexes

Electronic spectra of the Co^{II} 1,1-dithiolate complexes are overlaid in Figure 3.9. The spectra of $[Co(i\text{-mnt})_2]^{2-}$, $[Co(i\text{-mant})_2]^{2-}$ and $[Co(i\text{-ect})_2]^{2-}$ are similar: two intense LMCT bands are visible at higher energies in each complex, with signature LF transitions observed between 600 and 650 nm. The spectrum of $[Co(nmt)_2]^{2-}$ differs from the other complexes due to the changed ligand substituents.

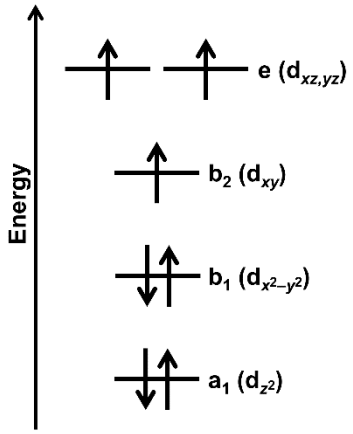

Figure 3.8 Crystal-Field Splitting of a Co^{II} 1,1-dithiolate complex in a D_{2d} coordination environment.

The CT bands in $[Co(i\text{-mnt})_2]^{2-}$, $[Co(i\text{-mant})_2]^{2-}$ and $[Co(i\text{-ect})_2]^{2-}$ occur at lower energies than the intraligand charge transfer bands in the respective free ligands, supporting the assignment as LMCT from fully-occupied orbitals centred on the anionic S atoms on the ligands to vacant orbitals on the Co^{II} ion, illustrated in Figure 3.8.

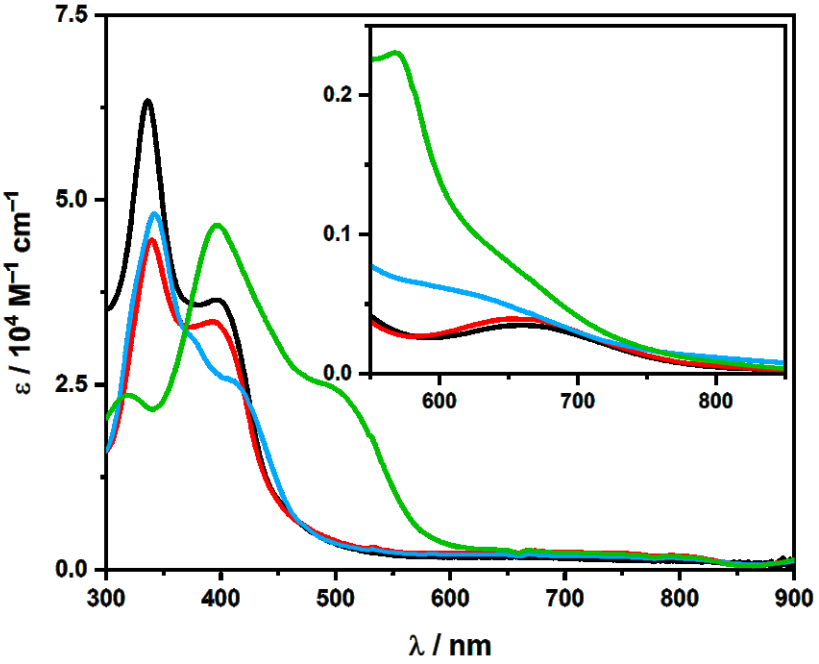

Figure 3.9 Comparison of the electronic spectra of $[Co(i\text{-mnt})_2]^{2-}$ (black), $[Co(i\text{-mant})_2]^{2-}$ (red), $[Co(i\text{-ect})_2]^{2-}$ (blue) and $[Co(nmt)_2]^{2-}$ (green); inset shows an expansion of the LF transitions.

The higher energy transitions to the e MOs remain relatively stable across the three species at 336 ± 3 nm, whilst the lower energy band arising from transitions to the b_2 orbital shift significantly, decreasing from 367 nm in $[Co(i\text{-mnt})_2]^{2-}$ to 394 and 410 nm in $[Co(i\text{-mant})_2]^{2-}$ and $[Co(i\text{-ect})_2]^{2-}$, respectively. The gap between the CT bands thus increases across the series from 2602 to 4117 then 4849 cm^{-1} respectively.

The difference in intensity between the two LMCT bands arises from the different number of vacancies in the acceptor MOs. The higher energy e orbital has twice the vacancies as the b_2 orbital, with the transitions to the e orbitals therefore correspondingly more intense.

As with the free ligand, the spectrum of $[Co(nmt)_2]^{2-}$ is uniquely different: three transitions are visible at 318, 397 and 500 nm. The higher energy transitions correspond to

the LMCT bands visible in the other spectra, but the lower energy transition arises from intraligand charge transfer facilitated by electron delocalisation throughout the ligands. Moreover, the LMCT intensities are reversed, as at 2.04 × 10^4 M^{-1} cm^{-1} the higher energy transition is less than as half intense as the lower energy band at 4.33 × 10^4 M^{-1} cm^{-1}: this difference also stems from the nitro groups facilitated mixing of σ- and π-systems.

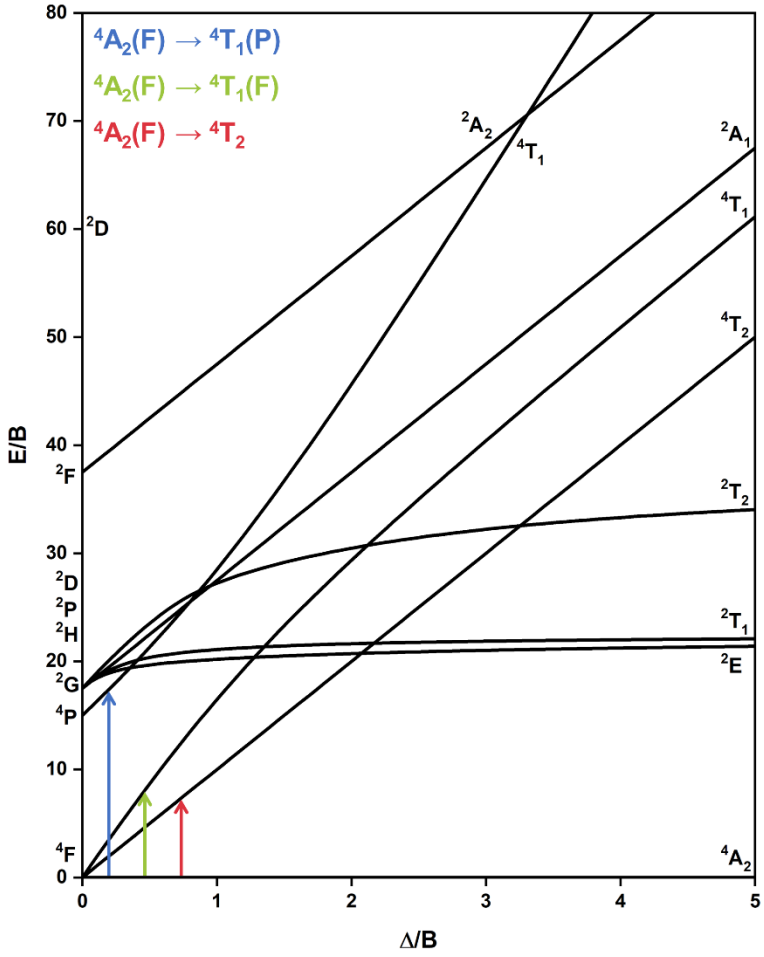

Figure 3.10 Tetrahedral d^7 Tanabe-Sugano Diagram with LF transitions illustrated.

As shown in Figure 2.10, three spin-allowed LF transitions are visible in the electronic spectra of tetrahedral Co^{II} complexes. The most intense is the highest energy $^4A_2(F) \rightarrow {}^4T_1(P)$ transition, followed by the NIR $^4A_2(F) \rightarrow {}^4T_1(F)$ transition, then the $^4A_2(F) \rightarrow {}^4T_2$ transition at the lowest energy. The range of the electronic spectra here prevent observation of the two lower-energy transitions, but the $^4A_2(F) \rightarrow {}^4T_1(P)$ transitions are visible in the electronic spectra between 550 and 750 nm. As mentioned above, in certain

systems intraligand π−π* transitions are known to occur in this region, obscuring the LF transitions.[172] The absence of the transitions in the spectra of the free salts combined with the presence of appropriate LF transitions in analogous Ni^{II} and Cu^{II} systems (discussed in Chapter 5) rules such transitions out however, confirming the nature of the $^4A_2(F) \rightarrow {}^4T_1(P)$ between 550 and 750 nm. The spectral parameters of this transition are collated in Table 3.3, with a magnification of the transitions visible inset in Figure 3.9.

Table 3.3 Spectral Parameters of the $^4A_2 \rightarrow {}^4T_1(P)$

	λ_{max} / nm	ε_{max} / M^{-1} cm^{-1}	Fwhm / cm^{-1}
$[Co(i\text{-mnt})_2]^{2-}$	659	347	3248
$[Co(i\text{-mant})_2]^{2-}$	654	393	3114
$[Co(i\text{-ect})_2]^{2-}$	606	608	4914
$[Co(nmt)_2]^{2-}$	639	888	2604

The LF transitions in $[Co(i\text{-mnt})_2]^{2-}$, $[Co(i\text{-mant})_2]^{2-}$ and $[Co(i\text{-ect})_2]^{2-}$ show the opposite trend to that of the lower energy LMCT bands, with the both energy and intensity increasing across the series. Although the transitions fall in the range typical of tetrahedral Co^{II} complexes,[178] LF bands in square-planar Co^{II} complexes occur at similar energies.[235]

To confirm the tetrahedral nature of the 1,1-dithiolate complexes, $[Co(dts)_2]^{2-}$ and $[Co(mnt)_2]^{2-}$ were prepared. As the former complex is tetrahedral and the latter square-planar, comparison of the LF bands within these complexes with those of the 1,1-dithiolates should definitively prove the coordination geometry of the species.

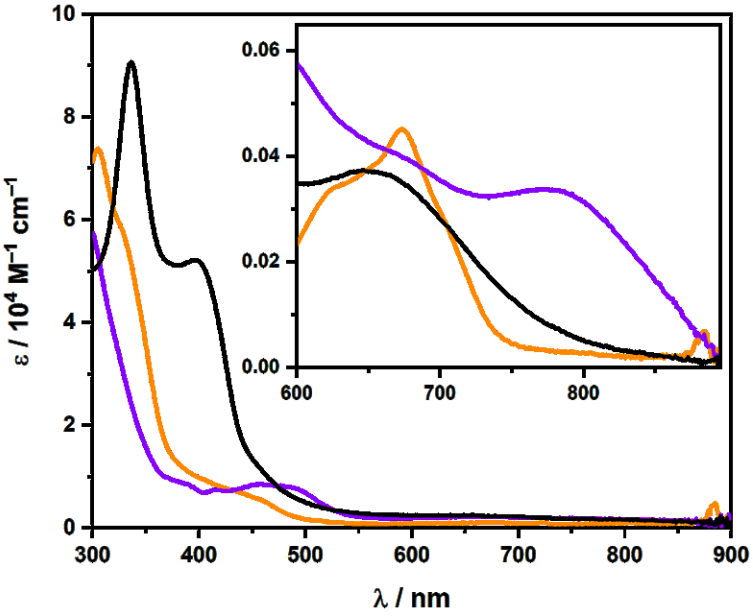

Figure 3.11 Overlay of the electronic spectra of $[Co(i\text{-}mnt)_2]^{2-}$ (black), $[Co(dts)_2]^{2-}$ (orange) and $[Co(mnt)_2]^{2-}$ (violet); the inset shows an expanded view of the LF transitions.

As shown in Figure 3.11, although the intensity of $[Co(i\text{-}mnt)_2]^{2-}$ is closer to that of $[Co(mnt)_2]^{2-}$, the transition energy is much closer to that of the tetrahedral $[Co(dts)_2]^{2-}$, with the LF transitions occurring at an even higher energy than observed in the dts species, supporting a tetrahedral structure of the 1,1-dithiolate species in solution. The visible similarities between the spectra of $[Co(i\text{-}mnt)_2]^{2-}$ and $[Co(mnt)_2]^{2-}$ should be noted, as should the differences between those of $[Co(i\text{-}mnt)_2]^{2-}$ and $[Co(dts)_2]^{2-}$. The LF transition envelope in $[Co(dts)_2]^{2-}$ is considerably more complex than in $[Co(i\text{-}mnt)_2]^{2-}$ and $[Co(mnt)_2]^{2-}$, as spin-forbidden transitions to the doublet excited states $^2A_1(G)$, $^2T_1(G)$ and $^2T_2(G)$ are visible. These are obscured in the 1,1-dithiolate and mnt^{2-} ligand systems, as the significant π-backbonding leads to admixing of excited states and less defined LF transitions.

Unlike the transitions in the 1,1-dithiolate salts, there are clear changes in CT and LF bands of the Co^{II} complexes as the ligand substituents are altered: trends understood through examination of the ligand substituent Hammett parameters.[236] Hammett parameters provide an experimentally quantified value (σ_P) for the electronic effect of a specific substituent, which can be broken into the field or inductive component (σ_I) and the resonance (σ_R) component as shown in Equation 3.1.[236]

$$\sigma_P = \sigma_I + \sigma_R \quad (3.1)$$

The Hammett parameters for the ligand substituents are given in Table 3.4, revealing a decrease in total σ_P when a cyano-substituent is replaced by an amide- or ester-substituent. The bulk of the decrease stems from a reduction in σ_I, with σ_R remaining relatively stable across the series.

Table 3.4 The Hammett parameters for the ligand substituents.

	σ_P	σ_I	σ_R
-CN	0.68	0.53	0.15
-$CONH_2$	0.33	0.23	0.10
-CO_2Et	0.30	0.19	0.11
-NO_2	0.79	0.66	0.13
-H	0.03	0.03	0.00

For the *i*-mnt^{2-}, *i*-mant^{2-} and *i*-ect^{2-} ligated species the trend is straightforward: as the inductive effect of the ligand decreases there is greater electron density on the S atoms, stabilising the lower energy MOs with mainly Co 3d character. This leads to the observed increase in LF transition energy as total σ_P decreases across the series, whilst the higher energy LMCT remains unaffected; the gap between the LMCT thus increases as total σ_P decreases. The Hammett parameters readily explain the change in energy of the LF bands of [Co(*i*-mnt)$_2$]$^{2-}$, [Co(*i*-mant)$_2$]$^{2-}$ and [Co(*i*-ect)$_2$]$^{2-}$, which increase as σ_P decreases. As the LF strength corresponds to the ligand S π-donor ability and concomitantly the Co 3d LF splitting, stronger S π-donors have higher LF transition energies. The increase in the lower LMCT and the decrease in LF transition energies therefore stem from the same effect.

The relationship between total σ_P and the electronic spectrum of [Co(nmt)$_2$]$^{2-}$ differ significantly from the other complexes. The LMCT bands are considerably higher in energy than the total σ_P would suggest; this is due to the unique nitro substituent properties, which in facilitating mixing of σ- and π-systems significantly change the energy of the LMCT bands.

The electronic spectra thus indicate the weaker the ligand inductive effect, the stronger the ligand field, consistent with greater M−L interaction in the systems with stronger S π-donors. Furthermore, the increase in intensity visible as σ_P decreases as the greater electron density in the $\{CoS_4\}$ moiety leads to increased mixing of the ground and excited states.

3.3.3 Magnetic Susceptibility Data

The $\{CoS_4\}$ coordination geometry is dictated by its environment: tetrahedral in solution and square planar in the solid state. The electronic spectra profiles have the hallmarks of tetrahedral compounds, with higher energy LF bands with high intensity stemming from the non-centrosymmetric coordination $\{CoS_4\}$ environments, while the solid-state Co K-edge indicate square-planar species. The different geometries suggest rapid intramolecular, or fluxional, rotations changing the geometry in solution. There is precedent for this in dithiolate chemistry; although generally observed in heteroleptic dithiolate species.

Magnetic measurements allow the probing of the spin ground state (*S*) of the complexes; as *S* depends on the ligand field, it is diagnostic of the geometry in a four-coordinate d^7 ion. Evans' method is an NMR technique that determines solution state magnetic moment at room temperature[179] from the mass susceptibility of the material, calculated from the difference in NMR solvent shifts for the sample solutions and the pure solvent. This the susceptibility is calculated using Equation 3.2.

$$X_g = \frac{3\Delta f}{4\pi f m} + X_o + \frac{X_o(d_o - d_s)}{m} \tag{3.2}$$

Where X_g is the mass susceptibility of the solute ($cm^3\ g^{-1}$), Δf is the frequency shift of the reference resonance (s^{-1}), f is the spectrometer frequency (s^{-1}), m is the concentration of the paramagnetic solution g cm^{-3} adjusted for the temperature dependence of solvent density,[237] X_o is the solvent mass susceptibility ($cm^3\ g^{-1}$), d_o is the solvent density (g cm^{-3}) and d_s is the solution density (g cm^{-3}). The low concentration of the paramagnetic solution means that Equation 3.2 can be simplified by approximating that $d_s = d_o + m$.[238] This results in the cancelation of the second and third terms, giving Equation 3.3, which was used in this study.

$$X_g = \frac{3\Delta f}{4\pi f m} \tag{3.3}$$

Note the $^3/_4\pi$ correction factor is due to the parallel orientation of the sample to the magnetic field; the factor changes with sample orientation. The mass susceptibility is converted into the molar mass susceptibility using Equation 3.4, where M is the molar mass. This is then converted into the susceptibility at 293 K using Equation 3.5, where T is the absolute temperature of the measurement.

$$X_{mT} = X_g \times M \tag{3.4}$$

$$X_{m20} = X_{mT} \times \frac{T}{293} \tag{3.5}$$

Once X_{m20} is known, the diamagnetically corrected magnetic susceptibility, X_{corr}, can then be calculated using Equation 3.6, where X_{dia} is the diamagnetic correction.

$$X_{corr} = X_{m20} \times X_{dia} \tag{3.6}$$

The diamagnetic correction can be calculated by summing the Pascal's constants for all the atoms in the species,[239] but a reasonable approximation can be more quickly using Equation 3.7, where M is the molar mass.

$$X_{dia} = (M \times 0.5) \times 10^{-6} \tag{3.7}$$

The mass susceptibility is converted to a molar quantity from which the magnetic moment of the sample can then be calculated using Equation 3.8.[3,238]

$$\mu_{eff} = 2.828\sqrt{T \times X_{corr}} \quad (3.8)$$

Where μ_{eff} is the effective magnetic moment in Bohr Magnetons and T is the absolute temperature of the measurement.

$$\mu_{eff} = g\sqrt{S(S+1)} \quad (3.9)$$

The net spin of the system can then be calculated using Equation 3.9, where S is the net spin and g is the gyromagnetic ratio. As the spin state is a product of the geometry it provides information about the $\{CoS_4\}$ coordination environment.

Table 3.5 Magnetic Moments (B.M.) for Complexes Calculated Using Evans' Method (Top) and RT Magnetic Susceptibility Measurements (Bottom).

	μ_{eff}	*g*-value	*S*
$[Co(i\text{-mnt})_2]^{2-}$	4.33	2.238	$^3/_2$
$[Co(i\text{-mant})_2]^{2-}$	4.28	2.210	$^3/_2$
$[Co(i\text{-ect})_2]^{2-}$	4.41	2.278	$^3/_2$
$[Co(nmt)_2]^{2-}$	4.22	2.180	$^3/_2$
$[Co(i\text{-mnt})_2]^{2-}$	2.23	2.575	$^1/_2$
$[Co(i\text{-mant})_2]^{2-}$	2.16	2.494	$^1/_2$
$[Co(i\text{-ect})_2]^{2-}$	2.18	2.517	$^1/_2$
$[Co(nmt)_2]^{2-}$	2.26	2.610	$^1/_2$

The solution phase magnetic moments are listed alongside the derived values for g and S in the upper part of Table 3.5.

Table 3.5, with all complexes showing values consistent with $S = {}^3/_2$. The g-values for all the complexes are consistently higher than value of 2.0023 for a free electron,[183] for

tetrahedral Co^{II} species with large SOC.[36] Variation in the recorded moments recorded observed across the series is within experimental error.[184]

A magnetic balance was used to measure the magnetic moment of neat powders; the results are given in the lower part of Table 3.5. The solid-state measurements prove the species to be a spin-doublet which can only arise in a square planar coordination geometry. The *g*-values are higher than recorded for the fluid solution measurements. Square-planar Co^{II} is known to have *g*-values ranging from 2.22[240] to 3.14[241] so although considerably higher than g_e, the values are reasonable for square-planar Co^{II} species.[235] The range of high *g*-values and associated magnetic moments stem from orbital contributions to the ground state, as SOC facilitates mixing of higher LF terms into the ground state.[241] This is determined by the energy gap between the SOMO and the filled d-orbitals (Δ in Figure 3.12), as the smaller the gap, the greater the mixing and the larger g-shift.

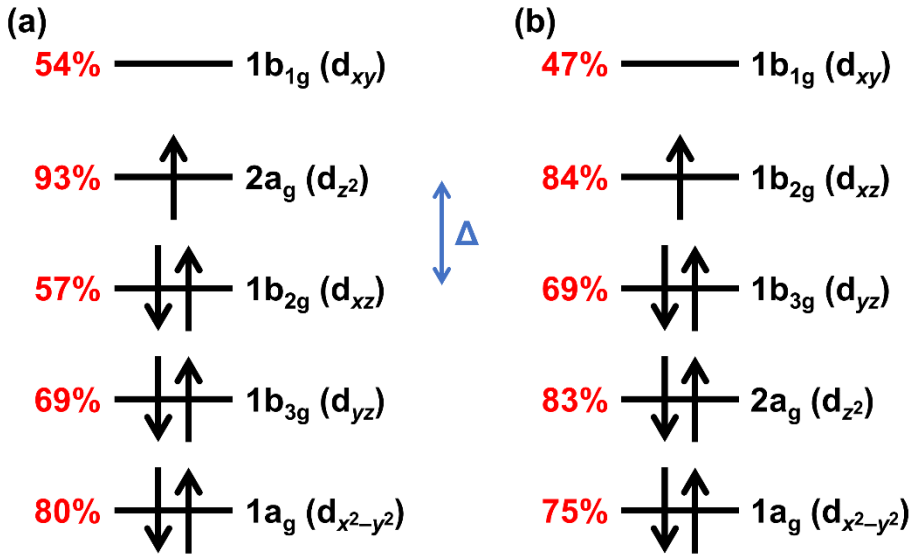

Figure 3.12 Crystal-field splitting diagrams of (a) [Co(*i*-mnt)$_2$]$^{2-}$ in D_{2h} and (b) [Co(mnt)$_2$]$^{2-}$ in D_{4h} symmetry; Co^{II} content shown on the left. Energy gap between the SOMO and the filled d-orbitals (Δ) shown in blue.

As the energy gap depends on the LF, it is affected by changes in both the coordination environment[241] and π-basicity of the ligand system.[242] As shown in Figure 3.12, altering the symmetry of the coordination environment from D_{2h} in [Co(*i*-mnt)$_2$]$^{2-}$ to D_{4h} in [Co(mnt)$_2$]$^{2-}$ changes the complex ground state. Therefore, even if Δ is identical in both

species, the anisotropic *g*-values will be very different: the greater mixing with the $2a_g$ MO in $[Co(i\text{-mnt})_2]^{2-}$ will result in an inverted ground state, with $g_\perp > g_\parallel$, contrasting with the axial $g_\parallel > g_\perp$ grounds state in $[Co(mnt)_2]^{2-}$. Moreover, the σ- and π-donor nature of the ligand systems also change Δ, and thus the SOC and *g*-values of the complex

Finally, although values of g_x, g_y and g_z may by differ between the complexes, the value for g_{iso} may remain constant. Square-planar Co^{II} complexes with similar isotropic *g*-values may still have significantly different electronic structures. The *g*-values measured in the solid state thus show the significant π-donor capabilities of the 1,1-dithiolates, in contrast to significantly lower *g*-value of 2.22 observed in Co^{II} phthalocyanine, where behaves as a pure σ-donor.[240]

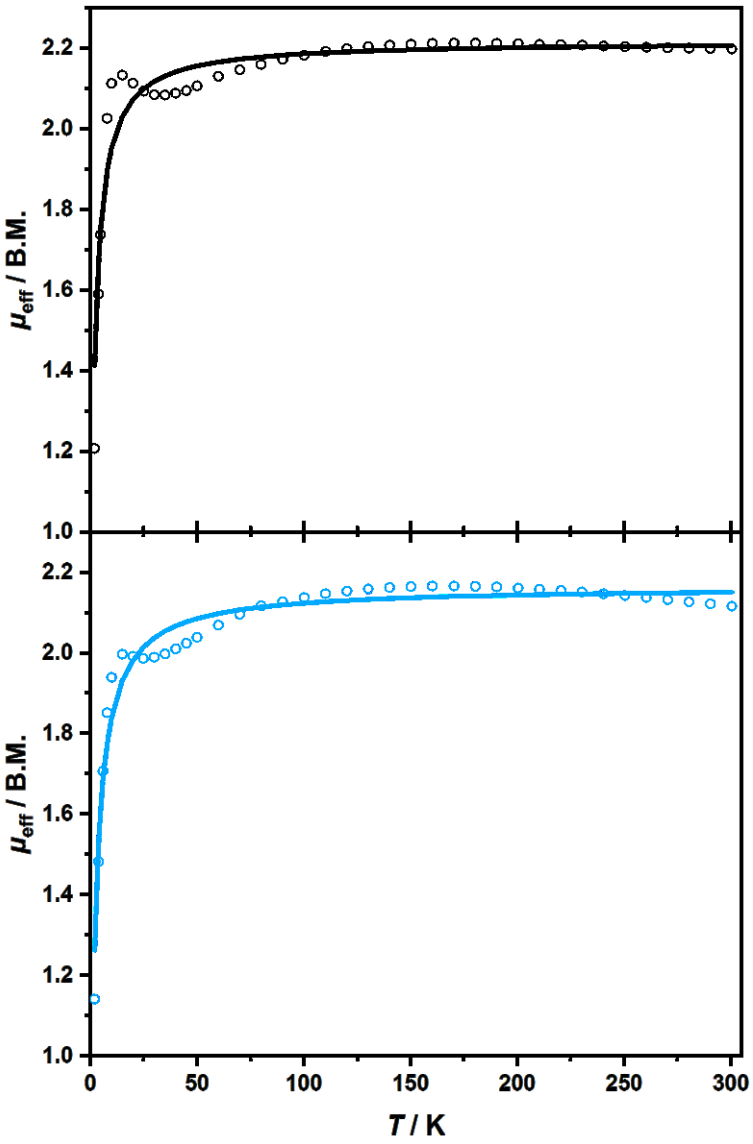

Figure 3.13 Temperature dependence of the magnetic moment μ_{eff} (B.M.) of powdered samples of $[Co(i\text{-mnt})_2]^{2-}$ (top) and $[Co(i\text{-ect})_2]^{2-}$ (bottom). Circles are experimental data; solid lines represent the best fit.

K-edge XAS can be used to compare the electronic structures of the complexes by revealing the electronic structure of both the Co and S atoms. However, before discussing this VT magnetic susceptibility measurements will be discussed. Information can be extracted examining the magnetic moments across a range of temperatures, with the variation determined by the nature of spin-state and exchange coupling within the complex.

The electronic ground states of $[Co(i\text{-mnt})_2]^{2-}$ and $[Co(i\text{-ect})_2]^{2-}$ have been established from variable temperature magnetic susceptibility measurements on powders using a SQUID magnetometer with an applied field of 1.0 T. The temperature dependence

of the effective magnetic moment, μ_{eff}, of both compounds is shown in Figure 3.13. The magnetic moments of $[Co(i\text{-mnt})_2]^{2-}$ and $[Co(i\text{-ect})_2]^{2-}$ are constant in the range from 30 to 300 K at 2.22 and 2.16 B.M., respectively. The values are indicative of $S = {}^1/_2$ species with *g*-values of 2.559 and 2.498, for $[Co(i\text{-mnt})_2]^{2-}$ and $[Co(i\text{-ect})_2]^{2-}$ respectively.

Table 3.6 Spin-Hamiltonian parameters for simulations of the SQUID measurements $[Co(i\text{-mnt})_2]^{2-}$ and $[Co(i\text{-ect})_2]^{2-}$.

	S	***g*-value**	***D* / cm^{-1}**	***Θ* / K**	***X*$_{TIP}$ / 10^{-6} emu**
$[Co(i\text{-mnt})_2]^{2-}$	$^1/_2$	2.559	0	−2.882	499.5
$[Co(i\text{-ect})_2]^{2-}$	$^1/_2$	2.498	0	−3.839	216.1

Between 30 and 15 K ferromagnetic coupling between stacked entities causes slight increases in μ_{eff}; below 15 K, μ_{eff} decreases due to field saturation. The fitting parameters are summarised in Table 3.6. Fits of the data needed no zero-field splitting parameters, but moderate temperature independent parameters (X_{TIP}) were included to account for a small amount of diamagnetic impurities. The fit required sizeable Weiss constant (θ) values of 2.884 and 3.839 K, for $[Co(i\text{-mnt})_2]^{2-}$ and $[Co(i\text{-ect})_2]^{2-}$ respectively, further indicating strong intermolecular exchange interactions.[243]

The magnetic measurements prove the fluxional nature of the complexes, showing the coordination environments to be square-planar in the solid state and tetrahedral in solution. The *g*-values recorded also prove there to be considerable SOC in all complexes, as mixing of higher LF terms into the ground state significantly increases the *g*-values. Although no anisotropic EPR spectrum could be obtained for any of the 1,1-dithiolate complexes, the $2a_g$ SOMO suggests that the large *g*-values stem from a significant increase in g_z, as SOC facilitates mixing of the z^2 with lower-energy filled MOs. As SOC depends on LF splitting, the results prove the π-donor abilities and coordination geometry of the 1,1-dithiolate ligands is reduces the energy between the $2a_g$ SOMO and the b_{2g}, b_{3g} and $1a_g$ MOs, facilitating the mixing of the SOMO with lower energy filled d-orbitals.

3.3.4 X-ray Absorption Spectroscopy

Co K-edge XAS was used to probe the solid-state coordination environment and allow comparison of the 1,1-dithiolate complexes with 1,2-dithiolate and arylthiolate species. S K-edge was also used to study the complexes and the free ligand salts.

3.3.4.1 Co K-edge XAS of Co^{II} 1,1-Dithiolate Complexes

The Co K-edge spectra of the Co^{II} 1,1-dithiolate complexes are shown in Figure 3.14, with the energies of the rising edge positions determined at the first inflection point of the edge summarised alongside the pre-edge energies in Table 3.7. The Co K-edge spectra of the Co^{II} 1,1-dithiolate species are very similar, with pre-edge features occurring at 7710.0 ± 0.1 eV with near identical intensities in each spectrum. The rising edges of the Co^{II} 1,1-dithiolate complexes are also virtually identical, occurring at 7716.6 ± 0.1 eV.

Table 3.7 Co K-edge XAS pre- and rising-edge energies (eV), and intensities (D_0) for four-coordinate cobalt−sulfur complexes.

	Pre-edge energy	D_0	Rising-edge energy[a]
$[Co(i\text{-}mnt)_2]^{2-}$	7710.0	0.009	7716.8
$[Co(i\text{-}mant)_2]^{2-}$	7710.1	0.011	7716.6
$[Co(i\text{-}ect)_2]^{2-}$	7709.9	0.010	7716.7
$[Co(nmt)_2]^{2-}$	7710.1	0.011	7716.7
$[Co(SPh)_4]^{2-}$	7709.6	0.047	7716.7
$[Co(dts)_2]^{2-}$	7709.4	0.042	7716.3
$[Co(mnt)_2]^{2-}$	7710.1	0.012	7716.8

[a] Determined at the first inflection point.

Despite the similarity in rising-edges, the pre-edge features in the 1,1-dithiolate complexes are higher in energy and a fraction of the intensity of the corresponding $[Co(SPh)_4]^{2-}$ transitions. As the pre-edge is known to be affected by the coordination environment,[187] the possibility of solid-state square-planarity of the Co 1,1-dithiolate complexes was considered. To test this theory, the Co K-edge of $[Co(mnt)_2]^{2-}$ and $[Co(dts)_2]^{2-}$ were measured.

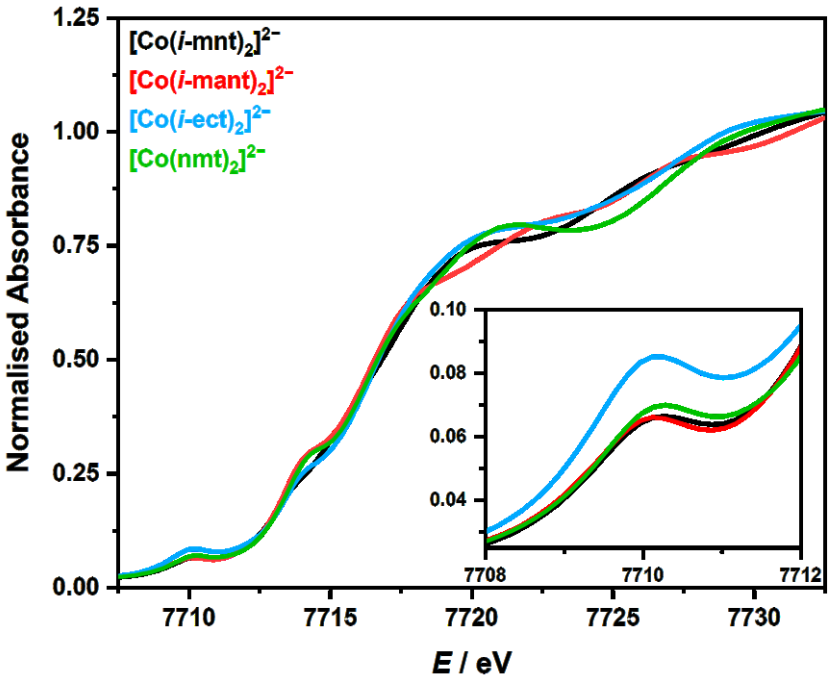

Figure 3.14 Overlay of the normalised Co K-edge XAS spectra of the Co^{II} 1,1-dithiolate complexes. The inset shows an expanded view of the pre-edge region.

The spectra are shown along with $[Co(i\text{-}mnt)_2]^{2-}$ and $[Co(SPh)_4]^{2-}$ in Figure 3.15, with salient data for all complexes given in Table 3.7. The comparison proves the hypothesis, with the intensity and energy of the pre-edge corresponding to the $\{CoS_4\}$ geometry.

The pre-edges of the T_d $[Co(SPh)_4]^{2-}$ and $[Co(dts)_2]^{2-}$ occur at 7709.5 ± 0.1 eV, contrasting with $[Co(mnt)_2]^{2-}$ were the higher transition energy is identical to the 1,1-dithiolate complexes. The energies are all known for 4-coordinate Co^{II},[193] but 7709.5 ± 0.1 eV is typical of T_d species.[192,193] The pre-edge energy thus supports the square-planarity of the 1,1-dithiolate complexes in the solid-state.

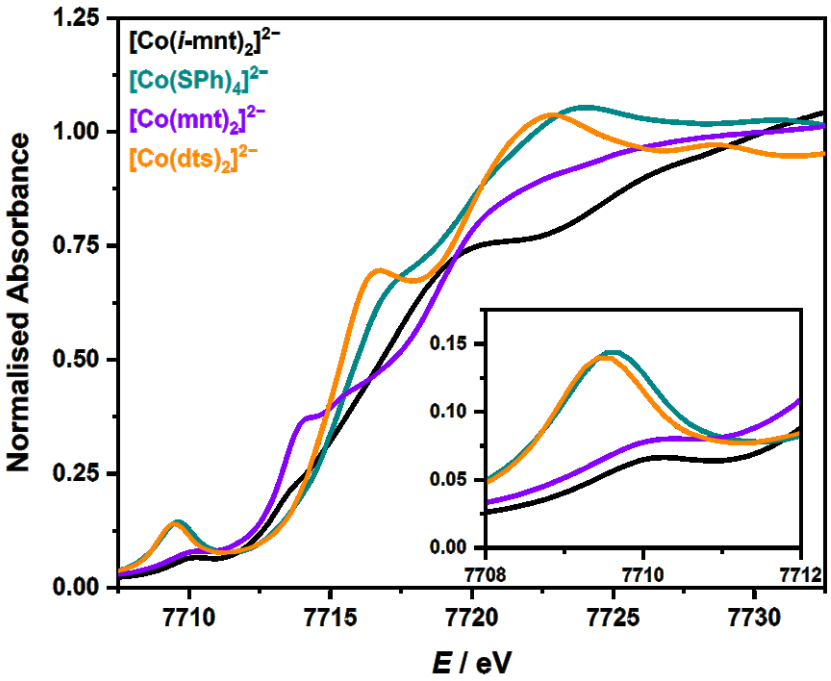

Figure 3.15 Comparison of the normalised Co K-edge XAS spectra of [Co(*i*-mnt)$_2$]$^{2-}$ and a series of Co^{II} complexes. The inset shows an expanded view of the pre-edge region.

The difference in intensity across the series also reflects the geometry, with intensity correlating inversely with the {CoS$_4$} centrosymmetry. As D_{2h} is centrosymmetric whilst D_{2d} is not, the pre-edge features are much more intense in [Co(SPh)$_4$]$^{2-}$ and [Co(dts)$_2$]$^{2-}$ than [Co(mnt)$_2$]$^{2-}$ and the 1,1-dithiolate species.

As stated in Chapter 2, the shifts in the rising-edge region of the spectra (ca. 7715 to 7725 eV) broadly reflect changes in charge at the Co centre, Z_{eff}, although interpretation is complicated by contributions from other processes to the edge structure.[185,192,194,195] With energies of 7716.7 ± 0.1 eV the rising edge energies are typical of Co^{II} species, something reflected in the identical rising edge energies of both [Co(SPh)$_4$]$^{2-}$ and [Co(mnt)$_2$]$^{2-}$.

3.3.4.2 S K-edge XAS of 1,1-Dithiolate Ligand Salts

The S K-edge spectra of the 1,1-dithiolate salts and their second derivatives are shown in Figure 3.16. There are two well resolved pre-edge features in the spectra of *i*-mnt^{2-}, *i*-mant^{2-} and *i*-ect^{2-}, with the lowest energy peak occurring at 2470.97, 2470.94 and 2470.81 eV, respectively. These peaks range between 1.3 and 1.7 eV lower in energy than the second pre-edge peaks, which occur at 2472.57, 2472.51 and 2472.53 respectively. The nmt^{2-} ligand has a similar lower energy peak at 2470.08 eV, but two higher energy peaks, at 2472.42 and 2473.16 eV.

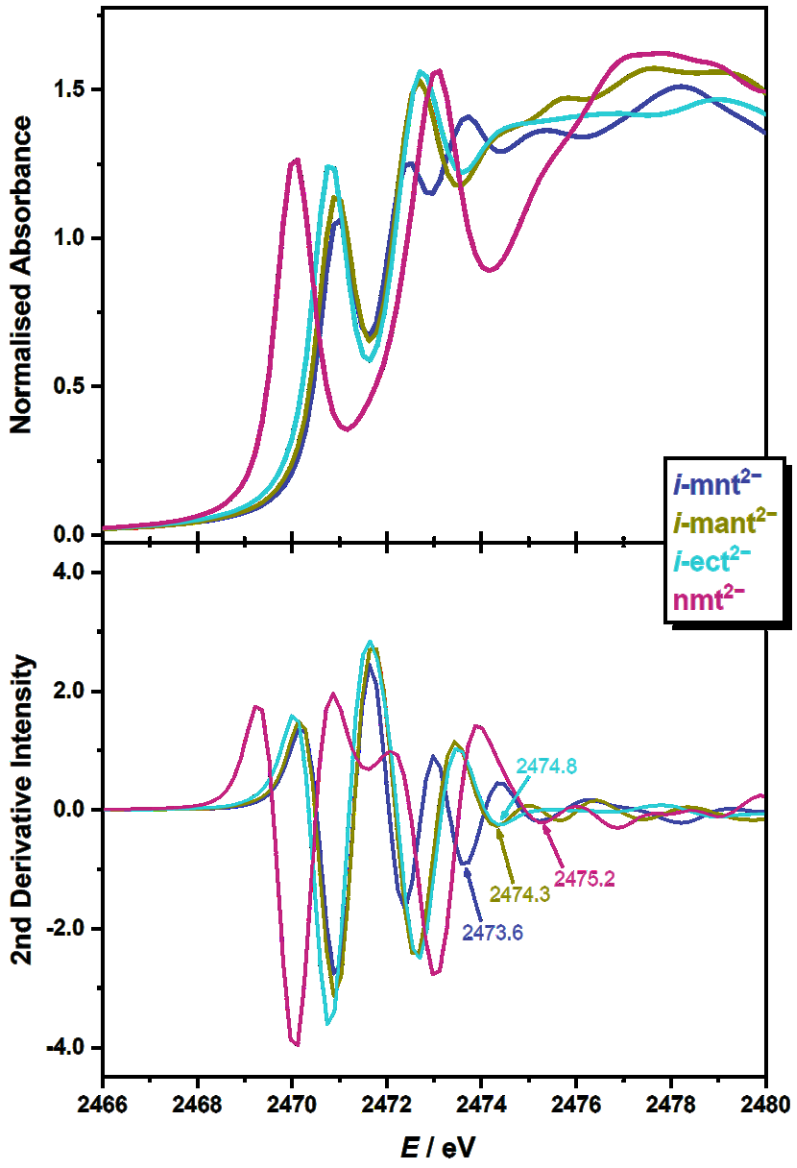

Figure 3.16 Comparison of the normalised S K-edge spectra (top) and their second derivatives for the free 1,1-dithiolate ligands. The 1s → 4p edge transitions are indicated in the plots of the second derivatives.

The closest comparison is to that of the mnt^{2-} ligand K-edge. In the analysis of the ligand the energy of the S 1s → 4p in $Na_2[Cu(mnt)_2]$ was calculated using the S K-edge spectra of $Na_2(mnt)$ and $Na_2[Cu(mnt)_2]$ correlated to DFT calculations, with additional features from low-energy CN π* orbitals with significant S content. For the 1,1-dithiolates, the lowest energy transition is assigned as the S 1s → C−S π* excitation, with the pre-edge peaks between 2470 and 2471 eV corresponding to similar S 1s → C−S π* transitions. As in the electronic spectra, variation in transition energies stems from substituent electronic effects. Transitions > 2472 eV are observed frequently in the XAS spectra of dithiolenes[191] and thiolates,[244] and are frequently attributed to transitions to C−S σ*: in the S K-edge spectrum of mnt^{2-} transitions at 2472.7 and 2473.0 eV are respectively assigned to 1s → C−S π* and 1s → C−S σ* transitions.

For *i*-mnt^{2-}, *i*-$mant^{2-}$, *i*-ect^{2-} and nmt^{2-} the reduction in total σ_P increases the Z_{eff} of the S atom. This in turn increases the energy of the 1s → 4p transitions, which increase by 0.7, 1.2 and 1.6 eV respectively, compared to *i*-mnt. Although no uniform trends are observed in the pre-edge feature energy, an inverse relationship with σ_P is seen in the energy of the rising-edge features, with the transition energies decreasing across the series.

The S K-edge XAS spectrum of nmt^{2-} illustrates the necessity of considering the total σ_P: the strong inductive effect of the nitro substituent should decrease the S Z_{eff}, and concomitantly the 1s → 4p energy, but as there is only one -NO_2 substituent, the overall effect is lessened.

3.3.4.3 S K-edge XAS of Co^{II} 1,1-Dithiolate Complexes

The S K-edge spectra of the Co^{II} 1,1-dithiolate complexes and their second derivatives are shown in Figure 3.17; individual pseudo-Voigt deconvolutions are displayed in Figure 3.18, with the pre-edge peak energies and intensities listed in Table 3.8.

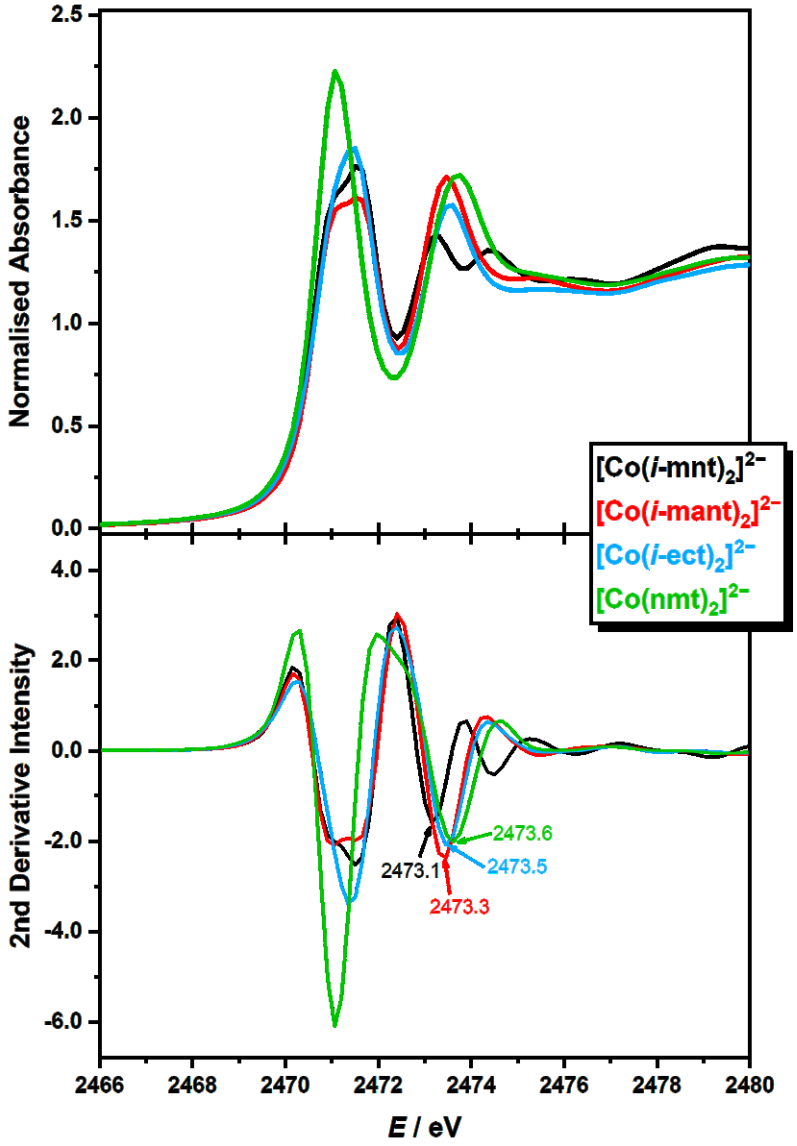

Figure 3.17 Comparison of the normalised S K-edge spectra (top) and their second derivatives for the Co^{II} 1,1-dithiolate complexes. The 1s → 4p edge transitions are indicated in the plots of the second derivatives.

As in the spectra of the respective 1,1-dithiolate salts, the S K-edge spectra of [Co(*i*-mnt)$_2$]$^{2-}$, [Co(*i*-mant)$_2$]$^{2-}$ and [Co(*i*-ect)$_2$]$^{2-}$ contain two well resolved pre-edge features, with lower energy transitions at 2470.95 ± 0.1 eV followed by higher energy transitions at

2471.60 ± 0.1 eV. As with the S K-edge of the free ligand, the XAS of $[Co(nmt)_2]^{2-}$ is distinctly different, with a single intense transition occurring at 2471.12 eV.

Table 3.8 Pre-Edge Peak Energies (E), Intensities (D_0), Number of Holes in Acceptor Orbitals (h), and Covalencies (α^2; S 3p%) for the Co^{II} 1,1-dithiolate complexes.

	Pre-edge energy	D_0	h	α^{2a}
$[Co(i\text{-}mnt)_2]^{2-}$	2470.97	0.32	2	24.1
	2471.68	0.26	2	19.5
$[Co(i\text{-}mant)_2]^{2-}$	2470.91	0.24	2	17.3
	2471.66	0.35	2	25.2
$[Co(i\text{-}ect)_2]^{2-}$	2470.95	0.24	2	16.6
	2471.56	0.39	2	26.9
$[Co(nmt)_2]^{2-}$	2471.12	0.63	4	42.6

[a] Determined from $\alpha^2 = 12D_0/(H \times I_S)$. I_S = 7.98, 8.34, 8.70, 8.88 (Estimated from the S 1s → 4p transition energies in Figure 3.17 and the correlation plot in reference 191)

Although the spectra visually appear like those of the free ligands, the coordinated species have very different orbital compositions. MOs have both metal and ligand character, with π-conjugation facilitated by the new Co−S bonds. In other systems this leads to a shortening of M−S bonds,[245] something associated with greater stabilisation of the M−S σ-orbitals. The absence of S-based MOs with appropriate symmetry to interact with the Co−S π* LUMO combined with this stabilisation results in an initial pre-edge transition to the Co−S σ* LUMO, followed by one in the rising edge to the C−S π*. The significant Co content of the Co−S σ* LUMO (Figure 3.12) limits the effect of the total σ_P, with the transition energy remaining broadly stable across the series. The second transition to the more-deeply affect C−S π* changes, with the transition energy increasing in tandem with total σ_P; the effect of this is such that in S K-edge for $[Co(nmt)_2]^{2-}$ it overlaps with the lower-energy transition to the Co−S σ* LUMO, resulting in a single feature with the intensity of the both features in the other spectra combined.

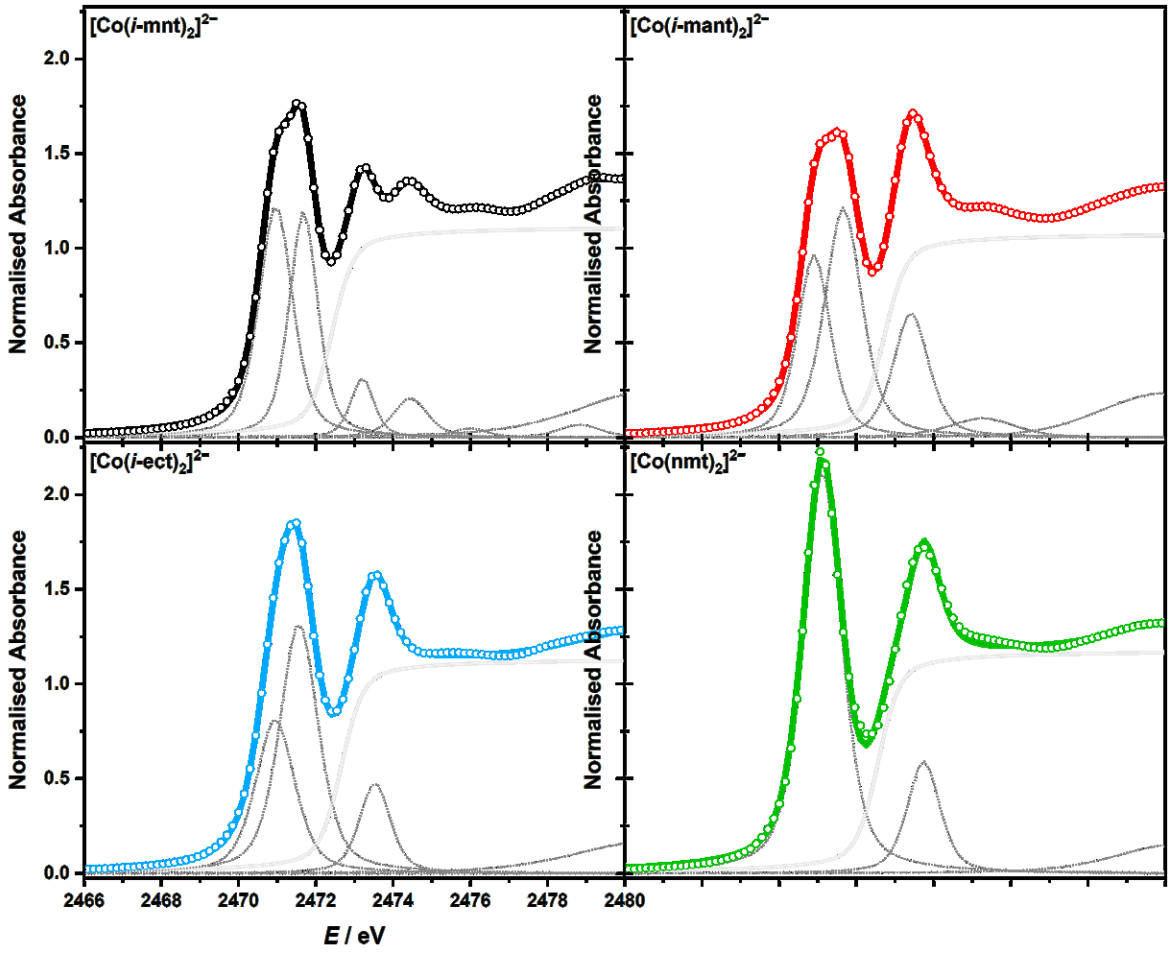

Figure 3.18 Pseudo-Voigt deconvolution of S K-edge spectra of the Co^{II} 1,1-dithiolate complexes. Circles represent the experimental data; dotted lines represent the pseudo-Voigt; the solid grey line the edge jump; and the solid coloured line is the sum of the fit.

A similar relationship with total σ_P is observed in the energy of the 1s → 4p transitions, with the transition energy increasing respectively by 0.2, 0.4 and 0.5 eV relative to $[Co(i\text{-}mnt)_2]^{2-}$ for $[Co(i\text{-}mant)_2]^{2-}$, $[Co(i\text{-}ect)_2]^{2-}$ and $[Co(nmt)_2]^{2-}$. The relationship is the same as that observed in the free ligands, as the reduced total σ_P increases the Z_{eff} of the S atom and thus the 1s → 4p transition energy. The coordination to the Co^{II} ion makes a huge difference however, with the an extended π-system present in the square-planar system decreasing the energy of the 1s → 4p transition and reducing the change in energy across the series.

Despite the change in 1s → 4p transition energies, the average bond covalencies remain consistent across the series. The indistinguishability of the two transitions in $[Co(nmt)_2]^{2-}$ limits comparability, but the bond covalency obtained using the four holes from

both the Co−S σ* and C−S π* MOs is comparable with the other transitions, with average covalencies of 21.8, 21.25, 21.75 and 21.3% for $[Co(i\text{-mnt})_2]^{2-}$, $[Co(i\text{-mant})_2]^{2-}$, $[Co(i\text{-ect})_2]^{2-}$ and $[Co(nmt)_2]^{2-}$, respectively. There is a clear trend between total σ_P and the bond covalencies in both transitions for $[Co(i\text{-mnt})_2]^{2-}$, $[Co(i\text{-mant})_2]^{2-}$ and $[Co(i\text{-ect})_2]^{2-}$ however, with the covalency of the lower energy transition increasing and the higher energy transition decreasing as total σ_P decreases.

Although the energy of the pre-edge transition to the Co−S σ* MO is not influenced, the bond covalency increases with total σ_P. The trend stems from the greater overlap of the Co and S orbitals in the MO; as mixing of the Co and S orbitals increases with total σ_P, the greater total σ_P, the greater bond covalency. An inverse relationship is seen in the transitions to the C−S π* MOs: as the total σ_P increases, the covalency decreases. This is due to the greater mixing of the C−S π* orbital with substituent-based orbitals occurring as total σ_P increases; the increased mixing reduces the S character of the MO, decreasing bond covalency and intensity.

3.4 Experimental

3.4.1 X-ray crystallographic data collection and refinement

Single crystals of $(PPh_4)_2[Co(dts)_2]$ were grown by chilling a saturated acetone solution of the complex to −35 °C, and of $(PPh_4)_2(dts)$ by slow diffusion of diethyl ether into a saturated acetonitrile solution of the complex. Green blocks of dimension 0.20 × 0.15 × 0.12 mm^3 of $(PPh_4)_2[Co(dts)_2]$, and yellow blocks of dimension 0.20 × 0.19 × 0.15 mm^3 of $(PPh_4)_2(dts)$ were mounted on a Bruker SMART APEX CCD diffractometer, and data collected using graphite monochromated Mo−Kα radiation (λ = 0.71073 Å) from a Mo-target rotating-anode X-ray source equipped with a Kryoflex attachment supplying a nitrogen stream at 150 K. The structures were solved by direct methods and refined by full-matrix least squares method with anisotropic thermal parameters for all atoms with SHELXS-97[246] and SHELXL-97,[247] using the WinGX[248] software package. Corrections for incident and diffracted beam absorption effects were applied using empirical absorption corrections.[249] CIF files were generated using Olex2,[247] with analysis and artwork creation performed using Mercury.[250] Crystal data are presented in Table 3.9.

3.4.2 Physical Measurements

Electronic absorption spectra were recorded using a Shimadzu UV-3600 UV-Vis-NIR spectrophotometer (200 – 1500 nm) in a 1 cm quartz cuvette at a scan rate of 1 nm per second. Infrared data were taken as pressed pellets using a Shimadzu FTIR-8400S spectrophotometer with a diamond anvil cell. ^1H and ^{13}C NMR spectra of the complexes were measured at 25 °C on a Bruker AVI 400MHz NMR spectrometer, with chemical shifts referenced to the protonated solvent residual.[199] Magnetic susceptibility measurements were on a Sherwood Scientific Mark 1 Magnetic Susceptibility Balance using an aqueous solution of $Hg[Co(CNS)_4]$ as a calibrant.[200] Mass spectrometry (MS) spectra (electrospray ionization, ESI) were obtained with a Bruker microTOF-Q Quadrupole Time-of-Flight Mass Spectrometer operating in positive- and negative-ion modes Elemental analyses were determined by the departmental microanalysis services using an EA 1110 CHNS, CE-440

Elemental Analyser. Magnetic susceptibility measurements of crystalline powdered samples (10−30 mg) were performed on a Quantum Design MPMS-5 SQUID magnetometer at 1 T between 2 and 300 K for both samples. The samples were measured in gelatine capsules, with the diamagnetic contribution from the sample container was subtracted from the experimental data. Paramagnetic susceptibilities were extracted by using Pascal's constants[239] to subtract diamagnetic contributions, with the program julX written by E. Bill used for simulation and analysis of the magnetic susceptibility data.

3.4.3 X-ray Absorption Spectroscopy

All X-ray Absorption data were measured at the Stanford Synchrotron Radiation Lightsource (SSRL).

Co K-edge data was measured in a high-magnetic field mode of 20 kG on the 16-pole beamline 9−3 under conditions of 3 GeV and 500 mA. A fully tuned Si(220) double-crystal monochromator was used for energy selection and a Rh-coated mirror set to an energy cut-off of 9 keV used for Harmonic rejection. Internal energy calibration was accomplished by the simultaneous measurement of the absorption of a Co foil placed between two ionisation chambers situated after the sample, with the first inflection point of the foil spectrum fixed at 7709.5 eV.[201] Samples were diluted in BN, pressed into a 1 mm Al spacer and sealed with 37 μm Kapton tape. Data was measured in the transmission mode using an N_2-filled ionisation chamber placed after the sample, which was maintained at 10 K using a liquid He flow cryostat. Data represent the average of 4 scans. Data were processed using the MAVE and PROCESS modules of the EXAFSPAK software package[202] by fitting a second-order polynomial to the pre-edge region and subtracting this background from the entire spectrum. A three-region cubic spline was used to model the smooth background above the edge. The absorbance was normalised by subtracting the spline and normalising the post-edge absorbance to 1.0.

S K-edge data was collected on the 20-pole wiggler beamline 4−3 in a high-magnetic field mode of 10 kG with a Ni-coated harmonic rejection mirror and a fully tuned Si(111)

double-crystal monochromator. Incident intensity was recorded using an ion chamber in a flowing helium flight path, with complete details for the optimisation of the setup for low energy described by Hedman et al.[203] All samples were measured at room temperature as fluorescence spectra using a Lytle detector. Samples were ground finely and dispersed as thinly as possible on Mylar tape to minimise the possibility of fluorescence saturation effects. Data represent 2−3 scan averages. All samples were monitored for photoreduction throughout the course of data collection. The energy was calibrated using the S K-edge spectrum of $Na_2S_2O_3 \cdot 5H_2O$, run at intervals between sample scans. The maximum of the first pre-edge feature in the spectrum was fixed at 2472.02 eV. A step size of 0.08 eV was used over the edge region. Data were averaged, and a smooth background was removed from all spectra by fitting a polynomial to the pre-edge region and subtracting this polynomial from the entire spectrum. Normalisation of the data was accomplished by fitting a flattened polynomial or straight line to the post-edge region and normalizing the post-edge to 1.0.

Table 3.9 Crystallographic Data for $(PPh_4)_2[Co(dts)_2]$ and $(PPh_4)_2(dts)\cdot MeCN$

formula	$C_{56}H_{40}CoO_4P_2S_4$	$C_{54}H_{43}NO_2P_2S_2$
fw	1025.99	863.95
crystal system	monoclinic	Monoclinic
space group	$P2_1/c$	$P2_1/c$
colour, habit	green, block	yellow, block
a, Å	9.303(1)	10.630(5)
b, Å	18.424(3)	33.310(2)
c, Å	28.831(4)	12.923(7)
α, °	90.00	90.00
β, °	96.738(2)	102.033(8)
γ, °	90.00	90.00
V, Å	4908(1)	4478(4)
T, K	150(2)	150(2)
ρ_{calcd}, $g\ cm^{-3}$	1.389	1.281
λ, Å / μ, mm^{-1}	0.71073 / 0.632	0.71073 / 0.234
refl. collected / $2\Theta_{max}$	33444 / 53.0	32748 / 53.1
unique refl. / $I > 2\sigma(I)$	10168 / 8525	9263 / 5616
no. of param. / restr.	604 / 0	551 / 0
R1[a] / goodness of fit[b]	0.0297 / 1.023	0.0762 / 1.079
wR2 [c] ($I > 2\sigma(I)$)	0.0668	0.2079
residual density, e $Å^{-3}$	0.333 / −0.235	2.005 /−0.0752

[a] Observation criterion: $I > 2\sigma(I)$. $R1 = \Sigma||F_o| - |F_c||/\Sigma|F_o|$. [b] $GoF = [\Sigma[w(F_o^2 - F_c^2)_2]/(n - p)]^{1/2}$. [c] $wR2 = [\Sigma[w(F_o^2 - F_c^2)^2]/\Sigma[w(F_o^2)^2]]^{1/2}$ where $w = 1/\sigma^2(F_o^2) + (aP)^2 + bP$, $P = (F_o^2 + 2F_c^2)/3$.

3.4.4 Syntheses

The compounds K_2(nmt),[251] Na_2(*i*-mnt),[252] K_2(*i*-mant),[253] K_2(*i*-ect)[253] and K_2(ded)[254] were prepared following the published methods. All other reagents were purchased from commercial sources and used as received. Unless stated otherwise, all reactions and manipulations were conducted in air at room temperature.

Dipotassium 1-nitro-2,2-ethenedithiolate (dipotassium nitromethanedithiolate), K_2(nmt). A suspension of KOH (16.83 g; 0.300 mol) in EtOH (100 mL) was prepared and added to a vigorously stirring solution of $MeNO_2$ (10.71 mL, 12.21 g; 0.200 mol) and CS_2 (12.00 mL, 15.12 g; 0.200 mol) in EtOH (20 mL). After stirring for 2 h the resulting precipitate was collected under suction, washed with EtOH (5 × 15 mL) and Et_2O (3 × 15 mL) and dried under vacuum for 3 h. Yield = 21.54 g (68%).

^{1}H NMR (400 Mhz, D_2O) δ: 7.95 (s, 1 H). ^{13}C NMR (400 Mhz, D_2O) 71 ppm (s, 2 C). IR (solid, cm^{-1}): v(C−H) 3096 w, 2637 w, 2357 m, 2334 w, 2317 w, 1547 m, 1478 w, v(N=O) 1414 s, 1387 s, 1337, 1252 w, 1227 s, v(C−S) 1182 s, 1069 w, 1036 w, 1007 s, 914 s, 820 w, 787 m, 737 s, 702 m, 669 w. ESI-MS: *m*/*z* 251.8 $[M+K]^+$.

Disodium 1,1-dicyano-2,2-ethenedithiolate (disodium isomaleonitriledithiolate), Na_2(*i*-mnt). A solution of malononitrile (6.61 g; 0.100 mol) was in EtOH (30 mL) was prepared, and CS_2 (6.04 mL, 7.61 g; 0.100 mol) added to it slowly whilst stirring vigorously. Powdered NaOH (8.00 g; 0.200 mol) in EtOH (30 mL) was then added, and the resulting mixture stirred for 2 h. After this time a tan yellow precipitate had formed, which was collected under suction, washed with EtOH (5 × 15 mL) and Et_2O (3 × 15 mL) and dried under vacuum for 2 h. Yield = 15.4 g (83%).

^{13}C NMR (D_2O): δ 123 ppm (s, 2 C), 30 ppm (s, 2 C). IR (solid, cm^{-1}): 3102 w, 2970 w, 2918 w, v(CN) 2174 s, 2108 m, 1736 m, 1724 w, 1618 m, 1435 w, v(C−S) 1341 s, 1238 m, 1206 w, 1128 w, 1107 w, 1092 w, 1055 w, 970 w, 953 s, 882 s, 814 w, 660 m, 621 m. ESI-MS: *m*/*z* 208.9 $[M+Na]^+$.

Dipotassium 1-cyano-1-propanamide-2,2-dithiolate (dipotassium *iso*-maleamidonitrilodithiolate), K_2(*i*-mant). A solution of cyanoacetamide (8.41 g; 0.100 mol) and CS_2 (6.04 mL, 7.61 g; 0.100 mol) in EtOH (100 mL) was prepared and a suspension of KOH (11.22 g; 0.200 mol) in EtOH (60 mL) rapidly added. The resulting solution was stirred for 72 h, before being filtered under suction. The precipitate was washed with ^{i}PrOH (5 × 15 mL) and Et_2O (5 × 15 mL) and dried under vacuum for 5 h to yield the final product. Yield = 21.4 g (91%).

^{1}H NMR (D_2O): 3.52 ppm (d, 2 H). ^{13}C NMR (D_2O): 171 ppm (s, 1 C), 126 ppm (s, 1 C), 49 ppm (s, 2 C). IR (solid, cm^{-1}): 3080 s, 29g70 w, ν(CN) 2164 s, ν(C=C) 1684 w, 1588 s, 1463 w, 1385 s, 1345 w, ν(C=O) 1311 s, 1291 w, 1263 w, 1158 m, 1140 w, 1118 w, 1101 w, ν(C−S) 1085 s, 1050 m, 1008 w, 997 w, 976 w, 924 s, 898 w, 852 s, 817 w. ESI-MS: *m*/*z* 274.8 $[M+K]^+$.

Dipotassium 1-cyano-1-ethoxycarbonyl-2,2-ethenedithiolate (dipotassium *iso*-ethylcyanoacetatedithiolate), K_2(*i*-ect). A solution of ethyl cyanoacetate (10.62 mL, 11.31 g; 0.100 mol) and CS_2 (6.04 mL, 7.61 g; 0.100 mol) in EtOH (20 mL) was prepared and placed in an ice-water bath, before the rapid addition of a suspension of KOH (11.22 g; 0.200 mol) in EtOH (60 mL). After stirring for 24 h, the reaction mixture was collected under suction and washed with ^{i}PrOH (5 × 15 mL) and Et_2O (5 × 15 mL), before being recrystallised from ^{i}PrOH and H_2O. The resulting microcrystalline product was washed with Et_2O (3 × 15 mL) and dried under vacuum for 3 h to yield the final product. Yield = 22.0 g (83%).

^{1}H NMR (D_2O): 4.16 ppm (q, 2 H), 1.29 ppm (t, 3 H). ^{13}C NMR (D_2O): 168 ppm (s, 1 C), 127 ppm (s, 1 C), 94 ppm (s, 1 C), 60 ppm (s, 2 C), 14 ppm (s, 1 C). IR (solid, cm^{-1}): 3000 w, 2961 w, ν(CN) 2151 s, ν(C=C) 1657 s, ν(C=O) 1615 m, 1452 m, 1437 w, 1382 w, 1356 m, ν(C−O) 1320 s, 1304 w, 1289 s, 1254 s, 1212 w, 1165 s, 1138 m, ν(C−S) 1120 s, 1107 w, 1091 m, 1055 w, 1017 s, 926 s, 902 m 849 w. ESI-MS: *m*/*z* 303.9 $[M+K]^+$.

Dipotassium 1,1-di(ethoxycarbonyl)-2,2-ethenedithiolate, K_2(ded). A solution of diethyl malonate (7.63 mL, 8.01 g; 0.05 mol) and CS_2 (3.02 mL, 3.81 g; 0.05 mol) in dioxane (25 mL) was prepared and added to a stirring suspension of KOH (5.61 g; 0.100 mol) in dioxane (50 mL). After 0.5 h the reaction mixture was diluted with Et_2O (125 mL), and stirred for a further 0.5 h. The resulting precipitate was collected under suction, washed with EtOH (3 × 15 mL) and Et_2O (5 × 15 mL), before being dried under vacuum for 5 h. Yield = 13.5 g (87%).

^{1}H NMR (D_2O): 4.16 ppm (q, 4 H), 1.27 ppm (t, 6 H). ^{13}C NMR (D_2O): 172 ppm (s, 2 C), 71 ppm (s, 2 C), 62 ppm (s, 2 C), 14 ppm (s, 2 C). IR (solid, cm^{-1}): 2986 m, 1724 m, ν(C=C) 1711 w, ν(C=O) 1618 s, 1597 m, ν(C−O) 1369 m, 1356 m, 1287 w, 1252 m, ν(C−S) 1105 s, 1043 w, 991 w, 912 s, 839 w, 812 w, 764 w, 685 m, 660 s, 635 m, 621 w. ESI-MS: *m*/*z* 272.9 $[M-K]^-$.

Bis(tetraethylammonium) bis(1,3-dithione-2-thione-4,5-dithiolato)zincate, $(NEt_4)_2$[Zn(dmit)$_2$]. A 500 mL three necked round bottom flask was dried in an oven for 3 h before being attached to a Schlenk line and placed under a continuous flow of dinitrogen. The flask was then charged with a large Teflon stirrer barn and Na shavings (4.26 g; 0.185 mol), placed in an ice-water bath, and purged with dinitrogen for a further 15 min. After this time degassed CS_2 (36 mL, 45.4 g; 0.596mol) was added slowly, and the combined reaction mixture set stirring. Anhydrous DMF (40 mL, 37.8 g; 0.517 mol) was then added dropwise over two hours; after the addition was complete the ice bath was removed, and the system left to warm to room temperature, before stirring for a further 18 h under a positive flow of nitrogen. After this time the system was visually inspected for any unreacted Na, and as a precaution placed in an ice bath before slow addition of MeOH (10.5 mL). After stirring a further 5 min a thoroughly degassed 4:3 mixture of H_2O and MeOH (175 mL) was rapidly added, quickly followed by a solution of $ZnCl_2$ (4.00 g; 29.3 mmol) in a 1:1 mixture of aqueous NH_4OH and MeOH (200 mL). Over the course of 1 h $NEt_4Cl{\cdot}H_2O$ (9.24 g; 50.3

mmol) in H_2O (30 mL) was then added dropwise and the resulting mixture stirred for a further 18 h. After this time the mixture was filtered, and the collected precipitate washed with ^{i}PrOH (4 × 30 mL), H_2O (4 × 30 mL), MeOH (30 mL) and Et_2O (2 × 30 mL), before being dried under vacuum for 8 h to isolate the final product. Yield = 19.8 g (55%).

^{1}H NMR (CD_3CN): 3.16 ppm (q, 16 H), 1.20 ppm (tt, 24 H). ^{13}C NMR (CD_3CN): 210 ppm (s, 2 C), 136 ppm (s, 2 C), 53 ppm (t, 8 C), 7 ppm (s, 8 C). IR (solid, cm^{-1}): 2918 w, 1688 s, 1670 s, 1593 m, 1578 m, 1479 w, ν(C=C) 1449 m, 1416 s, 1389 w, 1364 w, 1306 w, 1229 w, 1204 s, 1171 s, ν(C=S) 1057 s, 1038 m, ν(C=C) 999 s, c883 s, 849 w, 837 w, 766 s, 677 s, 637 s, 613 m. ESI-MS: *m*/*z* 587.8 $[M-NEt_4]^-$.

4,5-Dibenzoylthio-1,3-dithiole-1-thione. Over a period of 2.5 h benzoyl chloride (50 mL, 61.7 g; 0.439 mmol) was added to a solution of $(NEt_4)_2[Zn(dmit)_2]$ (19.8 g; 27.7 mmol) in acetone (500 mL). The reaction mixture was then stirred for 18 h, after which time the resultant precipitate was collected under suction and washed with H_2O (25 mL) and acetone (15 mL), before being recrystallised from CH_2Cl_2 and MeOH. Yield = 7.80 g (35%).

^{1}H NMR ($CDCl_3$): 7.95 ppm (m, 4 H), 7.66 ppm (m, 2 H), 7.51 ppm (m, 4 H). ^{13}C NMR ($CDCl_3$): 212 ppm (s, 1 C), 185 ppm (s, 2 C), 135 ppm (s, 2 C), 134 ppm (s, 2 C), 133 ppm (s, 2 C), 129 ppm (s, 4 C), 128 (s, 4 C). IR (solid, cm^{-1}): ν(C−H) 3080 w, 1740 w, ν(C=O) 1688 s, 1670 m, 1593 w, 1578 w, 1460 w, ν(C=C) 1449 m, 1308 w, 1229 w, ν(C=S) 1202 s, 1171 w, ν(C=S) 1057 s, 1030 w, ν(C−S) 999 m, 880 m, 849 w, 766 s, ν(C−H) 675 s, 637 s, 613 m. ESI-MS: *m*/*z* 428.3 $[M+Na]^+$.

Bis(tetraphenylphosphonium) bis(1,3-dithione-2-thione-4,5-dithiolato)cobaltate, $(PPh_4)_2[Co(dmit)_2]$. A solution of benzoyl dmit (1.70 g; 4.20 mmol) in dry degassed MeOH (20 mL) was prepared under an inert atmosphere of dinitrogen, and NaOMe (460 mg; 8.51 mmol). After stirring for 1 h, $CoCl_2$ (276 mg; 2.13 mmol) was added under a positive flow of dinitrogen, followed by PPh_4Br (1.64 g; 3.93 mmol). The reaction mixture was then stirred for a further 1 h, filtered, and the solid precipitate washed with Et_2O to yield the crude

product. This product was then recrystallised under nitrogen from warm MeCN to give the final product. Yield = 1.85 g (83%).

μ_{eff} (Gouy balance, 289 K) = 3.99 B.M.

Bis(tetraphenylphosphonium) bis(dithiosquarato)cobaltate, $(PPh_4)_2[Co(dts)_2]$. A solution of $CoCl_2{\cdot}6H_2O$ (400 mg; 2.40 mmol) in H_2O (4 mL) was prepared and added to a solution of K_2(dts) (900 mg; 4.00 mmol) in H_2O (6 mL). The resulting solution was mixed thoroughly and a solution of PPh_4Cl (1.50 g; 4.00 mmol) in H_2O (5 mL) added, causing the rapid formation of a green precipitate. This was recrystallised from warm acetone yielding dark green diffraction quality crystals. Yield = 1.33 g (65%).

IR (solid, cm^{-1}): 3022 w, 1838 w, 1825 m, 1721 s, 1682 s, 1661 m, 1585 m, 1485 m, 1437 s, 1385 m, 1360 m, 1342 w, 1315 w, 1167 s, 1107 s, 1061 w, 1026 w, 995 m, 934 w, 920 w, 912 w, 883 m, 847 w, 752 m, 743 w, 719 s, 681 s, 615 w, 521 s. ESI-MS: *m*/*z* 686.0 $[M-PPh_4]^-$. μ_{eff} (CD_3CN, 298 K) = 4.63 B.M.

Bis(tetraphenylphosphonium) bis(1,1-dicyano-2,2-ethenedithiolato)cobaltate, $(PPh_4)_2[Co(i\text{-}mnt)_2]$. A solution of PPh_4Cl (750 mg; 2.00 mmol) in H_2O (5 mL) was added to a solution of Na_2(*i*-mnt) (186 mg; 1.00 mmol) in H_2O (3 mL) resulting in a pale-yellow solution. $Co(OAc)_2{\cdot}4H_2O$ (125 mg; 0.500 mmol) in H_2O (5 mL) was then added, resulting in the formation of a dark green solution which rapidly yielded a green precipitate. This was collected under suction, washed with H_2O (5 × 5 mL) and Et_2O (3 × 5 mL), and dried under vacuum for 48 h. Yield = 423 mg (83%).

Anal. Calcd for $C_{56}H_{40}N_4CoP_2S_4$: C, 66.07; H, 3.87; N, 5.50. Found: C, 65.88; H, 3.96; N, 6.22. IR (solid, cm^{-1}): 3067 w, 2365 w, 2189 m, ν(CN) 2182 m, 2139 w, 1616 w, 1587 s, 1484 s, ν(C=C) 1436 s, 1398 s, 1358 s, 1292 w, 1234 w, 1188 s, 1165 m, 1107 s, 1075 w, 1053 w, 1028 m, 996 s, 949 s, ν(C−S) 900 s. ESI-MS: *m*/*z* 338.8 $[M]^-$. μ_{eff} (CD_3CN, 298 K) = 4.33 B.M.; μ_{eff} (Gouy balance, 288 K) = 2.23 B.M.

Bis(tetraphenylphosphonium) bis(1-cyano-1-propanamide-2,2-dithiolato)cobaltate, $(PPh_4)_2$[Co(*i*-mant)$_2$]. A solution of PPh_4Cl (750 mg; 2.00 mmol) in H_2O (5 mL) was added to a solution of K_2(*i*-mant) (236 mg; 1.00 mmol) in H_2O (3 mL) resulting in a tan solution/suspension. $Co(OAc)_2 \cdot 4H_2O$ (125 mg; 0.500 mmol) in H_2O (5 mL) was then added, resulting in the formation of a dark green solution which rapidly yielded a khaki precipitate. This was collected under suction, washed with H_2O (5 × 5 mL) and Et_2O (3 × 5 mL), and dried under vacuum for 48 h. Yield = 489 mg (93%).

Anal. Calcd for $C_{58}H_{44}N_4CoO_3P_2S_4$: C, 62.74; H, 4.33; N, 5.23. Found: C, 62.72; H, 4.17; N, 5.26. IR (solid, cm^{-1}): v(N−H) 3061 w, 2970 m, 2189 s, v(CN) 2175 s, 1739 w, v(C=O) 1709 m, 1587 m, 1484 s, v(C=C) 1437 s, 1398 m, v(CN) 1360 vs, 1218 s, 1188 m, 1165 m, 1107 vs, 1028 w, 996 s, 948 s, v(C−S) 905 s, 829 w. ESI-MS: *m*/*z* 374.9 $[M]^-$. μ_{eff} (CD_3CN, 298 K) = 4.28 B.M.; μ_{eff} (Gouy balance, 289 K) = 2.15 B.M.

Bis(tetraphenylphosphonium) bis(1-cyano-1-ethoxycarbonyl-2,2-ethenedithiolato)cobaltate, $(PPh_4)_2$[Co(*i*-ect)$_2$]. A solution of PPh_4Cl (750 mg; 2.00 mmol) in H_2O (5 mL) was added to a solution of K_2(*i*-ect) (265 mg; 1.00 mmol) in H_2O (3 mL) resulting in a tan solution/suspension. $Co(OAc)_2 \cdot 4H_2O$ (125 mg; 0.500 mmol) in H_2O (5 mL) was then added, resulting in the formation of a dark green solution which rapidly yielded a deep green precipitate. This was collected under suction, washed with H_2O (5 × 5 mL) and Et_2O (3 × 5 mL), and dried under vacuum for 48 h. Yield = 500 mg (90%).

Anal. Calcd for $C_{60}H_{50}N_2CoO4P_2S_4$: C, 64.80; H, 4.53; N, 2.52. Found: C, 64.89; H, 4.45; N, 2.61. IR (solid, cm^{-1}): 3057 w, 2189 m, v(CN) 2173 s, v(C=O) 1707 s, 1587 s, 1573 w, 1556 w, 1484 w, v(C=C) 1436 s, v(C−H) 1395 s, v(C−O) 1358 vs, 1224 w, 1219 w, 1188 m, 1164 m, 1107 s, 1028 m, 996 s, 949 s, 930 w, v(C−S) 900 s, 837 w. ESI-MS: *m*/*z* 432.9 $[M]^-$. μ_{eff} (CD_3CN, 298 K) = 4.41 B.M.; μ_{eff} (Gouy balance, 288 K) = 2.18 B.M.

Bis(tetraphenylphosphonium) bis(1-nitro-2,2-ethenedithiolate)cobaltate, $(PPh_4)_2[Co(nmt)_2]$. A solution of PPh_4Cl (750 mg; 2.00 mmol) in H_2O (5 mL) was added to a solution of $K_2(nmt)$ (213 mg; 1.00 mmol) in H_2O (3 mL) resulting in a deep red solution. $Co(OAc)_2{\cdot}4H_2O$ (125 mg; 0.500 mmol) in H_2O (5 mL) was then added, resulting in the formation of a red solution which rapidly yielded an ochre precipitate. This was collected under suction, washed with H_2O (5 × 5 mL) and Et_2O (3 × 5 mL), and dried under vacuum for 48 h. Yield = 456 mg (91%).

Anal. calc. for $C_{52}H_{42}N_2CoO_4P_2S_4$: C, 61.96; H, 4.20; N, 2.78. IR (solid, cm^{-1}): 3051 w, 3039 w, 3022 w, 2954 w, 1586 m, 1483 m, ν(C=C) 1434 s, ν(C−H) 1398 w, 1293 s, ν(N=O) 1212 s, 1183 m, 1160 m, 1105 s, 1075 w, 1023 m, 995 m, 959 w, ν(C−S) 917 s, 850 w, 818 w. ESI-MS: *m*/*z* 328.8 $[M]^-$. Found: C, 61.92; H, 4.18; N, 3.01%. μ_{eff} (CD_3CN, 298 K) = 4.22 B.M.; μ_{eff} (Gouy balance, 288 K) = 2.26 B.M

4 3d Tetrathiotungstate Complexes

4.1 Introduction

A rudimentary measure of SMM performance is the effective energy barrier, U_{eff}, dependent on the spin and single-ion anisotropy of the complex, defined by Equation 4.1 for a complex with integer spin.[24]

$$U_{eff} = S^2|D| \tag{4.1}$$

Most early research centred around the increase of the overall spin,[255] but the inverse relationship of D to S ensured large S did not lead to similarly increased U_{eff}.[34] Recent research into TM based SMMs has instead focussed on the development of mononuclear species containing 3d metal ions with unquenched orbital angular momentum, with high-spin Co^{II} a natural choice.[19,39,50,60,63,73,256]

Nonetheless polynuclear paramagnetic complexes remain attractive research targets as, in addition to SMM behaviour, they are suitable for use as models in molecular spintronics[14] and units for molecular refrigerants.[257] However, although the polynuclear cluster chemistry of Mn[258] and Fe[259] systems has been thoroughly researched, synthetic difficulties have retarded research into Co species.[260] Moreover, the challenges in understanding the magnetism of such systems[261] has still further limited such research.[262]

It is important to note the role quantum tunnelling of magnetisation (QTM) plays in SMM performance: even if a species has a huge U_{eff}, practical SMM performance will be limited if fast relaxation through the barrier (QTM) occurs.[30] Exchange coupling has been shown to combat the deleterious effect of QTM,[263-265] making the appeal of a strongly coupled polynuclear Co^{II} system obvious. If the strong angular momentum of the individual Co^{II} ion can be retained in a polynuclear system with strong exchange coupling, the possibility of an SMM with both large U_{eff} and suppressed QTM opens.

Aiming to realise such a species, complexes such as $[Co_4(\mu\text{-}NP^tBu_3)_4]^+$ (^{t}Bu = *tert*-butyl; Figure 4.1)[154] have been developed: homometallic polynuclear Co^{II} systems aiming to retain the performance of monometallic linear Co^{II} species.[22,154,256,266-271]

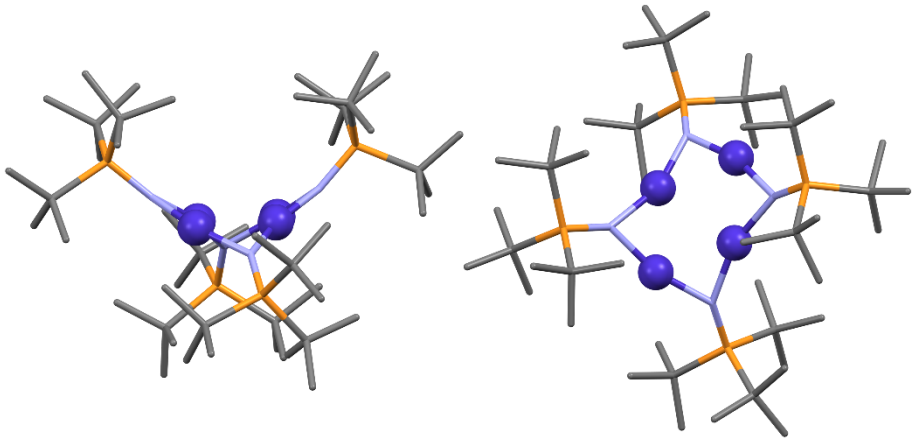

Figure 4.1 Two perspective of $[Co_4(\mu\text{-}NP^tBu_3)_4]^+$ (^{t}Bu = *tert*-butyl; cobalt, grape; carbon, charcoal; phosphorus, apricot; nitrogen, cornflower). Hydrogens omitted for clarity.

However, for the most part polymetallic Co^{II}-based complexes are heterometallic, aiming to harness the propitious properties of Co^{II} in systems with other metal ions. Co^{II}-3d clusters are known,[272-278] but Co^{II}-4f complexes have proven more popular[279-283] as interest increases in 3d-4f systems.[284-288] Although limited, research into Co^{II}-5d SMMs is also gaining momentum.[289,290] There is a substantial body of 5d SMMs research,[291] but 3d-5d SMMs are not common and most do not use Co^{II} ions.[292-296] The few Co^{II}-5d systems that have been reported show remarkable behaviour,[289,290] and given their potential their scarcity seems bizarre.

Polynuclear SMMs with a 5d component are attractive as spin-orbit coupling is a relativistic effect and is therefore stronger in 5d ions than 3d or 4d ions;[297] 5d systems could have higher single-ion or exchange anisotropies. The increased overlap offered by the larger 5d orbitals[298] has also been shown to promote superexchange,[291] putting a strongly exchange-coupled highly-anisotropic system within reach. Finally, the range of 5d oxidation states[299] that can be changed by external stimuli[300-302] allows access to SMMs with novel properties such as photomagnetism.[303]

An ideal Co^{II}-5d system would thus combine the traits of both metals to give a highly anisotropic system with suppressed QTM, as well as other useful properties.

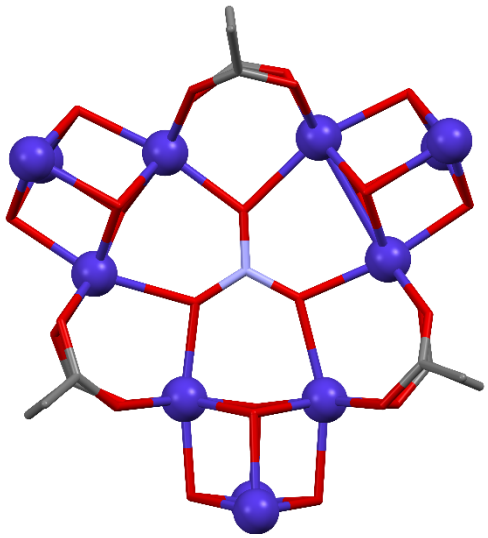

Figure 4.2 The molecular structure of the Co^{II}_{12} core in $[Co_{12}(bm)_{12}(NO_3)(O_2CMe)_6(EtOH)_6]^{5+}$ (cobalt, grape; carbon, charcoal; oxygen, scarlet; nitrogen, cornflower). Hydrogens omitted for clarity.

Rational synthesis of such a species is not easy, with serendipitous assembly[304] remaining the most popular approach to the synthesis of novel polynuclear Co^{II} systems. Although with polynuclear SMMs such as $[Co_{12}(bm)_{12}(NO_3)(O_2CMe)_6(EtOH)_6]^{5+}$ (Hbm = 1*H*-benzimidazol-2-yl)methanol; Figure 4.2) isolated the approach has had some successes,[305,306] control over the final species formed is inherently limited,[22] with few rational synthetic principles yielded. Moreover, heterometallic Co^{II} complexes with lower row TMs are known to have unpredictable behaviour, with introduction of a 4d component to a Co^{II}-based SMM found to switch off SMM behaviour.[307]

Rational synthesis of a Co^{II}-5d SMM thus requires greater understanding of behaviour in such systems, with knowledge of Co^{II}-5d exchange coupling a fundamental starting point. Finding an appropriate model for such coupling is difficult however, as the ideal species would include many molecular magnetism enhancing properties and few synthetic variables. A perfect system would also be redox active, allowing comparison of coupled and uncoupled systems.

Bis(tetrathiotungstate)cobaltate, $[Co(WS_4)_2]^{z-}$ (z = 2, 3), is accessible as both dianionic[308] and reduced trianionic[309] species (Figure 4.3[310]) and meets the criteria. The T_d $\{CoS_4\}$ core analogous to that in $[Co(SPh)_4]^{2-}$ (*vide supra*) will likely give similar SMM performance, whilst the presence of redox active ligands allows introduction of exchange coupling into the system.

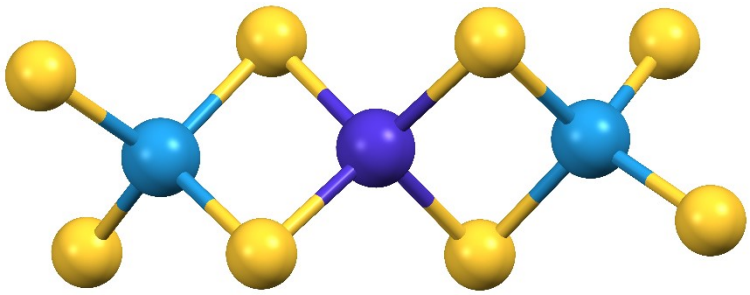

Figure 4.3 Molecular structure of the trianionic $[Co(WS_4)_2]^{2-}$ coordination complex.

Cyclic voltammetry shows the presence of a one-electron reduction at −0.88 V versus $Fc^{+/0}$ confirmed crystallography to be mainly W^{VI} centred, with W−S bond lengths increasing significantly on reduction. This should result in an exchange coupled W^{V}–Co^{II}–W^{VI} system where coupling is enhanced by the presence of large 3p S orbitals, allowing the effect of introducing of Co^{II}-5d exchange coupling to be recorded. Furthermore, as the WS_4^{2-} metalloligands consist of four sulfurs bound to a central W^{VI} d^0 ion, the well-known complex as ligand strategy[289] can be used to predictably synthesise the system.

To examine the changes in electronic structure the W^{VI}–Co^{II}–W^{VI} dianion was prepared and compared to the W^{V}–Co^{II}–W^{VI} trianion. The electronic structure was examined using electronic and X-ray absorbance spectroscopy, with the effect of exchange coupling also studied using magnetic susceptibility measurements. Further information was also obtained through comparison to other first row $[M(WS_4)_2]^{z-}$ species.

4.2 Synthesis

The tetraphenylphosphonium Ni^{II}, Co^{II} and Zn^{II} tetrathiotungstate species were prepared in good yield in aqueous MeCN media in ambient conditions, with the products precipitating on addition of excess counterion to mixed solutions with one equivalent of M^{II} salt and two equivalents WS_4^{2-} (Scheme 4.1).

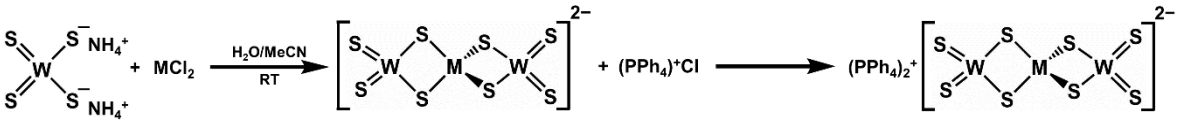

Scheme 4.1 General reaction scheme for tetrathiotungstate metal complexes.

Product purities and yields were improved through incorporation of improvements on the initial method[308] outlined by Callahan[311] and Crossland,[312] with sample purity confirmed using ESI-MS and electronic spectroscopy. Even under rigorously dry anaerobic conditions $[Cu^{II}(WS_4)_2]^{2-}$ proved to be spontaneously reduced by the WS_4^{2-} ligands present, giving $[Cu^{I}(WS_4)_2]^{3-}$.[313] The reduced species has been known for over three decades,[309] being discovered in the course of broader research into Cu tetrathiometallate complexes. Such complexes are typically isolated as polymetallic clusters, the exact nature determined by the initial solvent and metal stoichiometry.[314]

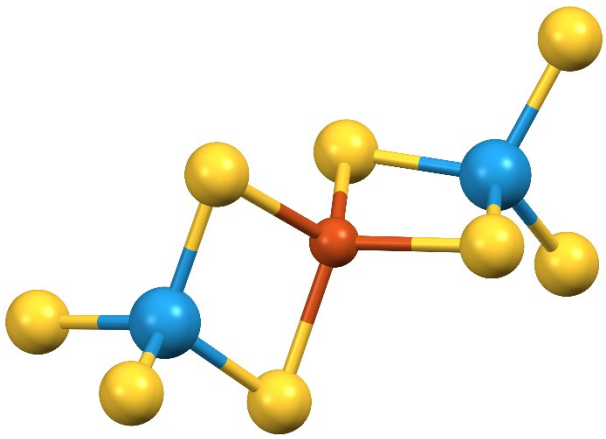

Figure 4.4 Molecular structure of the trianionic $[Cu(WS_4)_2]^{3-}$.

The fact that the mononuclear $[Cu^{I}(WS_4)_2]^{3-}$ forms spontaneously on addition of stochiometric equivalents of Cu^{II} and WS_4^{2-} in aqueous MeCN is thus both rare and remarkable, forming the basis of later research.[313] Whilst not directly related to the research here, the Cu^{I} trianion (Figure 4.4)[315] is isoelectronic to $[Zn^{II}(WS_4)_2]^{2-}$,[312] with the two complexes offering the opportunity to examine the effect of changing Z_{eff} on isoelectronic $[M(WS_4)_2]^{z-}$ complexes.

Reduction of the Co species has been well documented,[310] with cyclic voltammetry confirming the presence of a reversible reduction event at −0.88 V versus $Fc^{+/0}$. BH_4^- proved to be the ideal reductant for isolation of $[Co(WS_4)_2]^{3-}$, with electronic spectroscopy proving the formation and purity of the highly air-sensitive product.

4.3 Results and Discussion

4.3.1 Crystal Structures

Diffraction quality crystals of $(PPh_4)_2[Co(WS_4)_2]$ were obtained by vapour diffusion of diethyl ether into a concentrated acetonitrile solution.

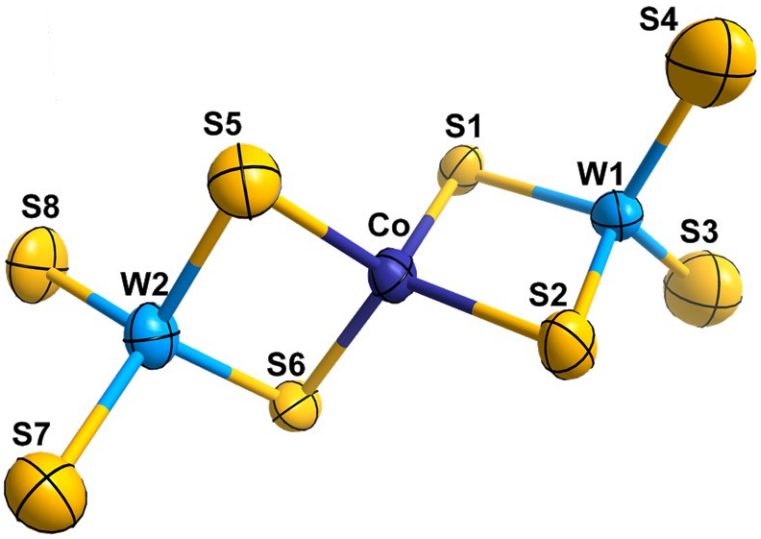

Figure 4.5 Structure of the anion in crystals of $(PPh_4)_2[Co(WS_4)_2]$. Thermal ellipsoids are shown at the 50% probability level.

The molecular structure of the $[Co(WS_4)_2]^{2-}$ is illustrated in Figure 4.5, with selected bond lengths and angles in Table 4.1. The complex consists of a central $\{CoS_4\}$ moiety with sulfurs from two bidentate tetrathiotungstato ligands; the charge of the complex is balanced by two PPh_4^+ counterions

Table 4.1 Selected Bond Distances (Å) and Angles (°) in $(PPh_4)_2[Co(WS_4)_2]$

Co–S1	2.245(8)	Co–S2	2.272(8)	Co–S5	2.277(8)
Co–S6	2.268(8)	W1–S1	2.228(8)	W1–S2	2.248(8)
W1–S3	2.138(8)	W1–S4	2.169(9)	W2–S5	2.249(8)
W2–S6	2.247(7)	W2–S7	2.059(4)	W2–S8	2.058(4)
Co–W1	2.810(4)	Co–W2	2.817(4)		
S1–Co–S2	101.8(3)	S5–Co–S6	102.3(3)	S1–Co–S6	111.5(3)
S1–Co–S5	114.2(3)	S2–Co–S5	112.7(3)	S2–Co–S6	114.9(3)
S1–W1–S2	103.1(3)	S3–W1–S4	109.7(4)	S5–W2–S6	103.8(3)
S7–W2–S8	109.5(5)				

The mean {CoS_2} planes are orthogonal with distortions of ca. 2° towards planarity, which combined with the ~102° bite-angle of the WS_4^{2-} ligand results in a tetragonally elongated pseudotetrahedral {CoS_4} coordination sphere. The coordinated WS_4^{2-} ligands consisting of four S atoms pseudo-tetrahedrally coordinated around a central W ion, with S−W−S angles <109.5° for the coordinated {WS_2} pocket, ≈109.5° for the reciprocal {WS_2} moiety, and >109.5° for the remaining {WS_2} angles.

The W−S bond lengths change significantly on coordination, changing from an average W−S bond length of 2.191(1) Å in the free WS_4^{2-},[316] to 2.106(7) Å in the terminal and 2.243(8) Å in the bridging W−S bonds when coordinated.

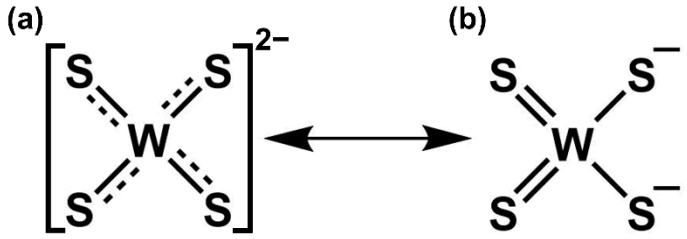

Figure 4.6 Resonance forms of the tetrathiotungstate dianion.

The changing bond lengths reflect a shift on coordination from resonance from (a) in Figure 4.6 to (b), as the bridging W−S bonds lose electron density whilst it increases in the terminal W−S bonds. This consistent with the $[Co(WS_4)_2]^{2-}$ structure, as the decreased electron density in the former bonds is facilitated by the formation of new Co−S bond on coordination.

With an average distance of 2.266(8) Å, the Co−S bonds in the complex fall in between the length of the M−S bonds in the analogous Ni^{II} and Zn^{II} species,[312] with average lengths of 2.226(1) Å and 2.335(1) Å, respectively. The fully occupied d-shell in Zn^{II} results in electron poorer M−S bonds compared to $[Co(WS_4)_2]^{2-}$, with the bridging W−S bonds retaining electron density. At 2.138(1) Å these bonds are thus shorter in the Zn^{II} species than the Co^{II} analogue, even as terminal W−S lengths remain constant. In contrast, the shorter Ni−S bonds stem from the square-planar nature of $[Ni(WS_4)_2]^{2-}$ delocalising of electron density throughout the complex, facilitated by the vacancies in the Ni^{II} d-shell. This

is reflected in the shorter W−S bonds, with lengths of 2.093 and 2.137 Å for the terminal and bridging W−S bonds respectively, and the greater convergence of W−S bond lengths in the Ni^{II} complex.

The Co−S bonds are considerably shorter than comparable 1,2-dithiolate species, with the equivalent bond lengths of ca. 2.303 Å in $[Co(dmit)_2]^{2-}$,[172] and are also shorter than the Co−S lengths of ca. 2.323 Å in $[Co(SPh)_4]^{2-}$.[43] The shorter bond lengths arise from the charge delocalisation on the $\{WS_4\}$ moieties in $[Co(WS_4)_2]^{2-}$, as although coordination pushed the resonance form towards (b) in Figure 4.6, there remains a significant contribution from form (a). This delocalisation is possible responsible for the ligand bite-angle of ~102°, which although significantly more acute than seen in ideal T_d complexes, is considerably larger than the bite-angles of ca. 91.1° in $[Co(dmit)_2]^{2-}$ and minimum S−Co−S angles of 97.4° observed in $[Co(SPh)_4]^{2-}$.[43,172]

4.3.2 Electronic Absorption Spectroscopy

4.3.2.1 Electronic Spectra of Bis(Tetrathiotungstate) 3d Metal Complexes

The spectra of $[Co(WS_4)_2]^{2-}$ and $[Co(WS_4)_2]^{3-}$ (Figure 4.7; individual spectra in Appendix 8.11) are richly featured, with the distinct spectral differences reflecting the reduction of the W^{IV} ions over the Co^{II}. Both spectra have prominent features in the visible-NIR region: $[Co(WS_4)_2]^{2-}$ has prominent spectral features at 814 and 719 nm that are blue-shifted to 652 and 545 nm in $[Co(WS_4)_2]^{3-}$, with a shoulder at 753 nm remaining. The intense bands obscure the Co^{II} LF transitions.

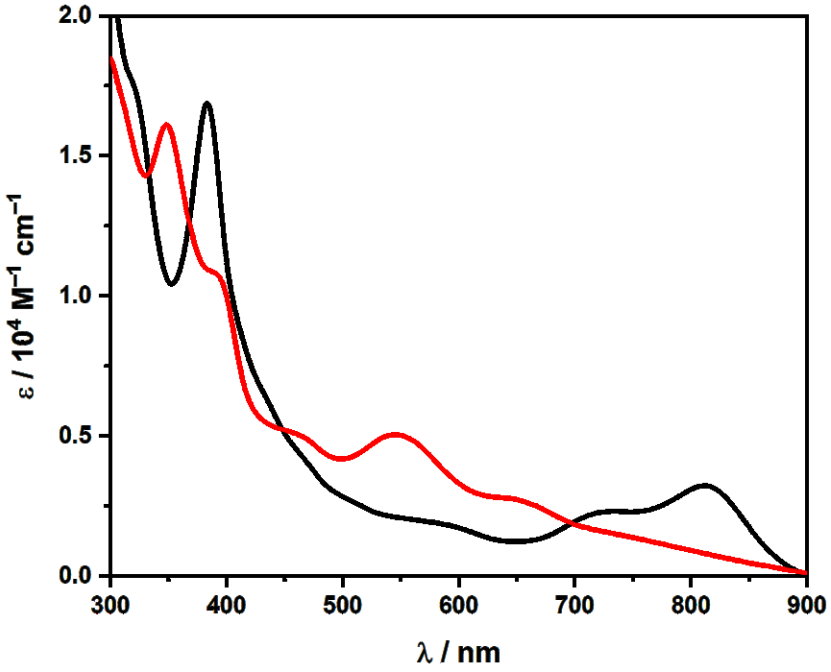

Figure 4.7 Overlay of the electronic spectra of $[Co(WS_4)_2]^{2-}$ (black) and $[Co(WS_4)_2]^{3-}$ (red) recorded in MeCN at room temperature.

The electronic structure of WS_4^{2-} has been established through electronic,[317] IR,[318] MCD[319] and S K-edge spectroscopic measurements,[320,321] as well as computational studies.[320,321] The studies show there are 12 symmetry-adapted linear combinations (SALCs) of S 3p atomic orbitals in the tetrahedral coordination environment around the W^{IV} centre (Figure 4.8a).[314] Four of these are σ-symmetric with respect to the W−S bond and span a_1 and t_2 symmetries, whilst the remaining eight are π-symmetric, spanning e, t_1 and t_2 symmetries.

W−S σ-interactions arise from symmetry-allowed mixing of the S s- and p-orbitals with the W s, p and d orbitals with a_1 and t_2 symmetries, with π-interactions forming from mixing of t_2 and e orbitals; the S 3p t_1 SALCs are non-bonding.

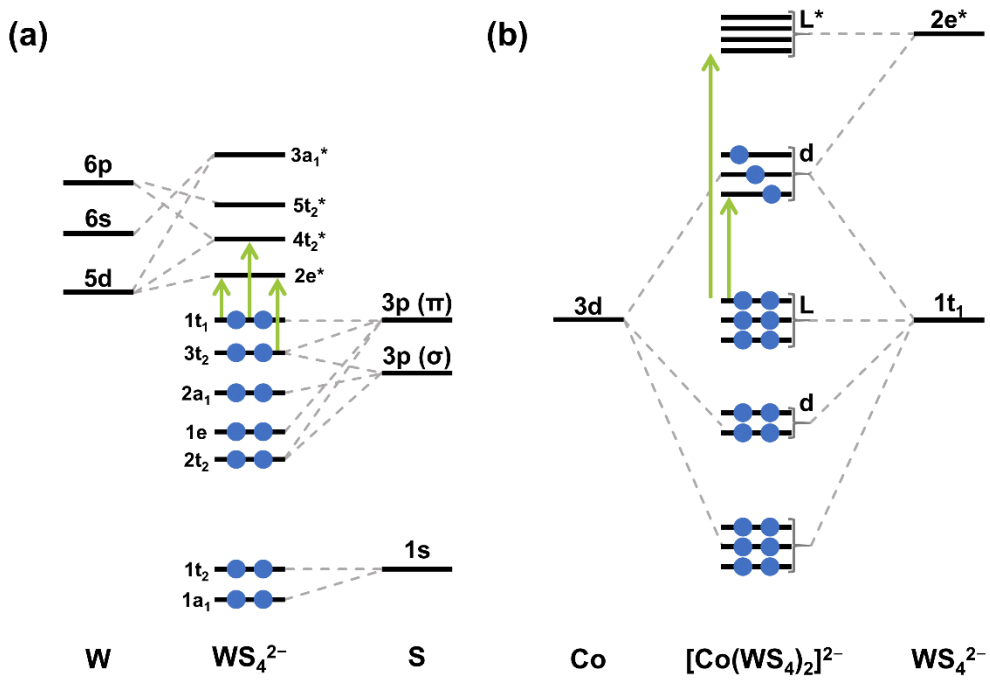

Figure 4.8 Qualitative MO schemes of (a) the tetrahedral WS_4^{2-} dianion and (b) trimetallic $[Co(WS_4)_2]^{2-}$. The braces link together MOs of approximately the same energy; transitions visible in the electronic spectra are marked in green; electrons are shown as blue circles.

Transitions from the $1t_1$ and $3t_2$ orbitals dominate the electronic spectrum of WS_4^{2-}, with the $1t_1 \rightarrow 2e$ transition lowest in energy, followed by $3t_2 \rightarrow 2e^*$ then $1t_1 \rightarrow 4t_2^*$.[322]

Such definite assignments are not retained on coordination: the higher energy bands are L → L* transitions, but the band energy is altered as coordination changes the {WS_4} coordination geometry and LF splitting. Müller was able to derive a qualitative MO diagram for $[Co(WS_4)_2]^{2-}$ (Figure 4.8b) however, with calculations confirming MO ordering.[323]

The L → L* assignment of the higher energy transitions was confirmed, but the possibility of transitions from nonbonding ligand orbitals to half-filled orbitals of mainly Co 3d character also revealed. The transition energy was found to be ca. 10000 cm^{-1} in $[Co(WS_4)_2]^{2-}$, suggesting LMCT is responsible for the intense lower energy transitions in the spectra of both complexes.[323] The shift between $[Co(WS_4)_2]^{2-}$ and $[Co(WS_4)_2]^{3-}$ is

significant, as the increased transition energy implies destabilisation of the mainly Co 3d orbitals and stabilisation of the non-bonding t_1 orbital. If reduction occurred solely at the Co centre these changes would not occur, suggest at least partial ligand reduction boding well for exchange coupling. However, as shown in Figure 4.8b, the lowest energy vacant orbitals in $[Co(WS_4)_2]^{2-}$ are mainly Co 3d in character so it is likely the Co centre is also significantly reduced.

Furthermore, although the LMCT energy bands clearly demonstrate the complex nature of the reduction event, it could be contended it is indeed $Co^{II} \rightarrow Co^{I}$, with the increased LMCT energy due to the greater Co 3d orbital electron density repelling the mainly 3d MOs from the other full orbitals. In this case, although $W^{VI} \rightarrow W^{V}$ reduction has not occurred, the increased energy of the mainly Co 3d HOMOs could lead to greater HOMO-LUMO mixing with the mainly W 5d LUMOs, possibly facilitating stronger exchange coupling.

Co and S K-edge allow the exact nature of the reduction event to be determined, but before this data is discussed the electronic spectra of $[Ni(WS_4)_2]^{2-}$, $[Cu(WS_4)_2]^{3-}$ and $[Zn(WS_4)_2]^{2-}$ will be studied to ensure all information is gleaned.

The square planar nature of $[Ni(WS_4)_2]^{2-}$ gives an electronic spectrum (Figure 4.9) different from those of $[Co(WS_4)_2]^{2-}$ and $[Co(WS_4)_2]^{3-}$. Intraligand CT bands still dominate the higher energy region of the spectrum, with intense peaks at 423 and 383 nm corresponding to the $1t_1 \rightarrow 2e^*$ and $3t_2 \rightarrow 2e^*$ transitions present, along with a shoulder at 331 nm corresponding to $1t_1 \rightarrow 4t_2^*$. The remaining transitions are much less intense, arising from Laporte- and spin-forbidden LF transitions: the higher energy shoulder at 527 nm from $^1A_{1g} \rightarrow {}^1B_{1g}$ and the weaker transition at 671 nm from $^1A_{1g} \rightarrow {}^1A_{2g}$.[308]

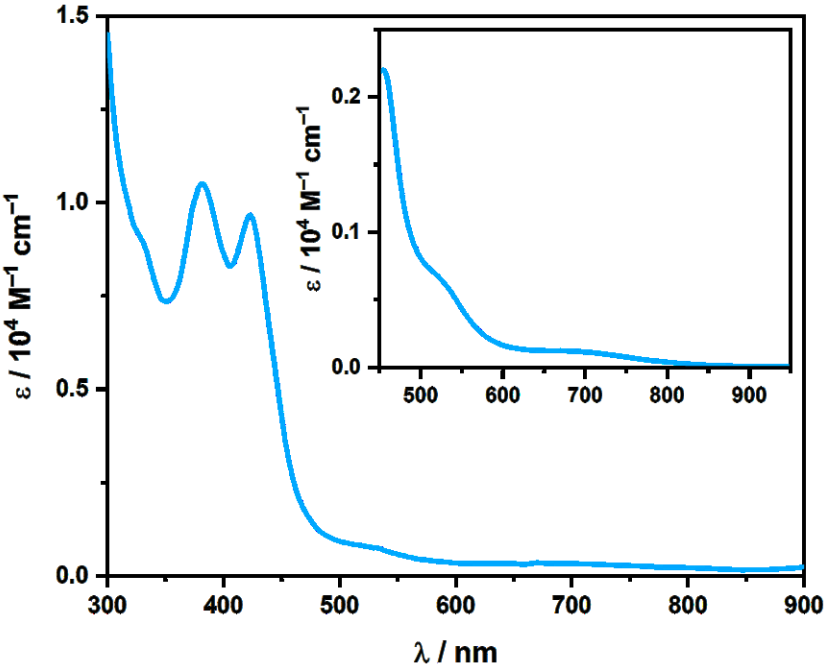

Figure 4.9 The electronic spectrum of $[Ni(WS_4)_2]^{2-}$ in MeCN; inset shows an expansion of the LF transitions.

The d^{10} ions in $[Cu(WS_4)_2]^{3-}$ and $[Zn(WS_4)_2]^{2-}$ mean only intraligand charge transfer features should be visible in the electronic spectra (Figure 4.10; individual spectra in Appendix 8.11). Nonetheless the spectra are noticeably different: $[Zn(WS_4)_2]^{2-}$ shows two distinct peaks at 462 and 392 nm corresponding respectively to the $1t_1 \rightarrow 2e^*$ and $3t_2 \rightarrow 2e^*$ transitions, whilst the features in $[Cu(WS_4)_2]^{3-}$ are far less defined. The Cu^{I} species has an intense broad peak at 386 nm likely corresponding to the $3t_2 \rightarrow 2e^*$ transition, followed by a series of broader lower energy shoulders at 447, 530 and 627 nm. The latter transitions likely stem from other intraligand CT features, but the poor resolution prevents definite assignment; the possibility of trace Cu^{II} was considered, but the lack of an EPR signal from any solution discounted this possibility.

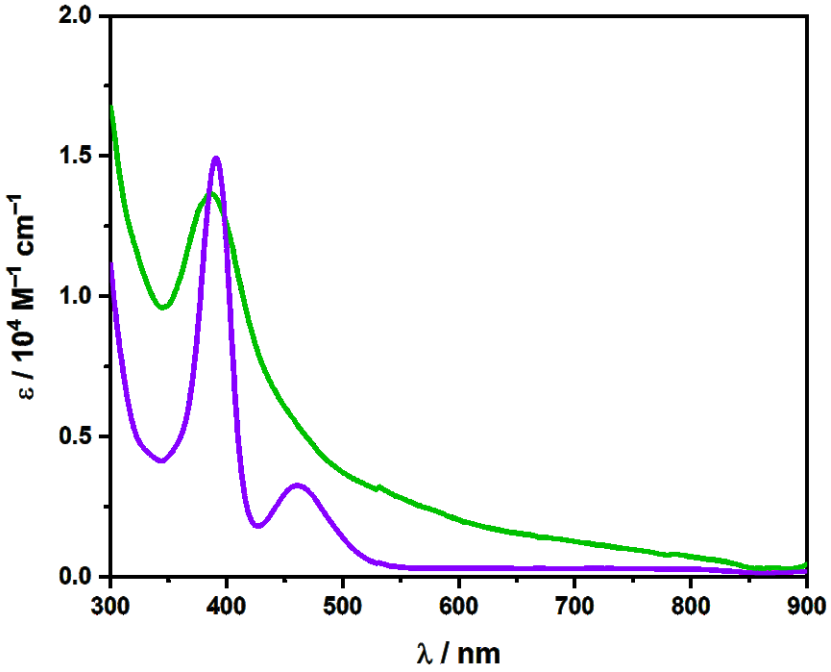

Figure 4.10 Overlay of the electronic spectra of $[Cu(WS_4)_2]^{3-}$ (green) and $[Zn(WS_4)_2]^{2-}$ (violet) in MeCN.

The energy shift of the intraligand CT bands in d^{10} systems has been attributed to distortions in the $\{WS_4\}$ moieties,[314] a thesis confirmed by the spectra examined here. The nonbonding $1t_1$ orbitals should shift significantly as the $\{WS_4\}$ geometry moves from T_d to D_{2d}, changing the $1t_1 \rightarrow 2e$ and $1t_1 \rightarrow 4t_2^*$ energy and intensity.[314] This is reflected in the electronic spectra, as severe $\{WS_4\}$ distortions observed in $[Ni(WS_4)_2]^{2-}$,[312] generate higher energy intraligand CT bands at 423 and 383 nm. The distortions in $[Zn(WS_4)_2]^{2-}$ more moderate,[312] with the resulting intraligand CT bands reduced in energy to 462 and 392 nm, respectively.

The $\{WS_4\}$ moieties in $[Cu(WS_4)_2]^{3-}$ are closest to T_d[315] and should be least affected, but the featureless spectrum prevents comparison. The origin of the dramatic differences in electronic spectra cannot be stated for certain, but it is possible due to fluxional motion of $[Cu(WS_4)_2]^{3-}$ in solution, with the Cu^{I} binding the WS_4^{2-} ligands less rigidly than Zn^{II}.

4.3.3 Magnetic Susceptibility Data

Although neither $[Co(WS_4)_2]^{2-}$ and $[Co(WS_4)_2]^{3-}$ have electronic spectral profiles with the hallmarks associated with T_d compounds, information on the effect of reduction on the electronic structure of the systems can be derived from the magnetic susceptibility data. Magnetic measurements allow the probing of the spin ground state (S) of the complexes – as both $\{CoS_4\}$ coordination environments are pseudotetrahedral[310] the Co LF is near constant, with changes of S on reduction stemming from the effect of exchange coupling.

Table 4.2 Magnetic Moments (B.M.) of Co^{II} Tetrathiotungstate Complexes.

	μ_{eff}	g-value	S
$[Co(WS_4)_2]^{2-}$	4.32	2.231	$^3/_2$
$[Co(WS_4)_2]^{3-}$	3.01	2.128	1

A magnetic balance was used to measure the magnetic moment of neat powders; the results are given in Table 4.2. The solid-state measurements prove the dianion to be the spin-triplet the tetrahedral coordination geometry predicts. As is typical for T_d Co^{II} species with large SOC,[36] the g-values for all the complexes are consistently higher than g_e.[183] Reduction reduces the magnetic moment, giving a value for a S = 1 complex. The g-value remains considerably higher than g_e and within experimental error of those found for $[Co(WS_4)_2]^{2-}$. Variation in the moments recorded for both complexes is within experimental error.[184]

The reduced magnetic moment in $[Co(WS_4)_2]^{3-}$ allows three possibilities: reduction of Co^{II} to Co^{I}, which on remaining D_{2d} has a S = 1 spin-state; reduction of the ligand, resulting in a S = $^1/_2$ ligand antiferromagnetically coupled to the S = $^3/_2$ Co^{II} centre, giving a net S = 1; the final possibility is well known in 1,2-dithiolate complexes: non-innocence.[153] This would be with a partial reduction of both the metal and ligand centres, with exchange coupling giving net S = 1.

K-edge XAS can be used to determine reduction nature of the reduction by revealing the electronic structure of both the Co and S atoms. However, before discussing this VT magnetic susceptibility measurements will be discussed. Information can be extracted

examining the magnetic moments across a range of temperatures, with the variation determined by the nature of spin-state and exchange coupling within the complex.

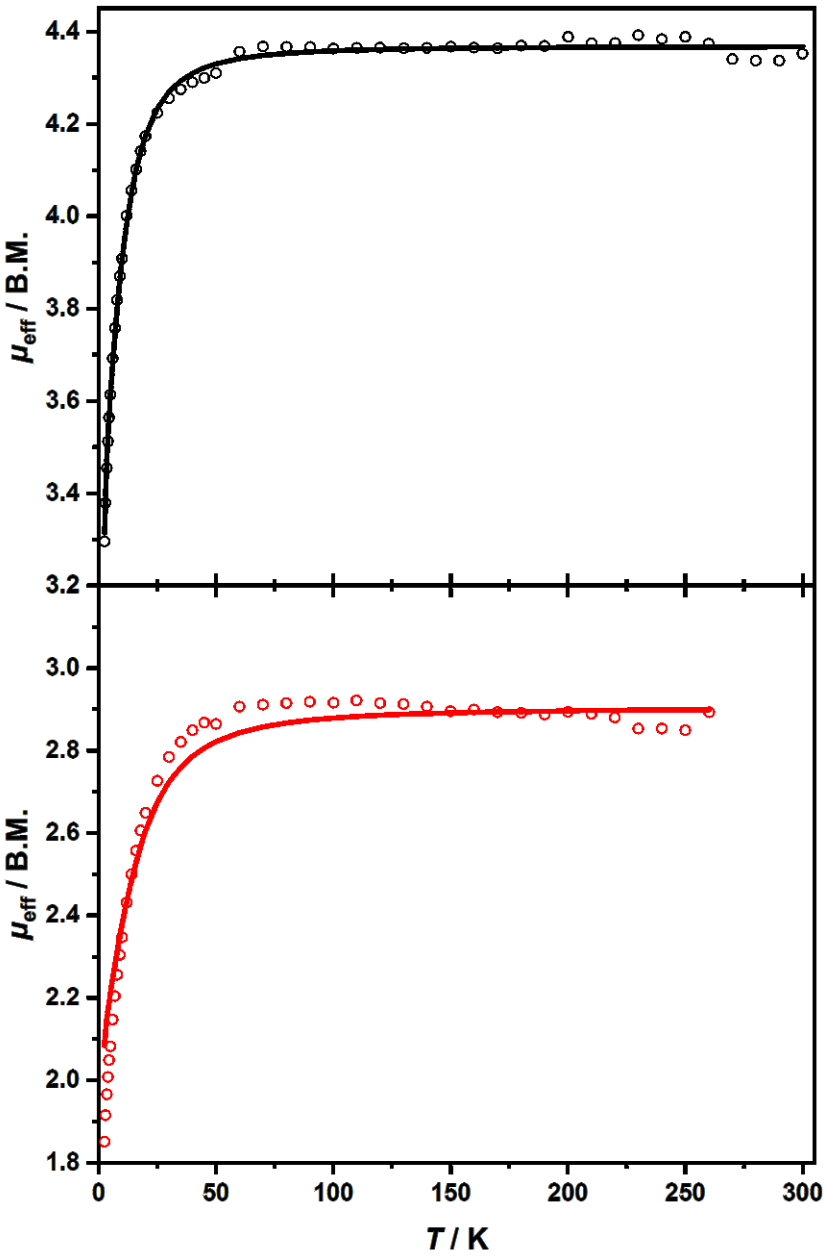

Figure 4.11 Temperature dependence of the magnetic moment μ_{eff} (B.M.) of powdered samples of $[Co(WS_4)_2]^{2-}$ (top) and $[Co(WS_4)_2]^{3-}$ (bottom). Circles are experimental data; solid lines represent the best fit.

The electronic ground states of $[Co(WS_4)_2]^{2-}$ and $[Co(WS_4)_2]^{3-}$ have been established from variable temperature magnetic susceptibility measurements on powders with an applied field of 1.0 T. The temperature dependence of the effective magnetic

moment, μ_{eff}, of both compounds is shown in Figure 4.11. The magnetic moments of $[Co(WS_4)_2]^{2-}$ and $[Co(WS_4)_2]^{3-}$ are constant in the range from 50 to 273 K at 4.37 and 2.90 B.M., respectively. The values are indicative of $S = {}^3/_2$ species with a *g*-value of 2.255 for $[Co(WS_4)_2]^{2-}$ and an $S = 1$ species with *g*-value of 2.052 for $[Co(WS_4)_2]^{3-}$, matching the RT solid state measurements.

Table 4.3 Spin-Hamiltonian parameters from fit of magnetic data

	S	***g*-value**	***D* / cm^{-1}**	***Θ* / K**	***X*$_{TIP}$ / 10^{-6} emu**
$[Co(WS_4)_2]^{2-}$	$^3/_2$	2.255	−12.87	0	334.3
$[Co(WS_4)_2]^{3-}$	1	2.052	−39.81	0	344.0

Below 50 K, μ_{eff} decreases slightly due to field saturation at 1 T and the influence of zero-field splitting. The sign of *D* for $[Co(WS_4)_2]^{2-}$ and $[Co(WS_4)_2]^{3-}$ was determined from the isofield magnetisation measurements. The fitting parameters are summarised in Table 3.6, with the data consistent with the respective $S = {}^3/_2$ and $S = 1$ spin ground states reported for $[Co(WS_4)_2]^{2-}$ and $[Co(WS_4)_2]^{3-}$.[309] No Weiss constants were required to fit the data, but minor temperature independent parameters (X_{TIP}) were included to account for a small amount of diamagnetic impurity in the sample. The observed drop of μ_{eff} with decreasing temperature (< 100 K) is due to large zero-field splittings of $D = -12.87$ and -39.81 cm^{-1} for $[Co(WS_4)_2]^{2-}$ and $[Co(WS_4)_2]^{3-}$, respectively.

4.3.4 X-ray Absorption Spectroscopy

Co K-edge XAS was used to probe the coordination environments and oxidation states of $[Co(WS_4)_2]^{2-}$ and $[Co(WS_4)_2]^{3-}$, and allow comparison to similar mono- and dithiolate Co species. S K-edge was also used to study and compare both Co complexes and $[Zn(WS_4)_2]^{2-}$.

4.3.4.1 Co K-edge XAS of Co Tetrathiotungstate Complexes

The Co K-edge spectra of $[Co(WS_4)_2]^{2-}$ and $[Co(WS_4)_2]^{3-}$ are shown in Figure 4.12, with the energies of the rising edge positions determined at the first inflection point of the edge summarised alongside the pre-edge energies in Table 4.4. A one-electron reduction of $[Co(WS_4)_2]^{2-}$ results in a shift of the rising edge energy of 0.4 eV. The rising edge is a good measure of the effective nuclear charge at the metal ion[196] and supports a partial reduction of the Co^{II}.

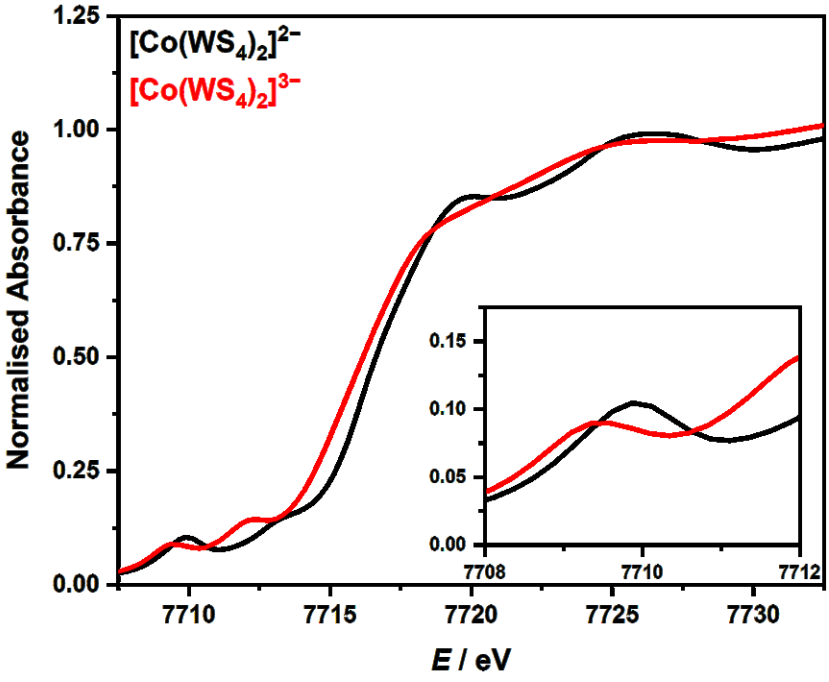

Figure 4.12 Overlay of the normalised Co K-edge XAS spectra of the Co tetrathiotungstate complexes. The inset shows an expanded view of the pre-edge region.

In the two compounds the pre-edge region does not reflect a change in the oxidation of the Co ion; the pre-edge peak energy shifts 0.6 eV on reduction, 0.2 eV greater than the shift of the rising edge. The different energy shifts highlight the confluence of factors in the pre-edge origins.

Table 4.4 Co K-edge XAS pre- and rising-edge energies (eV), and intensities (D_0) for four-coordinate cobalt−sulfur complexes.

	Pre-edge energy	D_0	Rising-edge energy[a]
$[Co(WS_4)_2]^{2-}$	7709.8	0.024	7716.6
$[Co(WS_4)_2]^{3-}$	7709.2	0.018	7716.2
$[Co(SPh)_4]^{2-}$	7709.6	0.047	7716.7
$[Co(dts)_2]^{2-}$	7709.4	0.042	7716.3
$[Co(mnt)_2]^{2-}$	7710.1	0.012	7716.8

[a] Determined at the first inflection point.

The pre-edge feature in $[Co(WS_4)_2]^{2-}$ occurs at 7709.8 eV, within the range reported for T_d Co^{II} complexes[192,193] but 0.4 eV higher than in $[Co(SPh)_4]^{2-}$ and $[Co(dts)_2]^{2-}$. As stated, the pre-edge energy is determined by a variety of factors, whilst the intensity is typically tied to the coordination geometry. Unusually, comparison of the Co K-edge spectra (Figure 4.13) shows the intensity of $[Co(WS_4)_2]^{2-}$ pre-edge feature to fall between that of $[Co(SPh)_4]^{2-}$ and $[Co(dts)_2]^{2-}$ and the planar $[Co(mnt)_2]^{2-}$. As the WS_4^{2-} ligated species should be most intense, the variation shows the limitations of using the pre-edge to define coordination geometry. The over-simplified interpretation typical of pre-edge data was first shown clearly in Cu K-edge spectra, which were shown to frequently rely on LF models neglecting ligand to metal π-backbonding[324]. Similar results were then found for Co complexes, with ligand acceptor orbitals profoundly affecting the pre-edge energy and intensity.[325]

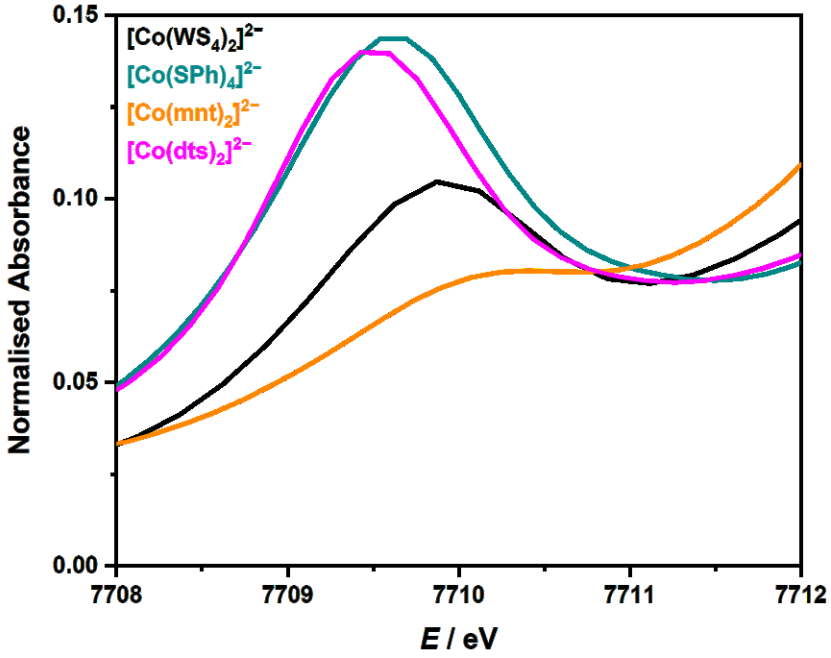

Figure 4.13 Comparison of the pre-edge regions of the normalised Co K-edge XAS spectra of $[Co(WS_4)_2]^{2-}$ and a series of Co^{II} complexes.

Unambiguous information can be obtained from the rising edges. Despite the significantly different pre-edge features $[Co(WS_4)_2]^{2-}$ and $[Co(SPh)_4]^{2-}$ have identical rising edge energies of 7716.6 ± 0.1 eV, confirming the Co^{II} oxidation state in the former complex. The 0.4 eV lower rising edge energy in $[Co(WS_4)_2]^{3-}$ reflects a partial reduction of the Co centre; the majority ligand-based reduction is not surprising given the d^0 W^{VI} ions and diffuse S 3p orbitals present. The resultant exchange interactions are shown to reduce the $\{CoS_4\}$ centrosymmetry,[310] something that would reduce the pre-edge energy. However, although $[Co(WS_4)_2]^{3-}$ is less centrosymmetric, pre-edge intensity decreases on reduction from $[Co(WS_4)_2]^{2-}$. As the pre-edge intensity has been shown to decrease on reduction in similar species,[326] any increased intensity from lowered centrosymmetry must be outweighed by the lower Co oxidation state.

4.3.4.2 S K-edge XAS of 3d Tetrathiotungstate Complexes

The S K-edge spectra of $[Co(WS_4)_2]^{2-}$, $[Co(WS_4)_2]^{3-}$ and $[Zn(WS_4)_2]^{2-}$ and their second derivatives are shown in Figure 4.14; individual pseudo-Voigt deconvolutions are displayed in Figure 4.15 with the pre-edge peak energies and intensities listed in Table 4.5. The S K-edge spectra all have three well resolved pre-edge features, with lower energy transitions at 2470.05 ± 0.15 eV followed by higher energy transitions at 2471.05 ± 0.1 eV and 2471.70 ± 0.1 eV.

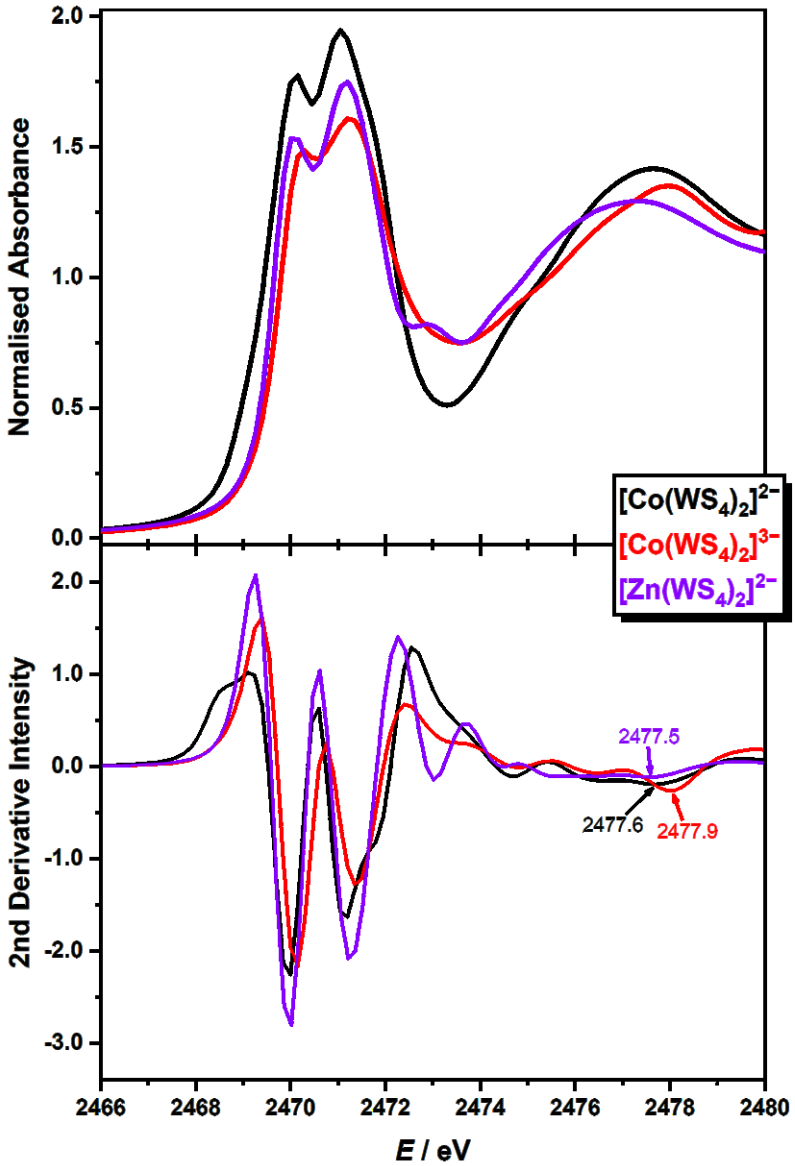

Figure 4.14 Comparison of the normalised S K-edge spectra (top) and their second derivatives (bottom) for $[Co(WS_4)_2]^{2-}$, $[Co(WS_4)_2]^{3-}$ and $[Zn(WS_4)_2]^{2-}$. The 1s → 4p edge transitions are indicated in the plots of the second derivatives.

The S K-edge of WS_4^{2-} has been detailed previously,[320,321] allowing comparison of the free and coordinated species. Unlike the coordinated systems, the S K-edge of free WS_4^{2-} has two pre-edge at 2470.1 and 2471.3 eV, corresponding respectively to the 1s → 2e* and 1s → $4t_2$* transitions from the S-based HOMOs to the mainly W LUMOs. The lowest energy peak in each metal complex corresponds to the 1s → 2e* transition, occurring at ~2470.0 eV in the dianionic species $[Co(WS_4)_2]^{2-}$ and $[Zn(WS_4)_2]^{2-}$ and at ~2470.2 eV in the reduced $[Co(WS_4)_2]^{3-}$. All occur within error of the transition in WS_4^{2-}.

Table 4.5 Pre-Edge Peak Energies (eV), Intensities (D_0), Number of Holes in Acceptor Orbitals (h), and Covalencies (α^2; S 3p%) for $[Co(WS_4)_2]^{2-}$, $[Co(WS_4)_2]^{3-}$ and $[Zn(WS_4)_2]^{2-}$.

	Pre-edge energy	D_0	*h*	α^{2a}
$[Co(WS_4)_2]^{2-}$	2469.96	0.42	4	7.8
	2471.03	0.39	2	14.6
	2471.80	0.26	4	4.9
$[Co(WS_4)_2]^{3-}$	2470.17	0.32	4	5.8
	2471.12	0.30	2	10.8
	2471.83	0.20	4	3.6
$[Zn(WS_4)_2]^{2-}$	2470.03	0.32	4	6.0
	2471.02	0.28	2	10.6
	2471.65	0.19	4	3.6

[a] Determined from $\alpha^2 = 12D_0/(H \times I_S)$. I_S = 16.08, 16.62, 15.90 (Estimated from the S 1s → 4p transition energies in Figure 4.14 and the correlation plot in reference 191)

Given the presence of three peaks in Zn^{II} the spectrum, the third peak cannot stem from S interactions with the 3d ion. Instead the origin is clarified through consideration of the relative intensities of each transition. If the intensity of 1s → 2e* is set to 2, corresponding to the two unoccupied acceptor orbitals, the summed intensity of the latter transitions corresponds to 3.10, 3.12 and 2.94, for $[Co(WS_4)_2]^{2-}$, $[Co(WS_4)_2]^{3-}$ and $[Zn(WS_4)_2]^{2-}$, respectively.

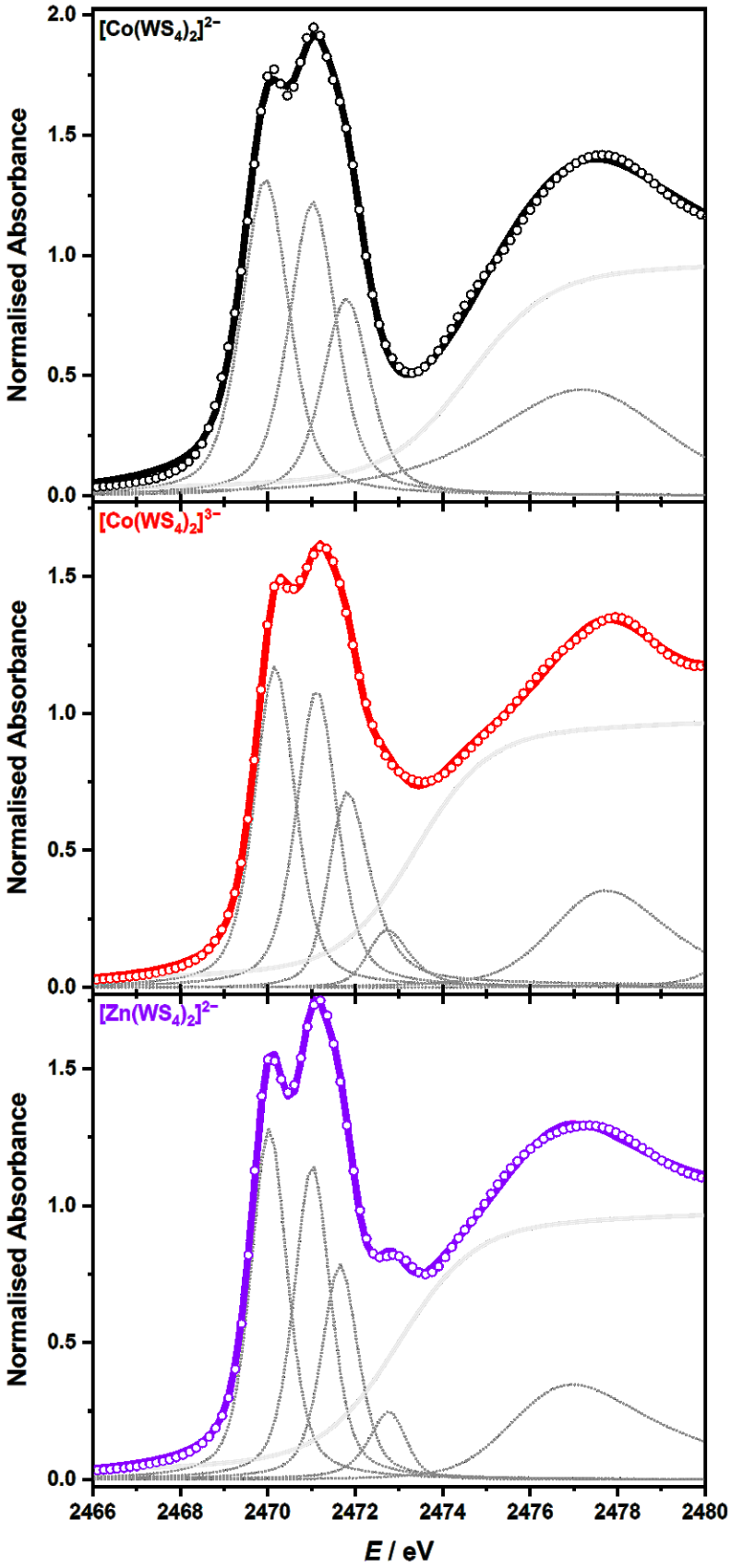

Figure 4.15 Pseudo-Voigt deconvolution of S K-edge spectra of $[Co(WS_4)_2]^{2-}$, $[Co(WS_4)_2]^{3-}$ and $[Zn(WS_4)_2]^{2-}$. Circles represent the experimental data; dotted lines represent the pseudo-Voigt; the solid grey line the edge jump; and the solid coloured line is the sum of the fit.

This means the two higher-energy transitions are to a total of three unoccupied d-orbitals, corresponding to the 1s → $4t_2$* in the WS_4^{2-} S K-edge. On coordination the $4t_2$* MO is thus split into one single and two doubly degenerate MOs (see Figure 4.16).

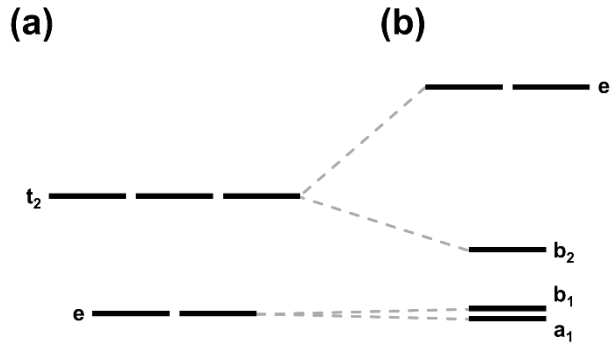

Figure 4.16 Qualitative MO schemes of the mainly W 5d LUMOs in (a) the T_d free WS_4^{2-} ligand and (b) the D_{2d} coordinated ligand.

On coordination the geometry changes considerably, distorting towards D_{2d} as S−W−S angle deviations increase to >5°. This deviation causes a breaking of the degeneracy of the 2e* state into a_1 and b_1 states, which remain close enough in energy to appear as one transition. The $4t_2$* degeneracy is broken far more significantly, with energy gaps between the resultant e and b_2 MOs of 0.77, 0.71 and 0.63 eV, for $[Co(WS_4)_2]^{2-}$, $[Co(WS_4)_2]^{3-}$ and $[Zn(WS_4)_2]^{2-}$, respectively.

This is because on distortion to D_{2d} symmetry the d_{xy} (b_2) orbital will be stabilised far more than the d_{xz} and d_{yz} (e) orbitals, meaning that whilst there is relatively little covalency in the lowest energy "2e*" orbitals, the M−S bond of the stabilised b_2 orbital is far more covalent. In contrast the 1s → e occurs at much higher energies than the original 1s → $4t_2$* transition, occurring at 0.5, 0.53 and 0.35 eV higher than the 1s → $4t_2$*. This destabilisation isolates the mainly W 5d MOs from the lower energy majority S 3p orbitals, resulting in much lower covalencies than the b_2 MOs.

4.4 Experimental

4.4.1 X-ray crystallographic data collection and refinement

Single crystals of $(PPh_4)_2[Co(WS_4)_2]$ were grown by slow diffusion of diethyl ether into a saturated acetonitrile solution of the complex. Orange blocks of dimension 0.10 × 0.03 × 0.02 mm^3 of $(PPh_4)_2[Co(WS_4)_2]$ were mounted on a Bruker SMART APEX CCD diffractometer, and data collected using graphite monochromated Mo−Kα radiation (λ = 0.71073 Å) from a Mo-target rotating-anode X-ray source equipped with a Kryoflex attachment supplying a nitrogen stream at 150 K. The structures were solved by direct methods and refined by full-matrix least squares method with anisotropic thermal parameters for all atoms with SHELXS-97[246] and SHELXL-97,[247] using the WinGX[248] software package. Corrections for incident and diffracted beam absorption effects were applied using empirical absorption corrections.[249] CIF files were generated using Olex2,[247] with analysis and artwork creation performed using Mercury.[250] Crystal data are presented in Table 4.6.

4.4.2 Physical Measurements

Electronic absorption spectra were recorded using a Shimadzu UV-3600 UV-Vis-NIR spectrophotometer (200 – 1500 nm) in a 1 cm quartz cuvette at a scan rate of 1 nm per second. Infrared data were taken as pressed pellets using a Shimadzu FTIR-8400S spectrophotometer with a diamond anvil cell. ^{1}H and ^{13}C NMR spectra of the complexes were measured at 25 °C on a Bruker AVI 400MHz NMR spectrometer, with chemical shifts referenced to the protonated solvent residual.[199] Magnetic susceptibility measurements were on a Sherwood Scientific Mark 1 Magnetic Susceptibility Balance using an aqueous solution of $Hg[Co(CNS)_4]$ as a calibrant.[200] Mass spectrometry (MS) spectra (electrospray ionization, ESI) were obtained with a Bruker microTOF-Q Quadrupole Time-of-Flight Mass Spectrometer operating in positive- and negative-ion modes Elemental analyses were determined by the departmental microanalysis services using an EA 1110 CHNS, CE-440 Elemental Analyser.

Magnetic susceptibility measurements of crystalline powdered samples (10−30 mg) were performed on a Quantum Design PPMS DynaCool Vibrating Sample Magnetometer at 1 T between 2 and 300 K for both samples. The samples were measured in gelatine capsules, with the diamagnetic contribution from the sample container was subtracted from the experimental data. Paramagnetic susceptibilities were extracted by using Pascal's constants[239] to subtract diamagnetic contributions, with the program julX written by E. Bill used for simulation and analysis of the magnetic susceptibility data.

4.4.3 X-ray Absorption Spectroscopy

All X-ray Absorption data were measured at the Stanford Synchrotron Radiation Lightsource (SSRL). Co and S K-edge data were collected as described in Chapter 3.4.3.

Table 4.6 Crystallographic Data for $(PPh_4)_2[Co(WS_4)_2]$

formula	$C_{48}H_{40}CoP_2S_8W_2$
fw	1361.85
crystal system	monoclinic
space group	$P2_1/c$
colour, habit	orange, block
a, Å	18.422(11)
b, Å	15.070(9)
c, Å	18.600(11)
α, °	90.00
β, °	109.154(10)
γ, °	90.00
V, Å	4878(5)
T, K	150
ρ_{calcd}, $g\ cm^{-3}$	1.854
λ, Å / μ, mm^{-1}	5.483
refl. collected / $2\Theta_{max}$	31731 / 25.770
unique refl. / $I > 2\sigma(I)$	8102 / 3743
no. of param. / restr.	540 / 48
R1[a] / goodness of fit[b]	0.0993 / 0.995
wR2 [c] ($I > 2\sigma(I)$)	0.1748
residual density, e $Å^{-3}$	1.465 / −2.055

[a] Observation criterion: $I > 2\sigma(I)$. $R1 = \Sigma||F_o| - |F_c||/\Sigma|F_o|$. [b] GoF = $[\Sigma[w(F_o^2 - F_c^2)_2]/(n - p)]^{1/2}$. [c] wR2 = $[\Sigma[w(F_o^2 - F_c^2)^2]/\Sigma[w(F_o^2)^2]]^{1/2}$ where $w = 1/\sigma^2(F_o^2) + (aP)^2 + bP$, $P = (F_o^2 + 2F_c^2)/3$.

4.4.4 Syntheses

All reagents were purchased from commercial sources and used as received. Dry solvents were either dried with a system of drying columns from the Glass Contour Company or distilled according to standard procedures,[206] before being stored under an inert atmosphere of dinitrogen over 3 Å molecular sieves prior to use. Unless stated otherwise, all reactions and manipulations were conducted in air at room temperature.

Tetraphenylphosphonium borohydride, $(PPh_4)(BH_4)$. A solution of PPh_4Cl (2.00 g; 5.34 mmol) in H_2O (35 mL) was prepared and raised to pH 8 by the slow addition of NaOH, before the solution was cooled to 0 °C in an ice-water bath. A solution of $NaBH_4$ (300 mg; 7.93 mmol) in H_2O (2 mL) was added rapidly, causing the instant formation of a white precipitate. The solid was collected under suction, washed with H_2O (3 × 5 mL) cooled to 0 °C, and dried under vacuum for 18 h. Yield = 1.54 g (83%).

IR (solid, cm^{-1}): 3055 w, 2797 w, 2218 w, 1672 m, 1575 s, 1483 m, 1435 s, 1398 m, 1373 s, 1340 s, 1315 w, 1163 w, 1107 s, 1072 w, 1026 w, 995 m, 889 m, 870 w, 758 m, 719 s, 689 s, 615 w, 523 s, 437 w, 405 w.

Bis(tetraphenylphosphonium) bis(tetrathiotungstato)cobaltate, $(PPh_4)_2[Co(WS_4)_2]$. A solution of $(NH_4)_2[WS_4]$ (175 mg; 0.500 mmol) in a 1:3 mixture of H_2O and MeCN (7 mL) was prepared and added to a solution of $Co(NO_3)_2{\cdot}6H_2O$ (73.0 mg; 0.250 mmol) in a 1:1 mixture of H_2O and MeCN mixture (5 mL) acidified with four drops of glacial acetic acid. Immediately afterwards a solution of PPh_4Br (839 mg; 2.00 mmol) in a 1:1 mixture of H_2O and MeCN mixture (7 mL), causing the instant formation of a dark green precipitate. The solid was collected under suction, washed with Et_2O (3 × 5 mL) and dried under vacuum for 6 h before being recrystallised from dry MeCN under an inert dinitrogen atmosphere to give the final product. Yield = 230 mg (68%).

μ_{eff} (Gouy balance, 289 K) = 4.32 B.M.

Tris(tetraphenylphosphonium) bis(tetrathiotungstato)cobaltate $(PPh)_3[Co(WS_4)_2]$. Under an inert atmosphere of dinitrogen a solution of $(PPh_4)_2[Co(WS_4)_2]$ (320 mg; 0.225 mmol) in dry MeCN (30 mL) was prepared and stirred for 15 min. After this time $(PPh_4)(BH_4)$ (80 mg; 0.226 mmol) was added under a positive flow of dinitrogen, resulting in a rapid colour change from dark green to burgundy . The resulting solution was cannula filtered into a second Schlenk flask and concentrated under reduced pressure, sealed under nitrogen and stored in a freezer at −35 °C for 24 h. The resulting precipitate was collected in a sintered glass funnel inside a dinitrogen glovebox, washed with dry Et_2O (3 × 5 mL), and dried under vacuum for 24 h. Yield = 186 mg (49%).

μ_{eff} (Gouy balance, 288 K) = 3.01 B.M.

Bis(tetraphenylphosphonium) bis(tetrathiotungstato)nickelate $(PPh_4)_2[Ni(WS_4)_2]$. A solution of $(NH_4)_2[WS_4]$ (175 mg; 0.500 mmol) in a 1:3 mixture of H_2O and MeCN (7 mL) was prepared and added to a solution of $NiCl_2{\cdot}6H_2O$ (59.0 mg; 0.250 mmol) in a 1:1 mixture of H_2O and MeCN mixture (5 mL) acidified with four drops of glacial acetic acid. Immediately afterwards a solution of PPh_4Br (789 mg; 1.89 mmol) in a 1:1 mixture of H_2O and MeCN mixture (7 mL), causing the instant formation of an ochre precipitate. The solid was collected under suction, washed with Et_2O (3 × 5 mL) and dried under vacuum for 6 h before being recrystallised from MeCN/Et_2O. Yield = 302 mg (89%).

IR (solid, cm^{-1}): 3168 w, 3050 w, 1585 m, 1481 m, 1433 s, 1187 w, 1181 w, 1106 s, 1000 m, 993 m, 906 w, 854 w, 759 m, 751 m, 719 s, 688 s 676 m. ESI-MS: *m*/*z* 1020.7 $[M-PPh_4]^-$

Tris(tetraphenylphosphonium) bis(tetrathiotungstato)cuprate $(PPh_4)_3[Cu(WS_4)_2]$. A solution of $(NH_4)_2[WS_4]$ (175 mg; 0.500 mmol) in a 1:3 mixture of H_2O and MeCN (7 mL) was prepared and added to a solution of $Cu(NO_3)_2{\cdot}3H_2O$ (60.0 mg; 0.250 mmol) in a 1:1 mixture of H_2O and MeCN mixture (5 mL) acidified with four drops of glacial acetic acid. Immediately afterwards a solution of PPh_4Cl (751 mg; 2.00 mmol) in a 1:1 mixture of H_2O and MeCN mixture (7 mL), causing the instant formation of a brown precipitate. The solid

was collected under suction, washed with Et_2O (3 × 5 mL) and dried under vacuum for 4 h before being recrystallised from MeCN/Et_2O. Yield = 198 mg (47%).

IR (solid, cm^{-1}): 3171 w, 3055 w, 1584 m, 1481 w, 1433 s, 1337 w, 1312 m, 1184 w, 1161 m, 1107 s, 1072 w, 1026 m, 995 s, 978 w, 932 w, 851 w, 816 m, 804 w, 748 s, 721 s, 687 s. ESI-MS: *m*/*z* 1025.7 [M−2PPh_4]

5 Further 3d 1,1-Dithiolate Complexes

5.1 Introduction

Bis(dithiolene) Ni^{II} and Cu^{II} complexes were amongst the earliest dithiolene complexes studied, with $[Ni(S_2C_2Ph_2)_2]$ (Figure 5.1) the first homoleptic bis(dithiolene) reported.[83] Their remarkable properties ensured an initial surge of interest, as they are strongly chromophoric, possess multiple reversible redox processes and are persistently square-planar. Since then Ni^{II} and Cu^{II} dithiolene complexes have shown remarkable properties such as superconductivity[327] and non-linear optical[328] and magnetic interactions,[329] spurring investigations in an array of fields.

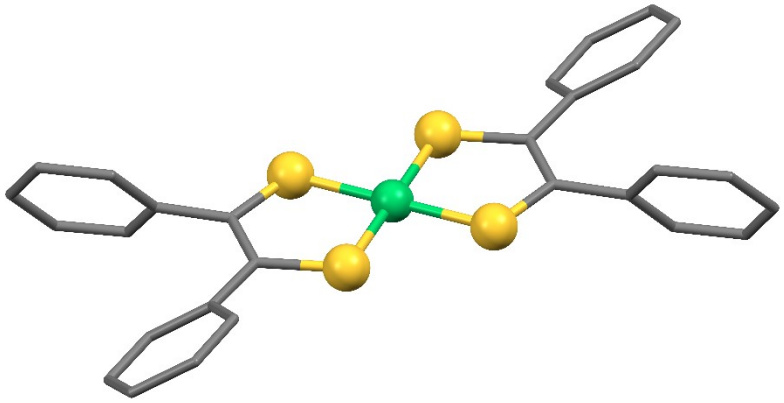

Figure 5.1 Molecular structure of the $[Ni(S_2C_2Ph_2)_2]$ (nickel, seafoam; sulfur, pineapple; carbon, charcoal). Hydrogen atoms omitted for clarity.

Despite their concurrent discovery, the richness of Ni^{II} and Cu^{II} 1,2-dithiolate research contrasts related 1,1-dithiolates. A series of Ni^{II} and Cu^{II} 1,1-dithiolate complexes were first reported by Coucouvanis.[210] The latter paper illustrates the usefulness of Ni^{II} and Cu^{II} in investigating 1,1-dithiolates, as the paramagnetic Cu^{II} ion allowed the EPR to be used to probe the electronic structures of the complexes.

The 1,1-dithiolates lack the attributes of their 1,2-dithiolate counterparts[330] and have a more limited range of substituents (see Chapter 1), the resulting complexes are therefore fewer in number, and research more limited in scope. Early work by Bereman provided information on $[Cu(Cpdt)_2]^{2-}$ and $[Ni(Cpdt)_2]^{2-}$ (Cpdt = cyclopentadienedithiolate)[104,105] that

related more to prior work on the Co^{II} analogue[212] than to other Ni^{II} or Cu^{II} 1,1-dithiolate systems. Whilst EPR of the Cu^{II} species revealed the out-of-plane π-bonding to be more covalent than in equivalent dithiocarbamate species,[104] nothing was done to examine Cu^{II} 1,1-dithiolate species.

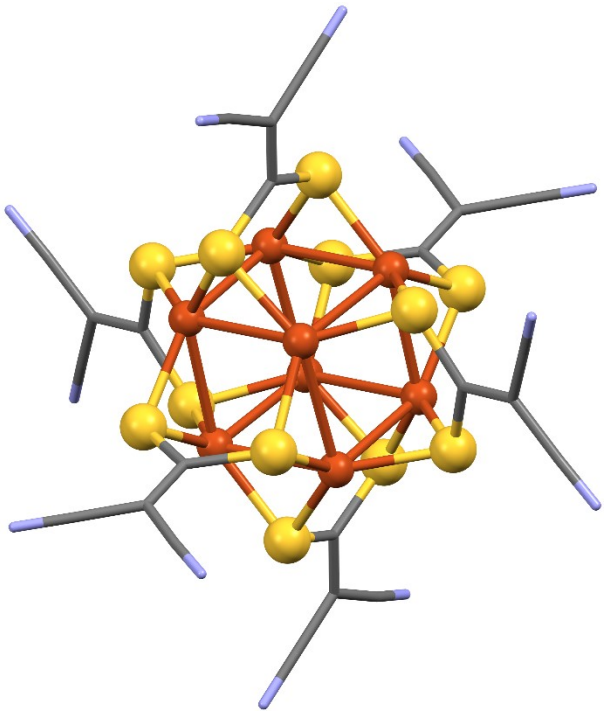

Figure 5.2 Molecular structure of the $[Cu_8(i\text{-mnt})_6]^{4-}$ (copper, orange; sulfur, pineapple; carbon, charcoal; nitrogen, cornflower).

The discovery of *i*-mnt^{2-} ligated Cu^{I} clusters[211] (Figure 5.2) resulted in a steady flow of research into 1,1-dithiolate clusters, but did not translate to concomitant research into Cu^{II} bis(dithiolene) species. $[Cu(i\text{-mnt})_2]^{2-}$ was used in research examining $\{Cu^{II}S_4\}$ complex quadrupole coupling constants[331] approximately the same time as more exhaustive EPR studies of the complex by Reinhard Kirmse.[332-334] These formed a starting point for comprehensive examinations of ligand exchange reactions[335,336] that took advantage of the possibility of isolating heteroleptic species of both Ni^{II} and Cu^{II} 1,1-dithiolates. Beyond this research proves scattered, with research sporadically yielding new Ni^{II} and Cu^{II} 1,1-dithiolate complexes.

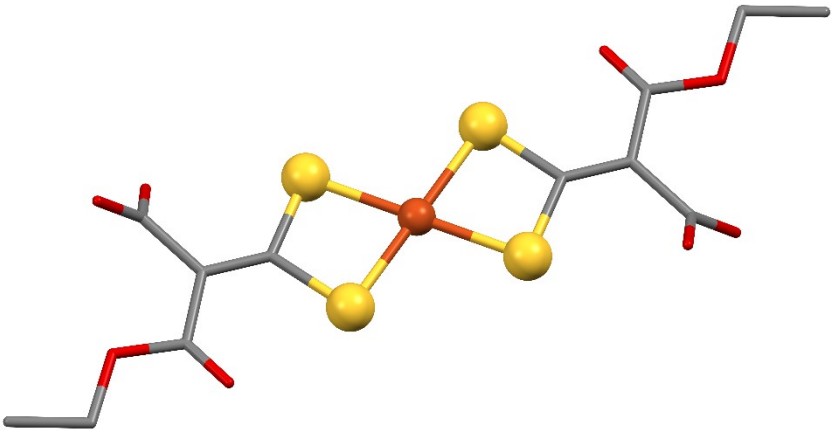

Figure 5.3 Molecular structure of $[Cu(ded)_2]^-$ (copper, orange; sulfur, pineapple; carbon, charcoal; oxygen, scarlet). Hydrogen atoms omitted for clarity.

Amongst the most interesting of these is ded^{2-}, which was used by Coucouvanis successfully isolate the rare oxidised $[Cu(ded)_2]^-$ (Figure 5.3) along with $[Ni(ded)_2]^{2-}$.[337] No further Cu^{III} 1,1-dithiolate species have been isolated, with only the Cu^{II} complexes of 1,3-diethiepin-2-carbodithiolate,[338] 1-cyano-1-chlorophenyl-2,2-ethylenedithiolato[245] and 2,7-di-tert-butylfluoren-9-ylidene[339] prepared.

The remaining research centred around the use of Ni^{II} and Cu^{II} 1,1-dithiolates as in organic conductors: *i*-mnt^{2-} and ded^{2-}complexes were research first,[340-343] followed by conductance studies of heterobimetallic salts with *i*-ect^{2-}, nmt^{2-} and bcd^{2-} (bcd^{2-} = 1-benzoyl-1-cyanoethene-2,2,-dithiolate) Ni^{II} and Cu^{II} complex components.[344-348]

As illustrated, Ni^{II} and Cu^{II} 1,1-dithiolate species are typically investigated jointly. There are some exceptions however, typically when the $Ni^{II}/Pd^{II}/Pt^{II}$ series is studied.[349,350] Other exceptions include Raman[351] and XES and XPS[352] spectroscopic studies, and research aimed at isolating heteroleptic 1,1-dithiolate species.[353,354] The final area of follows earlier research into 1,2-dithiolene charge transfer complexes,[355,356] studying the effect of counterions on the structure and conductivity of Ni^{II} 1,1-dithiolate complexes.[357,358] The information gained is aimed at rationalising lattice architectures,[359] aiding development of efficient catalysts for hydrogen production.[360]

The lack of more Ni-centric research is surprising given the huge avenues of studies that remain available, ranging from the isolation of adducts similar to those found in

comparable ligand systems[361,362] to examination of the geometric changes known to occur on going from 1,2- to 1,1-dithiolate systems (see Chapter 3).[90,92,93,217]

Research into both Ni^{II} and Cu^{II} 1,1-dithiolates has much appeal, providing opportunities to study a suite of 1,1-dithiolate complexes with clearly defined $\{MS_4\}$ coordination environments using spectroscopic methods not possible with the Co^{II} species: EPR and XAS measurements can be used jointly to obtain bonding parameter information. The Cu species offer the tantalising possibility of isolation new Cu^{III} species similar to $[Cu(ded)_2]^-$, with none of the non-innocence associated with comparable 1,2-dithiolate complexes. Finally, the spectroscopic data obtained should allow the effects of alterations to ligand substituents to be examined across the series, along with the effect of tighter S−M−S bite-angles against the likely increase in M−S bond length. All this will place the 1,1-dithiolate complexes in the broader field of $\{MS_4\}$ complexes.

5.2 Synthesis

All ligands used have been well studied and are discussed in detail in Chapter 3. Except for dts^{2-} all ligands used were 1,1-dithiolates (Figure 5.4); dts^{2-} was included as another point of comparison for the 1,1-dithiolate species.

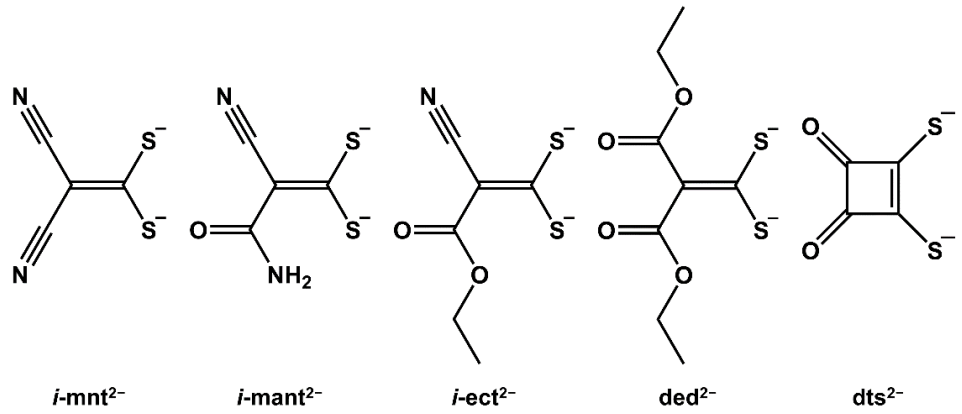

Figure 5.4 Dithiolate ligands and their abbreviations

5.2.1 1,1-Dithiolate Metal Complexes

Syntheses of the Cu^{II} 1,1-dithiolate complexes were performed in ambient conditions using similar synthetic methods. All reactions combined Cu^{II} and ligand salts along with a counterion (Figure 5.5), but differing product properties necessitated changes of solvents. The *i*-mnt^{2-} and *i*-$mant^{2-}$ species were prepared through combination of methanolic Cu^{II} and ligand solutions that were then filtered into a MeOH solution of the counterion. Cooling induced precipitation of the final product, with H_2O added to induce precipitation of $[Cu(i\text{-mant})_2]^{2-}$.

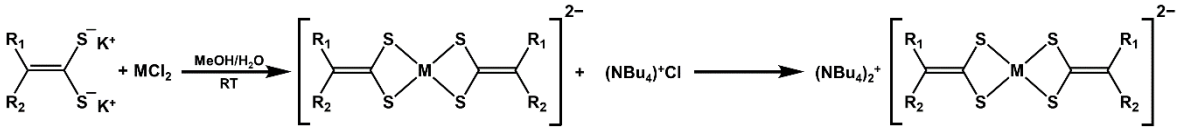

Figure 5.5 General reaction scheme for M^{II} bis(1,1-dithiolato) tetrabutylammonium salts.

Synthesis of $[Cu(i\text{-ect})_2]^{2-}$ required a 4:1 H_2O/MeOH mixture, with the combined solution filtered into an aqueous solution of the counterion to give the final product. A fully

aqueous medium was used to synthesise $[Cu(ded)_2]^{2-}$, with an intractable tarry substance forming if any alcohol was present. For the *i*-ect^{2-} and ded^{2-} Cu^{II} species the first stage required strict addition of the Cu^{II} salt to the ligand; the order is necessary as oxidised Cu^{III} species can form on addition of the ligands to the Cu^{II}, especially with *i*-ect^{2-} and ded^{2-} ligands. The Cu^{III} species are water-insoluble, so will be removed by the filtration before contaminating the final product. The Cu^{III} *i*-ect^{2-} and ded^{2-} species proved easy to isolate by reversing the order and adding the ligand salt to an excess of Cu^{II}. Addition of an appropriate counterion to the reaction mixture yielded the desired product.

The Ni^{II} 1,1-dithiolate complexes were synthesised using the same general procedures outlined above (Figure 5.5), with reaction conditions remaining consistent apart from changes in solvent media. Once again MeOH solutions were used for the *i*-mnt^{2-} and *i*-$mant^{2-}$ species, with H_2O inducing precipitation of the latter product. A mixed H_2O/MeOH medium was used to synthesise $[Ni(i\text{-}ect)_2]^{2-}$, whilst a fully aqueous medium was used for $[Ni(ded)_2]^{2-}$.

EPR spectroscopy was used to examine the Cu^{II} complexes (*vide infra*), whilst NMR provided structural information for the diamagnetic Ni^{II} species. ^{13}C NMR resonances from the two olefinic carbons occur at 60 ppm in all spectra, with NMR shifts corresponding to the CN carbons visible in the cyano-substituted ligands at 119 ppm. C=O shifts are also visible in the complexes with amide-[224] and ester-substituents[225] at 165 ppm, with $[Ni(i\text{-}ect)_2]^{2-}$ and $[Ni(ded)_2]^{2-}$ showing further features at 92 and 15, and 77 and 15 ppm, corresponding to the methylene and methyl groups, respectively.[221,222] All spectra also show ^{13}C NMR resonances corresponding to the $(N^nBu_4)^+$ counterions[363] are visible at 59, 24, 20 and 14 ppm.

The ^1H NMR spectra are comparable to those of the free ligands: $[Ni(i\text{-}mant)_2]^{2-}$ has a sole doublet at 2.23 ppm corresponding to the $-NH_2$ substituents, whilst the spectra of $[Ni(i\text{-}ect)_2]^{2-}$ and $[Ni(ded)_2]^{2-}$ remain similar with features corresponding to the ester ethyl groups visible in both spectra. All compounds show the ^1H NMR shifts of the $(N^nBu_4)^+$ counterions.

ESI-MS, IR and electronic spectroscopy were used to prove the formation of the desired product, with the mass spectra showing $[M-NBu_4]^-$ *m*/*z* peaks for all the complexes. The IR spectra are worth discussing briefly as they show clear trends; IR data of interest is given in Table 5.1, with the complete data available in the experimental section.

As is typical of 1,1-dithiolate ligand systems,[82,211,330,343,357] both the Cu^{II} and Ni^{II} complexes show characteristics bands between 1300 and 1400 cm^{-1} and 880 and 950 cm^{-1} assigned to v(C=C) and symmetric v(C−S) IR stretches, respectively.[218]The *i*-mnt^{2-}, *i*-$mant^{2-}$ and *i*-ect^{2-} ligated species also show stretches close to 2200 cm^{-1} typical of v(CN), whilst along with the ded^{2-} complexes, the latter two systems show stretches near 1650 cm^{-1} corresponding to v(C=O). The stretches are consistent with those reported[82,211,245] and confirm non-involvement of the CN and C=O groups in metal coordination.[347]

Table 5.1 Selected IR data for Cu^{II} and Ni^{II} 1,1-dithiolate complexes.

	v(CN)	**v(C=O)**	**v(C−O)**	**v(C=C)**	**v(C−S)**
$[Cu(i\text{-}mnt)_2]^{2-}$	2195			1396	912
$[Cu(i\text{-}mant)_2]^{2-}$	2191	1638		1375	914
$[Cu(i\text{-}ect)_2]^{2-}$	2176	1661	1636	1346	930
$[Cu(ded)_2]^{2-}$		1646	1580	1330	944
$[Ni(i\text{-}mnt)_2]^{2-}$	2195			1400	887
$[Ni(i\text{-}mant)_2]^{2-}$	2193	1639		1371	912
$[Ni(i\text{-}ect)_2]^{2-}$	2190	1678	1630	1353	922
$[Ni(ded)_2]^{2-}$		1661	1553	1321	923

Clear trends in the IR stretching energies are visible, with substituent stretching energies decreasing as v(C−S) increases. Consideration of the ligand substituent Hammett parameters (σ_P) discussed in Chapter 3 (Table 3.4) clarifies the origin of the trend, with the relationship between the energy of the C−S stretch and that of the C=C and substituent bonds reflect the ligand π-donor ability as determined by the total σ_P: with the highest total σ_P *i*-mnt^{2-} is the weakest π-donor.

5.3 Results and Discussion

5.3.1 Crystal Structures

Diffraction quality crystals of $(NBu_4)_2[Cu(i\text{-}mnt)_2]$ were grown through slow evaporation of an acetonitrile solution of the complex; $(PPh_4)_2[Cu(dts)_2]$ by cooling a saturated acetone solution of the complex to −35 °C. The molecular structure of the $[Cu(dts)_2]^{2-}$ is illustrated in Figure 5.6; selected bond lengths and angles are listed in Table 5.2. The complex consists of a discrete monometallic $\{CuS_4\}$ moiety where the central Cu ion is surrounded by four sulfurs from two bidentate dithiosquarato ligands; the charge of the complex is balanced by two PPh_4^+ counterions.

Crystal twinning made solution of the structure challenging, with a lowest *w*R2 value of 0.4749. Despite this, the parameters for the immediate $\{CuS_4\}$ coordination sphere could be obtained with an acceptable degree of certainty. This fact, and the existence of satisfactory baseline data,[233] gave enough information to warrant inclusion for comparison with $[Cu(i\text{-}mnt)_2]^{2-}$.

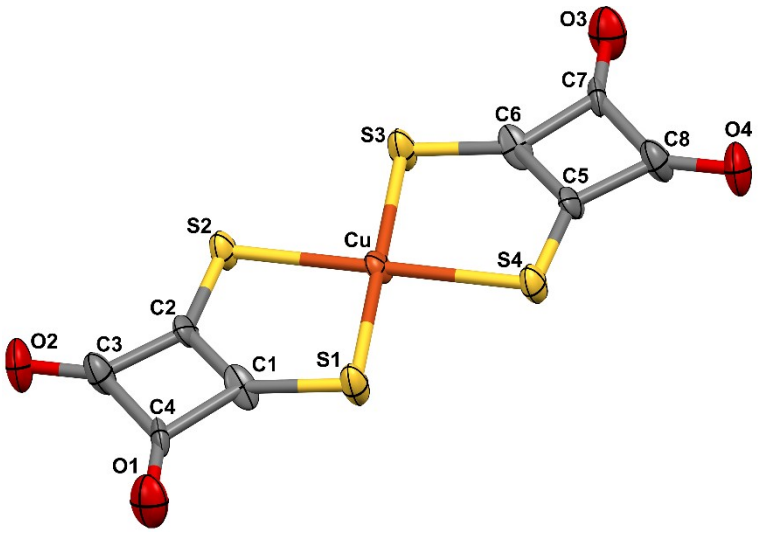

Figure 5.6 Structure of the anion in crystals of $(PPh_4)_2[Cu(dts)_2]$. Thermal ellipsoids are shown at the 50% probability level.

The mean $\{CuS_2\}$ planes are parallel which in combination with the dts^{2-} bite-angle results in a distorted square-planar $\{CuS_4\}$ coordination environment; the S−Cu−S bite-angles of 93.34(1)° and 93.27(2)° place the distortion away from D_{4h} toward D_{2h}. The bite-

angles are ~4.5° more acute than those of 96.64(2)° and 97.50(2)° observed in the D_{2d} $[Co(dts)_2]^{2-}$ due to the formation of an extended π-system in the planar Cu^{II} complex. This delocalises electron density throughout the complex, increasing the electron density in the M−S bonds; the shorter M−S bond lengths in turn decrease the metal-ligand bite-angles.

The Cu−S and C−S bond lengths confirm the effect of the extended π-system: the bond lengths are on average 0.023 and 0.019 Å shorter in $[Cu(dts)_2]^{2-}$ than in the analogous Co complex, confirming the increased bond electron density in the latter species. The bond lengths decrease such the C−S bond lengths are ca. 0.005 Å shorter than in the free ligand. No other bond lengths have a high enough level of accuracy to allow further comparisons, but data obtained by Strauch et al. reveals a general decrease in bond lengths throughout the complex; the reported crystal data uses a different benzytributylammonium counterion, noting that changing the cation had little effect on structural properties.[233]

Table 5.2 Selected Bond Distances (Å) and Angles (°) in $(PPh_4)_2[Cu(dts)_2]$

Cu−S1	2.323(4)	Cu−S2	2.309(4)	Cu−S3	2.312(4)
Cu−S4	2.331(4)	C1−S1	1.668(2)	C2−S2	1.659(2)
C6−S3	1.724(2)	C5−S4	1.666(2)	C4−O1	1.20(2)
C3−O2	1.19(2)	C7−O3	1.178(2)	C8−O4	1.18(2)
C1−C2	1.41(2)	C3−C4	1.54(2)	C5−C6	1.40(2)
C5−C6	1.40(2)	C1−C4	1.49(2)	C2−C3	1.51(2)
C5−C8	1.47(2)	C6−C7	1.47(2)		
S1−Cu−S2	93.34(1)	S3−Cu−S4	93.27(2)	S1−Cu−S4	86.73(2)
S1−Cu−S4	86.73(2)	S1−C1−C2	125.7(1)	S2−C2−C1	126.4(1)
S3−C6−C5	124.0(1)	S4−C5−C6	127.3(1)	O1−C1−C2	134.9(1)
O2−C3−C4	137.9(1)	O3−C8−C7	136.2(1)	O4−C7−C8	135.2(1)

The molecular structure of $[Cu(i\text{-mnt})_2]^{2-}$ is illustrated in Figure 5.7; selected bond lengths and angles are listed in Table 5.3. The complex consists of a discrete monometallic $\{CuS_4\}$ moiety where the central Cu ion is surrounded by four sulfurs from two bidentate *iso*-maleonitriledithiolato ligands; the charge of the complex is balanced by two $N^nBu_4^+$ counterions. The structure of the $[Cu(i\text{-mnt})_2]^{2-}$ was the sole structure of a 1,1-dithiolate

complex isolated here and matches the data previously reported, proving the couterion has no effect on the Cu^{II} coordination environment.

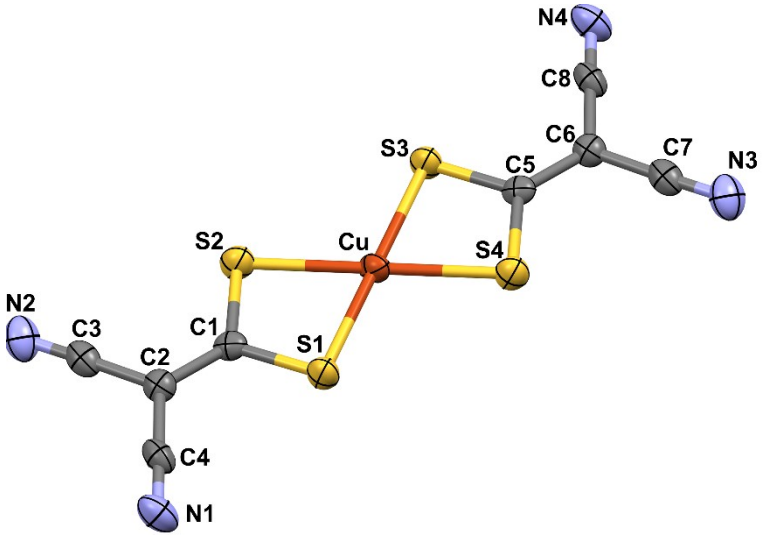

Figure 5.7 Structure of the anion in crystals of $(PPh_4)_2[Cu(i\text{-}mnt)_2]$. Thermal ellipsoids are shown at the 50% probability level.

The mean $\{CuS_2\}$ planes are parallel which in combination with the *i*-mnt^{2-} bite-angle results in a distorted square-planar $\{CuS_4\}$ coordination environment, with the S−Cu−S bite-angles of 76.83(2)° and 103.17(2)° resulting in a D_{2h} coordination environment. The S−Cu−S bite-angles are distorted almost 10° more away from ideal D_{4h} than the 1,2-dithiolate ligated $[Cu(dts)_2]^{2-}$ system, a change stemming from the shift from a five- to four-membered ring. Despite the more acute metal-ligand bite-angles, at 2.309(1) Å the average Cu−S bond lengths in $[Cu(i\text{-}mnt)_2]^{2-}$ are close to the average of 2.319(4) Å reported for $[Cu(dts)_2]^{2-}$. The bond length consistency likely stems from the greater electron-withdrawing strength of the cyano- substituents in *i*-mnt^{2-} reducing the S electron density relative to dts^{2-}; the effect of S atom proximity is thus offset by the changing electron density.

Similar deviations from ideal D_{4h} are observed on moving from $[Cu(mnt)_2]^{2-}$ to $[Cu(i\text{-}mnt)_2]^{2-}$, with the S−Cu−S bite-angles decreasing from 88.6(1)° to 76.83(2)° and Cu−S lengths increasing from 2.163(3) to 2.309(1) Å.[364]

Table 5.3 Selected Bond Distances (Å) and Angles (°) in $(NBu_4)_2[Co(i\text{-}mnt)_2]$

Cu−S1	2.2992(6)	Cu−S2	2.3183(6)
C1−S2	1.728(2)	C1−S2	1.728(2)
C1−C2	1.374(3)	C2−C3	1.428(3)
C2−C4	1.431(3)	C3−N2	1.149(3)
C4−N1	1.147(3)		
S1−Cu−S2	76.83(2)	S1−Cu−S4	103.17(2)
C3−C2−C4	116.8(2)		

At 2.299(1) and 2.318(1) Å the Cu−S bond lengths are also ~0.1 Å longer than the Cu−S lengths of 2.195(1) and 2.213(1) Å reported for $[Cu(ccpd)_2]^{2-}$ (ccpd = 1-cyano-1-chlorophenyl-2,2-ethenedithiolate).[245] The longer bond lengths in $[Cu(i\text{-}mnt)_2]^{2-}$ are accompanied by increased distortion towards D_{2h}, with S−Cu−S angles of 76.83(2)° compared to 78.39(2)° for $[Cu(i\text{-}mnt)_2]^{2-}$ and $[Cu(ccpd)_2]^{2-}$, respectively.[245] An identical trend is observed on going from $[Cu(i\text{-}mnt)_2]^{2-}$ to $[Ni(i\text{-}mnt)_2]^{2-}$, with ~0.1 Å shorter M−S bond lengths of 2.215(1) and 2.202(1) Å reported for the latter complex.[365] The Ni complex is similarly less distorted away from the ideal D_{4h}, with S−M−S angles of 78.82(2)° and 101.18(2)° approximately 2° less distorted than those in $[Cu(i\text{-}mnt)_2]^{2-}$.[365]

The series provides clear insight into the effect of changing metal ion and ligand systems: replacing $i\text{-}mnt^{2-}$ with a stronger π-donor ligand[245] or the Cu^{II} ion with an electron-deficient metal ion[365] leads to a decrease M−S bond lengths accompanied by increases in metal-ligand bite-angles.

5.3.2 Electronic Absorption Spectroscopy of Cu 1,1-Dithiolates

Electronic spectra of the Cu^{II} 1,1-dithiolate complexes are overlaid in Figure 5.8. The spectra of all the Cu^{II} complexes are comparable, with intense LMCT bands from fully-occupied orbitals centred on the anionic S atoms on the ligands to the vacant orbital on the Cu^{II} ion illustrated in Figure 5.9 dominating the higher energy regions. LF transitions are observed between 600 and 700 nm. The $[Cu(i\text{-mnt})_2]^{2-}$ spectra matches that described by Werden *et al*.,[82] but unlike the Co^{II} complexes there are significant differences in the LMCT band profiles across the series. These are due to solution effects from the different solvent shells around the rigidly square planar Cu^{II} species.

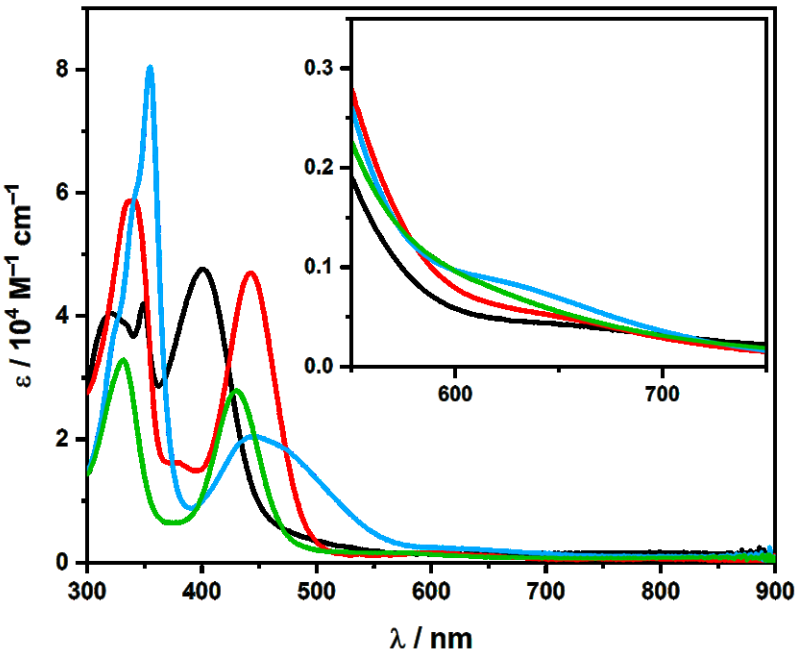

Figure 5.8 Overlay of the electronic spectra of $[Cu(i\text{-mnt})_2]^{2-}$ (black), $[Cu(i\text{-mant})_2]^{2-}$ (red), $[Cu(i\text{-ect})_2]^{2-}$ (blue) and $[Cu(ded)_2]^{2-}$ (green); inset shows an expansion of the LF transitions.

The spectral parameters of the $^1A_{1g} \rightarrow {}^1B_{1g}$ transition provide insight into the Cu^{II} electronic structures, with collated data show in Table 5.4. Although higher in energy and intensity than comparable 1,2-dithiolate complexes,[366,367] the LF transitions are typical of square-planar Cu^{II} complexes and similar to those previously reported for Cu^{II} 1,1-dithiolates.[82,104,245] $^1A_{1g} \rightarrow {}^1B_{1g}$ transition in Cu^{II} dithiocarbamate complexes occur at higher

energies and intensities,[368] illustrating the effect of the {CuS_4} coordination environment on the LF.

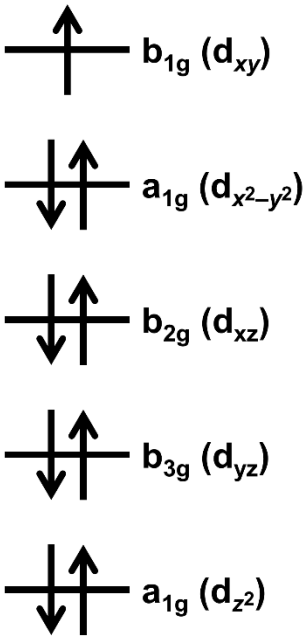

Figure 5.9 Crystal-Field Splitting of a Cu^{II} 1,1-dithiolate complex in a D_{2h} coordination environment.

As with the Co^{II} complexes discussed in Chapter 3, the Cu^{II} 1,1-dithiolate the LF transition energies and intensities increase as total σ_P decreases. This is due to the greater M−L interaction in the systems with stronger S π-donors, which strengthen the LF as the ligand inductive ability weakens. The increase in intensity observed as σ_P decreases is due to the greater {CuS_4} moiety electron density leading to increased mixing of ground and excited states.

Table 5.4 Spectral parameters of the $^1A_{1g} \rightarrow {}^1B_{1g}$ transition

	λ_{max} / nm	ε_{max} / M^{-1} cm^{-1}
$[Cu(i\text{-mnt})_2]^{2-}$	658	555
$[Cu(i\text{-mant})_2]^{2-}$	649	718
$[Cu(i\text{-ect})_2]^{2-}$	631	812
$[Cu(ded)_2]^{2-}$	607	889

As oxidised $[Cu(ded)_2]^-$ had been previously reported[337] the possibility of isolating Cu^{III} species of the other 1,1-dithiolate complexes was investigated. The only species successfully isolated was $[Cu(i\text{-ect})_2]^-$, prepared using an excess of $CuCl_2$ or I_2 as an oxidant. The electronic spectra of $[Cu(i\text{-ect})_2]^{2-}$ and $[Cu(i\text{-ect})_2]^-$ are overlaid in Figure 5.10.

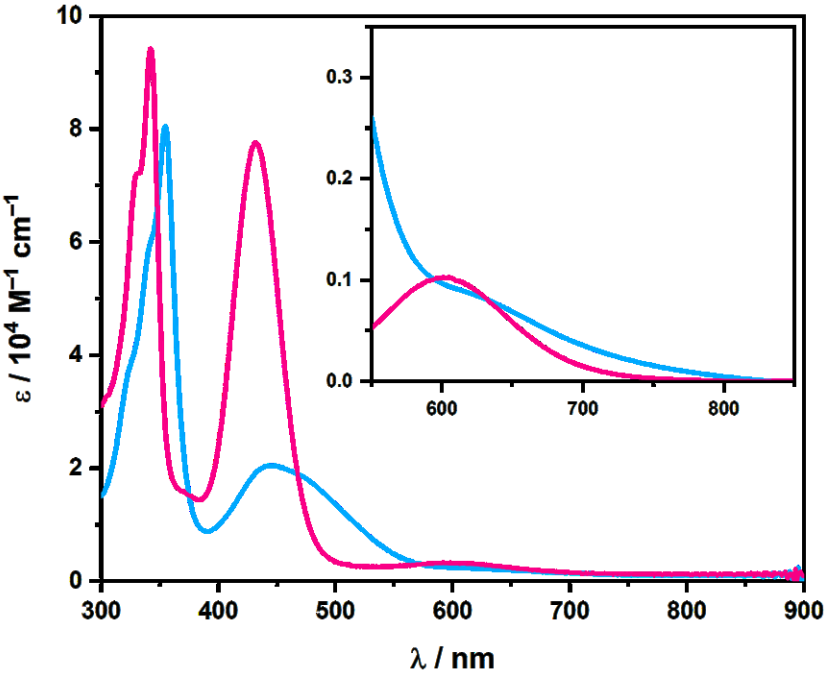

Figure 5.10 Overlay of the electronic spectra of $[Cu(i\text{-ect})_2]^{2-}$ (blue) and $[Cu(i\text{-ect})_2]^-$ (magenta); inset shows an expansion of the.

The spectra confirm the formation of $[Cu(i\text{-ect})_2]^-$, with the energy and intensity of the lower energy LMCT increasing dramatically due to the increased vacancy in the Cu d-orbitals. The LF transition energy also decreases by 27 nm, with the absence of overlapping LMCT features present in $[Cu(i\text{-ect})_2]^{2-}$ increasing the transition visibility. The change in LF transition shows both the increased influence of the $i\text{-ect}^{2-}$ ligands on the oxidised Cu^{III} LF, and the greater mixing of ground- and excited-states facilitated by the increased Cu d-orbital vacancy.

5.3.3 Electrochemistry of Cu^{II} 1,1-Dithiolates

Reversible one-electron electrochemical redox events in $[Cu(i\text{-mnt})_2]^{2-}$ and $[Cu(ded)_2]^{2-}$ have been reported before by Dietzsch[336] and Hollander *et al.*,[90]. The cyclic voltammograms (CVs) of all complexes have therefore been re-examined under standardised conditions of CH_2Cl_2 solutions containing 0.1 M $(N^nBu_4)PF_6$ as a supporting electrolyte at a glassy carbon working electrode and a scan rate of 100 mV s^{-1} at 293 K. All potentials are referenced against the ferrocenium/ferrocene ($Fc^{+/0}$) couple as internal standard.

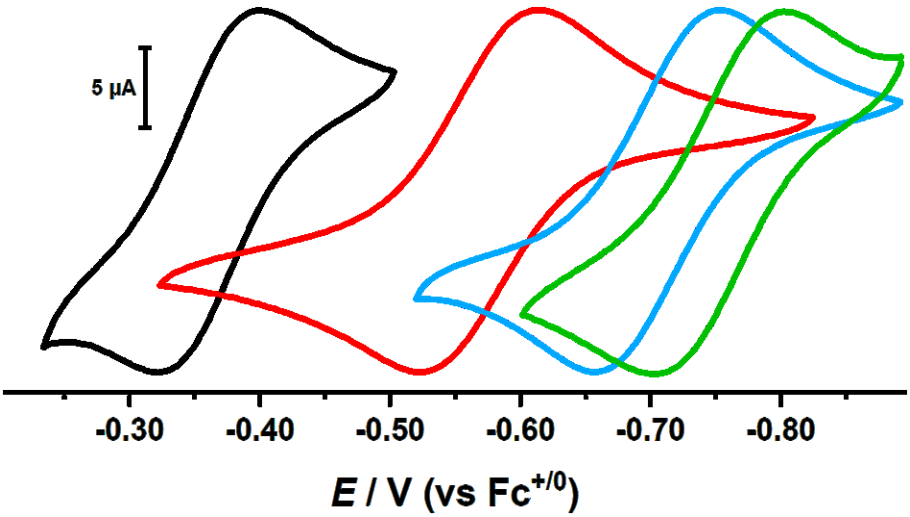

Figure 5.11 Overlay of the $Cu^{II/III}$ redox couples of $[Cu(i\text{-mnt})_2]^{2-}$ (black), $[Cu(i\text{-mant})_2]^{2-}$ (red), $[Cu(i\text{-ect})_2]^{2-}$ (blue) and $[Cu(ded)_2]^{2-}$ (green); all measurements in CH_2Cl_2 at 293 K; 0.10 M $(N^nBu_4)PF_6$; scan rate 100 mV s^{-1}; glassy carbon working electrode; platinum auxiliary electrode; Ag/AgCl reference electrode.

The resulting CVs are shown in Figure 5.11 with oxidation event potentials listed in Table 5.5; full CVs at 100 mV s^{-1} and CVs of the reversible redox event at scan rates between 50 and 500 mV s^{-1} are available in Appendices 8.17 and 8.18. All Cu^{II} 1,1-dithiolate complexes show a feature corresponding to a reversible one-electron oxidation event. Oxidised $[Cu(i\text{-ect})_2]^-$ and $[Cu(ded)_2]^-$ were successfully isolated, with their EPR silent nature indicating the $Cu^{II} \rightarrow Cu^{III} + e^-$ nature of the oxidation event.

Table 5.5 Reduction Potentials for Cu^{II} 1,1-Dithiolates (V versus $Fc^{+/0}$).

	$E_{1/2}$	E_{pc}
$[Cu(i\text{-mnt})_2]^{2-}$	−0.36	−0.40
$[Cu(i\text{-mant})_2]^{2-}$	−0.57	−0.53
$[Cu(i\text{-ect})_2]^{2-}$	−0.71	−0.66
$[Cu(ded)_2]^{2-}$	−0.75	−0.70

The position of the redox feature correlates with total σ_P of the ligand substituents. While it is observed at −400 mV in $[Cu(i\text{-mnt})_2]^{2-}$, it shifts to more negative potentials as total σ_P decreases, with oxidation correspondingly easier. The potentials for $[Cu(i\text{-mant})_2]^{2-}$, $[Cu(i\text{-ect})_2]^{2-}$ and $[Cu(ded)_2]^{2-}$ are −530, −660 and −700 mV, respectively. The trend reflects the increase in π-donor strength as total σ_P decreases, with the π-donors destabilising the $^2B_{1g}$ MO, facilitating oxidation.

5.3.4 EPR Spectroscopy of Cu^{II} 1,1-Dithiolates

Electron paramagnetic (spin) resonance (EPR) spectroscopy is used to probe the electronic structure of species with unpaired electrons. In the presence of an external magnetic field (*H*) the energy difference between electrons aligned parallel and antiparallel to *H* leads to the separation of the energy levels of the electronic term (*S*); this is known as Zeeman splitting (Figure 5.12).

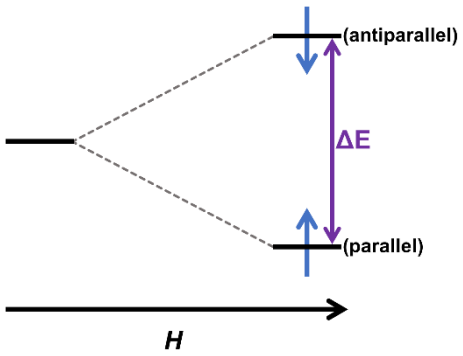

Figure 5.12 Representation of the energy difference (ΔE = *h*ν) of caused by Zeeman splitting in a magnetic field (*H*).

EPR is based on the resonant absorption of microwave radiation stemming from the transitions between the split energy levels, with continuous wave (cw) EPR measured keeping the microwave frequency is constant and varying *H*. The microwave absorption is recorded, and the first derivative of absorbance plotted against *H*; plotting the derivative improves the signal-to-noise ratio and spectral resolution. Several different microwave frequencies (bands) are used in EPR (Table 5.6).

Table 5.6 Parameters of common microwave bands used in EPR.

Microwave band	Frequency[a] / × 10^9 Hz	Field[b] / T	Waveguide Dimension[c] / mm
L	1.0	0.036	196 × 98
S	3.5	0.13	72 × 34
X	9.5	0.34	23 × 10
Q	34	1.21	4.7 × 2.8
W	95	3.4	2.5 × 1.3

[a] Typical frequency: within each band a range of frequencies are used; [b] Field in units of Tesla for *g* = 2.0023; [c] Approximate dimensions.

The *g*-value is related to the energy difference between the two spin states (ΔE in Figure 5.12) and the strength of, $\vec{H}$ is as shown in Equation 5.1 where *h* is the Planck constant, *v* is the microwave radiation frequency and μ_B is the Bohr magneton.

$$\Delta E = hv = g\mu_B\vec{H} \tag{5.1}$$

The *g*-value is a dimensionless parameter corresponding to the magnetic field strength where the microwave frequency and spin-state energy gap are in resonance. The *g*-value for a free electron in a vacuum, g_e, is 2.0023, with *g* in transition metal compounds varying due to zero-field splitting and spin-orbit coupling effects (*vide supra*).[369] The *g*-value is independent of the measurement microwave frequency. Further splitting of the m_s states known as hyperfine splitting (*A*-matrix) arises from interactions between nuclear magnetic moment and the magnetic field of the electron. The dipole-dipole interaction perturbs the energy levels of transition metal complexes and can be used to determine the position of the unpaired electron in the metal d orbitals, showing the extent the electron associates with each d orbital. Interaction of the unpaired electrons with the surrounding nuclei can lead to further splitting of the energy levels called hyperfine splitting.

Appropriate assessment of the *g*- and *A*-matrices of the EPR spectrum allow derivation of detailed information about the symmetry and electronic environments metal centres. Cu^{II} is an EPR active $S = {}^1/_2$ ion, allowing probing of the structures of the Cu 1,2- and 1,1-dithiolate species, which can then be compared to the large volume of data available about similar species. Two natural Cu isotopes exist: ^{63}Cu and ^{65}Cu with respective abundancies of 69 and 31%. Both isotopes have a nuclear spin, *I*, of $^3/_2$, with the overall energy of the system defined by the Hamiltonian defined in Equation 5.2.

$$\hat{H} = \mu_B S g\overrightarrow{H} + IAS \tag{5.2}$$

The relationship allows *g* and *A* to be derived using EPR. To this end both the fluid and frozen spectra were measured, from which the isotropic and anisotropic values of *g* and *A* were obtained. In the anisotropic frozen spectra, it was assumed *g* and *A* have the same principle axis, with the spin-Hamiltonian written as Equation 5.3; the expanded form is given in Equation 5.4. μ_B is the Bohr magneton, $\vec{H}$ is the magnetic field, and $\vec{S}$ and $\vec{I}$ are the electron and nuclear spin operators, respectively.

$$\hat{H} = \mu_B \vec{S}\boldsymbol{g}\vec{H} + \vec{I}\boldsymbol{A}\vec{S} \tag{5.3}$$

$$\hat{H} = \mu_B \left(g_x S_x H_x + g_y S_y H_y + g_z S_z H_z \right) + A_x I_x S_x + A_y I_y S_y + A_z I_z S_z \tag{5.4}$$

The principle values of *g* (g_x, g_y, g_z) and *A* (A_x, A_y, A_z) are obtained through analysis of the data. In the fluid solution the *g*- and *A*-values are the isotropic values of the complex, with $g_{iso} \approx \langle g \rangle$ and $A_{iso} \approx \langle A \rangle$, representing the sum of all three directions of the *g*- and *A*-matrices, Equations 5.5 and 5.6.

$$\langle g \rangle = \frac{\left(g_x + g_y + g_z \right)}{3} \tag{5.5}$$

$$\langle A \rangle = \frac{\left(A_x + A_y + A_z \right)}{3} \tag{5.6}$$

The room temperature the EPR spectra of $[Cu(i\text{-mnt})_2]^{2-}$ and $[Cu(i\text{-mant})_2]^{2-}$ were recorded in acetone, and the spectra of $[Cu(i\text{-ect})_2]^{2-}$ and $[Cu(ded)_2]^{2-}$ in $CHCl_3$, as was the 1,2-dithiolate complex $[Cu(dts)_2]^{2-}$. The frozen solutions were all measured at 130 K in CH_2Cl_2, with four drops of DMF added to 1 mL of the CH_2Cl_2 solution of each complex to aid glassing.

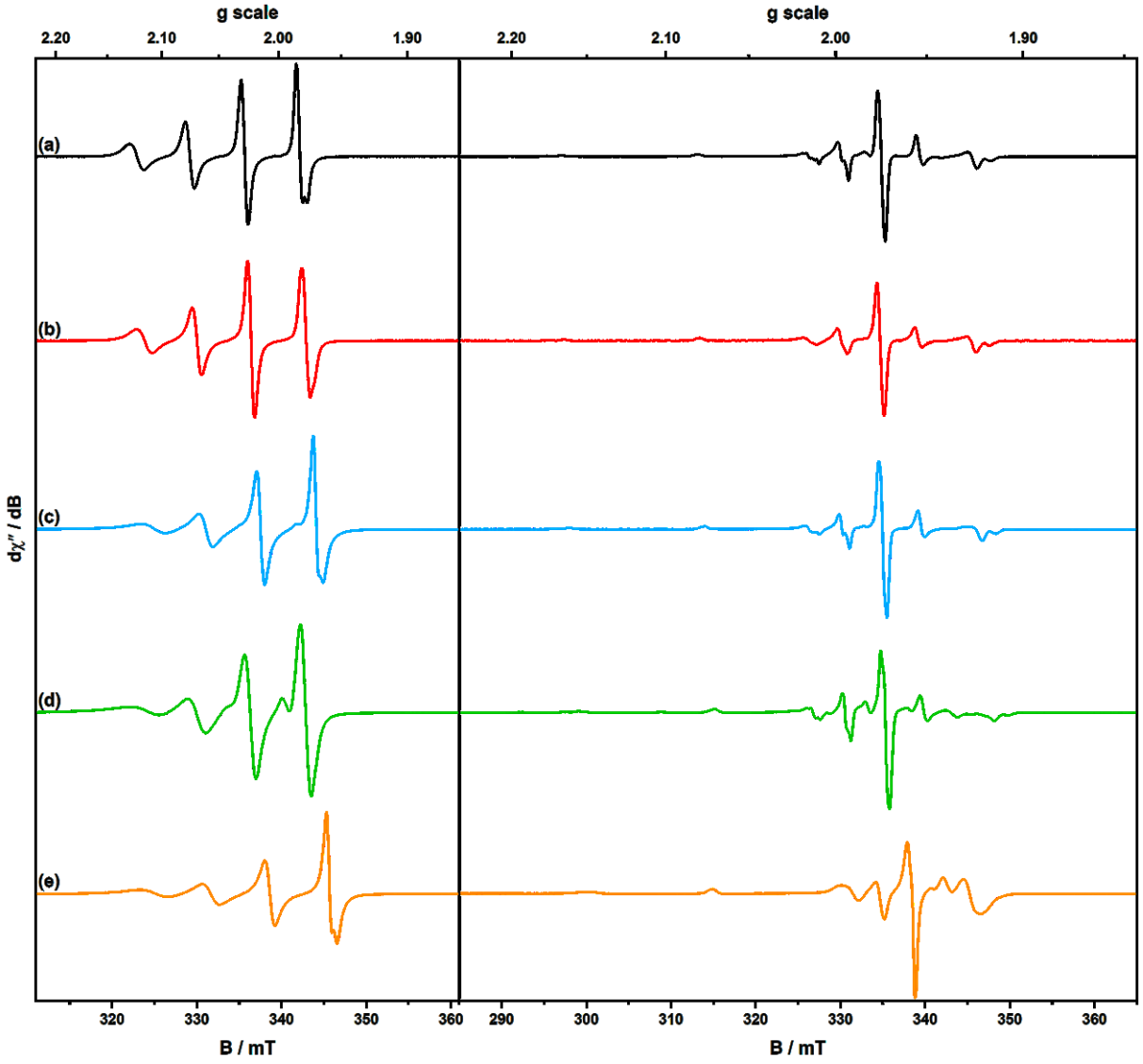

Figure 5.13 Comparison of the X-band EPR spectra of (a) $[Cu(i\text{-mnt})_2]^{2-}$, (b) $[Cu(i\text{-mant})_2]^{2-}$, (c) $[Cu(i\text{-ect})_2]^{2-}$, (d) $[Cu(ded)_2]^{2-}$ and (e) $[Cu(dts)_2]^{2-}$, recorded at 293 K (left panel) and 130 K (right panel).

Stacked EPR spectra of the Cu^{II} complexes are shown in Figure 5.13, with, spin Hamiltonian parameters collated in Table 5.7; full experimental and simulated spectra and experimental details are available in Appendices 8.15 and 8.16. Except for $[Cu(ded)_2]^{2-}$, the hyperfine and *g*-tensors are orthorhombic due to distortion of symmetries away from D_{4h} caused by < 90° ligand bite-angles and variation in Cu−S bond lengths. The distortions split the d_{xz} and d_{yz} orbitals, resulting in a non-axial EPR spectra.[370] As crystal structures of the Cu^{III} analogue confirm the D_{2h} coordination environment in $[Cu(ded)_2]^{2-}$,[90] the axial EPR spectrum will be due to minor structural distortions of the molecule in the frozen glass.

Table 5.7 Spin Hamiltonian parameters determined from solution and solid EPR measurements.

	g_{iso}	g_x	g_y	g_z	A_{iso}[a]	A_x[a]	A_y[a]	A_z[a]
$[Cu(i\text{-mnt})_2]^{2-}$	2.0451	2.017	2.021	2.094	72.3	33.0	40.0	155.8
$[Cu(i\text{-mant})_2]^{2-}$	2.0441	2.018	2.022	2.0935	71.7	34.0	34.0	157.5
$[Cu(i\text{-ect})_2]^{2-}$	2.0420	2.0151	2.021	2.089	71.6	34.0	34.0	157.5
$[Cu(ded)_2]^{2-}$	2.0410	2.018	2.018	2.082	71.0	40.0	40.0	159.0
$[Cu(dts)_2]^{2-}$	2.0595	2.029	2.025	2.1225	65.7	32.0	32.0	143.0

[a] $\times 10^{-4}$ cm^{-1}

The spin Hamiltonian parameters of the 1,1-dithiolate complexes are comparable to those reported for 1,1-dithiolates[104,338] and dithiocarbamates,[370,371] and close to those for 1,2-dithiolates.[233,372,373] The values for $[Cu(dts)_2]^{2-}$ are comparable to those reported.[233] Using a Gouy balance respective magnet moments of μ_{eff} = 1.78, 1.76, 1.71 and 1.70 were calculated for $[Cu(i\text{-mnt})_2]^{2-}$, $[Cu(i\text{-mant})_2]^{2-}$, $[Cu(i\text{-ect})_2]^{2-}$ and $[Cu(ded)_2]^{2-}$, with the resulting *g*-values of 2.00 ± 5% comparable to those determined by EPR.

The distortions of $\{CuS_4\}$ symmetry away from D_{4h} toward D_{2h} in the 1,1-dithiolate complexes (*vide supra*) are also reflected in the EPR spectra. Crystal field calculations for $\{Cu^{II}S_4\}$ systems with D_{2h} symmetry give a $^2B_{1g}$ ground state,[374] which research into Cu^{II} bis(dithiocarbamate) complexes typically considers x^2-y^2.[375] Examination of dianionic 1,1-dithiolate systems reveals there to be an xy ground state, however,[82] the same as in the D_{4h} Cu^{II} 1,2-dithiolate systems,[372] illustrating the additional importance of the ligand charge in determining the electronic ground state.

Information from the EPR spectra of the Cu^{II} complexes can be derived using two methods. The first of these uses a basis set of the d atomic orbitals, with spin-delocalisation accounted for through reductions in the spin-orbit coupling parameter, ξ, and average inverse cube electron-nuclear distance, r^{-3}, with the base value of these parameters deduced from the electronic spectra of the free ion. This approach was first promulgated by Griffith for d^n strong field complexes,[376] then developed further by Maki and co-workers using a basis set of real d-orbitals.[377] As done here, the method assumes as d_{xy} ground state for Cu^{II} complexes and for simplicity neglects any rhombicity, obtaining $g_\perp$ and $A_\perp$ from the median of x and y values. The *g* and *A* values are then related to the dipolar hyperfine

coupling parameter, P, and Fermi contact term, k, configurational excitation energies, φ, with the relationship defined by Equations 5.7 through 5.10.

$$g_{\perp} = 2 - 2\varphi_2 \tag{5.7}$$

$$g_{\parallel} = 2 - 8\varphi_1 \tag{5.8}$$

$$A_{\perp} = P\left[-2\varphi_2 - k + \frac{2}{7} + \frac{3}{7}\varphi_2\right] \tag{5.9}$$

$$A_{\perp} = P\left[-8\varphi_1 - k + \frac{4}{7} + \frac{3}{7}(2\varphi_2)\right] \tag{5.10}$$

P is defined by Equation 5.11, where g_e and g_N are the electronic and nuclear g-factors, μ_B and μ_N are the Bohr and nuclear magnetons, and $(r^{-3})_{av}$ the averaged value of r^{-3} of the radial wave functions, in this case for a free Cu^{II} ion.[378,379]

$$P = g_e g_N \mu_B \mu_N \left(r^{-3}\right)_{av} \tag{5.11}$$

Historically the values of $(r^{-3})_{av}$ and turn P_0 were obtained using the Hartree-Fock calculations of Freeman and Watson,[380] but as a standard of $P_0 = 360 \times 10^{-4}$ cm^{-1} was measured,[375] this is used here. The values of φ_1 and φ_2 obtained for each complex using the averaged $g_{\perp}$ and $g_{\parallel}$ in Equations 5.7 and 5.8 are collated in Table 5.8, along with the equations determining the relationship of P (in cm^{-1}) and k (in units of P) to $A_{\parallel}$ and $A_{\perp}$ obtained from Equation 5.9 and 5.10.

Table 5.8 Configurational excitation energies and bonding parameters of the Cu^{II} Dithiolates.

	$^{a}\varphi_1$	$^{a}\varphi_2$	$A_\perp$	$A_\parallel$
$[Cu(i\text{-mnt})_2]^{2-}$	−23.75	−470.0	$P(0.3999-k)$	$P(-0.5121-k)$
$[Cu(i\text{-mant})_2]^{2-}$	−25.00	−467.5	$P(0.3592-k)$	$P(-0.5114-k)$
$[Cu(i\text{-ect})_2]^{2-}$	−26.26	−445.0	$P(0.3556-k)$	$P(-0.5152-k)$
$[Cu(ded)_2]^{2-}$	−22.50	−410.0	$P(0.3501-k)$	$P(-0.5183-k)$
$[Cu(dts)_2]^{2-}$	−33.75	−562.5	$P(0.3741-k)$	$P(-0.4962-k)$

[a] × 10^{-4} cm^{-1}

The observed hyperfine coupling constant in solution (ca. 70 × 10^{-4} cm^{-1}) is only consistent with A_x, A_y and A_z of the same sign, and as $|A_z| \gg |A_x|,|A_y|$, the sign of each must be negative (P is positive for $^{63,65}Cu$).[377] Solution of the simultaneous equations derived for $A_\parallel$ and $A_\perp$ generates values of k and P for each complex, with the latter parameter compared to the value of ca. 360 × 10^{-4} cm^{-1} for the free ion P_0.[375] The ratio between the two is given alongside k in Table 5.9.

Table 5.9 Salient parameters for bond covalency of Cu^{II} dithiolate species

	$g_\parallel$	$g_\perp$	$A_\parallel{}^{a}$	$A_\perp{}^{a}$	P/P_0	k	Reference
$[Cu(i\text{-mnt})_2]^{2-}$ [b]	2.094	2.019	155.8	36.5	0.363	0.679	this work
$[Cu(i\text{-mant})_2]^{2-}$ [b]	2.0935	2.020	157.5	34.0	0.394	0.599	this work
$[Cu(i\text{-ect})_2]^{2-}$ [b]	2.089	2.0181	157.5	34.0	0.394	0.595	this work
$[Cu(ded)_2]^{2-}$ [b]	2.082	2.018	159.0	40.0	0.381	0.642	this work
$[Cu(dts)_2]^{2-}$ [c]	2.1225	2.027	143.0	32.0	0.354	0.625	this work
$[Cu(Cpdt)_2]^{2-}$ [b]	2.094	2.022	177.1	47.6	0.493	0.590	104
$[Cu(dtdc)_2]^{2-}$ [b]	2.0998	2.0426	162.56	44.54	0.449	0.610	338
$[Cu(mnt)_2]^{2-}$ [c]	2.082	2.024	154.5	37.9	0.470	0.555	377
$[Cu(bdt)_2]^{2-}$ [c]	2.087	2.021	167.0	38.0	0.461	0.531	373, 381
$[Cu(qdt)_2]^{2-}$ [c]	2.090	2.023	146.7	43.0	0.368	0.629	382, 383
$[Cu(tdt)_2]^{2-}$ [c]	2.091	2.0026	148.6	40.2	0.383	0.598	384
$[Cu(dmit)_2]^{2-}$ [c]	2.099	2.0235	156.0	35.2	0.463	0.527	385
$[Cu(dddt)_2]^{2-}$ [c]	2.101	2.0416	142.3	33.4	0.416	0.555	386

[a] × 10^{-4} cm^{-1}; [b] 1,1-dithiolate; [c] 1,2-dithiolate

The P/P_0 ratio allows comparisons of values of r^{-3} between the complexes and free ion term, in this instance showing that r^{-3} for the 1,1-dithiolate species have 35 to 40% the free-ion value. The values indicate strong covalent σ-bonding in all the complexes, and are

comparable to those reported for both 1,1- and 1,2-dithiolates (see Table 5.9). The smaller P/P_0 ratios calculated for the complexes here indicates greater σ-bonding in the 1,1-dithiolate complexes than their 1,2-dithiolate counterparts, although the value of P/P_0 = 0.354 reported for $[Cu(dts)_2]^{2-}$ at least part of the difference could stem from experimental error.

This information provides insight into complex bonding strength and allows comparison with related species. It is however a crude tool, allowing only general insight into σ-bonding strength and neither quantifying that strength, nor providing information about any π-bonding interactions. More information can be obtained by developing spin-Hamiltonians for the complexes through the use of a basis set of molecular orbitals consisting of linear combinations of metal ligand orbitals.[387,388] The approach is unwieldy for d^7 metal centres,[377] but is relatively straightforward for d^9 ions.[375,378]

Pettersson and Vänngård first used this approach to model bonding interactions in a series of bis(dithiocarbomato) Cu^{II} complexes;[389] since then it has been used to provide a wealth of information on many systems of this type,[370,371,373] including an investigation by Kirmse into $[Cu(i\text{-mnt})_2]^{2-}$.[332]

Building on Kirmse's foundations,[332] group theory is applied to obtain the following antibonding wavefunctions through the combination of the correct linear combination of ligand orbitals with the Cu^{II} d-orbitals.[378,390] Using the notification developed by Germann and Swalen[391] as outlined by Herring *et al.*,[370] these are defined by Equations 5.12 through 5.16.

$$\psi_{B_{1g}} = \alpha d_{xy} - \frac{1}{2}\alpha'\left[-\sigma_{xy}{}^{(1)} + \sigma_{xy}{}^{(2)} + \sigma_{xy}{}^{(3)} - \sigma_{xy}{}^{(4)}\right] \qquad (5.12)$$

$$\psi_{B_{1g}} = \beta d_{x^2-y^2} - \frac{1}{2}\beta'\left[-p_{xy}{}^{(1)} - p_{xy}{}^{(2)} + p_{xy}{}^{(3)} + p_{xy}{}^{(4)}\right] \qquad (5.13)$$

$$\psi_{A_g} = \gamma d_{z^2} - \frac{1}{2}\gamma'\left[\sigma_{xy}{}^{(1)} + \sigma_{xy}{}^{(2)} - \sigma_{xy}{}^{(3)} - \sigma_{xy}{}^{(4)}\right] \quad (5.14)$$

$$\psi_{B_{3g}} = \delta d_{yz} - \frac{1}{2}\delta'\left[p_z{}^{(1)} + p_z{}^{(2)} - p_z{}^{(3)} - p_z{}^{(4)}\right] \quad (5.15)$$

$$\psi_{B_{2g}} = \varepsilon d_{yz} - \frac{1}{2}\varepsilon'\left[p_z{}^{(1)} - p_z{}^{(2)} - p_z{}^{(3)} + p_z{}^{(4)}\right] \quad (5.16)$$

The magnetic parameters are defined by Equations 5.17 through 5.22, where α indicates the covalency of the metal-ligand σ-bonding parameter, β of the in-plane metal-ligand π-bonding character, and δ and ε of the out of plane metal-ligand π-bonding character.

$$g_x = g_e - \left(\frac{2\xi}{\Delta E_{xz}}\right)\left(\alpha^2\varepsilon^2\right) \quad (5.17)$$

$$g_y = g_e - \left(\frac{2\xi}{\Delta E_{yz}}\right)\left(\alpha^2\delta^2\right) \quad (5.18)$$

$$g_z = g_e - \left(\frac{8\xi}{\Delta E_{x^2-y^2}}\right)\left(\alpha^2\beta^2\right) \quad (5.19)$$

$$A_x = -K + \frac{2}{7}\alpha^2 P - \frac{22}{14}\frac{\xi\alpha^2\varepsilon^2}{\Delta E_{xz}} \quad (5.20)$$

$$A_y = -K + \frac{2}{7}\alpha^2 P - \frac{22}{14}\frac{\xi\alpha^2\delta^2}{\Delta E_{yz}} \quad (5.21)$$

$$A_y = -K - \frac{4}{7}\alpha^2 P - 2\xi\alpha^2 P\left(\frac{4\beta^2}{\Delta E_{x^2-y^2}} + \frac{3}{14}\frac{\delta^2}{\Delta E_{yz}} + \frac{3}{14}\frac{\varepsilon^2}{\Delta E_{xz}}\right) \quad (5.22)$$

ξ is the spin-orbit coupling constant of the free Cu^{II} ion, with a standard value of −828 cm^{-1},[392] K is the Fermi contact term, and P is the isotropic dipolar hyperfine coupling parameter as previously defined by Equation 5.11.

The representation here of the Fermi contact term by K rather than $\alpha^2 k$ as although the latter form is seen in early investigations into Cu^{II} complexes, this was due to a misconception that the Fermi contact term for d^9 systems was proportional to the square of the molecular orbital coefficient of the *d*-orbital in the single-electron molecular orbital.[375] This was proven incorrect in a seminal paper by McGarvey,[379] with the correct value for K instead calculated using Equation 5.23, with the hyperfine parameters once again all taken as negative (*vide supra*).

$$-K = \frac{\left[\left(A_x + A_y + A_z\right) - P\left(g_x + g_y + g_z\right)\right]}{3} \tag{5.23}$$

Using the value of K obtained, α can then be calculated using Equation 5.24, where $\Delta g_i = g_i - g_e$.

$$\alpha^2 = \frac{7\left[-A_z - K + P\left(\Delta g_z + \frac{3}{14}\Delta g_x + \frac{3}{14}\Delta g_y\right)\right]}{(4P)} \tag{5.24}$$

The presence of ΔE_{xz} etc. in Equations 5.17 through 5.22 means that in addition to spin-Hamiltonian parameters, information from the electronic spectra the of Cu^{II} 1,1-dithiolate complexes is required to evaluate the bonding parameters β, δ and ε.[370] No comprehensive study of 1,1-dithiolates has yet occurred, although data from a basic investigation by Gray and co-workers[82] was extrapolated further by Kirmse who, neglecting structural deviations, treated the complex as D_{4h}.[332]

Using this along with studies of related compounds[374] allows derivation of principles for predicting the LF splitting in each complex, enabling extraction of values for ΔE_{xz} etc. from the electronic spectral data. The collected bonding parameter data is shown in Table

5.10; the absence of required electronic spectroscopy data means some compounds in Table 5.9 are absent in Table 5.10.

Table 5.10 Bonding parameters deduced from spin Hamiltonian and spectral parameters.

	α^a	β^b	δ^c	α'^d	$K^{e,f}$	**Reference**
$[Cu(i\text{-mnt})_2]^{2-\,g}$	0.678	0.676	0.705	0.738	91.3	this work
$[Cu(i\text{-mant})_2]^{2-\,g}$	0.706	0.652	0.672	0.711	90.4	this work
$[Cu(i\text{-ect})_2]^{2-\,g}$	0.713	0.639	0.626	0.705	89.4	this work
$[Cu(ded)_2]^{2-\,g}$	0.687	0.647	0.644	0.729	92.9	this work
$[Cu(dts)_2]^{2-\,h}$	0.709	0.576	0.872	0.709	89.4	this work
$[Cu(Cpdt)_2]^{2-\,g}$	0.720	0.703	0.720	0.640	106.7	104
$[Cu(dtdc)_2]^{2-\,g}$	0.692	0.716	1.121	0.725	105.3	338
$[Cu(bdt)_2]^{2-\,h}$	0.713	0.634	0.736	0.704	95.7	373, 381
$[Cu(qdt)_2]^{2-\,h}$	0.656	0.667	0.847	0.758	93.1	382, 383
$[Cu(dmit)_2]^{2-\,h}$	0.704	0.734	0.803	0.714	92.2	385, 393
$[Cu(mdtc)_2]^i$	0.683	0.701	0.657	0.734	87.2	394
$[Cu(edtc)_2]^i$	0.690	0.715	0.762	0.727	93.6	395
$[Cu(pddtc)_2]^i$	0.694	0.723	0.717	0.723	92.2	370
$[Cu(modtc)_2]^i$	0.705	0.741	0.750	0.713	90.5	370
$[Cu(pdtc)_2]^i$	0.699	0.792	0.775	0.718	85.7	396

[a] σ-bonding parameter; [b] in-plane π-bonding parameter; [c] out-of-plane π-bonding parameter; [d] ligand σ-bonding parameter; [e] the Fermi contact term; [f] $\times 10^{-4}$ cm^{-1}; [g] 1,1-dithiolate; [h] 1,2-dithiolate; [i] dithiocarbamate

As discussed, Cu^{II} 1,1-dithiolates have B_{2g} ground states with the unpaired electron in the d_{xy} orbital. The $A_g \rightarrow B_{1g}$ transition from the x^2-y^2 to xy orbital is the lowest energy, with the next, $B_{2g} \rightarrow B_{1g}$, considerably higher in energy. However, the *xz* and *yz* orbitals are close enough in energy that the $B_{2g} \rightarrow B_{1g}$ and $B_{3g} \rightarrow B_{1g}$ transitions can be approximated to a single $E_g \rightarrow B_{1g}$ transition, with ΔE_{xz} and ΔE_{yz} treated as identical. As above this effectively neglects rhombic distortion, setting $\delta^2 = \varepsilon^2$ to give an average value for δ^2. The values for $\Delta E_{x^2-y^2}$ are listed in Table 5.4, with values for ΔE_{xz} and ΔE_{yz} considered identical and obtained from the electronic spectra visible in the appendix. Following Gersmann and Swalen[391] the overlap of the $\psi_{B_{1g}}$ state was included, with α and α' related by Equation 5.25,

where the σ-orbitals are hybridised sp orbitals, and S is the metal-ligand overlap term (0.005 for sulfur ligands).[391]

$$\alpha^2 + \alpha'^2 - 2\alpha\alpha' S = 1 \qquad (5.25)$$

For clarity, a value of 0.5 for α, β and δ in Table 5.10 indicates purely covalent metal-ligand bonds, and 1.0 bonds that are purely ionic. The δ value for $[Cu(dtdc)_2]^{2-}$ must therefore be incorrect, as it suggests >100% ionic bonding. This is impossible, indicating errors in the reported EPR and electronic data.

The α bonding parameters calculated for the 1,1-dithiolate species reveal σ-bonding that is more covalent than ionic, to a similar degree as both the 1,2-dithiolate and dithiocarbamate complexes.

In contrast, the β parameters for the 1,1-dithiolate complexes are much smaller than either the 1,2-dithiolate or dithiocarbamate species. They are closest to the β parameters reported for 1,2-dithiolate complexes, with $[Cu(bdt)_2]^{2-}$ and $[Cu(qdt)_2]^{2-}$ showing even smaller values. As the *i*-ect^{2-} and ded^{2-} ligated species show the highest in-plane π-bond covalencies, dianionic ligand systems clearly favour in-plane π-bonding most, with the bond covalency increasing as total σ_P is reduced. The more ionic nature of the in-plane π-bonding in $[Cu(dmit)_2]^{2-}$ supports this, as the ligand is the hardest 1,2-dithiolate amongst those listed.

The in-plane π-bonding behaviour of 1,1-dithiolate complexes dovetails well with the δ parameters. Out-of-plane π-bonding in 1,2-dithiolate systems is relatively ionic, with parameters greater than 0.8 observed. In contrast, the 1,1-dithiolate species show bonding closer in covalent to that in dithiocarbamates, with out-of-plane π-bonding in the *i*-ect^{2-} and ded^{2-} systems in fact more covalent than the in-plane parameters. The difference suggests ligand charge dominates the in-plane π-bonding, but metal-ligand bite-angle has greater influence on the out-of-plane π-bond covalency.

5.3.5 X-ray Absorption Spectroscopy

Cu K-edge XAS was used to probe the coordination environments and oxidation states of $[Cu(i\text{-ect})_2]^{2-}$ and $[Cu(i\text{-ect})_2]^{-}$, and allow comparison to similar Cu species. S K-edge was also used to study and compare both Cu species and related Cu^{II} 1,1-dithiolates.

5.3.5.1 Cu K-edge XAS of Cu 1,1-Dithiolate Complexes

The Cu K-edge spectra of $[Cu(i\text{-ect})_2]^{2-}$ and $[Cu(i\text{-ect})_2]^{-}$ are shown in Figure 5.14, with the energies of the rising edge positions determined at the first inflection point of the edge summarised alongside the pre-edge energies in Table 5.11; the inset in Figure 5.14 shows the second-derivative spectra of the pre-edge region. The pre-edge feature observed at ~8980 eV is the dipole-forbidden, quadrupole-allowed 1s → 3d transition that gains intensity 4p-3d mixing caused by departures from centrosymmetry.

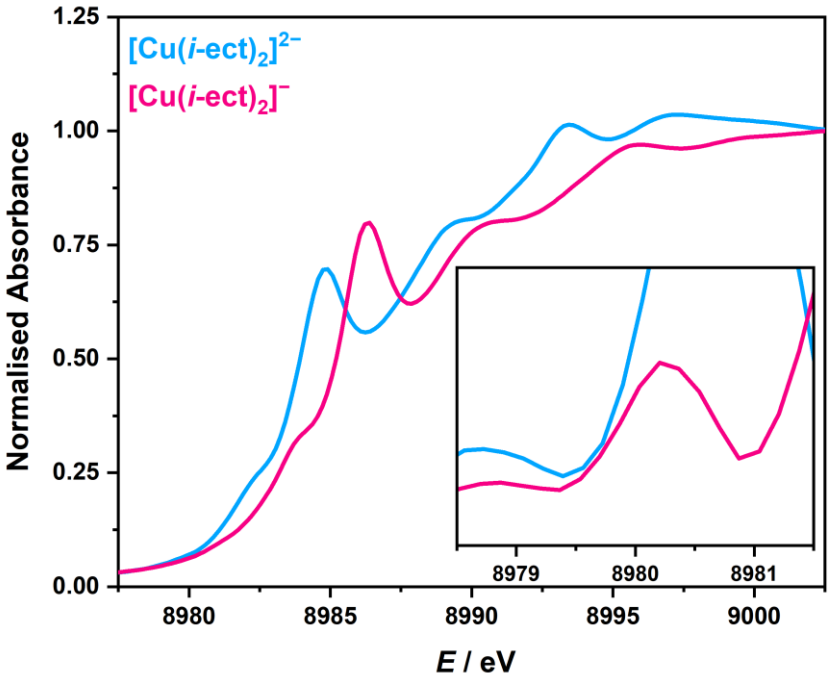

Figure 5.14 Normalised Cu K-edge spectra of $[Cu(i\text{-ect})_2]^{2-}$ and $[Cu(i\text{-ect})_2]^{-}$; inset shows second derivative of the pre-edge region (1s → 3d transition, ~8978 − 8982 eV), indicating a 1.4 eV shift.

The pre-edge feature occurs 8979.4 eV in $[Cu(i\text{-ect})_2]^{2-}$ and is shifted ~1.4 eV higher in energy in $[Cu(i\text{-ect})_2]^{-}$ to 8980.8 eV. The transition energies are consistent with those previously reported for four-coordinate Cu^{II} species bound by closed-shell ligands,[324,397] and

are close to those reported for the 1,2-dithiolate $[Cu(mnt)_2]^{X-}$ (X = 1, 2).[191] The mnt^{2-} complexes show the same ~1.4 eV shift on oxidation visible here.[191]

Table 5.11 Cu K-edge XAS pre- and rising-edge energies (eV) for $[Cu(i\text{-ect})_2]^{2-}$ and $[Cu(i\text{-ect})_2]^{-}$.

	Pre-edge	**Rising-edge**[a]
$[Cu(i\text{-ect})_2]^{2-}$	8979.4	8984.7
$[Cu(i\text{-ect})_2]^{-}$	8980.8	8986.2

[a] Determined at the first inflection point.

The intense rising-edge feature observed at ~8985 eV is a result of a formally two-electron 1s → 4p + LMCT shakedown transition[397,398] (*vide supra*) allowed due to final-state relaxation.[399] The transition occurs at 8984.7 eV in $[Cu(i\text{-ect})_2]^{2-}$, and is shifted ~1.5 eV higher in energy to 8986.2 eV in $[Cu(i\text{-ect})_2]^{-}$. the intensity of the shakedown transition increases on oxidation. As shown, the energy of the rising-edge feature is the most reliable indicator of changing oxidation states, with increase of 1.5 eV in 1s → 4p + LMCT in $[Cu(i\text{-ect})_2]^{-}$ supporting a $Cu^{II} \rightarrow Cu^{III} + e^{-}$ oxidation.

5.3.5.2 S K-edge XAS of Cu 1,1-Dithiolate Complexes

The S K-edge spectra of $[Cu(i\text{-mnt})_2]^{2-}$, $[Cu(i\text{-mant})_2]^{2-}$ and $[Cu(i\text{-ect})_2]^{2-}$ and their second derivatives are shown in Figure 5.15; individual pseudo-Voigt deconvolutions are displayed in Figure 5.16 with the pre-edge peak energies and intensities listed in Table 5.12, along with data for $[Cu(i\text{-ect})_2]^{-}$. The S K-edge spectra all have three well resolved pre-edge features, with lower energy transitions at 2469.80 ± 0.15 eV followed by higher energy transitions at 2471.00 ± 0.25 eV and 2472.15 ± 0.15 eV.

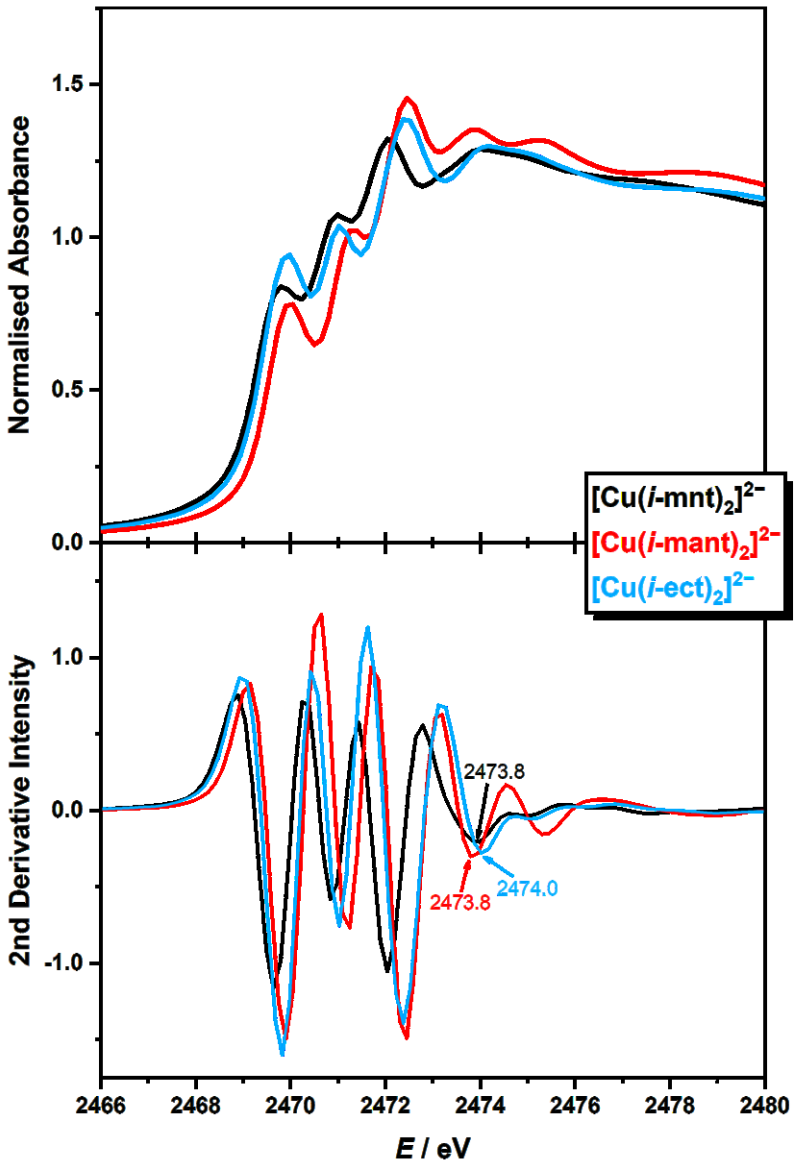

Figure 5.15 Comparison of the normalised S K-edge spectra (top) and their second derivatives for the Cu^{II} 1,1-dithiolate complexes. The 1s → 4p edge transitions are indicated in the plots of the second derivatives.

Interpretation of the spectral data is aided by prior analysis of the S K-edge of $[Cu(mnt)_2]^{2-}$.[191] As in the mnt^{2-} system, the lowest energy S K-edge transition in the 1,1-dithiolate species corresponds to a 1s → Cu−S π* LUMO, with the reduction in transition energy relative to the $[Cu(mnt)_2]^{2-}$ stemming from different coordination geometries. The absence of the transition in the Co 1,1-dithiolates (*vide supra*) stems from the lower S content of the acceptor orbitals.

Table 5.12 Pre-Edge Peak Energies (eV), Intensities (D_0), Number of Holes in Acceptor Orbitals (h), and Covalencies (α^2; S 3p%) for Cu 1,1-Dithiolate Complexes.

	Pre-edge energy	D_0	h	α^{2a}
$[Cu(i\text{-mnt})_2]^{2-}$	2469.70	0.14	1	18.2
	2470.80	0.13	2	8.4
	2472.02	0.35	2	22.7
$[Cu(i\text{-mant})_2]^{2-}$	2469.94	0.15	1	19.5
	2471.25	0.16	2	10.4
	2472.33	0.22	2	14.3
$[Cu(i\text{-ect})_2]^{2-}$	2469.85	0.19	1	23.8
	2471.04	0.18	2	11.3
	2472.28	0.20	2	12.5
$[Cu(i\text{-ect})_2]^{-}$	2469.69	0.35	2	20.5
	2471.63	0.16	2	9.6
	2472.61	0.20	2	12.1

[a] Determined from $\alpha^2 = 12D_0/(H \times I_S)$. I_S = 9.24, 9.24, 9.60, 9.96 (Estimated from the S 1s → 4p transition energies in Figure 5.15 and Figure 5.17 and the correlation plot in reference 191)

The remaining transitions are the same as those visible in the analogous Co 1,1-dithiolate S K-edge spectra: a lower energy pre-edge transition to the Cu−S σ*, followed by one in the rising edge to the C−S π*. Unlike their Co^{II} analogues discussed in Chapter 3, the total σ_P and S K-edge transition energies of the Cu^{II} complexes have no clear relationship, remaining relatively consistent across the series.

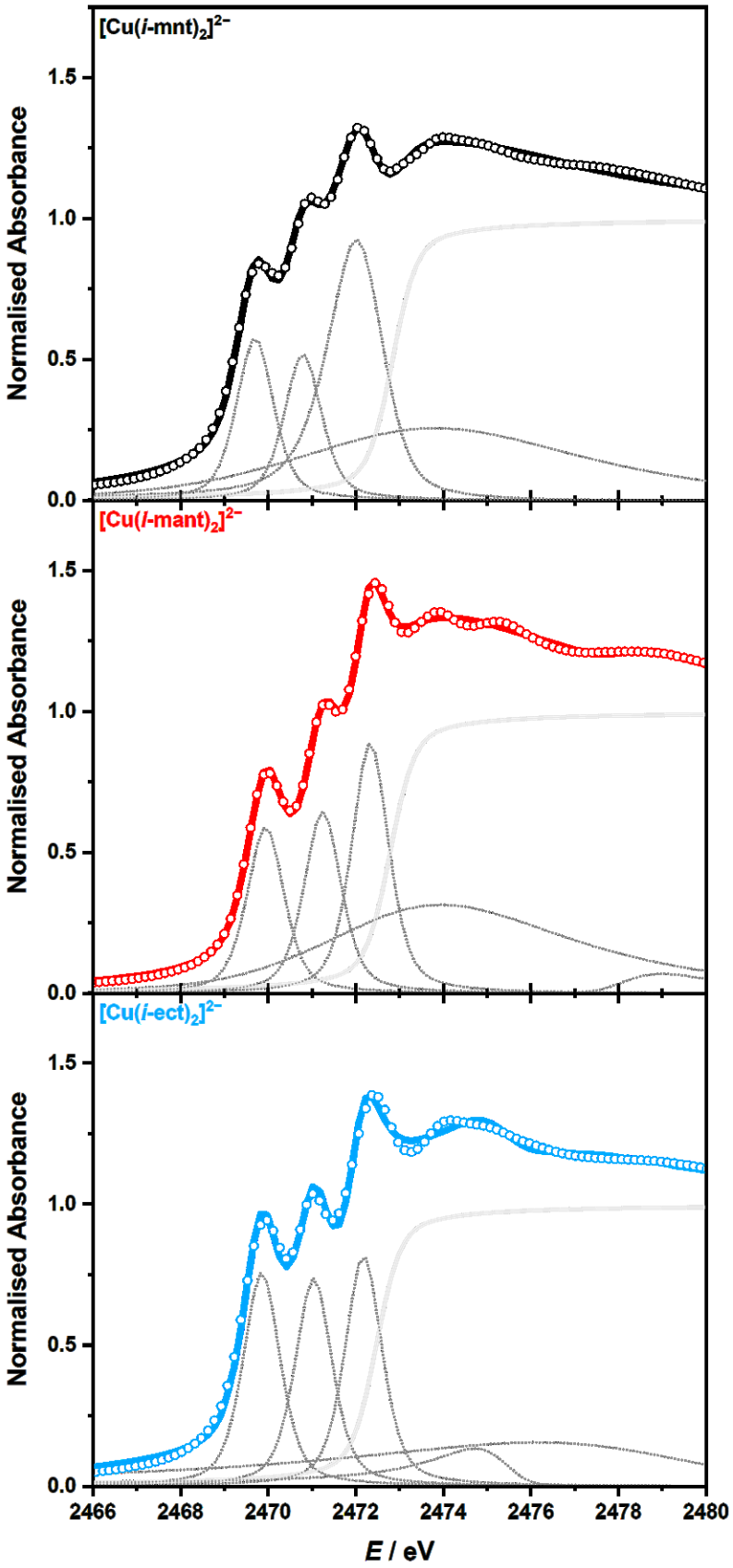

Figure 5.16 Pseudo-Voigt deconvolution of S K-edge spectra of the Cu^{II} 1,1-dithiolate complexes. Circles represent the experimental data; dotted lines represent the pseudo-Voigt; the solid grey line the edge jump; and the solid coloured line is the sum of the fit.

A trend is observed in the transtion intensities, with the intensity of the two pre-edge features increasing and the rising edge intensity decreasing as total σ_P decreases. Bond covalencies reflect the trend, with the Cu−S π* LUMO covalency decreasing as ligand π-donor abilities weaken with increased total substituent σ_P; Cu−S σ* covalency also decreases with total σ_P as S mixing with the mainly Co-based MO is reduced. In contrast, the covalency of the C−S π* increases as total σ_P does, as the stronger electron-withdrawing ligand substituents remove electron density from the $\{CuS_4\}$ to the ligand-based C−S π* MO.

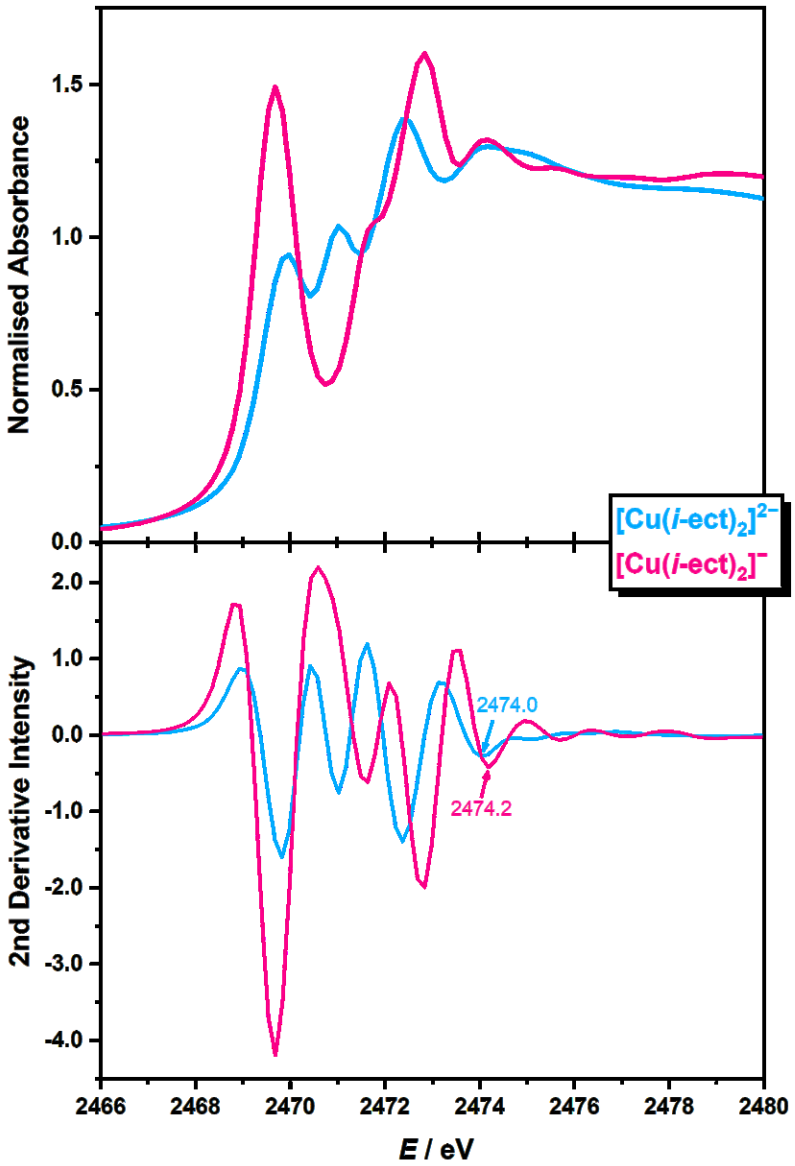

Figure 5.17 Comparison of the normalised S K-edge spectra (top) and their second derivatives for $[Cu(i\text{-ect})_2]^{2-}$ and $[Cu(i\text{-ect})_2]^{-}$. The 1s → 4p edge transitions are indicated in the plots of the second derivatives.

Comparisons of the the S K-edge spectra of $[Cu(i\text{-ect})_2]^{2-}$ the oxidised $[Cu(i\text{-ect})_2]^{-}$ can be made. The S K-edge spectra are shown along with their second derivatives in Figure 5.17; individual pseudo-Voigt deconvolutions are displayed in Figure 5.18,Figure 5.16 with pre-edge peak energies and intensities listed in Table 5.12. The spectra of both compounds consist of three transtions between 2469 and 2473 eV, corresponding to the three transitions discussed above.

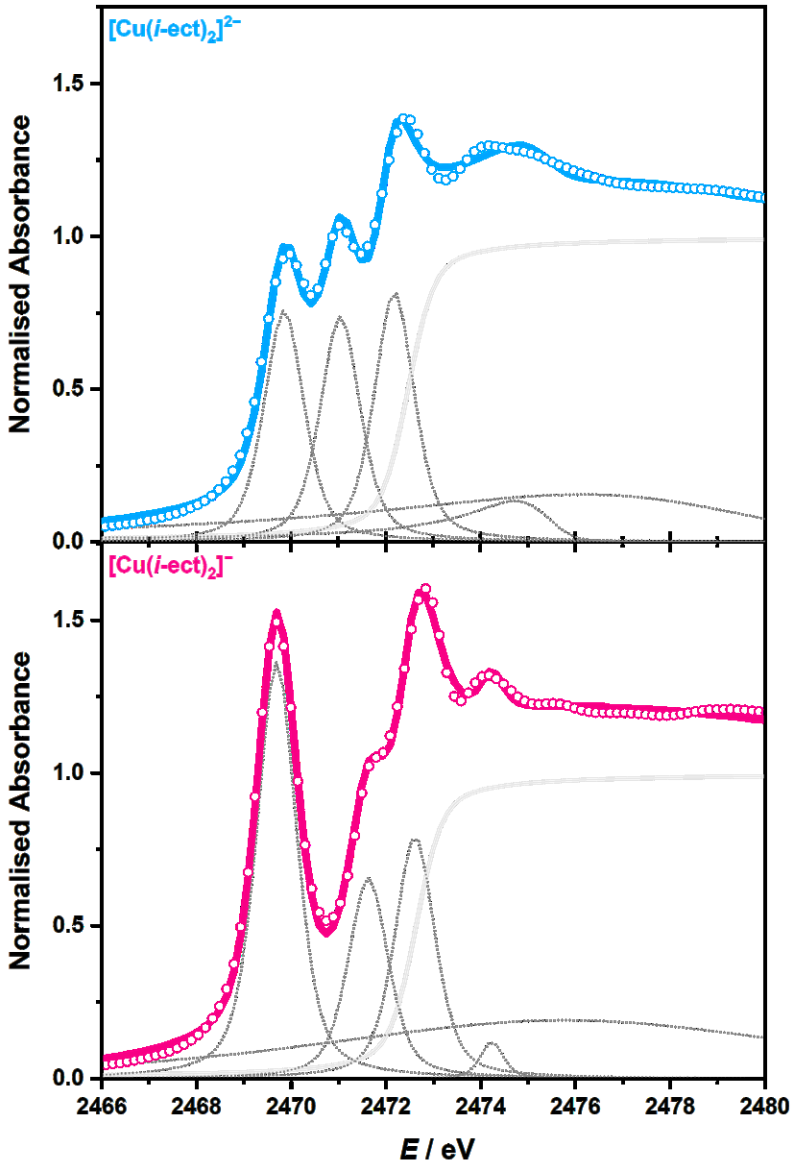

Figure 5.18 Pseudo-Voigt deconvolution of S K-edge spectra of $[Cu(i\text{-ect})_2]^{2-}$ and $[Cu(i\text{-ect})_2]^{-}$. Circles represent the experimental data; dotted lines represent the pseudo-Voigt; the solid grey line the edge jump; and the solid coloured line is the sum of the fit.

The first transition to the Cu−S π* LUMO occurs at 2469.85 in $[Cu(i\text{-ect})_2]^{2-}$, while it is ~0.15 eV in $[Cu(i\text{-ect})_2]^{-}$, occurring at 2469.69 eV. In contrast, the two higher-energy transitions that occur at 2471.04 and 2472.28 eV in $[Cu(i\text{-ect})_2]^{2-}$ are shifted to ~0.6 and ~0.3 eV higher energy in in $[Cu(i\text{-ect})_2]^{-}$ and occur at 2471.63 and 2472.61 eV. The trend is identical to that observed in the S K-edge of $[Cu(mnt)_2]^{2-}$ and $[Cu(mnt)_2]^{-}$.[191]

The intensity of the 1s → Cu−S π* LUMO feature provides a measure of S 3p character in the orbital. The total integrated areas under the S K-edge pre-edge peaks of $[Cu(i\text{-ect})_2]^{2-}$ and $[Cu(i\text{-ect})_2]^{-}$ are 0.19 and 0.35, respectively (Table 5.12); as $[Cu(i\text{-ect})_2]^{-}$ is a two-hole system the renormalised per-hole intensity is 0.175. The reduced per-hole S character of the Cu−S π* in $[Cu(i\text{-ect})_2]^{-}$ is the reverse of the trend reported for $[Cu(mnt)_2]^{-}$,[191] and is manifest in decreased covalencies in $[Cu(i\text{-ect})_2]^{-}$.

5.3.6 Electronic Absorption Spectroscopy of Ni^{II} 1,1-Dithiolates

Electronic spectra of the Ni^{II} 1,1-dithiolate complexes are overlaid in Figure 5.19. The spectra of all the complexes are broadly similar: two intense LMCT bands are visible at higher energies in each complex, with signature LF transitions observed between 600 and 650 nm. Minor differences are visible in the spectra $[Ni(i\text{-ect})_2]^{2-}$ and $[Ni(ded)_2]^{2-}$, which display further features between the two LMCT bands.

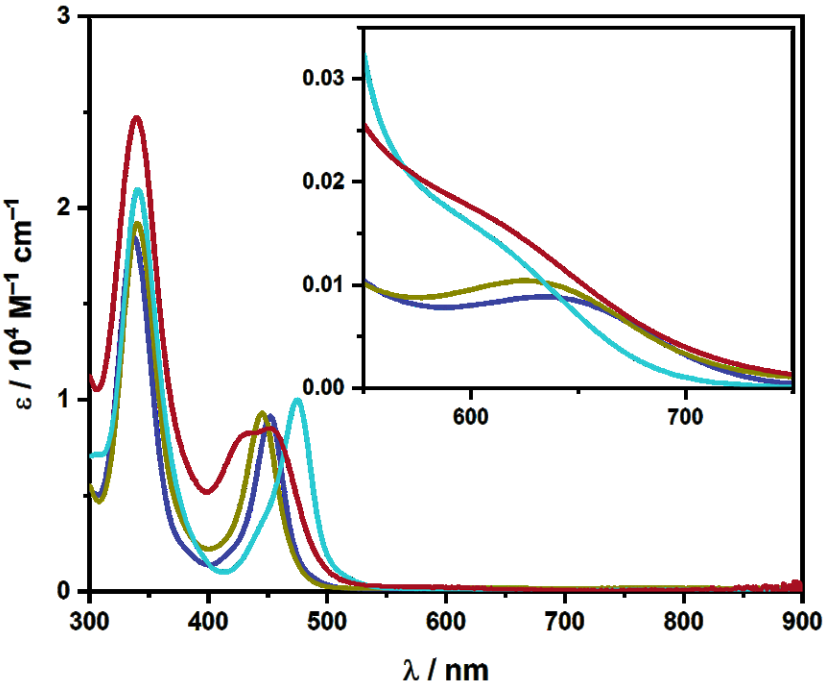

Figure 5.19 Comparison of the electronic spectra of $[Ni(i\text{-mnt})_2]^{2-}$ (navy), $[Ni(i\text{-mant})_2]^{2-}$ (khaki), $[Ni(i\text{-ect})_2]^{2-}$ (teal) and $[Ni(ded)_2]^{2-}$ (ochre); inset shows an expansion of the LF transitions.

The LF transition are consistent with square-planar Ni^{II} complexes[368] and once again illustrate the influence of the total σ_P (*vide supra*). Although, with transition energies remaining constant at 339 nm, the total σ_P does not affect the energy of orbitals involved in the transition however, the higher energy LMCT band intensity increases as total σ_P decreases and more electron density is donated to the Ni^{II} centre.

A straightforward trend is not visible in the lower energy bands, as transition intensity increases with lower total σ_P for $[Ni(i\text{-mnt})_2]^{2-}$, $[Ni(i\text{-mant})_2]^{2-}$ and $[Ni(i\text{-ect})_2]^{2-}$, but not $[Ni(ded)_2]^{2-}$. A second feature at 434 nm appears in the latter, with the higher intensities in

the other species thus corresponding to two overlapping transitions; the second transition is visible as a shoulder at 448 nm in $[Ni(i\text{-ect})_2]^{2-}$. The lower energy transition varies more that the first but remains broadly constant at 449 ± 5 nm.

Table 5.13 Spectral parameters of the $^1A_{1g} \rightarrow {}^1B_{1g}$ transition

	λ_{max} / nm	ε_{max} / M^{-1} cm^{-1}
$[Ni(i\text{-mnt})_2]^{2-}$	637	88
$[Ni(i\text{-mant})_2]^{2-}$	627	104
$[Ni(i\text{-ect})_2]^{2-}$	616	136
$[Ni(ded)_2]^{2-}$	602	174

LF transitions are visible in the spectra of the Ni^{II} 1,1-dithiolate complexes between 600 and 650 nm, with spectral parameters collated in Table 5.13. Gray and co-workers assign the transition as $^1A_{1g} \rightarrow {}^1B_{1g}$ ($x^2 - y^2 \rightarrow xy$),[82] as such transitions are typical for square-planar Ni^{II} dithiolate complexes, with the lower transition energy reported[400] for $[Ni(mnt)_2]^{2-}$ a function of the difference in LF splittings between the 1,1- and 1,2-dithiolate complexes. The LF transitions follow the same pattern as in the Co^{II} and Cu^{II} complexes: as total σ_P decreases the transitions get more intense and decrease in energy, supporting the prior links between substituent σ_P and LF splitting in the central 3d ion.

5.3.7 Electrochemistry of Ni^{II} 1,1-Dithiolates

Oxidation events in $[Ni(i\text{-mnt})_2]^{2-}$, $[Ni(i\text{-ect})_2]^{2-}$ and $[Ni(ded)_2]^{2-}$ have been reported before by Dietzsch *et al.*[336] However, differing experimental conditions (solvents, electrodes, electrolytes) and the lack of data concerning $[Ni(i\text{-mant})_2]^{2-}$ prevent a full comparison of redox properties within the series.

Table 5.14 Reduction Potentials for Ni^{II} 1,1-Dithiolates (V versus $Fc^{+/0}$).

	E_{pc}
$[Ni(i\text{-mnt})_2]^{2-}$	0.10
$[Ni(i\text{-mant})_2]^{2-}$	−0.09
$[Ni(i\text{-ect})_2]^{2-}$	−0.16
$[Ni(ded)_2]^{2-}$	−0.22

The resulting CVs are shown in Appendix 8.22; collated potentials of the oxidation events are given in Table 5.14.

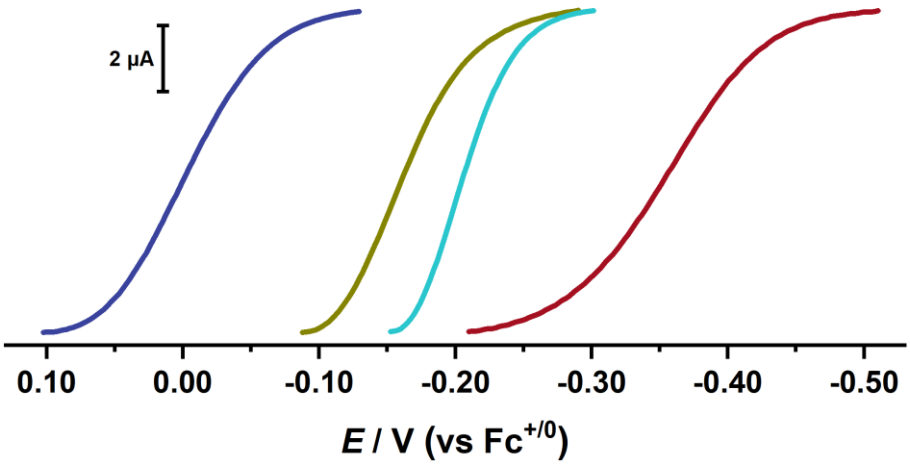

Figure 5.20 Overlay of the $Ni^{II/III}$ oxidation events of [Ni (i-mnt)$_2$]$^{2-}$ (navy), $[Ni(i\text{-mant})_2]^{2-}$ (khaki), $[Ni(i\text{-ect})_2]^{2-}$ (teal) and $[Ni(ded)_2]^{2-}$ (ochre).

All complexes showed an irreversible oxidation event assigned to $Ni^{II} \rightarrow Ni^{III} + e^-$. The event position correlates with the total σ_P of the ligand system, with the event reduction potential decreasing with reductions in total σ_P. While it is observed at 100 mV in $[Ni(i\text{-mnt})_2]^{2-}$, the potentials shift to −100, −160 and −220 mV for $[Ni(i\text{-mant})_2]^{2-}$, $[Ni(i\text{-ect})_2]^{2-}$ and

$[Ni(ded)_2]^{2-}$, respectively (Figure 5.20). The trend reflects the increased ligand π-donor abilities destabilising the Ni^{II} HOMO and facilitating oxidation. Unlike the $Cu^{III/II}$, the $Ni^{III/II}$ redox couple is irreversible, reflecting the fundamental differences in complex behaviour. While bis(1,1-dithiolate) Cu complexes have been shown to exist stably as Cu^{III} species,[90] oxidation of bis(1,1-dithiolate) Ni^{II} complexes results instead in the formation of Ni^{IV} tris-chelates, with the Ni^{III} present only as intermediates existing alongside by-products from ligand oxidation.[336]

5.4 Experimental

5.4.1 X-ray crystallographic data collection and refinement

Single crystals of $(NBu_4)_2[Cu(i\text{-}mnt)_2]$ were grown by were grown by slow evaporation of an acetonitrile solution of the complex, crystals of $(PPh_4)_2[Co(dts)_2]$ by chilling a saturated acetonitrile solution of the complex to −35 °C, and of $(PPh_4)_2(dts)$ by slow diffusion of diethyl ether into a saturated acetonitrile solution of the complex. Orange blocks of dimension 0.20 × 0.18 × 0.10 mm^3 of $(NBu_4)_2[Cu(i\text{-}mnt)_2]$, brown blocks of dimension 0.20 × 0.18 × 0.10 mm^3 of $(PPh_4)_2[Cu(dts)_2]$, and yellow blocks of dimension 0.20 × 0.19 × 0.15 mm^3 of $(PPh_4)_2(dts)$ were mounted on a Bruker SMART APEX CCD diffractometer, and data collected using graphite monochromated Mo−Kα radiation (λ = 0.71073 Å) from a Mo-target rotating-anode X-ray source equipped with a Kryoflex attachment supplying a nitrogen stream at 150 K. The structures were solved by direct methods and refined by full-matrix least squares method with anisotropic thermal parameters for all atoms with SHELXS-97[246] and SHELXL-97,[247] using the WinGX[248] software package. Corrections for incident and diffracted beam absorption effects were applied using empirical absorption corrections.[249] CIF files were generated using Olex2,[247] with analysis and artwork creation performed using Mercury.[250] Crystal data are presented in Table 5.15.

5.4.2 Physical Measurements

Electronic absorption spectra were recorded using a Shimadzu UV-3600 UV-Vis-NIR spectrophotometer (200 – 1500 nm) in a 1 cm quartz cuvette at a scan rate of 1 nm per second. Infrared data were taken as pressed pellets using a Shimadzu FTIR-8400S spectrophotometer with a diamond anvil cell. ^{1}H and ^{13}C NMR spectra of the complexes were measured at 25 °C on a Bruker AVI 400MHz NMR spectrometer, with chemical shifts referenced to the protonated solvent residual.[199] Magnetic susceptibility measurements were on a Sherwood Scientific Mark 1 Magnetic Susceptibility Balance using an aqueous solution of $Hg[Co(CNS)_4]$ as a calibrant.[200] Mass spectrometry (MS) spectra (electrospray

ionization, ESI) were obtained with a Bruker microTOF-Q Quadrupole Time-of-Flight Mass Spectrometer operating in positive- and negative-ion modes. Elemental analyses were determined by the departmental microanalysis services using an EA 1110 CHNS, CE-440 Elemental Analyser.

5.4.3 X-ray Absorption Spectroscopy

All X-ray Absorption data were measured at the Stanford Synchrotron Radiation Lightsource (SSRL).

Cu K-edge data was measured in a high-magnetic field mode of 20 kG on the 16-pole beamline 9−3 under conditions of 3 GeV and 60−100 mA. A fully tuned Si(220) double-crystal monochromator was used for energy selection and a Rh-coated mirror set to an energy cut-off of 13 keV used for Harmonic rejection. Internal energy calibration was accomplished by the simultaneous measurement of the absorption of a Cu foil placed between two ionisation chambers situated after the sample, with the first inflection point of the foil spectrum fixed at 8930.3 eV.[201,324] Samples were diluted in BN, pressed into a 1 mm Al spacer and sealed with 37 μm Kapton tape. Data was measured in the transmission mode using an N_2-filled ionisation chamber placed after the sample, which was maintained at 10 K using a liquid He flow cryostat. Data represent the average of 5 scans. Data were processed using the MAVE and PROCESS modules of the EXAFSPAK software package[202] by fitting a second-order polynomial to the pre-edge region and subtracting this background from the entire spectrum. A three-region cubic spline was used to model the smooth background above the edge. The absorbance was normalised by subtracting the spline and normalising the post-edge absorbance to 1.0. S K-edge data was collected as described in Chapter 3.4.3.

Table 5.15 Crystallographic Data for $(NBu_4)_2[Cu(i\text{-}mnt)_2]$ and $(PPh_4)_2[Cu(dts)_2]$

formula	$C_{40}H_{72}CuN_6S_4$	$C_{56}H_{40}CuO_4P_2S_4$
fw	828.81	1030.60
crystal system	monoclinic	Triclinic
space group	$P\,2_1/n$	$P\,\bar{1}$
colour, habit	orange, block	brown, block
a, Å	9.925(1)	10.820(5)
b, Å	16.819(3)	14.390(7)
c, Å	13.796(2)	15.331(7)
α, °	90	93.126(8)
β, °	92.124(2)	90.972(8)
γ, °	90	95.420(8)
V, Å	2301.5(6)	2372.3(2)
T, K	150(2)	150(2)
ρ_{calcd}, g cm^{-3}	1.196	1.443
λ, Å / μ, mm^{-1}	0.71073 / 0.689	0.71073 / 0.753
refl. collected / $2\Theta_{max}$	16940 / 0.997	36874 / 0.928
unique refl. / $I > 2\sigma(I)$	4819 / 3590	9817 / 6208
no. of param. / restr.	236 / 0	607 / 0
R1[a] / goodness of fit[b]	0.0357 / 1.030	0.1763 / 1.098
wR2[c] ($I > 2\sigma(I)$)	0.0835	0.4510
residual density, e Å^{-3}	0.535 / −0.244	3.540 / −1.475

5.4.4 Syntheses

The compounds $(NBu_4)_2[Cu(i\text{-}mnt)_2]$, $(NBu_4)_2[Cu(i\text{-}mant)_2]$, $(NBu_4)_2[Ni(i\text{-}mnt)_2]$, $(NBu_4)_2[Ni(i\text{-}mant)_2]$ and $(NBu_4)_2[Ni(i\text{-}ect)_2]$ were prepared using methods based on that used for $(NBu_4)_2[Cu(i\text{-}mnt)_2]$.[82] Modified literature methods were used to prepare $(NBu_4)_2[Cu(i\text{-}ect)_2]$[245] and $(NBu_4)_2[Cu(ded)_2]$[343], with literature methods also used to prepare $(PPh_4)_2(dts)$ and $(PPh_4)_2[Cu(dts)_2]$.[366] As outlined Chapter 3, $K_2(nmt)$,[251] $Na_2(i\text{-}mnt)$,[252] $K_2(i\text{-}mant)$,[253] $K_2(i\text{-}ect)$[253] and $K_2(ded)$[254] were prepared following the published methods. All other reagents were purchased from commercial sources and used as received. Unless stated otherwise, all reactions and manipulations were conducted in air at room temperature.

Bis(tetrabutylammonium) bis(1,1-dicyanoethylene-2,2-dithiolato)cuprate, $(NBu_4)_2[Cu(i\text{-}mnt)_2]$. A solution of $CuCl_2{\cdot}2H_2O$ (170 mg; 1.00 mmol) in MeOH (5 mL) was prepared and added dropwise to a solution of $Na_2(i\text{-}mnt)$ (390 mg; 2.10 mmol) in MeOH (10 mL). The reaction mixture was then filtered into a stirring solution of NBu_4Br (650 mg; 2.02 mmol) in MeOH (10 mL). A relatively small amount of product precipitated out initially, so EtOH was added and the reaction mixture chilled for 4 h in a freezer at −35 °C to yield more product. This was recrystallised from acetone and EtOH, before being collected under suction, washed with Et_2O (3 × 5 mL), and dried under vacuum to give the final product. Yield = 423 mg (51%).

IR (solid, cm^{-1}): 2959 w, 2872 w, ν(CN) 2195 m, 1619 w, 1597 w, ν(C=C) 1396 s, 1356 s, 1252 w, 1229 w, 1150 s, 1105 w, 1026 m, 974 s, 941 s, ν(C−S) 912 s, 885 m, 799 w, 739 w, 671 s, 635 m, 615 w. ESI-MS: *m*/*z* 585.1 $[M-NBu_4]^-$. μ_{eff} (Gouy balance, 290 K) = 1.78 B.M.

Bis(tetrabutylammonium) bis(1-cyano-1-propanamide-2,2-dithiolato)cuprate, $(NBu_4)_2[Cu(i\text{-}mant)_2]$. A solution of NBu_4Br (644 mg; 2.00 mmol) in MeOH (5 mL) was added to a stirring solution of $K_2(i\text{-}mant)$ (472 mg; 2.00 mmol) in MeOH (5 mL), with

additional MeOH added dropwise until all the compound had dissolved. The solution was then filtered and added severally to a solution of $CuCl_2 \cdot 2H_2O$ (170 mg; 2.00 mmol) in MeOH, with H_2O added immediately afterwards to induce precipitation. The resulting precipitate was filtered off, washed with H_2O (3 × 5 mL), and recrystallised from acetone and H_2O to yield the final product. This was collected under suction, washed with H_2O (3 × 5 mL) and Et_2O (3 × 5 mL), and dried under vacuum. Yield = 618 mg (72%).

IR (solid, cm^{-1}): 3347 m, ν(N−H) 3134 w, 2959 m, 2872 w, ν(CN) 2191 s, 2046 w, ν(C=O) 1638 m, 1576 s, 1422 m, ν(C=C) 1375 s, 1153 w, 1109 w, 1026 w, ν(C−S) 914 s, 870 m, 783 m, 677 m. ESI-MS: *m*/*z* 621.2 $[M-NBu_4]^-$. μ_{eff} (Gouy balance, 289 K) = 1.76 B.M.

Bis(tetrabutylammonium) bis(1-cyano-1-ethoxycarbonyl-2,2-ethenedithiolato) cuprate, $(NBu_4)_2$[Cu(*i*-ect)$_2$]. A solution of $CuSO_4 \cdot 5H_2O$ (250 mg; 1.00 mmol) in a 4:1 mixture of H_2O and MeOH mixture (10 mL) was prepared and added slowly to a stirring solution of K_2(*i*-ect) (540 mg; 2.00 mmol) in a 4:1 mixture of H_2O and MeOH mixture (40 mL) with vigorous stirring. The reaction mixture was filtered into a solution of NBu_4Br (650 mg; 2.02 mmol) in H_2O (5 mL), resulting in the immediate formation of an ochre precipitate. The solid was collected under suction, washed with H_2O (2 × 5 mL), EtOH (5 mL) and Et_2O (3 × 5 mL), and dried under vacuum to yield the final product. Yield = 585 mg (63%).

IR (solid, cm^{-1}): 2961 m, 2874 w, ν(CN) 2176 s, 1661 m, ν(C=O) 1636 m, ν(C−O) 1477 m, ν(C=C) 1346 s, 1290 w, 1263 m, 1165 w, 1121 s, 1092 w, ν(C−S) 930 s, 881 w, 843 m, 787 m, 762 m, 737 m. ESI-MS: *m*/*z* 436.9 $[M]^-$. μ_{eff} (Gouy balance, 291 K) = 1.71 B.M.

Bis(tetrabutylammonium) bis(1,1-di(ethoxycarbonyl)-2,2-ethenedithiolato) cuprate, $(NBu_4)_2$[Cu(ded)$_2$]. A solution of $Cu(NO_3)_2 \cdot 3H_2O$ (216 mg; 0.900 mmol) in H_2O (10 mL) was prepared and added to a solution of K_2(ded) (780 mg; 2.50 mmol) in H_2O (30 mL). After stirring for 10 min, the solution was filtered into a solution of NBu_4Cl (1.50 g; 5.42 mmol) in H_2O (10 mL), causing the slow precipitation of an ochre product. This was collected under

suction, washed with H_2O (5 × 5 mL) and dried under vacuum for 72 h. Yield = 700 mg (77%).

IR (solid, cm^{-1}): 2960 m, 2874 w, 2208 s, 1642 m, v(C=O) 1646 m, v(C−O) 1580 m, v(C=C) 1330 s, 1267 w, 1260 m, 1159 w, 1111 s, 1092 w, 1057 m, 1026 s, v(C−S) 944 m, 853 w, 791 w, 764 m, 737 m. ESI-MS: *m*/*z* 436.9 $[M]^-$. μ_{eff} (Gouy balance, 289 K) = 1.70 B.M.

Tetrabutylammonium bis(1,1-di(ethoxycarbonyl)-2,2-ethenedithiolato) cuprate, $(NBu_4)[Cu(i\text{-}ect)_2]$. A solution of K_2(*i*-ect) (165 mg; 0.625 mmol) in H_2O (3 mL) was prepared and added to a stirring solution of $Cu(MeCO_2)_2{\cdot}H_2O$ (160 mg; 0.800 mmol) in H_2O (1 mL). A dark ochre precipitate initially formed, but on continual stirring the solution began to turn green. After stirring for 15 min NBu_4Cl (384 mg; 1.25 mmoL) was added, causing the rapid precipitate of a dark brown-green precipitate. This was collected under suction, washed thoroughly with H_2O (6 × 5 mL), and recrystallised from acetone and H_2O. The pure product was then collected under suction, washed with Et_2O (3 × 5 mL), and dried under vacuum. Yield = 150 mg (35%).

m/*z* 436.9 $[M]^-$.

Bis(tetraphenylphosphonium) bis(dithiosquarato)cuprate, $(PPh_4)_2[Cu(S_2C_4O_2)_2]$, $(PPh_4)_2[Cu(dts)_2]$. A solution of $CuCl_2{\cdot}2H_2O$ (127 mg; 0.750 mmol) in hot MeCN (6 mL) was added dropwise to a solution of $(PPh_4)_2$(dts) (1.23 g; 1.50 mmol) in warmed MeCN (10 mL) and cooled to 0 °C in an ice bath. Crystallisation of the product immediately occurred, with further product precipitating out on storing the reaction solution in a freezer at −35 °C for four hours. The crystalline precipitate was then collected under suction, washed with Et_2O (4 × 5 mL), and dried under vacuum. Yield = 440 mg (57%).

ESI-MS: *m*/*z* 689.9 $[M-PPh_4]^-$. μ_{eff} (Gouy balance, 291 K) = 1.76 B.M.

Bis(tetrabutylammonium) bis(1,1-dicyanoethylene-2,2-dithiolato)nickelate, $(NBu_4)_2[Ni(i\text{-}mnt)_2]$. $NiCl_2{\cdot}6H_2O$ (360 mg; 1.51 mmol) in MeOH (2 mL) was added dropwise

to a solution of Na_2(*i*-mnt) (480 mg; 2.58 mmol) in MeOH (3 mL) under stirring. The resulting mixture was stirred for 5 min before being filtered into NBu_4Br (892 mg; 2.77 mmol) in MeOH (2 mL). The resulting solution was cooled in a freezer at −35 °C for 0.5 h and the resulting solution collected under suction and recrystallised from MeOH, before being washed with Et_2O (3 × 5 mL) and dried under vacuum. Yield = 523 mg (49%).

IR (solid, cm^{-1}): 2959 s, 2874 m, ν(CN) 2195 s, 1485 w, 1477 w, ν(C=C) 1400 m, 1377 s, 1233 m, 1184 w, 1150 w, 1107 w, 1053 w, 1024 w, 935 m, ν(C−S) 887 s, 799 m, 741 s, 665 s, 620 w, 610 m. ESI-MS: *m*/*z* 580.2 $[M-NBu_4]^-$.

Bis(tetrabutylammonium) bis(1-cyano-1-propanamide-2,2-dithiolato) nickelate, $(NBu_4)_2$[Ni(*i*-mant)$_2$]. $NiCl_2·6H_2O$ (360 mg; 1.51 mmol) in MeOH (2 mL) was added dropwise to a solution of K_2(*i*-mant) (610 mg; 2.58 mmol) in MeOH (5 mL) under stirring. The resulting mixture was stirred for 5 min before being filtered into NBu_4Br (892 mg; 2.77 mmol) in MeOH (2 mL), and H_2O (5 mL) added to induce precipitation of the product. The product was collected under suction, washed with H_2O (2 × 5 mL) and Et_2O (3 × 5 mL) before being dried under vacuum for 18 h. Yield = 763 mg (69%).

IR (solid, cm^{-1}): 3370 s, ν(N−H) 3296 m, 2959 m, 2872 w, 2743 w, ν(CN) 2193 s, 2006 w, ν(C=O) 1639 m, 1578 m, 1427 m, ν(C=C) 1371 w, 1175 w, 1155 w, 1105 m, 1066 s, 1028 w, ν(C−S) 912 m, 878 w, 783 m, 737 w, 679 m. ESI-MS: *m*/*z* 616.2 $[M-NBu_4]^-$.

Bis(tetrabutylammonium) bis(1-cyano-1-ethoxycarbonyl-2,2-ethenedithiolato) nickelate, $(NBu_4)_2$[Ni(*i*-ect)$_2$]. A solution of $NiCl_2·6H_2O$ (360 mg; 1.51 mmol) in MeOH (2 mL) was added dropwise to a solution of K_2(*i*-ect) (685 mg; 2.58 mmol) in MeOH (5 mL) under stirring. The resulting solution was filtered into NBu_4Br (892 mg; 2.77 mmol) in MeOH (2 mL), and H_2O (5 mL) added to induce precipitation of the product, which was collected under suction, washed with H_2O (3 × 5 mL) and Et_2O (3 × 5 mL), and dried under vacuum for 18 h. Yield = 653 mg (55%).

IR (solid, cm^{-1}): 2959 m, 2930 w, 2872 w, ν(CN) 2190 s, 1985 w, ν(C=O) 1678 m, ν(C−O) 1630 m, 1487 w, 1476 w, ν(C=C) 1353 s, 1294 s, 1252 s, 1167 m, 1125 w, 1094 m, 1078 w, 1028 w, ν(C−S) 922 s, 876 s, 847 m, 787 w, 768 s, 752 m, 734 m. ESI-MS: *m*/*z* 674.2 $[M-NBu_4]^-$.

Bis(tetrabutylammonium) bis(1,1-di(ethoxycarbonyl)-2,2-ethenedithiolato) nickelate, $(NBu_4)_2[Ni(ded)_2]$. A solution of $Ni(NO_3)_2{\cdot}6H_2O$ (300 mg; 1.03 mmol) in H_2O (10 mL) was added slowly to vigorously stirring solution of $K_2(ded)$ (630 mg; 2.02 mmol) in H_2O (50 mL). After stirring for 15 min, the solution was filtered into a solution of NBu_4Cl (1.50 g; 5.42 mmol) in H_2O (20 mL), resulting in the immediate formation of a red-brown precipitate, which was collected under suction, washed with H_2O (3 × 5 mL), and dried under vacuum for 18 h. Yield = 506 mg (50%).

IR (solid, cm^{-1}): 2959 m, 2872 w, 1688 m, ν(C=O) 1661 s, ν(C−O) 1553 m, 1474 w, 1416 s, ν(C=C) 1321 m, 1281 s, 1186 s, 1074 m, 1038 m, ν(C−S) 926 s, 910 m, 880 w, 856 w, 793 m, 737 m, 677 s. ESI-MS: *m*/*z* 768.3 $[M-NBu_4]^-$

6 Results Summary and Future Research

In summary, this thesis has probed the structure of three classes of sulfur-ligated TM complexes: Co^{II} arylthiolate species, 3d 1,1-dithiolate complexes and 3d tetrathiotungstate complexes.

Electronic and XAS spectroscopic and magnetic susceptibility measurements showed the electronic structures of the monometallic $\{CoS_4\}$ arylthiolate species to remain relatively stable on modification of the second-coordination sphere, even as chemical behaviour changed dramatically across the series. In the course of study two $[Co_4(SAr)_{10}]^{2-}$ clusters were isolated which showed similar amounts of antiferromagnetic exchange coupling, with the yield proving contingent on the electron-withdrawing strength of the arylthiolate substituents.

Studies into the 1,1-dithiolate coordination complexes initially focussed on investigating the effect of the tight bite-angle on the electronic and magnetic properties of Co^{II} bis(1,1-dithiolato) species. Electronic absorption spectroscopy proved the link between the energy and intensity of the $^4A_2 \rightarrow {}^4T_1(P)$ transitions in each D_{2d} complex and the electron-withdrawing strength of the ligand substituents, but magnetic susceptibility measurements proved inconclusive. In the solid-state results consistent with a $S = {}^1/_2$ were obtained, whilst fluid solution results were consistent with $S = {}^3/_2$. Co K-edge XAS confirmed the square-planar nature in the solid-state, with the difference attributed to the fluxional Co^{II} species changing $\{CoS_4\}$ coordination in solution. S K-edge XAS confirmed the link between substituent electron-withdrawing strength and $\{CoS_4\}$ electronic structure, with transition energies correlating strongly with the substituent electron-withdrawing strength in both the Co^{II} complexes and the free ligand salt.

To probe the ligand behaviour further Ni^{II} and Cu^{II} 1,1-dithiolate complexes were prepared, with electronic absorption spectroscopy confirming the trend, as in both cases the energy and intensity of the ligand field transitions increased as the electron-withdrawing strength decreased. EPR of the Cu^{II} species showed *g*- and *A*-values to be broadly similar across the series, however, whilst still revealing that the substituent-facilitated ligand charge

dominates the in-plane π-bonding in the complexes. The out-of-plane π-bond covalency was shown to be more influenced by the metal-ligand bite-angle. Cyclic voltammetry confirmed the presence of reversible $Cu^{III/II}$ redox events in each 1,1-dithiolate species, with the analogous $Ni^{III/II}$ oxidation events proving irreversible. Once again, the substituent effects were clear, with the redox potentials lowering as the substituent electron-withdrawing strength was reduced. The new Cu^{III} species $[Cu(i\text{-ect})_2]^-$ was successfully isolated, with Cu K-edge of the Cu^{II} and Cu^{III} species confirming oxidation of the parent species. S K-edge XAS revealed the same trend as the Co^{II} complexes and the free ligands, with the C−S π* covalency also increasing as substituent electron-withdrawing strength does.

Electronic absorption spectra confirmed the formation and purity of the Co, Ni, Cu and Zn bis(tetrathiotungstate) species, with $[Co(WS_4)_2]^{z-}$ (z = 2, 3) the focal point of the investigation into 3d tetrathiotungstate species. Magnetic susceptibility measurements showed a reduced magnetic moment in the reduced species, with the introduced electron coupling antiferromagnetically to the S = $^3/_2$ system. Co K-edge XAS showed the Co^{II} to be partially reduced, with the bulk of the reduction taking place on the tetrathiotungstate ligands. S K-edge showed the impact of the reduction, with the 1s → 4p transition energy of $[Co(WS_4)_2]^{3-}$ higher than both $[Co(WS_4)_2]^{2-}$ and $[Zn(WS_4)_2]^{2-}$.

In successfully probing the electronic structures of the complexes discussed above, the research here clearly demonstrates the value of using electronic and XAS spectroscopy in tandem. The value of using EPR in conjunction with both techniques has also been shown, with triangulation of the data obtained giving much more information about the Cu^{II} complexes than the simple sum of each measurement. The usefulness of the spectroscopic trident is thus clearly illustrated, although due to complexity in data analysis future use remains mostly confined to simple d^1 and d^9 paramagnetic complexes.

Many other avenues of exploration have also been left open, including broader studies into the effect of more significant alterations to the second coordination sphere on monometallic transition metal arylchalcogenate complexes, including studies specifically

examining the effect of the second coordination sphere in systems with varying coordination chalcogens. Examination of exchange coupling in other tetrachalcogenmetallate systems should also be undertaken, along with ac magnetic susceptibility measurements of both $[Co(WS_4)_2]^{2-}$ and $[Co(WS_4)_2]^{3-}$. Finally, broader investigations of the 1,1-dithiolate complexes should be undertaken, with research specifically focussing on the fluxional nature of the Co^{II}, and the isolation of further Cu^{III} species. The fact that there is reduced Cu−S π* per-hole S character in $[Cu(i\text{-ect})_2]^-$ relative to $[Cu(i\text{-ect})_2]^{2-}$ should also be noted, as it is the reverse of the trend reported for mnt^{2-} ligated species; further studies will clarify whether or not it is a trend, and in doing so possibly shed light on whether true Cu^{III} species do exist.

7 References

1. G. Wächtershäuser, *Prog. Biophys. Mol. Bio.*, 1992, **58**, 85.
2. S. Ōae, *Organic Chemistry of Sulfur*, Plenum Press, New York, NY, USA, 1977.
3. O. Kahn, *Molecular Magnetism*, Wiley-VCH, Weinheim, Germany, 1993.
4. D. W. Bruce, D. O'Hare and R. I. Walton, *Molecular Materials*, Wiley, Chichester, UK, 2011.
5. A. Abragam and B. Bleaney, *Electron Paramagnetic Resonance of Transition Ions*, Oxford University Press, Oxford, UK, 1970.
6. S. V. Vonsovskiĭ, *Ferromagnetic Resonance: The Phenomenon of Resonant Absorption of a High-Frequency Magnetic Field in Ferromagnetic Substances*, Pergamon Press, Oxford, UK, 1966.
7. D. J. Craik, *Magnetism: Principles and Applications*, Wiley-VCH, Weinheim, Germany,2003.
8. O. Smith, *Electr. World*, 1888, 116.
9. E. D. Daniel, C. D. Mee and M. H. Clark, *Magnetic Recording: The First 100 Years*, Wiley, Chichester, UK, 1999.
10. A. Katal, M. Wazid and R. H., *Big Data: Issues, Challenges, Tools and Good Practices*, Sixth International Conference on Contemporary Computing, Institute of Electrical and Electronics Engineers, Piscataway, NJ, USA, 2013.
11. G. Aromí and E. K. Brechin, in *Single-Molecule Magnets and Related Phenomena*, ed. R. Winpenny, Springer Berlin Heidelberg, Berlin, Heidelberg, Germany, 2006, 1.
12. M. N. Leuenberger and D. Loss, *Nature*, 2001, **410**, 789.
13. A. Ardavan, O. Rival, J. J. L. Morton, S. J. Blundell, A. M. Tyryshkin, G. A. Timco and R. E. P. Winpenny, *Phys. Rev. Lett.*, 2007, **98**, 057201.
14. L. Bogani and W. Wernsdorfer, *Nat. Mater.*, 2008, **7**, 179.
15. S. Hill, R. S. Edwards, N. Aliaga-Alcalde and G. Christou, *Science*, 2003, **302**, 1015.
16. E. Moreno-Pineda, C. Godfrin, F. Balestro, W. Wernsdorfer and M. Ruben, *Chem. Soc. Rev.*, 2018, **47**, 501.

17. C. Godfrin, A. Ferhat, R. Ballou, S. Klyatskaya, M. Ruben, W. Wernsdorfer and F. Balestro, *Phys. Rev. Lett.*, 2017, **119**, 187702.

18. F.-S. Guo, B. M. Day, Y.-C. Chen, M.-L. Tong, A. Mansikkamäki and R. A. Layfield, *Science*, 2018, **362**, 1400.

19. J. M. Zadrozny and J. R. Long, *J. Am. Chem. Soc.*, 2011, **133**, 20732.

20. M. Feng and M.-L. Tong, *Chem.: Eur. J.*, 2018, **24**, 7574.

21. D. E. Freedman, W. H. Harman, T. D. Harris, G. J. Long, C. J. Chang and J. R. Long, *J. Am. Chem. Soc.*, 2010, **132**, 1224.

22. M. Murrie, *Chem. Soc. Rev.*, 2010, **39**, 1986.

23. D. Gatteschi, R. Sessoli and J. Villain, *Molecular Nanomagnets*, Oxford University Press, Oxford, 2011.

24. S. M. J. Aubin, D. N. Hendrickson, S. M. J. Aubin, S. Spagna, H. J. Eppley, R. E. Sager, H. J. Eppley and G. Christou, *Chem. Commun.*, 1998, 803.

25. D. N. Woodruff, R. E. P. Winpenny and R. A. Layfield, *Chem. Rev.*, 2013, **113**, 5110.

26. S. M. J. Aubin, S. Spagna, H. J. Eppley, R. E. Sager, K. Folting, G. Christou and D. N. Hendrickson, *Mol. Cryst. Liq. Cryst. A*, 1997, **305**, 181.

27. Y.-S. Ding, K.-X. Yu, D. Reta, F. Ortu, R. E. P. Winpenny, Y.-Z. Zheng and N. F. Chilton, *Nat. Commun.*, 2018, **9**, 3134.

28. M. J. Giansiracusa, A. K. Kostopoulos, D. Collison, R. E. P. Winpenny and N. F. Chilton, *Chem. Commun.*, 2019, **55**, 7025.

29. U. Albold, H. Bamberger, P. P. Hallmen, J. v. Slageren and B. Sarkar, *Angew. Chem. Int. Ed.*, 2019, **58**, 9802.

30. D. Gatteschi and R. Sessoli, *Angew. Chem. Int. Ed.*, 2003, **42**, 268.

31. H. A. Kramers, *Proc. Acad. Sci. Amsterdam*,1930, **33**, 959.

32. F. Kouichi, O.-N. Hiroaki and H. Noboru, *Bull. Chem. Soc. Jpn.*, 1991, **64**, 1205.

33. A. M. Ako, I. J. Hewitt, V. Mereacre, R. Clérac, W. Wernsdorfer, C. E. Anson and A. K. Powell, *Angew. Chem. Int. Ed.*, 2006, **45**, 4926.

34. F. Neese and D. A. Pantazis, *Faraday Discuss.*, 2011, **148**, 229.

35. W. H. Harman, T. D. Harris, D. E. Freedman, H. Fong, A. Chang, J. D. Rinehart, A. Ozarowski, M. T. Sougrati, F. Grandjean, G. J. Long, J. R. Long and C. J. Chang, *J. Am. Chem. Soc.*, 2010, **132**, 18115.

36. J. M. Zadrozny, J. Telser and J. R. Long, *Polyhedron*, 2013, **64**, 209.

37. E. A. Suturina, D. Maganas, E. Bill, M. Atanasov and F. Neese, *Inorg. Chem.*, 2015, **54**, 9948.

38. M. R. Saber and K. R. Dunbar, *Chem. Commun.*, 2014, **50**, 12266.

39. L. Smolko, J. Černák, M. Dušek, J. Miklovič, J. Titiš and R. Boča, *Dalton Trans.*, 2015, **44**, 17565.

40. X.-N. Yao, M.-W. Yang, J. Xiong, J.-J. Liu, C. Gao, Y.-S. Meng, S.-D. Jiang, B.-W. Wang and S. Gao, *Inorg. Chem. Front.*, 2017, **4**, 701.

41. S. Sottini, G. Poneti, S. Ciattini, N. Levesanos, E. Ferentinos, J. Krzystek, L. Sorace and P. Kyritsis, *Inorg. Chem.*, 2016, **55**, 9537.

42. E. Ferentinos, M. Xu, A. Grigoropoulos, I. Bratsos, C. P. Raptopoulou, V. Psycharis, S.-D. Jiang and P. Kyritsis, *Inorg. Chem. Front.*, 2019, **6**, 1405.

43. E. A. Suturina, J. Nehrkorn, J. M. Zadrozny, J. Liu, M. Atanasov, T. Weyhermüller, D. Maganas, S. Hill, A. Schnegg, E. Bill, J. R. Long and F. Neese, *Inorg. Chem.*, 2017, **56**, 3102.

44. M. Craven, M. H. Nygaard, J. M. Zadrozny, J. R. Long and J. Overgaard, *Inorg. Chem.*, 2018, **57**, 6913.

45. S. Vaidya, S. Tewary, S. K. Singh, S. K. Langley, K. S. Murray, Y. Lan, W. Wernsdorfer, G. Rajaraman and M. Shanmugam, *Inorg. Chem.*, 2016, **55**, 9564.

46. S. Vaidya, P. Shukla, S. Tripathi, E. Rivière, T. Mallah, G. Rajaraman and M. Shanmugam, *Inorg. Chem.*, 2018, **57**, 3371.

47. A. Świtlicka, B. Machura, R. Kruszynski, J. Cano, L. M. Toma, F. Lloret and M. Julve, *Dalton Trans.*, 2018, **47**, 5831.

48. S. Gomez-Coca, E. Cremades, N. Aliaga-Alcalde and E. Ruiz, *J. Am. Chem. Soc.*, 2013, **135**, 7010.

49. A. K. Bar, C. Pichon and J.-P. Sutter, *Coord. Chem. Rev.*, 2016, **308**, 346.

50. J. M. Zadrozny, M. Atanasov, A. M. Bryan, C.-Y. Lin, B. D. Rekken, P. P. Power, F. Neese and J. R. Long, *Chem. Sci.*, 2013, **4**, 125.

51. J. M. Zadrozny, D. J. Xiao, M. Atanasov, G. J. Long, F. Grandjean, F. Neese and J. R. Long, *Nat. Chem.*, 2013, **5**, 577.

52. Y.-S. Meng, Z. Mo, B.-W. Wang, Y.-Q. Zhang, L. Deng and S. Gao, *Chem. Sci.*, 2015, **6**, 7156.

53. R. C. Poulten, M. J. Page, A. G. Algarra, J. J. Le Roy, I. López, E. Carter, A. Llobet, S. A. Macgregor, M. F. Mahon, D. M. Murphy, M. Murugesu and M. K. Whittlesey, *J. Am. Chem. Soc.*, 2013, **135**, 13640.

54. C. G. Werncke, P. C. Bunting, C. Duhayon, J. R. Long, S. Bontemps and S. Sabo-Etienne, *Angew. Chem. Int. Ed.*, 2015, **54**, 245.

55. P. P. Samuel, K. C. Mondal, N. Amin Sk, H. W. Roesky, E. Carl, R. Neufeld, D. Stalke, S. Demeshko, F. Meyer, L. Ungur, L. F. Chibotaru, J. Christian, V. Ramachandran, J. van Tol and N. S. Dalal, *J. Am. Chem. Soc.*, 2014, **136**, 11964.

56. P. E. Kazin, M. A. Zykin, L. A. Trusov, A. A. Eliseev, O. V. Magdysyuk, R. E. Dinnebier, R. K. Kremer, C. Felser and M. Jansen, *Chem. Commun.*, 2017, **53**, 5416.

57. P. E. Kazin, M. A. Zykin, W. Schnelle, Y. V. Zubavichus, K. A. Babeshkin, V. A. Tafeenko, C. Felser and M. Jansen, *Inorg. Chem.*, 2017, **56**, 1232.

58. M. A. Zykin, K. A. Babeshkin, O. V. Magdysyuk, E. O. Anokhin, W. Schnelle, C. Felser, M. Jansen and P. E. Kazin, *Inorg. Chem.*, 2017, **56**, 14077.

59. P. C. Bunting, M. Atanasov, E. Damgaard-Møller, M. Perfetti, I. Crassee, M. Orlita, J. Overgaard, J. van Slageren, F. Neese and J. R. Long, *Science*, 2018, **362**, 7319.

60. Y. Rechkemmer, F. D. Breitgoff, M. van der Meer, M. Atanasov, M. Hakl, M. Orlita, P. Neugebauer, F. Neese, B. Sarkar and J. van Slageren, *Nat. Commun.*, 2016, **7**, 10467.

61. D. C. Bradley, M. B. Hursthouse and P. F. Rodesiler, *J. Chem. Soc. Chem. Comm.*, 1969, 14.

62. P.-H. Lin, N. C. Smythe, S. I. Gorelsky, S. Maguire, N. J. Henson, I. Korobkov, B. L. Scott, J. C. Gordon, R. T. Baker and M. Murugesu, *J. Am. Chem. Soc.*, 2011, **133**, 15806.

63. A. Eichhöfer, Y. Lan, V. Mereacre, T. Bodenstein and F. Weigend, *Inorg. Chem.*, 2014, **53**, 1962.

64. A. M. Bryan, G. J. Long, F. Grandjean and P. P. Power, *Inorg. Chem.*, 2013, **52**, 12152.

65. Y.-F. Deng, T. Han, B. Yin and Y.-Z. Zheng, *Inorg. Chem. Front.*, 2017, **4**, 1141.

66. N. Ge, Y.-Q. Zhai, Y.-F. Deng, Y.-S. Ding, T. Wu, Z.-X. Wang, Z. Ouyang, H. Nojiri and Y.-Z. Zheng, *Inorg. Chem. Front.*, 2018, **5**, 2486.

67. W. Lin, T. Bodenstein, V. Mereacre, K. Fink and A. Eichhöfer, *Inorg. Chem.*, 2016, **55**, 2091.

68. D. Pinkowicz, F. J. Birk, M. Magott, K. Schulte and K. R. Dunbar, *Chem.: Eur. J.*, 2017, **23**, 3548.

69. K. A. Schulte, K. R. Vignesh and K. R. Dunbar, *Chem. Sci.*, 2018, **9**, 9018.

70. Y.-F. Deng, T. Han, Z. Wang, Z. Ouyang, B. Yin, Z. Zheng, J. Krzystek and Y.-Z. Zheng, *Chem. Commun.*, 2015, **51**, 17688.

71. M. S. Fataftah, J. M. Zadrozny, D. M. Rogers and D. E. Freedman, *Inorg. Chem.*, 2014, **53**, 10716.

72. T. Wu, Y.-Q. Zhai, Y.-F. Deng, W.-P. Chen, T. Zhang and Y.-Z. Zheng, *Dalton Trans.*, 2019, **48**, 15419.

73. D. Tu, D. Shao, H. Yan and C. Lu, *Chem. Commun.*, 2016, **52**, 14326.

74. E. Carl, S. Demeshko, F. Meyer and D. Stalke, *Chem.: Eur. J.*, 2015, **21**, 10109.

75. D. R. Alcoba, O. B. Oña, G. E. Massaccesi, A. Torre, L. Lain, J. I. Melo, J. E. Peralta and J. M. Oliva-Enrich, *Inorg. Chem.*, 2018, **57**, 7763.

76. O. B. Oña, D. R. Alcoba, G. E. Massaccesi, A. Torre, L. Lain, J. I. Melo, J. M. Oliva-Enrich and J. E. Peralta, *Inorg. Chem.*, 2019, **58**, 2550.

77. A. Cornia, M. Mannini, P. Sainctavit and R. Sessoli, *Chem. Soc. Rev.*, 2011, **40**, 3076.

78. E. Kiefl, M. Mannini, K. Bernot, X. Yi, A. Amato, T. Leviant, A. Magnani, T. Prokscha, A. Suter, R. Sessoli and Z. Salman, *ACS Nano*, 2016, **10**, 5663.

79. M. Mannini, F. Pineider, C. Danieli, F. Totti, L. Sorace, P. Sainctavit, M. A. Arrio, E. Otero, L. Joly, J. C. Cezar, A. Cornia and R. Sessoli, *Nature*, 2010, **468**, 417.

80. D. Coucouvanis, *Prog. Inorg. Chem.*, 1970, **11**, 233.

81. N. Rettberg, U. Wagner and K. Hartke, *Arch. Pharm.*, 1993, **326**, 977.

82. B. G. Werden, E. Billig and H. B. Gray, *Inorg. Chem.*, 1966, **5**, 78.

83. G. N. Schrauzer and V. Mayweg, *J. Am. Chem. Soc.*, 1962, **84**, 3221.

84. R. Eisenberg and H. B. Gray, *Inorg. Chem.*, 2011, **50**, 9741.

85. S. Sproules, *Prog. Inorg. Chem.*, 2014, **58**, 1.

86. W. E. Newton and S. Otsuka, *Molybdenum Chemistry of Biological Significance*, Springer, New York, NY, USA,1980.

87. P. Cassoux, C. J. Bowlas, K. Lahlil, A. Moradpour, J. Bonvoisin and J.-P. Launay, *Acta Phys. Pol. A*, 1995, **87**, 743.

88. W. O. Foye, J. M. Kauffman, J. J. Lanzillo and E. F. Lasala, *J. Pharm. Sci.*, 1975, **64**, 1371.

89. F. J. Hollander, R. Pedelty and D. Coucouvanis, *J. Am. Chem. Soc.*, 1974, **96**, 4032.

90. F. J. Hollander, M. L. Caffery and D. Coucouvanis, *J. Am. Chem. Soc.*, 1974, **96**, 4682.

91. J. R. Dilworth and N. Wheatley, *Coord. Chem. Rev.*, 2000, **199**, 89.

92. K. Akiko and S. Yukiyoshi, *Bull. Chem. Soc. Jpn.*, 1977, **50**, 2650.

93. G. Dong, F. R. Fronczek, S. F. Watkins and I. Bernal, *Acta Crystallogr. C*, 1998, **54**.

94. M. Bonamico, G. Dessy, C. Mariani, A. Vaciago and L. Zambonelli, *Acta Crystallogr.*, 1965, **19**, 619.

95. Q. Fernando and C. D. Green, *J. Inorg. Nucl. Chem.*, 1967, **29**, 647.

96. B. F. Hoskins, E. R. T. Tiekink and G. Winter, *Z. Kristallogr. Cryst. Mater.*, 1985, **172**, 257.

97. G. Hogarth, *Prog. Inorg. Chem.*, 2005, **53**, 71

98. N. M. Comerlato, W. T. A. Harrison, R. A. Howie, J. N. Low, A. C. Silvino, J. L. Wardell and S. M. S. V. Wardell, *Acta Crystallogr. C*, 2002, **58**, 105.

99. D. Long, H. Hou, X. Xin, K. Yu, B. Luo and L. Chen, *J. Coord. Chem.*, 1996, **38**, 15.

100. H. Klug, *Acta Crystallogr.*, 1966, **21**, 536.

101. M. Bonamico, G. Mazzone, A. Vaciago and L. Zambonelli, *Acta Crystallogr.*, 1965, **19**, 898.

102. D. Coucouvanis, *Prog. Inorg. Chem.*, 1979, **26**, 301.

103. M. Green, R. B. L. Osborn and F. G. A. Stone, *J. Chem. Soc. A*, 1970, 944.

104. P. C. Savino and R. D. Bereman, *Inorg. Chem.*, 1973, **12**, 173.

105. R. D. Bereman and D. Nalewajek, *Inorg. Chem.*, 1976, **15**, 2981.

106. D. M. Baird and R. D. Bereman, *J. Org. Chem.*, 1981, **46**, 458.

107. H. M. Colquhoun, J. F. Stoddart and D. J. Williams, *Angew. Chem. Int. Ed.*, 1986, **25**, 487.

108. P. E. M. Siegbahn and R. H. Crabtree, *J. Am. Chem. Soc.*, 1996, **118**, 4442.

109. W. Beck and K. Stetter, *Inorg. Nucl. Chem. Lett.*, 1966, **2**, 383.

110. W. Beck, K. H. Stetter, S. Tadros and K. E. Schwarzhans, *Chem. Ber.*, 1967, **100**, 3944.

111. W. Beck and S. Tadros, *Z. Anorg. Allg. Chem.*, 1970, **375**, 231.

112. W. Beck, J. Evers, M. Göbel, G. Oehlinger and T. M. Klapötke, *Z. Anorg. Allg. Chem.*, 2007, **633**, 1417.

113. B. R. Hollebone and R. S. Nyholm, *J. Chem. Soc. A*, 1971, 332.

114. I. G. Dance, *J. Am. Chem. Soc.*, 1979, **101**, 6264.

115. I. G. Dance and J. C. Calabrese, *J. Chem. Soc. Chem. Comm.*, 1975, 762.

116. T. Herskovitz, B. A. Averill, R. H. Holm, J. A. Ibers, W. D. Phillips and J. F. Weiher, *Proc. Natl. Acad. Sci. U.S.A.*, 1972, **69**, 2437.

117. W. Lovenberg and B. E. Sobel, *Proc. Natl. Acad. Sci. U.S.A.*, 1965, **54**, 193.

118. J. C. M. Tsibris and R. W. Woody, *Coord. Chem. Rev.*, 1970, **5**, 417.

119. P. Venkateswara Rao and R. H. Holm, *Chem. Rev.*, 2004, **104**, 527.

120. R. H. Holm, in *Comprehensive Coordination Chemistry II*, eds. J. A. McCleverty and T. J. Meyer, Pergamon, Oxford, UK, 2003, 61.

121. G. Christou and C. D. Garner, *J. Chem. Soc. Dalton*, 1979, 1093.

122. A. Kostikas, V. Petrouleas, A. Simopoulos, D. Coucouvanis and D. G. Holah, *Chem. Phys. Lett.*, 1976, **38**, 582.

123. D. Coucouvanis, D. Swenson, P. Stremple and N. C. Baenziger, *J. Am. Chem. Soc.*, 1979, **101**, 3392.

124. K. S. Hagen, J. M. Berg and R. H. Holm, *Inorganica Chim. Acta*, 1980, **45**, L17.

125. K. S. Hagen, J. G. Reynolds and R. H. Holm, *J. Am. Chem. Soc.*, 1981, **103**, 4054.

126. K. S. Hagen and R. H. Holm, *J. Am. Chem. Soc.*, 1982, **104**, 5496.

127. J. F. You, B. S. Snyder, G. C. Papaefthymiou and R. H. Holm, *J. Am. Chem. Soc.*,1990, **112**, 1067.

128. W. Mertz, *Science*, 1981, **213**, 1332.

129. M. A. Halcrow and G. Christou, *Chem. Rev.*, 1994, **94**, 2421.

130. S. W. May and J.-Y. Kuo, *Biochemistry*, 1978, **17**, 3333.

131. A. T. Kowal, I. C. Zambrano, I. Moura, J. J. G. Moura, J. LeGall and M. K. Johnson, *Inorg. Chem.*, 1988, **27**, 1162.

132. M. Millar, S. A. Koch and R. Fikar, *Inorganica Chim. Acta*, 1984, **88**, L15.

133. M. Millar, J. F. Lee, S. A. Koch and R. Fikar, *Inorg. Chem.*, 1982, **21**, 4105.

134. R. Fikar, S. A. Koch and M. M. Millar, *Inorg. Chem.*, 1985, **24**, 3311.

135. M. Millar, J. F. Lee, T. O'Sullivan, S. A. Koch and R. Fikar, *Inorganica Chim. Acta*, 1996, **243**, 333.

136. A. Silver, S. A. Koch and M. Millar, *Inorganica Chim. Acta*, 1993, **205**, 9.

137. K. Ruhlandt-Senge and P. P. Power, *J. Chem. Soc. Dalton*, 1993, 649.

138. P. P. Power and S. C. Shoner, *Angew. Chem. Int. Ed.*, 1991, **30**, 330.

139. S. A. Koch, R. Fikar, M. Millar and T. O'Sullivan, *Inorg. Chem.*, 1984, **23**, 121.

140. P. P. Power, *Chem. Rev.*, 2012, **112**, 3482.

141. T. Nguyen, A. Panda, M. M. Olmstead, A. F. Richards, M. Stender, M. Brynda and P. P. Power, *J. Am. Chem. Soc.*, 2005, **127**, 8545.

142. S. Petit, G. Pilet, D. Luneau, L. F. Chibotaru and L. Ungur, *Dalton Trans.*, 2007, 4582.

143. B. N. Figgis, M. Gerloch, R. Mason and S. Nyholm Ronald, *Proc. R. Soc. A.*, 1964, **279**, 210.

144. B. N. Figgis and M. A. Hitchman, *Ligand Field Theory and Its Applications*, Wiley-VCH, Weinheim, Germany, 2000.

145. R. Herchel, P. Zoufalý and I. Nemec, *RSC Adv.*, 2019, **9**, 569.

146. R. Maurice, L. Vendier and J.-P. Costes, *Inorg. Chem.*, 2011, **50**, 11075.

147. V. Balzani, N. Sabbatini and F. Scandola, *Chem. Rev.*, 1986, **86**, 319.

148. J. M. Stauber, G. E. Alliger, D. G. Nocera and C. C. Cummins, *Inorg. Chem.*, 2017, **56**, 7615.

149. G. D. Stucky, J. B. Folkers and T. J. Kistenmacher, *Acta Crystallogr*, 1967, **23**, 1064.

150. K. Fukui, H. Masuda, H. Ohya-Nishiguchi and H. Kamada, *Inorganica Chim. Acta*, 1995, **238**, 73.

151. W. P. Chung, J. C. Dewan and M. A. Walters, *J. Am. Chem. Soc.*, 1991, **113**, 525.

152. R. C. Walroth, J. T. Lukens, S. N. MacMillan, K. D. Finkelstein and K. M. Lancaster, *J. Am. Chem. Soc.*, 2016, **138**, 1922.

153. S. Sproules and K. Wieghardt, *Coord. Chem. Rev.*, 2011, **255**, 837.

154. K. Chakarawet, P. C. Bunting and J. R. Long, *J. Am. Chem. Soc.*, 2018, **140**, 2058.

155. A. I. Biggs, *Trans. Faraday Soc.*, 1956, **52**, 35.

156. J. R. Gandler and W. P. Jencks, *J. Am. Chem. Soc.*, 1982, **104**, 1937.

157. W. P. Jencks and K. Salvesen, *J. Am. Chem. Soc.*, 1971, **93**, 4433.

158. E. M. Tyapochkin and E. I. Kozliak, *J Porphyr. Phthalocyanines*, 2001, **05**, 405.

159. C. L. Liotta, E. M. Perdue and H. P. Hopkins, *J. Am. Chem. Soc.*, 1974, **96**, 7981.

160. P. De Maria and A. Fini, *J. Chem. Soc., Perkin Trans. 2*, 1973, 1773.

161. V. A. Shreider, *Bull. Acad. Sci. USSR, Div. Chem. Sci.*, 1984, **33**, 1675.

162. P. Robson, M. Stacey, R. Stephens and J. C. Tatlow, *J. Chem. Soc.*, 1960, 475.

163. M. Kulka, *J. Org. Chem.*, 1959, **24**, 235.

164. E. J. Forbes, R. D. Richardson, M. Stacey and J. C. Tatlow, *J. Chem. Soc.*, 1959, 2019.

165. S. Chattopadhyay, T. Deb, J. L. Petersen, V. G. Young and M. P. Jensen, *Inorg. Chem.*, 2010, **49**, 457.

166. J. Zhou, J. W. Raebiger, C. A. Crawford and R. H. Holm *J. Am. Chem. Soc.*, 1997, **119**, 6242.

167. Y. Zang and L. Que, *Inorg. Chem.*, 1995, **34**, 1030.

168. A. Eichhöfer and S. Lebedkin, *Inorg. Chem.*, 2018, **57**, 602.

169. A. Eichhöfer and G. Buth, *Eur. J. Inorg. Chem.*, 2019, 639.

170. A. Eichhöfer and G. Buth, *Dalton Trans.*, 2016, **45**, 17382.

171. D. T. Corwin, E. S. Gruff and S. A. Koch, *Inorganica Chim. Acta*, 1988, **151**, 5.

172. F. Matsuda, H. Tamura and G.-e. Matsubayashi, *Inorganica Chim. Acta*, 1999, **295**, 239.

173. M. Nakata, N. Ueyama, A. Nakamura, T. Nozawa and M. Hatano, *Inorg. Chem.*, 1983, **22**, 3028.

174. J. Ferguson, *J. Chem. Phys.*, 1960, **32**, 528.

175. E. I. Solomon, S. I. Gorelsky and A. Dey, *J. Comput. Chem.*, 2006, **27**, 1415.

176. A. M. Thomas, B.-L. Lin, E. C. Wasinger and T. D. P. Stack, *J. Am. Chem. Soc.*, 2013, **135**, 18912.

177. L. L. Funck and T. R. Ortolano, *Inorg. Chem.*, 1968, **7**, 567.

178. F. A. Cotton, D. M. L. Goodgame and M. Goodgame, *J. Am. Chem. Soc.*, 1961, **83**, 4690.

179. D. F. Evans, *J. Chem. Soc.*, 1959, 2003.

180. F. G. Baddar, O. M. M. Hilal and S. Sugden, *J. Chem. Soc.*, 1949, 132.

181. J. Pelzl, R. Meckenstock, D. Spoddig, F. Schreiber, J. Pflaum and Z. Frait, *J. Phys. Condens. Matter*, 2003, **15**, S451.

182. M.-L. Du and M.-G. Zhao, *Phys. Status Solidi B*, 1989, **153**, 249.

183. B. Odom, D. Hanneke, B. D'Urso and G. Gabrielse, *Phys. Rev. Lett.*, 2006, **97**, 030801.

184. L. A. Yatsunyk and F. A. Walker, *Inorg. Chem.*, 2004, **43**, 757.

185. N. Kosugi, T. Yokoyama, K. Asakura and H. Kuroda, *Chem. Phys.*, 1984, **91**, 249.

186. B. Hedman, K. O. Hodgson and E. I. Solomon, *J. Am. Chem. Soc.*, 1990, **112**, 1643.

187. T. Glaser, B. Hedman, K. O. Hodgson and E. I. Solomon, *Acc. Chem. Res*, 2000, **33**, 859.

188. E. I. Solomon, B. Hedman, K. O. Hodgson, A. Dey and R. K. Szilagyi, *Coord. Chem. Rev.*, 2005, **249**, 97.

189. S. E. Shadle, B. Hedman, K. O. Hodgson and E. I. Solomon, *J. Am. Chem. Soc.*, 1995, **117**, 2259.

190. K. Rose Williams, B. Hedman, K. O. Hodgson and E. I. Solomon, *Inorganica Chim. Acta*, 1997, **263**, 315.

191. R. Sarangi, S. DeBeer George, D. J. Rudd, R. K. Szilagyi, X. Ribas, C. Rovira, M. Almeida, K. O. Hodgson, B. Hedman and E. I. Solomon, *J. Am. Chem. Soc.*, 2007, **129**, 2316.

192. R. Sarangi, J. Cho, W. Nam and E. I. Solomon, *Inorg. Chem.*, 2011, **50**, 614.

193. L. Robinet, M. Spring, S. Pagès-Camagna, D. Vantelon and N. Trcera, *Anal. Chem.*, 2011, **83**, 5145.

194. R. A. Bair and W. A. Goddard, *Phys. Rev. B*, 1980, **22**, 2767.

195. P. Frank, M. Benfatto, B. Hedman and K. O. Hodgson, *Inorg. Chem.*, 2008, **47**, 4126.

196. C. Milsmann, S. Sproules, E. Bill, T. Weyhermüller, S. D. George and K. Wieghardt, *Chem.: Eur. J.*, 2010, **16**, 3628.

197. A. Vairavamurthy, *Spectrochim. Acta A*, 1998, **54**, 2009.

198. P. Frank, B. Hedman and K. O. Hodgson, *Inorg. Chem.*, 1999, **38**, 260.

199. G. R. Fulmer, A. J. M. Miller, N. H. Sherden, H. E. Gottlieb, A. Nudelman, B. M. Stoltz, J. E. Bercaw and K. I. Goldberg, *Organometallics*, 2010, **29**, 2176.

200. C. J. O'Connor, E. Sinn, E. J. Cukauskas and B. S. Deaver Jr, *Inorganica Chim. Acta*, 1979, **32**, 29.

201. K. Ray, S. DeBeer George, E. I. Solomon, K. Wieghardt and F. Neese, *Chem.: Eur. J.*, 2007, **13**, 2783.

202. G. N. George, *EXAFSPAK & EDG_FIT*, Stanford Synchrotron Radiation Laboratory, Stanford Linear Accelerator Center, Stanford University, CA, 2000.

203. B. Hedman, P. Frank, S. F. Gheller, A. L. Roe, W. E. Newton and K. O. Hodgson, *J. Am. Chem. Soc.*, 1988, **110**, 3798.

204. W. Rundel, *Chem. Ber.*, 1968, **101**, 2956.

205. N. S. Gill, F. B. Taylor, W. E. Hatfield, W. E. Parker, C. S. Fountain and F. L. Bunger, *Inorg. Synth.*, 2007, **9**, 136.

206. W. L. F. Armarego, *Purification of Laboratory Chemicals*, Elsevier, Amsterdam, Netherlands, 2017.

207. A. Zarkadoulas, E. Koutsouri and C. A. Mitsopoulou, *Coord. Chem. Rev.*, 2012, **256**, 2424.

208. A. J. Clough, J. M. Skelton, C. A. Downes, A. A. de la Rosa, J. W. Yoo, A. Walsh, B. C. Melot and S. C. Marinescu, *J. Am. Chem. Soc.*, 2017, **139**, 10863.

209. W. R. McNamara, Z. Han, P. J. Alperin, W. W. Brennessel, P. L. Holland and R. Eisenberg, *J. Am. Chem. Soc.*, 2011, **133**, 15368.

210. J. P. Fackler and D. Coucouvanis, *Chem. Commun.*, 1965, 556.

211. J. P. Fackler and D. Coucouvanis, *J. Am. Chem. Soc.*, 1966, **88**, 3913.

212. B. J. Kalbacher and R. D. Bereman, *Inorg. Chem.*, 1973, **12**, 2997.

213. J. P. Fackler and D. G. Holah, *Inorg. Nucl. Chem. Lett.*, 1966, **2**, 251.

214. T. Selby-Karney, D. A. Grossie, K. Arumugam, E. Wright and P. Chandrasekaran, *J. Mol. Struct.*, 2017, **1141**, 477.

215. J. A. McCleverty, N. M. Atherton, N. G. Connelly and C. J. Winscom, *J. Chem. Soc. A*, 1969, 2242.

216. B. Kang, J. Peng, M. Hong, D. Wu, X. Chen, L. Weng, X. Lei and H. Liu, *J. Chem. Soc., Dalton*, 1991, 2897.

217. S. A. Baudron and P. Batail, *Acta Crystallogr. C*, 2002, **58**, 575.

218. C. N. R. Rao, R. Venkataraghavan and T. R. Kasturi, *Can. J. Chem.*, 1964, **42**, 36.

219. E. Barchiesi, S. Bradamante, R. Ferraccioli and G. A. Pagani, *J. Chem. Soc., Perkin Trans. 2*, 1990, 375.

220. S. Pedersoli, C. F. Tormena and R. Rittner, *J. Mol. Struct.*, 2008, **875**, 235.

221. N. Ouwerkerk, Jacques v. Boom, J. Lugtenburg and J. Raap, *Eur. J. Org. Chem.*, 2002, 2356.

222. L. Wang, W. Huang, R. Li, D. Gehrig, P. W. M. Blom, K. Landfester and K. A. I. Zhang, *Angew. Chem. Int. Ed.*, 2016, **55**, 9783.

223. H. E. Gottlieb, V. Kotlyar and A. Nudelman, *J. Org. Chem.*, 1997, **62**, 7512.

224. M. U. Hasan, *Org. Magn. Reson.*, 1980, **14**, 447.

225. K. L. Williamson, M. U. Hasan and D. R. Clutter, *J. Magn. Reson.*, 1978, **30**, 367.

226. J. D. Forrester, A. Zalkin and D. H. Templeton, *Inorg. Chem.*, 1964, **3**, 1500.

227. M. S. Fataftah, S. C. Coste, B. Vlaisavljevich, J. M. Zadrozny and D. E. Freedman, *Chem. Sci.*, 2016, **7**, 6160.

228. A. Davison, N. Edelstein, R. H. Holm and A. H. Maki, *J. Am. Chem. Soc.*, 1963, **85**, 3049.

229. M. R. Truter, *Acta Crystallogr.*, 1967, **22**, 55.

230. M. S. Weininger, J. E. O'Connor and E. L. Amma, *Inorg. Chem.*, 1969, **8**, 424.

231. S. Swaminathan, B. M. Craven and R. K. McMullan, *Acta Crystallogr. B*, 1984, **40**, 300.

232. J. Han, C.-W. Yau, C.-K. Lam and T. C. W. Mak, *J. Am. Chem. Soc.*, 2008, **130**, 10315.

233. P. Strauch, A. Kossmann, A. Kelling and U. Schilde, *Chem. Pap.*, 2016, **70**, 61.

234. K. L. McEwen, *J. Chem. Phys.*, 1960, **32**, 1801.

235. Y. Nishida, K. Hayashida, A. Sumita and S. Kida, *Inorganica Chim. Acta*, 1978, **31**, 19.

236. C. Hansch, A. Leo and R. W. Taft, *Chem. Rev.*, 1991, **91**, 165.

237. S. Valkai, J. Liszi and I. Szalai, *J. Chem. Thermodyn.*, 1998, **30**, 825.

238. C. Piguet, *J. Chem. Educ.*, 1997, **74**, 815.

239. G. A. Bain and J. F. Berry, *J. Chem. Educ.*, 2008, **85**, 532.

240. R. Rousseau, A. Ozarowski, R. Aroca, L. de A. Soares and M. Trsic, *J. Mol. Struct.*, 1994, **317**, 287.

241. Y. K. Nishida, Sigeo, *Bull. Chem. Soc. Jpn.*, 1972, **45**, 461.

242. Y. Nishida and S. Kida, *Coord. Chem. Rev.*, 1979, **27**, 275.

243. R. M. Haas, M. Arshad, J. Anthony, P. J. Altmann, A. Pöthig, F. H. Köhler and C. R. Hess, *Inorg. Chem. Front.*, 2016, **3**, 616.

244. A. Dey, T. Glaser, M. M. J. Couture, L. D. Eltis, R. H. Holm, B. Hedman, K. O. Hodgson and E. I. Solomon, *J. Am. Chem. Soc.*, 2004, **126**, 8320.

245. H. H. Alkam, K. M. Kanan and C. C. Hadjikostas, *Polyhedron*, 2005, **24**, 2944.

246. G. Sheldrick, *Acta Crystallogr. A*, 1990, **46**, 467.

247. G. Sheldrick, *Acta Crystallogr. A*, 2008, **64**, 112.

248. L. Farrugia, *J. Appl. Crystallogr.*, 1999, **32**, 837.

249. R. C. Clark and J. S. Reid, *Acta Crystallogr. A*, 1995, **51**, 887.

250. C. F. Macrae, P. R. Edgington, P. McCabe, E. Pidcock, G. P. Shields, R. Taylor, M. Towler and J. van de Streek, *J. Appl. Crystallogr.*, 2006, **39**, 453.

251. H. S. P. Rao and S. Sivakumar, *J. Org. Chem.*, 2005, **70**, 4524.

252. W. R. Hatchard, *J. Org. Chem.*, 1964, **29**, 660.

253. K. A. Jensen and L. Henriksen, *Acta Chem. Scand.*, 1968, **22**, 1107.

254. E. Söderbäck, *Acta Chem. Scand.*, 1963, **17**, 362.

255. M. Murugesu, M. Habrych, W. Wernsdorfer, K. A. Abboud and G. Christou, *J. Am. Chem. Soc.*, 2004, **126**, 4766.

256. Y.-Y. Zhu, C. Cui, Y.-Q. Zhang, J.-H. Jia, X. Guo, C. Gao, K. Qian, S.-D. Jiang, B.-W. Wang, Z.-M. Wang and S. Gao, *Chem. Sci.*, 2013, **4**, 1802.

257. Y.-Z. Zheng, G.-J. Zhou, Z. Zheng and R. E. P. Winpenny, *Chem. Soc. Rev.*, 2014, **43**, 1462.

258. G. Aromí, D. Aguilà, P. Gamez, F. Luis and O. Roubeau, *Chem. Soc. Rev.*, 2012, **41**, 537.

259. L. F. Jones, E. K. Brechin, D. Collison, M. Helliwell, T. Mallah, S. Piligkos, G. Rajaraman and W. Wernsdorfer, *Inorg. Chem.*, 2003, **42**, 6601.

260. D.-C. Hu, H. Feng, K.-X. Shang, Y.-J. Wu, J. Sun and J.-C. Liu, *ChemistrySelect*, 2017, **2**, 9024.

261. A. V. Palii, B. S. Tsukerblat, E. Coronado, J. M. Clemente-Juan and J. J. Borrás-Almenar, *J. Chem. Phys.*, 2003, **118**, 5566.

262. G. E. Kostakis, S. P. Perlepes, V. A. Blatov, D. M. Proserpio and A. K. Powell, *Coord. Chem. Rev.*, 2012, **256**, 1246.

263. J. D. Rinehart, M. Fang, W. J. Evans and J. R. Long, *J. Am. Chem. Soc.*, 2011, **133**, 14236.

264. J. D. Rinehart, M. Fang, W. J. Evans and J. R. Long, *Nat. Chem.*, 2011, **3**, 538.

265. I.-R. Jeon, J. G. Park, D. J. Xiao and T. D. Harris, *J. Am. Chem. Soc.*, 2013, **135**, 16845.

266. Y.-Z. Zheng, M. Speldrich, H. Schilder, X.-M. Chen and P. Kögerler, *Dalton Trans.*, 2010, **39**, 10827.

267. S. Hu, J.-L. Liu, Z.-S. Meng, Y.-Z. Zheng, Y. Lan, A. K. Powell and M.-L. Tong, *Dalton Trans.*, 2011, **40**, 27.

268. Y.-L. Zhou, M.-H. Zeng, X.-C. Liu, H. Liang and M. Kurmoo, *Chem.: Eur. J.*, 2011, **17**, 14084.

269. A. V. Funes, L. Carrella, L. Sorace, E. Rentschler and P. Alborés, *Dalton Trans.*, 2015, **44**, 2390.

270. L. Jiang, D.-Y. Zhang, J.-J. Suo, W. Gu, J.-L. Tian, X. Liu and S.-P. Yan, *Dalton Trans.*, 2016, **45**, 10233.

271. S. Manna, A. Bhunia, S. Mistri, J. Vallejo, E. Zangrando, H. Puschmann, J. Cano and S. C. Manna, *Eur. J. Inorg. Chem.*, 2017, 2585.

272. D. Li, S. Parkin, G. Wang, G. T. Yee, A. V. Prosvirin and S. M. Holmes, *Inorg. Chem.*, 2005, **44**, 4903.

273. F. Karadas, E. J. Schelter, M. Shatruk, A. V. Prosvirin, J. Bacsa, D. Smirnov, A. Ozarowski, J. Krzystek, J. Telser and K. R. Dunbar, *Inorg. Chem.*, 2008, **47**, 2074.

274. L.-C. Kang, M.-X. Yao, X. Chen, Y.-Z. Li, Y. Song, J.-L. Zuo and X.-Z. You, *Dalton Trans.*, 2011, **40**, 2204.

275. S. K. Langley, N. F. Chilton, B. Moubaraki and K. S. Murray, *Dalton Trans.*, 2012, **41**, 1033.

276. G. P. Guedes, S. Soriano, L. A. Mercante, N. L. Speziali, M. A. Novak, M. Andruh and M. G. F. Vaz, *Inorg. Chem.*, 2013, **52**, 8309.

277. H. Zheng, L. Zhao, T. Liu, P.-F. Zhuang, C.-Q. Jiao, J.-X. Hu, Y. Xu, C. He and C.-Y. Duan, *Inorg. Chem. Commun.*, 2015, **57**, 33.

278. F. Kobayashi, R. Ohtani, S. Kusumoto, L. F. Lindoy, S. Hayami and M. Nakamura, *Dalton Trans.*, 2018, **47**, 16422.

279. B. Berkoff, K. Griffiths, A. Abdul-Sada, G. J. Tizzard, S. J. Coles, A. Escuer and G. E. Kostakis, *Dalton Trans.*, 2015, **44**, 12788.

280. S. Hazra, J. Titiš, D. Valigura, R. Boča and S. Mohanta, *Dalton Trans.*, 2016, **45**, 7510.

281. M. C. Majee, S. M. Towsif Abtab, D. Mondal, M. Maity, M. Weselski, M. Witwicki, A. Bieńko, M. Antkowiak, G. Kamieniarz and M. Chaudhury, *Dalton Trans.*, 2018, **47**, 3425.

282. H.-B. Quan, L.-B. Sheng, H.-H. Zou, Z.-Y. Liu, D.-C. Liu, B. Li, M.-S. Chen and F.-P. Liang, *J. Clust. Sci.*, 2018, **29**, 75.

283. Y. Xu, F. Luo and J.-M. Zheng, *Polymers*, 2019, **11**, 196.

284. A. Chakraborty, J. Goura, P. Kalita, A. Swain, G. Rajaraman and V. Chandrasekhar, *Dalton Trans.*, 2018, **47**, 8841.

285. K. Liu, W. Shi and P. Cheng, *Coord. Chem. Rev.*, 2015, **289-290**, 74.

286. S. I. Sampani, S. Aubert, M. Cattoen, K. Griffiths, A. Abdul-Sada, G. R. Akien, G. J. Tizzard, S. J. Coles, S. Arseniyadis and G. E. Kostakis, *Dalton Trans.*, 2018, **47**, 4486.

287. H.-L. Wang, L.-B. Sheng, H.-H. Zou, K. Wang, B. Li, M.-S. Chen and F.-P. Liang, *J. Clust. Sci.*, 2018, **29**, 1313.

288. S. Roy, S. Ghosh, D. O. T. A. Martins, F. Tuna and S. Mohanta, *Eur. J. Inorg. Chem.*, 2018, 5191.

289. J. Martínez-Lillo, T. F. Mastropietro, G. De Munno, F. Lloret, M. Julve and J. Faus, *Inorg. Chem.*, 2011, **50**, 5731.

290. Y. Wang, X. Ma, S. Hu, Y. Wang, C. Tan, Y. Wen, X. Zhang, T. Sheng and X. Wu, *Polyhedron*, 2014, **83**, 137.

291. X.-Y. Wang, C. Avendaño and K. R. Dunbar, *Chem. Soc. Rev.*, 2011, **40**, 3213.

292. S. W. Choi, D. W. Ryu, J. W. Lee, J. H. Yoon, H. C. Kim, H. Lee, B. K. Cho and C. S. Hong, *Inorg. Chem.*, 2009, **48**, 9066.

293. K. S. Pedersen, M. Schau-Magnussen, J. Bendix, H. Weihe, A. V. Palii, S. I. Klokishner, S. Ostrovsky, O. S. Reu, H. Mutka and P. L. W. Tregenna-Piggott, *Chem.: Eur. J.*, 2010, **16**, 13458.

294. S. K. Singh and G. Rajaraman, *Chem.: Eur. J.*, 2014, **20**, 113.

295. V. Hoeke, A. Stammler, H. Bögge, J. Schnack and T. Glaser, *Inorg. Chem.*, 2014, **53**, 257.

296. L. Zhao, T. Liu, P.-F. Zhuang, H. Zheng, C.-Q. Jiao, J.-X. Hu, J.-L. Wang, L.-X. Ren, C. He and C.-Y. Duan, *Inorg. Chem. Commun.*, 2015, **57**, 29.

297. M. Vijayakumar and M. S. Gopinathan, *J. Mol. Struct.*, 1996, **361**, 15.

298. D. Visinescu, C. Desplanches, I. Imaz, V. Bahers, R. Pradhan, F. A. Villamena, P. Guionneau and J.-P. Sutter, *J. Am. Chem. Soc.*, 2006, **128**, 10202.

299. S. Riedel and M. Kaupp, *Angew. Chem. Int. Ed.*, 2006, **45**, 3708.

300. C. Avendano, M. G. Hilfiger, A. Prosvirin, C. Sanders, D. Stepien and K. R. Dunbar, *J. Am. Chem. Soc.*, 2010, **132**, 13123.

301. Z. Huang, J. E. Auckett, P. E. R. Blanchard, B. J. Kennedy, W. Miiller, Q. Zhou, M. Avdeev, M. R. Johnson, M. Zbiri, G. Garbarino, W. G. Marshall, Q. Gu and C. D. Ling, *Angew. Chem. Int. Ed.*, 2014, **53**, 3414.

302. M. Reczyński, B. Nowicka, C. Näther, M. Kozieł, K. Nakabayashi, S.-i. Ohkoshi and B. Sieklucka, *Inorg. Chem.*, 2018, **57**, 13415.

303. A. Bleuzen, V. Marvaud, C. Mathoniere, B. Sieklucka and M. Verdaguer, *Inorg. Chem.*, 2009, **48**, 3453.

304. R. E. P. Winpenny, *J. Chem. Soc. Dalton*, 2002, 1.

305. M. Murrie, S. J. Teat, H. Stœckli-Evans and H. U. Güdel, *Angew. Chem. Int. Ed.*, 2003, **42**, 4653.

306. M.-H. Zeng, M.-X. Yao, H. Liang, W.-X. Zhang and X.-M. Chen, *Angew. Chem. Int. Ed.*, 2007, **46**, 1832.

307. D. M. Piñero Cruz, D. N. Woodruff, I.-R. Jeon, I. Bhowmick, M. Secu, E. A. Hillard, P. Dechambenoit and R. Clérac, *N. J. Chem.*, 2014, **38**, 3443.

308. A. Müller, E. Diemann and H.-H. Heinsen, *Chem. Ber.*, 1971, **104**, 975.

309. A. Müller, W. Hellmann, J. Schneider, U. Schimanski, U. Demmer, A. Trautwein and U. Bender, *Inorganica Chim. Acta*, 1982, **65**, L41.

310. A. Müller, R. Jostes, W. Hellmann, C. Römer, H. Bögge, U. Schimanski, B. Zhuang, L. D. Rosenheim, J. W. McDonald and W. E. Newton, *Z. Anorg. Allg. Chem.*, 1986, **533**, 125.

311. K. P. Callahan and P. A. Piliero, *Inorg. Chem.*, 1980, **19**, 2619.

312. C. J. Crossland, I. R. Evans and J. S. O. Evans, *Dalton Trans.*, 2008,1597.

313. M. S. P. Carepo, S. R. Pauleta, A. G. Wedd, J. J. G. Moura and I. Moura, *J. Biol. Inorg. Chem.*, 2014, **19**, 605.

314. A. Müller, E. Diemann, R. Jostes and H. Bögge, *Angew. Chem. Int. Ed.*, 1981, **20**, 934.

315. A. Müller, H. Bögge, U. Schimanski, M. Penk, K. Nieradzik, M. Dartmann, E. Krickemeyer, J. Schimanski, C. Römer, M. Römer, H. Dornfeld, U. Wienböker, W. Hellmann and M. Zimmermann, *Monatsh. Chem.*, 1989, **120**, 367.

316. B. R. Srinivasan, A. R. Naik, M. Poisot, C. Näther and W. Bensch, *Polyhedron*, 2009, **28**, 1379.

317. A. Müller, E. Diemann and C. K. Jørgensen, *Struct. Bond.*, 1973, **14**, 23.

318. K. H. Schmidt and A. Müller, *Spectrochim. Acta A*, 1972, **28**, 1829.

319. R. H. Petit, B. Briat, A. Müller and E. Diemann, *Mol. Phys.*, 1974, **27**, 1373.

320. A. Müller, V. Wittneben, E. Diemann, J. Hormes and U. Kuetgens, *Chem. Phys. Lett.*, 1994, **225**, 359.

321. A. C. Olson, J. M. Keith, E. R. Batista, K. S. Boland, S. R. Daly, S. A. Kozimor, M. M. MacInnes, R. L. Martin and B. L. Scott, *Dalton Trans.*, 2014, **43**, 17283.

322. A. Müller and E. Diemann, *Chem. Phys. Lett.*, 1971, **9**, 369.

323. A. Müller, R. Jostes, V. Flemming and R. Potthast, *Inorganica Chim. Acta*, 1980, **44**, L33.

324. N. C. Tomson, K. D. Williams, X. Dai, S. Sproules, S. DeBeer, T. H. Warren and K. Wieghardt, *Chem. Sci.*, 2015, **6**, 2474.

325. A. R. Corcos, O. Villanueva, R. C. Walroth, S. K. Sharma, J. Bacsa, K. M. Lancaster, C. E. MacBeth and J. F. Berry, *J. Am. Chem. Soc.*, 2016, **138**, 1796.

326. J. F. Berry, E. Bill, E. Bothe, S. D. George, B. Mienert, F. Neese and K. Wieghardt, *Science*, 2006, **312**, 1937.

327. P. Cassoux, *Coord. Chem. Rev.*, 1999, **185-186**, 213.

328. D. Espa, L. Pilia, C. Makedonas, L. Marchiò, M. L. Mercuri, A. Serpe, A. Barsella, A. Fort, C. A. Mitsopoulou and P. Deplano, *Inorg. Chem.*, 2014, **53**, 1170.

329. P. Cassoux and L. V. Interrante, *Comment Inorg. Chem.*, 1991, **12**, 47.

330. D. Coucouvanis and J. P. Fackler, *J. Am. Chem. Soc.*, 1967, **89**, 1346.

331. L. K. White and R. L. Belford, *J. Am. Chem. Soc.*, 1976, **98**, 4428-4438.

332. R. Kirmse, *Chem. Phys. Lett.*, 1973, **23**, 83.

333. R. Kirmse, W. Dietzsch and E. Hoyer, *Z. Anorg. Allg. Chem.*, 1973, **397**, 198.

334. R. Kirmse, B. V. Solovev and B. G. Tarasov, *Ann. Phys.*, 1974, **486**, 352.

335. W. Dietzsch, J. Reinhold, R. Kirmse, E. Hoyer, I. N. Marov and V. K. Belyaeva, *J. Inorg. Nucl. Chem.*, 1977, **39**, 1377.

336. W. Dietzsch, J. Lerchner, J. Reinhold, J. Stach, R. Kirmse, G. Steimecke and E. Hoyer, *J. Inorg. Nucl. Chem.*, 1980, **42**, 509.

337. D. Coucouvanis, F. J. Hollander and M. L. Caffery, *Inorg. Chem.*, 1976, **15**, 1853.

338. C. J. Long, D. Tortorice and R. D. Bereman, *Inorganica Chim. Acta*, 1991, **185**, 169.

339. J. Vicente, P. González-Herrero, Y. García-Sánchez, P. G. Jones and D. Bautista, *Eur. J. Inorg. Chem.*, 2006, 115.

340. N. K. Singh, P. P. Agrawal and N. Singh, *Syn. React. Inorg. Met.*, 1991, **21**, 541.

341. D. Zhu, X. C. Xing, P. J. Wu, P. Wang, D. M. Zhang and D. L. Yang, *Synthetic Met.*, 1991, **42**, 2541.

342. N. Singh and S. Gupta, *Synthetic Met.*, 1999, **107**, 167.

343. N. Singh and S. Gupta, *Synthetic Met.*, 2000, **110**, 207.

344. R. Aggarwal and R. Mitra, *Indian J. Chem. A*, 1994, **33**, 55.

345. N. Singh and S. Kumar Rai, *J. Organomet. Chem.*, 2000, **605**, 102.

346. N. Singh and S. Gupta, *Inorg. Chem. Commun.*, 2000, **3**, 446.

347. N. Singh and A. P. S. Gupta, *Transit. Metal Chem.*, 2005, **30**, 383.

348. V. Singh, A. Kumar, M. K. Yadav, L. B. Prasad and N. Singh, *Synthetic Met.*, 2013, **176**, 65.

349. A. Flamini, *J. Coord. Chem.*, 1975, **4**, 205.

350. F. Y. Dong, J. M. Dou, X. K. Gao, D. C. Li and D. Q. Wang, *Indian J. Chem. A*, 2005, **44**, 1144.

351. M. T. S. De Mello, M. C. C. Ribeiro and P. S. Santos, *J. Raman Spectrosc.*, 1995, **26**, 173.

352. A. Meisel, R. Szargan, K.-H. Hallmeier, I. Uhlig and J.-A. Momand, *J. Phys. Colloq.*, 1987, **48**, 981.

353. V. Abram, W. Dietzsch and R. Kirmse, *Z. Chem.*, 1982, **22**, 305.

354. J. Piotroschke, P. Strauch, S. Abram and U. Abram, *Z. Anorg. Allg. Chem.*, 1994, **620**, 1659.

355. G. Schmauch, F. Knoch and H. Kisch, *Chem. Ber.*, 1994, **127**, 287.

356. F. Nüßlein, R. Peter and H. Kisch, *Chem. Ber.*, 1989, **122**, 1023.

357. M. L. Caffery and D. Coucouvanis, *J. Inorg. Nucl. Chem.*, 1975, **37**, 2081.

358. X. Chen, W.-Q. Chen, D.-D. Zhou, W.-T. Yin, L.-B. Liang, S. Han, X.-P. Liu, J.-R. Zhou, L.-M. Yang and C.-L. Ni, *Synth. React. Inorg. Met.-Org. Nano-Metal Chem.*, 2011, **41**, 472.

359. N. Kobayashi, T. Naito and T. Inabe, *Mol. Cryst. Liq. Cryst.*, 2002, **376**, 233.

360. J.-M. Lei, Q.-X. Peng, S.-P. Luo, Y. Liu, S.-Z. Zhan and C.-L. Ni, *Mol. Catal.*, 2018, **448**, 10.

361. G. S. Vigee and C. L. Watkins, *J. Inorg. Nucl. Chem.*, 1975, **37**, 1739.

362. B. B. Kaul and K. B. Pandeya, *J. Inorg. Nucl. Chem.*, 1978, **40**, 229.

363. E. M. Hanawalt, J. Farkas and H. G. Richey, *Organometallics*, 2004, **23**, 416.

364. J. D. Forrester, A. Zalkin and D. H. Templeton, *Inorg. Chem.*, 1964, **3**, 1507.

365. Y. L. Hu, L. B. Liang, J. F. Liu, W. Q. Chen, J. R. Zhou, X. P. Liu, L. M. Yang and C. L. Ni, *J. Struct. Chem.*, 2013, **54**, 801.

366. D. Coucouvanis, D. G. Holah and F. J. Hollander, *Inorg. Chem.*, 1975, **14**, 2657.

367. J. A. McCleverty, *Prog. Inorg. Chem.*, 1968, **10**, 49.

368. V. F. Plyusnin, I. P. Pozdnyakov, V. P. Grivin, A. I. Solovyev, H. Lemmetyinen, N. V. Tkachenko and S. V. Larionov, *Dalton Trans.*, 2014, **43**, 17766.

369. F. E. Mabbs and D. Collison, *Electron Paramagnetic Resonance of d Transition Metal Compounds*, Elsevier, Amsterdam, Netherlands, 1992.

370. F. G. Herring, J. M. Park, S. J. Rettig and J. Trotter, *Can. J. Chem.*, 1979, **57**, 2379.

371. N. D. Yordanov and D. Shopov, *Inorganica Chim. Acta*, 1971, **5**, 679.

372. E. Billig, R. Williams, I. Bernal, J. H. Waters and H. B. Gray, *Inorg. Chem.*, 1964, **3**, 663.

373. B. K. Maiti, L. B. Maia, K. Pal, B. Pakhira, T. Avilés, I. Moura, S. R. Pauleta, J. L. Nuñez, A. C. Rizzi, C. D. Brondino, S. Sarkar and J. J. G. Moura, *Inorg. Chem.*, 2014, **53**, 12799.

374. S. N. Choi, E. R. Menzel and J. R. Wasson, *J. Inorg. Nucl. Chem.*, 1977, **39**, 417.

375. D. Kivelson and R. Neiman, *J. Chem. Phys.*, 1961, **35**, 149.

376. J. S. Griffith, *The Theory of Transition-Metal Ions*, Cambridge University Press, Cambridge, UK, 1961.

377. A. H. Maki, N. Edelstein, A. Davison and R. H. Holm, *J. Am. Chem. Soc.*, 1964, **86**, 4580.

378. A. H. Maki and B. R. McGarvey, *J. Chem. Phys.*, 1958, **29**, 31.

379. B. R. McGarvey, *J. Phys. Chem.*, 1967, **71**, 51.

380. A. J. Freeman and R. E. Watson, *Phys. Rev.*, 1962, **127**, 2058.

381. P. Machata, P. Herich, K. Lušpai, L. Bucinsky, S. Šoralová, M. Breza, J. Kozisek and P. Rapta, *Organometallics*, 2014, **33**, 4846.

382. L. J. Theriot, K. K. Ganguli, S. Kavarnos and I. Bernal, *J. Inorg. Nucl. Chem.*, 1969, **31**, 3133.

383. O. V. Mikhailov, *Transit. Met. Chem.*, 1997, **22**, 535.

384. R. Williams, E. Billig, J. H. Waters and H. B. Gray, *J. Am. Chem. Soc.*, 1966, **88**, 43.

385. G. Steimecke, R. Kirmse and E. Hoyer, *Z. Chem.*, 1975, **15**, 28.

386. C. T. Vance, J. H. Welch and R. D. Bereman, *Inorganica Chim. Acta*, 1989, **164**, 191.

387. J. H. Van Vleck, *Phys. Rev.*, 1932, **41**, 208.

388. H. B. Gray and E. Billig, *J. Am. Chem. Soc.*, 1963, **85**, 2019.

389. R. Pettersson and T. Vänngård, *Ark. Kemi.*, 1961, **17**, 249.

390. J. H. Van Vleck, *J. Chem. Phys.*, 1935, **3**, 803.

391. H. R. Gersmann and J. D. Swalen, *J. Chem. Phys.*, 1962, **36**, 3221.

392. J. C. Donini, *Recent Advances in Group Theory and Their Application to Spectroscopy*, Springer, New York, NY, USA, 1979.

393. S. K. Hoffmann, J. Goslar, S. Lijewski, K. Tadyszak, A. Zalewska, A. Jankowska, P. Florczak and S. Kowalak, *Micropor. Mesopor. Mat.*, 2014, **186**, 57.

394. F. G. Herring and J. M. Park, *J. Magn. Reson.*, 1979, **36**, 311.

395. M. J. Weeks and J. P. Fackler, *Inorg. Chem.*, 1968, **7**, 2548.

396. R. Eisenberg, *Prog. Inorg. Chem.*, 1970, **12**, 295.

397. L. S. Kau, D. J. Spira-Solomon, J. E. Penner-Hahn, K. O. Hodgson and E. I. Solomon, *J. Am. Chem. Soc.*, 1987, **109**, 6433.

398. J. L. DuBois, P. Mukherjee, A. M. Collier, J. M. Mayer, E. I. Solomon, B. Hedman, T. D. P. Stack and K. O. Hodgson, *J. Am. Chem. Soc.*, 1997, **119**, 8578.

399. J. L. DuBois, P. Mukherjee, T. D. P. Stack, B. Hedman, E. I. Solomon and K. O. Hodgson, *J. Am. Chem. Soc.*, 2000, **122**, 5775.

400. H. B. Gray, R. Williams, I. Bernal and E. Billig, *J. Am. Chem. Soc.*, 1962, **84**, 3596.

8 Appendices

8.1 Co^{II} Arylthiolate Electronic Spectra

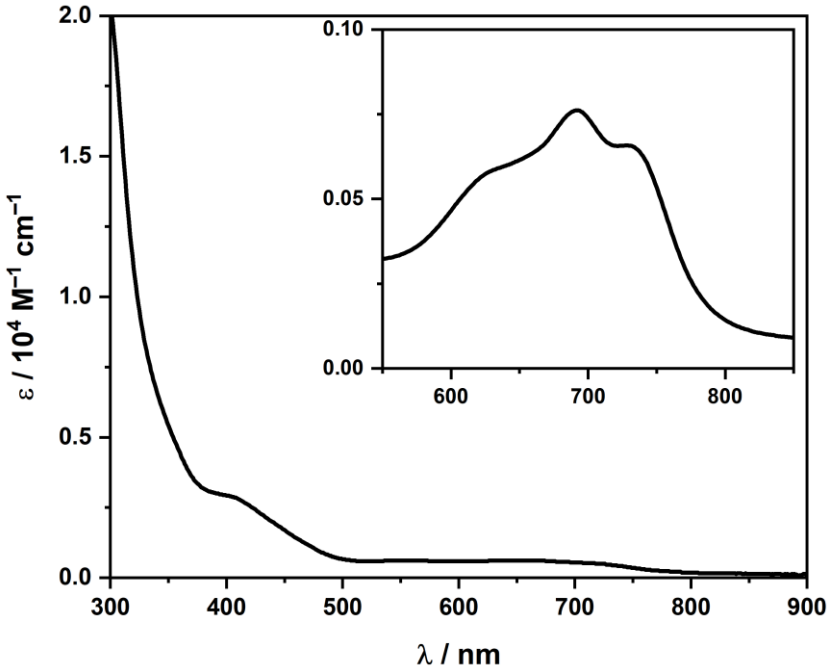

Figure 8.1 Electronic spectrum of $(PPh_4)_2[Co(SPh)_4]$ recorded in MeCN.

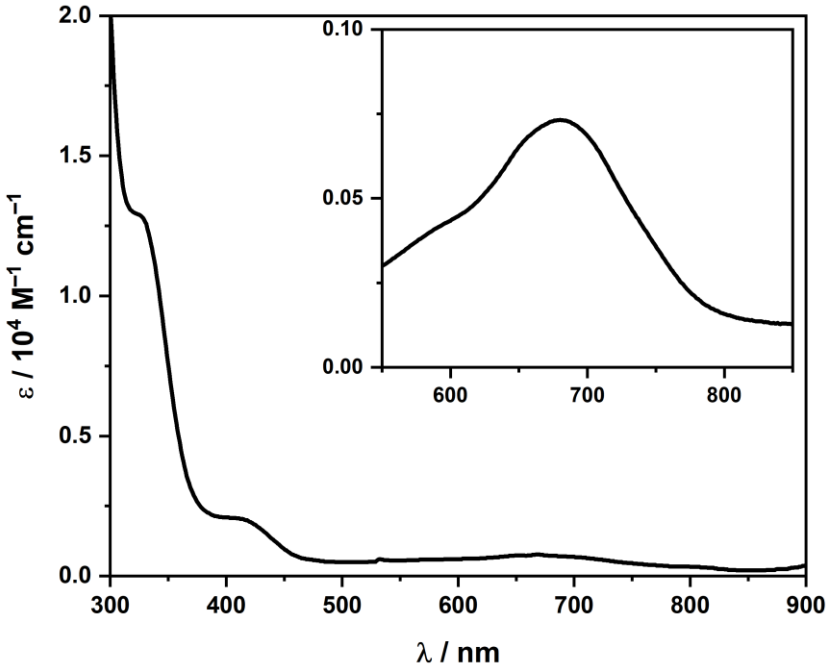

Figure 8.2 Electronic spectrum of $(PPh_4)_2[Co(SC_6F_5)_4]$ recorded in MeCN.

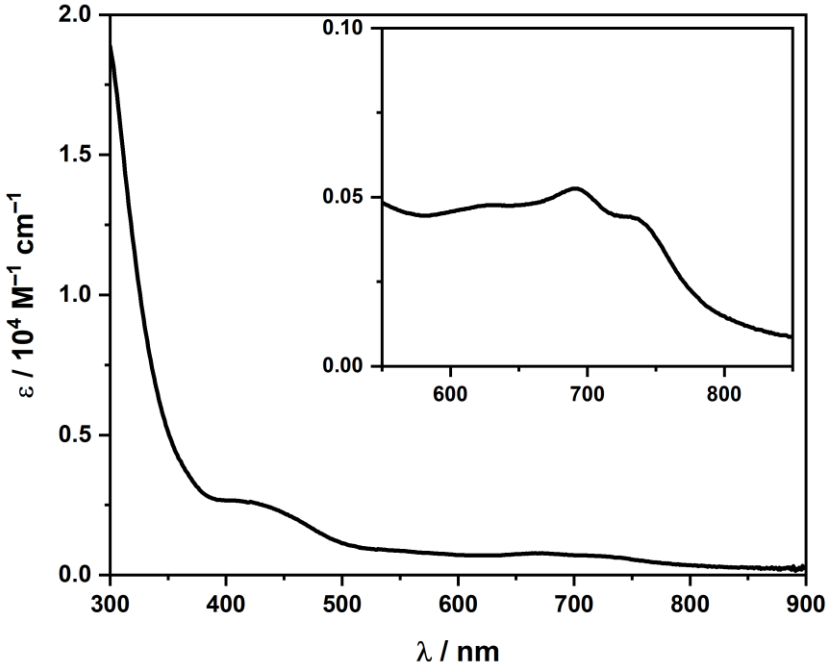

Figure 8.3 Electronic spectrum of $(PPh_4)_2[Co(STol)_4]$ recorded in MeCN.

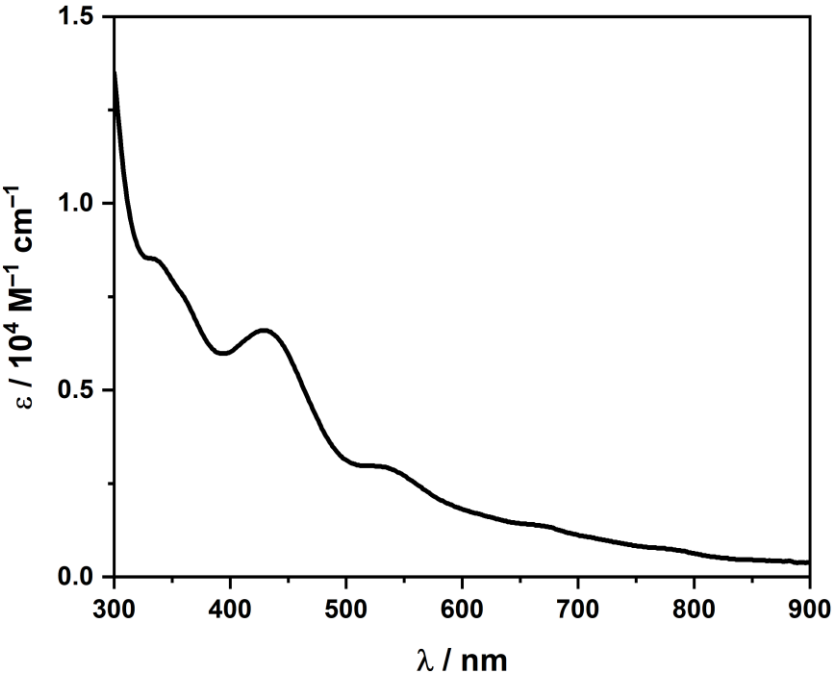

Figure 8.4 Electronic spectrum of $(PPh_4)_2[Co_4(SPh)_{10}]$ recorded in MeCN.

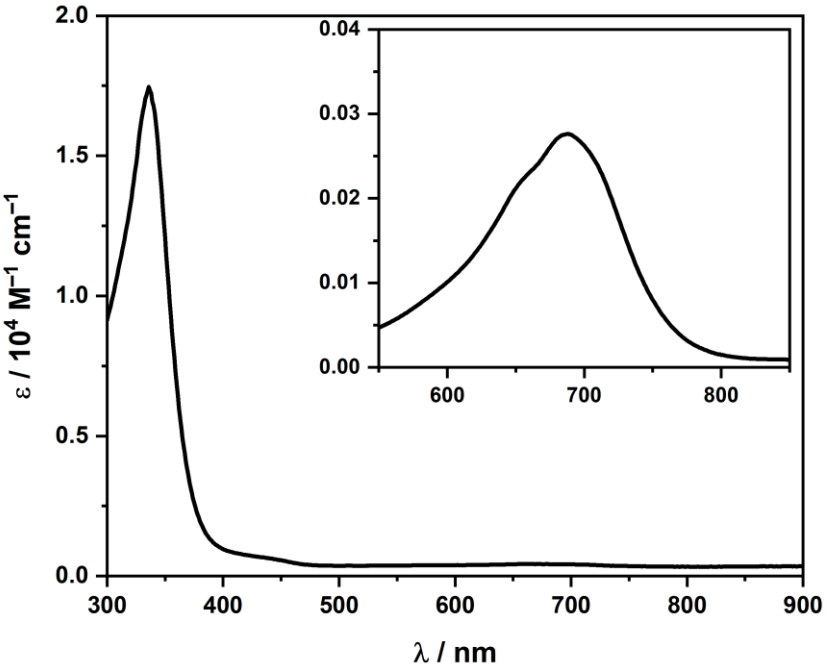

Figure 8.5 Electronic spectrum of $(PPh_4)_2[Co_4(SC_6F_5)_{10}]$ recorded in MeCN.

8.2 Co^{II} Arylthiolate Co K-edge Spectra

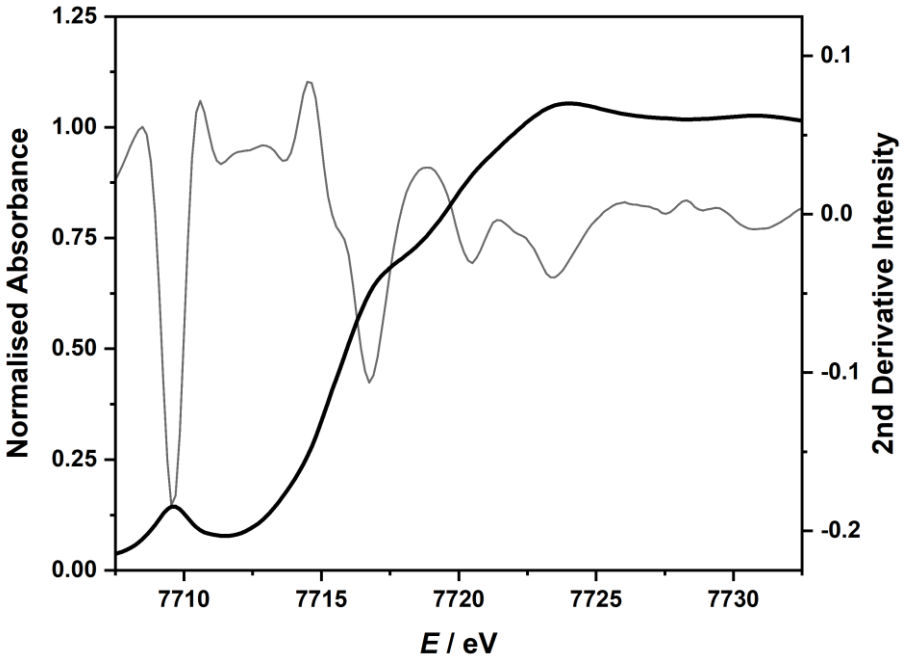

Figure 8.6 Normalised Co K-edge spectrum and second derivative of $(PPh_4)_2[Co(SPh)_4]$.

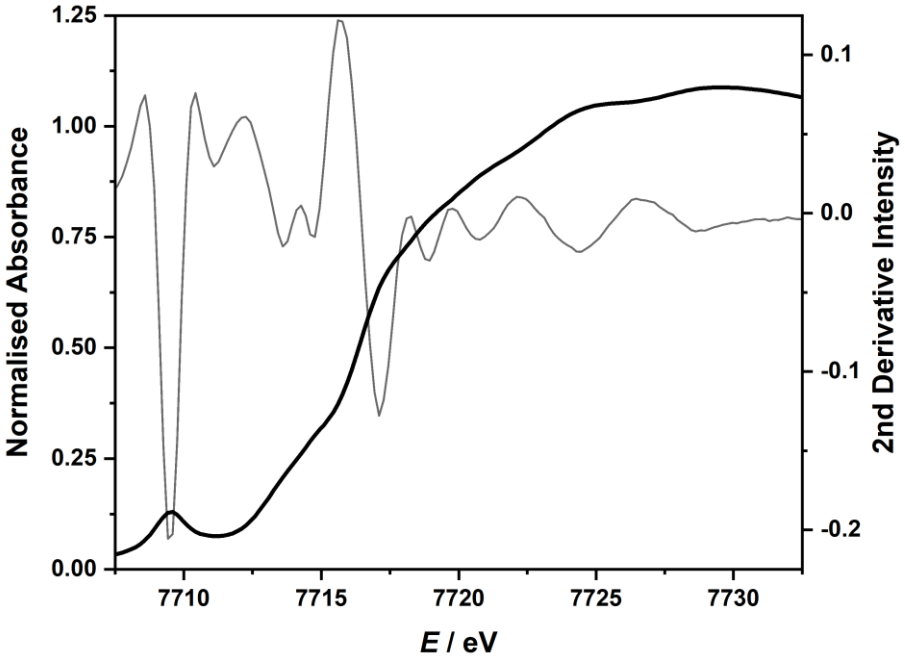

Figure 8.7 Normalised Co K-edge spectrum and second derivative of $(PPh_4)_2[Co(SC_6F_5)_4]$.

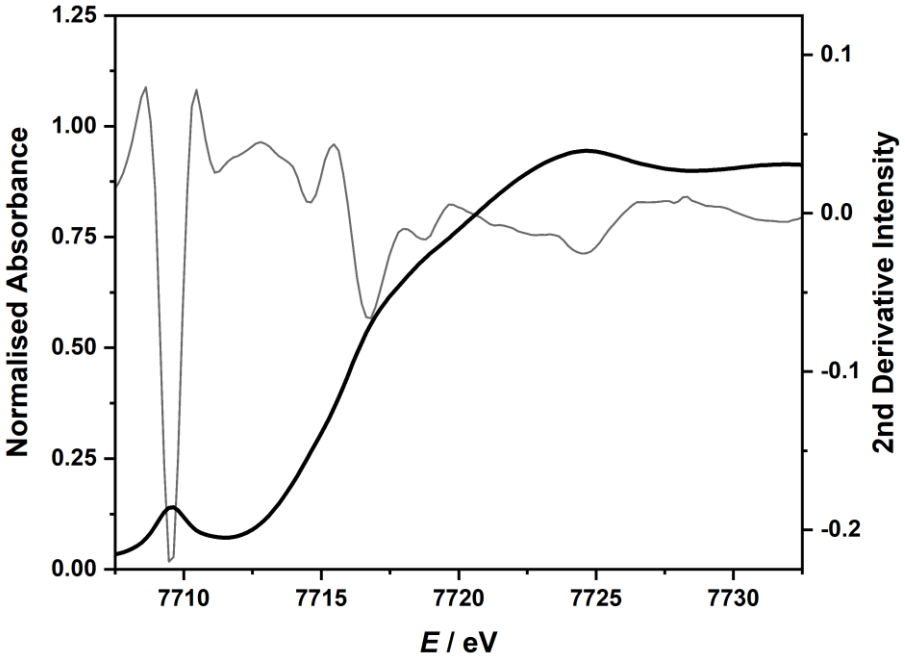

Figure 8.8 Normalised Co K-edge spectrum and second derivative of $(PPh_4)_2[Co(STol)_4]$.

8.3 Co^{II} Arylthiolate S K-edge Spectra

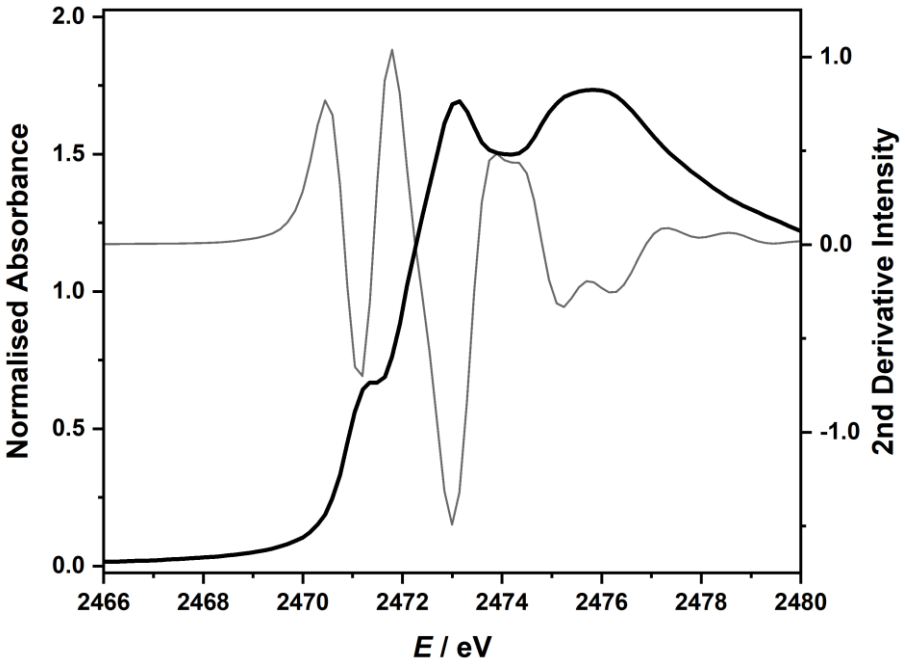

Figure 8.9 Normalised S K-edge spectrum and second derivative of $(PPh_4)_2[Co(SPh)_4]$.

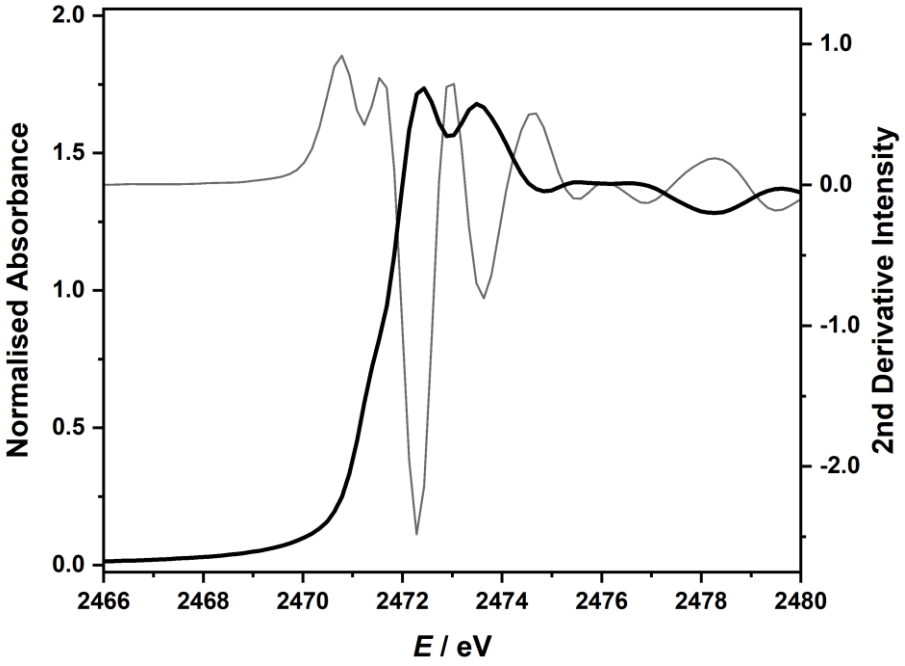

Figure 8.10 Normalised S K-edge spectrum and second derivative of $(PPh_4)_2[Co(SC_6F_5)_4]$.

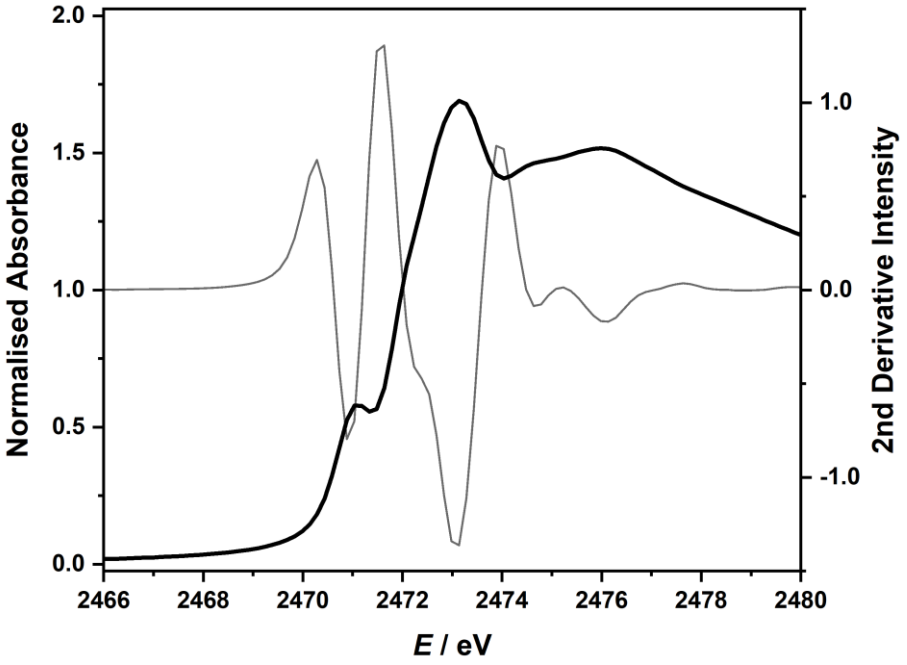

Figure 8.11 Normalised S K-edge spectrum and second derivative of $(PPh_4)_2[Co(STol)_4]$.

8.4 Ligand Salt Electronic Spectra

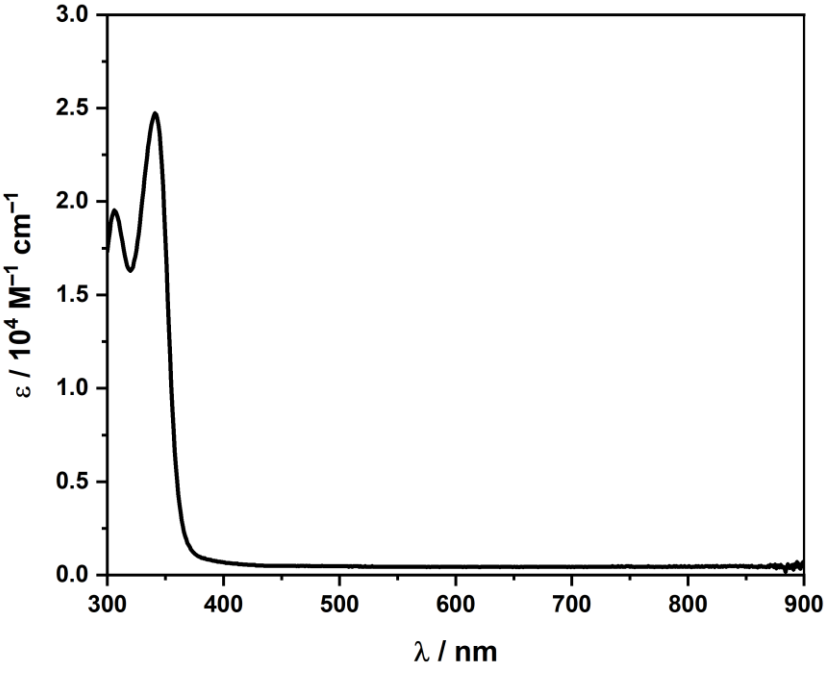

Figure 8.12 Electronic spectrum of Na_2(*i*-mnt) recorded in H_2O.

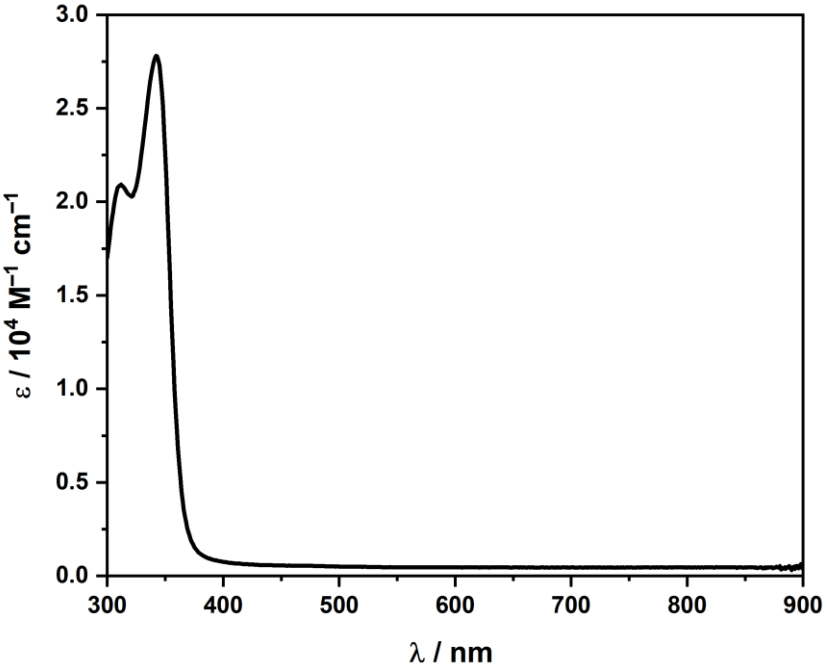

Figure 8.13 Electronic spectrum of K_2(*i*-mant) recorded in H_2O.

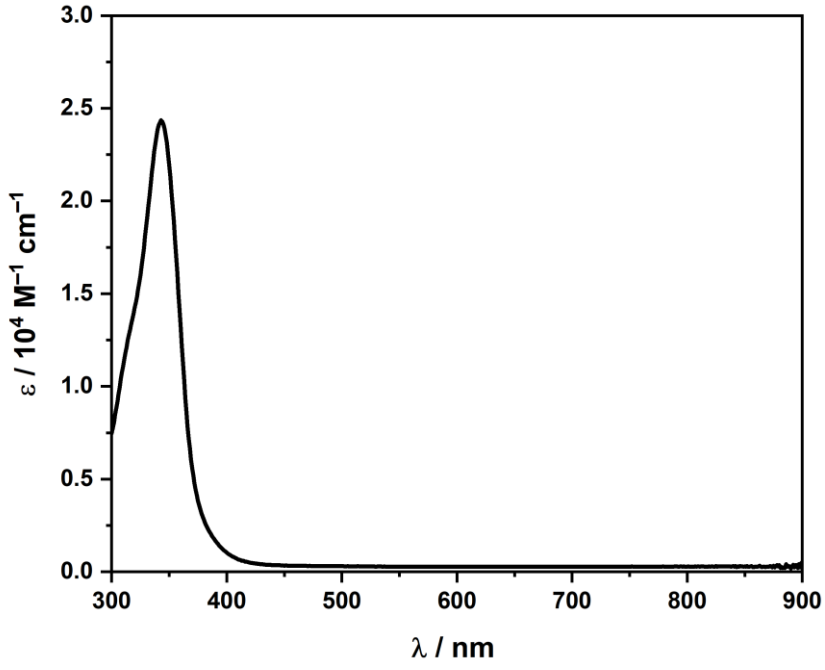

Figure 8.14 Electronic spectrum of K_2(*i*-ect) recorded in H_2O.

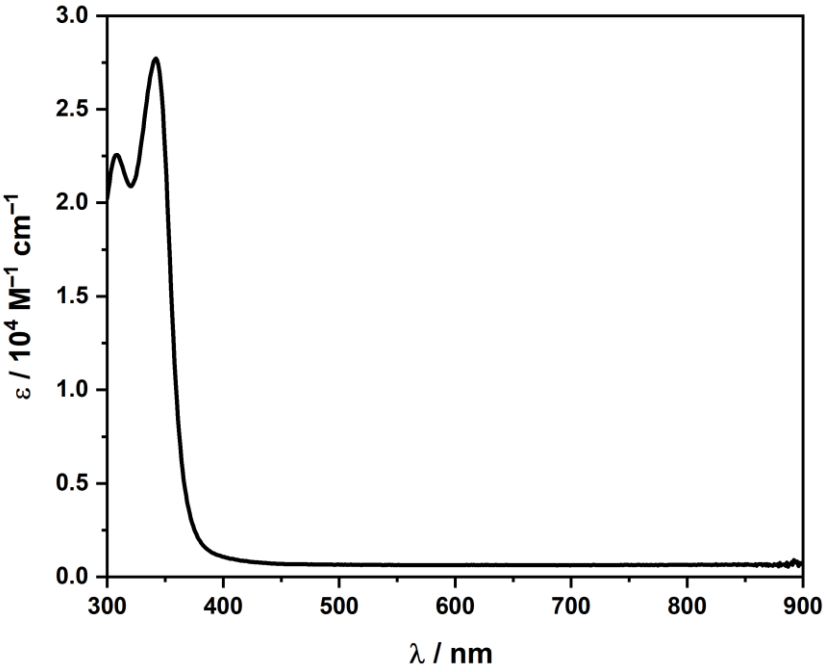

Figure 8.15 Electronic spectrum of K_2(ded) recorded in H_2O.

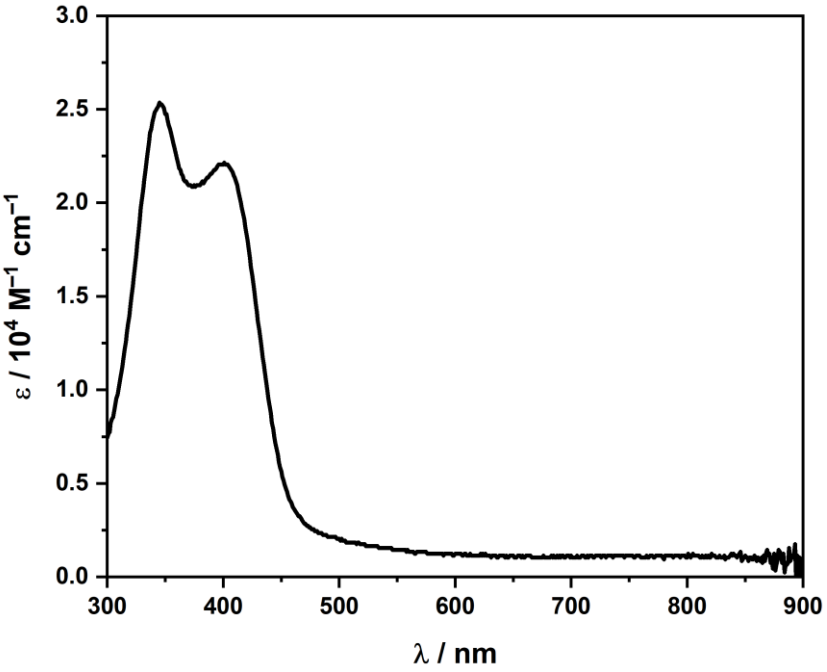

Figure 8.16 Electronic spectrum of K_2(nmt) recorded in H_2O.

Table 8.1 Electronic spectral parameters of 1,1-dithiolate alkali metal salts.

	λ_{max} / nm	ε_{max} / 10^4 M^{-1} cm^{-1}
Na_2(*i*-mnt)	306	1.95
	341	2.47
K_2(*i*-mant)	312	2.09
	342	2.78
K_2(*i*-ect)	314	1.25
	343	2.44
K_2(ded)	308	2.26
	342	2.77
K_2(nmt)	515	0.17
	401	2.21
	345	2.53

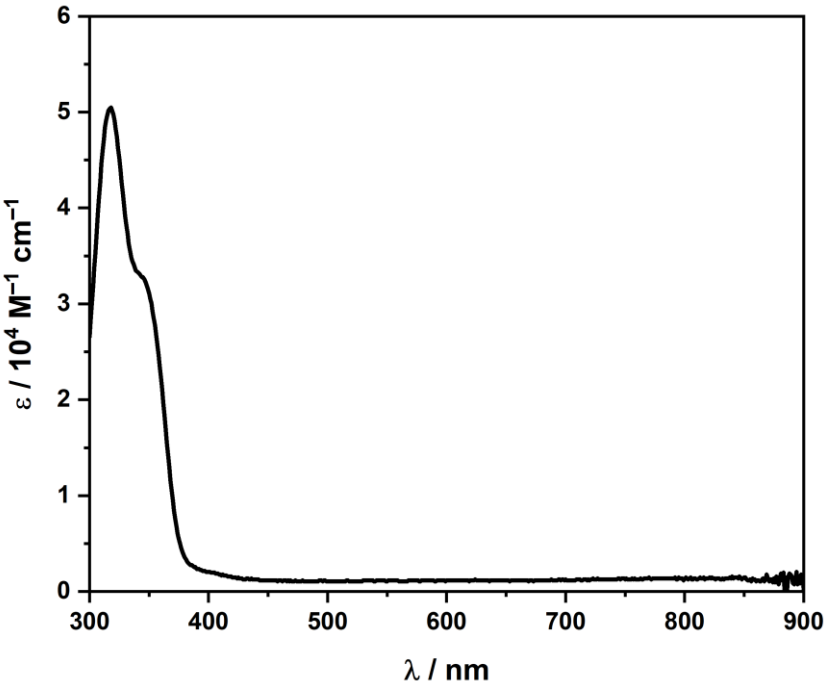

Figure 8.17 Electronic spectrum of K_2(dts) recorded in H_2O.

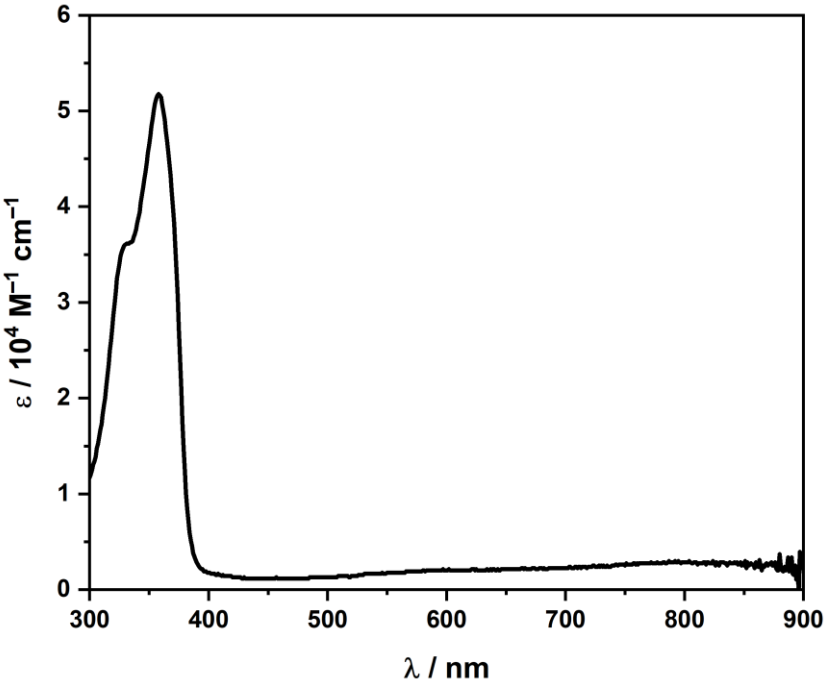

Figure 8.18 Electronic spectrum of $(PPh_4)_2(dts)$ recorded in MeCN.

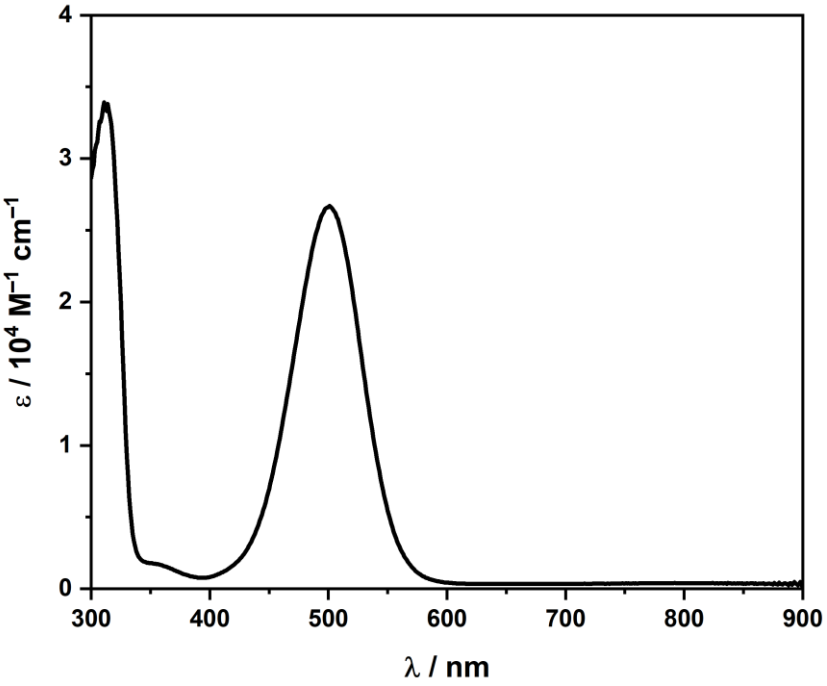

Figure 8.19 Electronic spectrum of $(NEt_4)_2[Zn(dmit)_2]$ recorded in MeCN.

8.5 1,1-Dithiolate Ligand Salt ^{1}H NMR Spectra

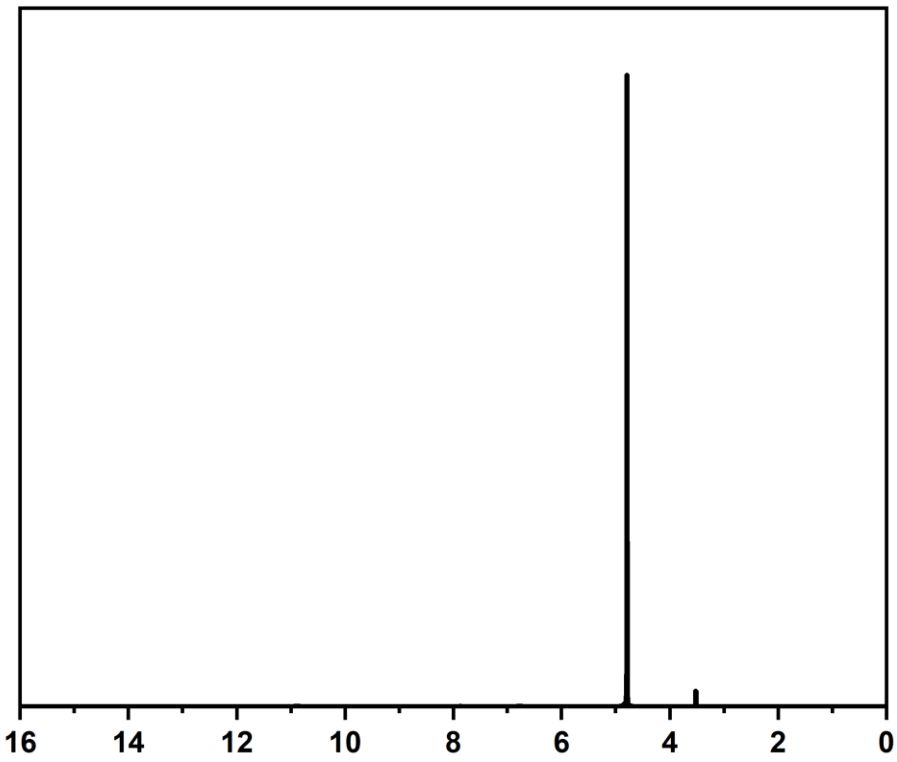

Figure 8.20 ^{1}H NMR Spectrum of K_2(*i*-mant) in D_2O.

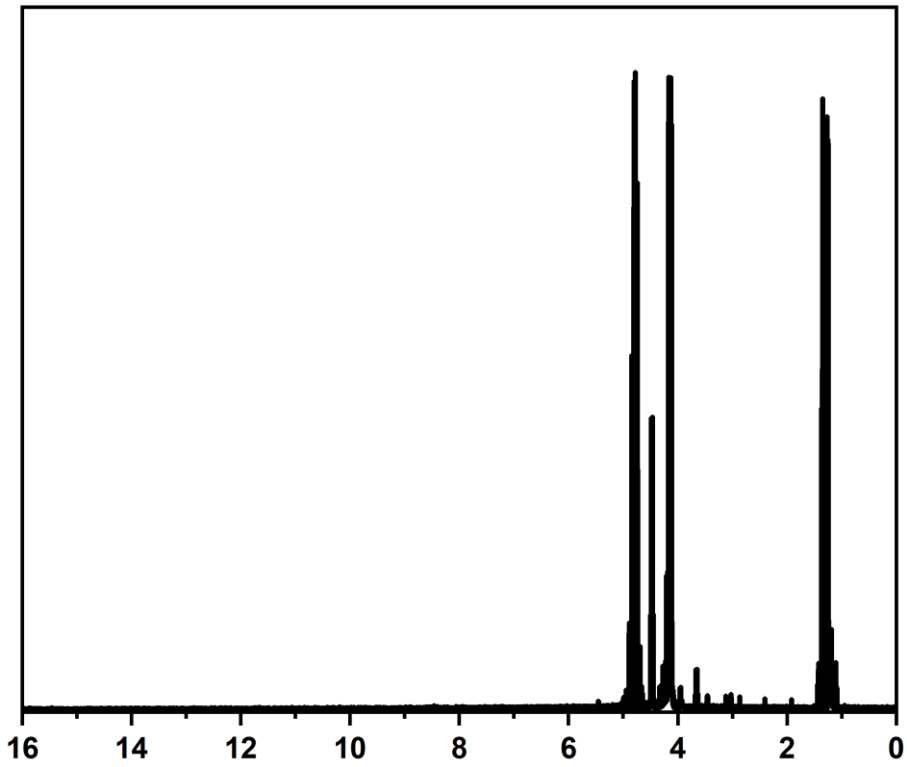

Figure 8.21 ^{1}H NMR Spectrum of K_2(*i*-ect) in D_2O.

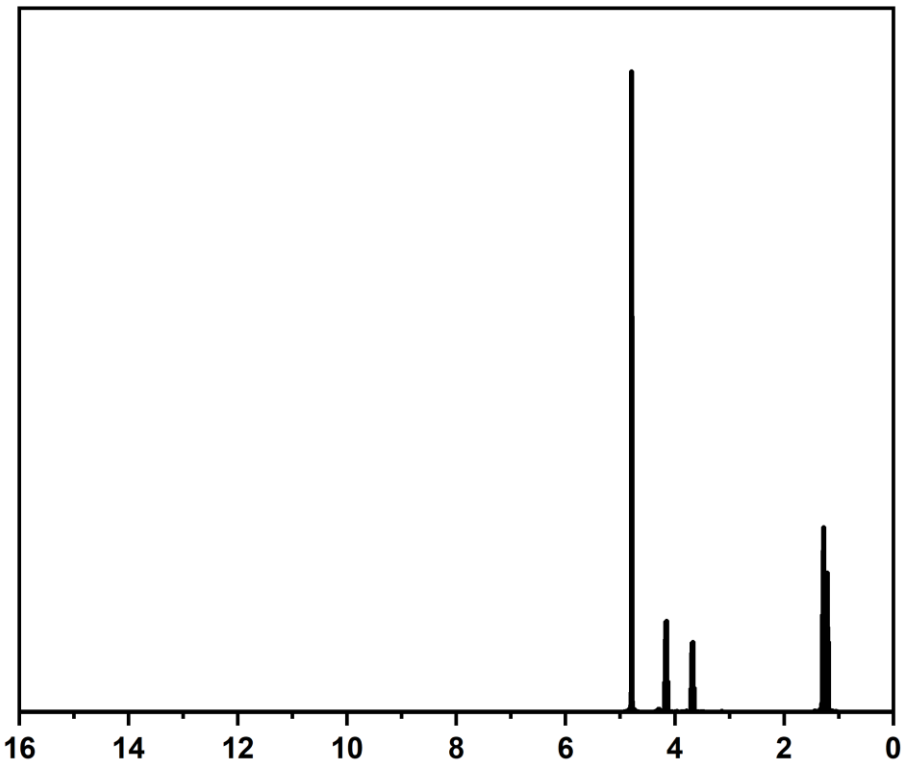

Figure 8.22 ^{1}H NMR Spectrum of K_2(ded) in D_2O.

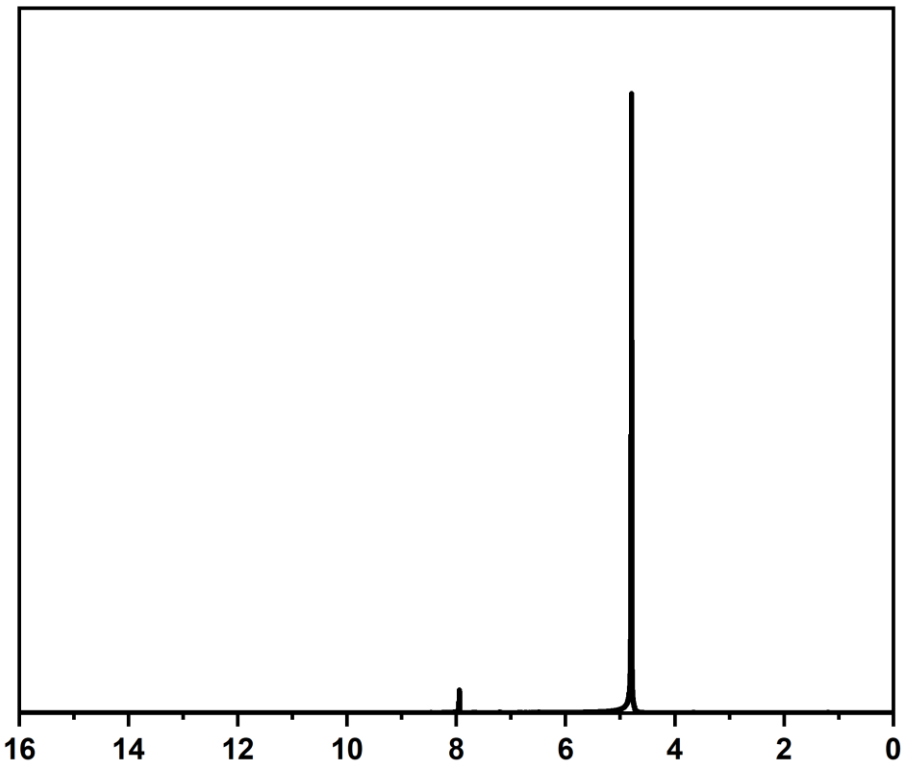

Figure 8.23 ^{1}H NMR Spectrum of K_2(ded) in D_2O.

8.6 1,1-Dithiolate Ligand Salt ^{13}C NMR Spectra

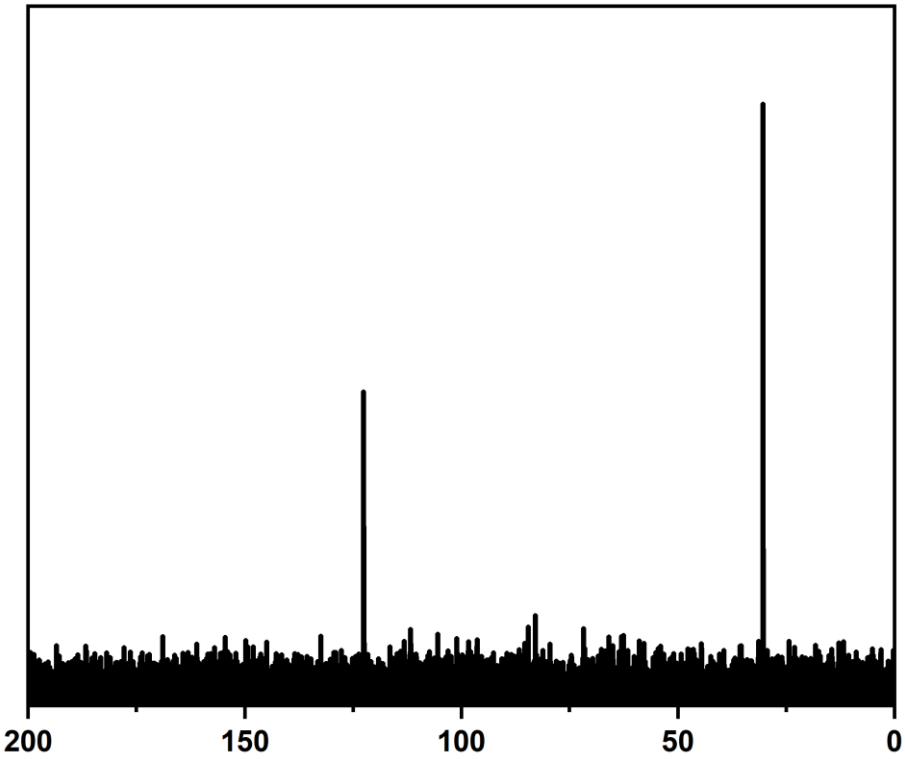

Figure 8.24 ^{13}C NMR Spectrum of Na_2(*i*-mnt) in D_2O.

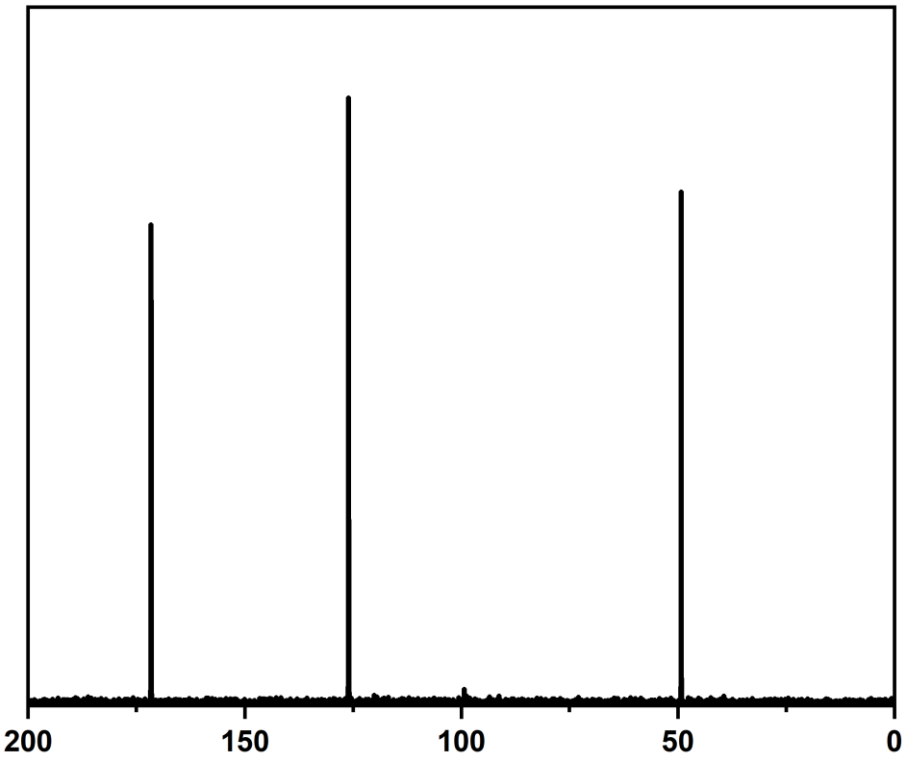

Figure 8.25 ^{13}C NMR Spectrum of K_2(*i*-mant) in D_2O.

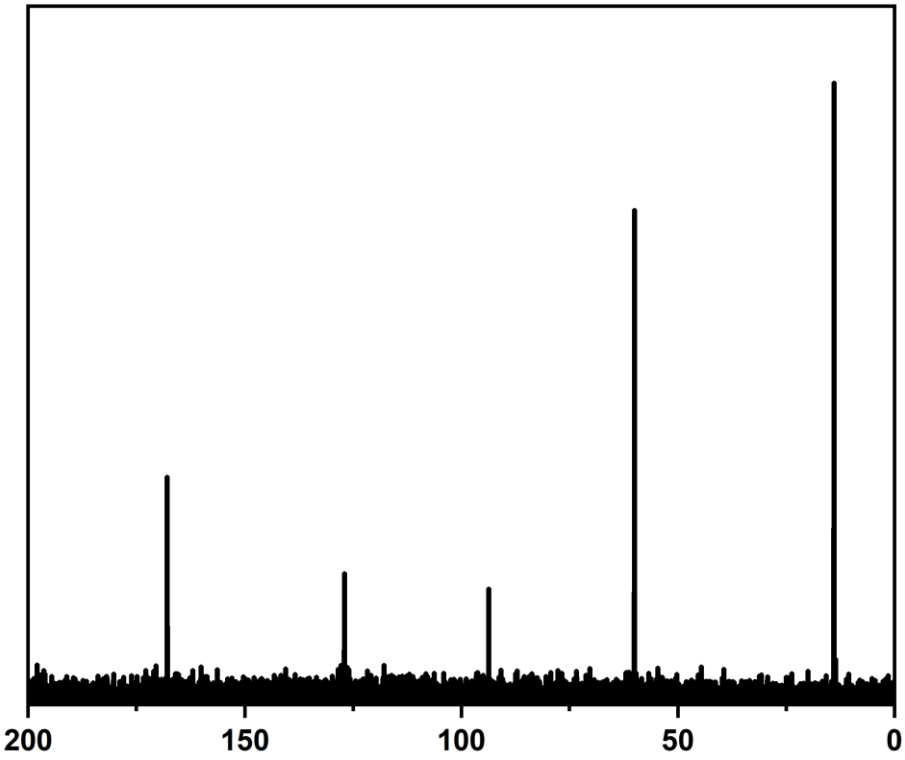

Figure 8.26 ^{13}C NMR Spectrum of K_2(*i*-ect) in D_2O.

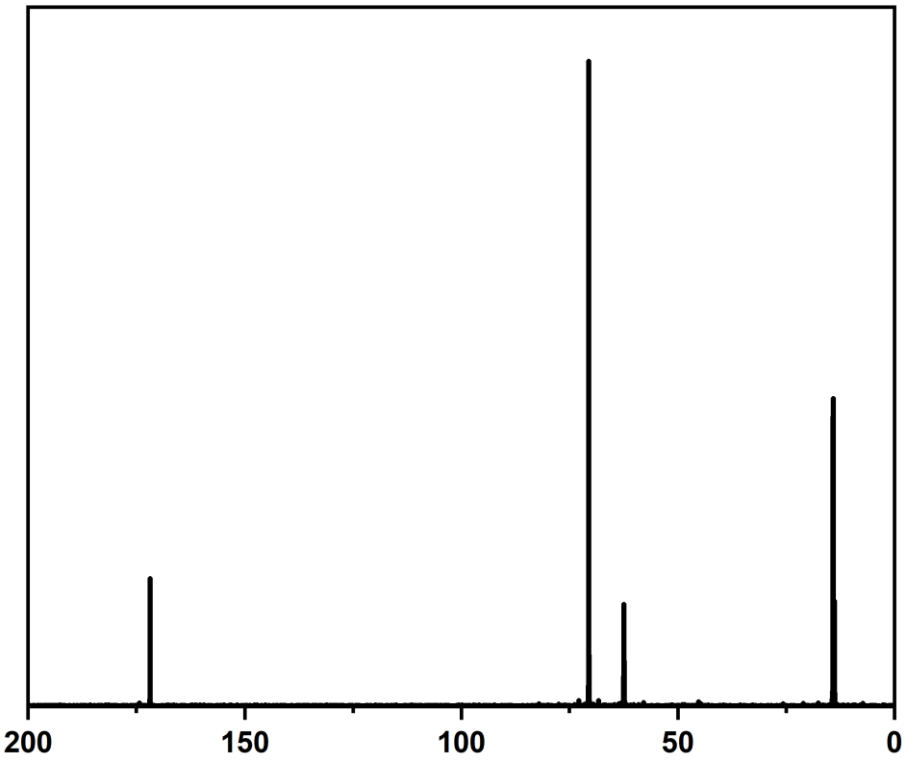

Figure 8.27 ^{13}C NMR Spectrum of K_2(ded) in D_2O.

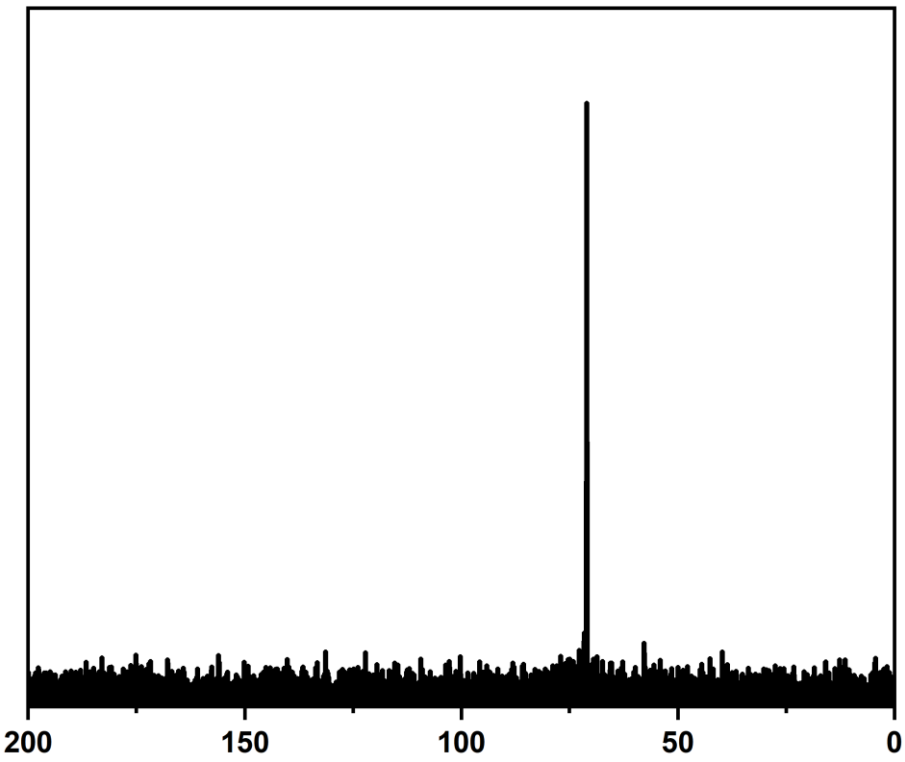

Figure 8.28 ^{13}C NMR Spectrum of K_2(nmt) in D_2O.

8.7 1,1-Dithiolate Ligand Salt S K-edge Spectra

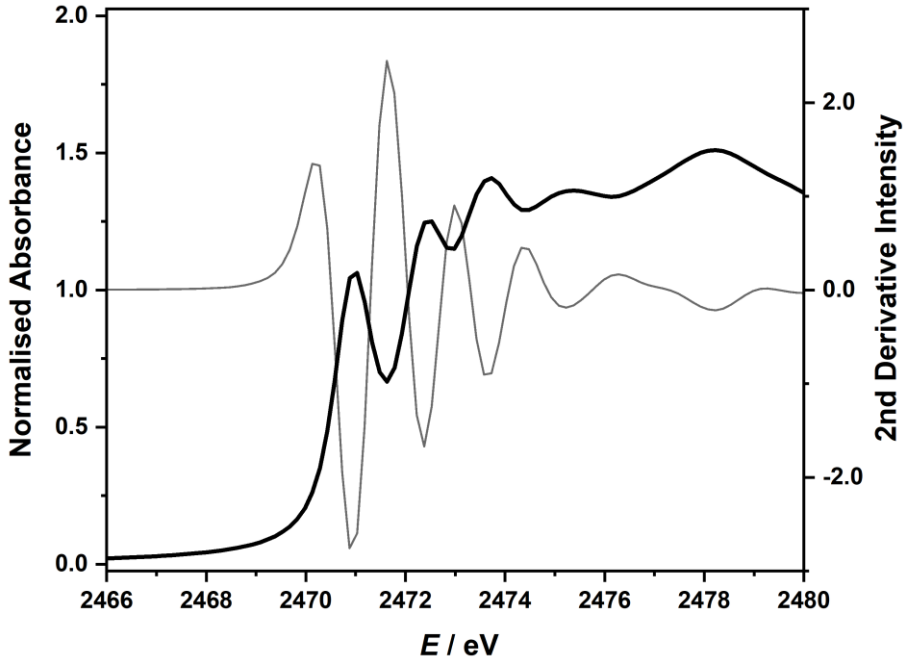

Figure 8.29 Normalised S K-edge spectrum and second derivative of Na_2(*i*-mnt).

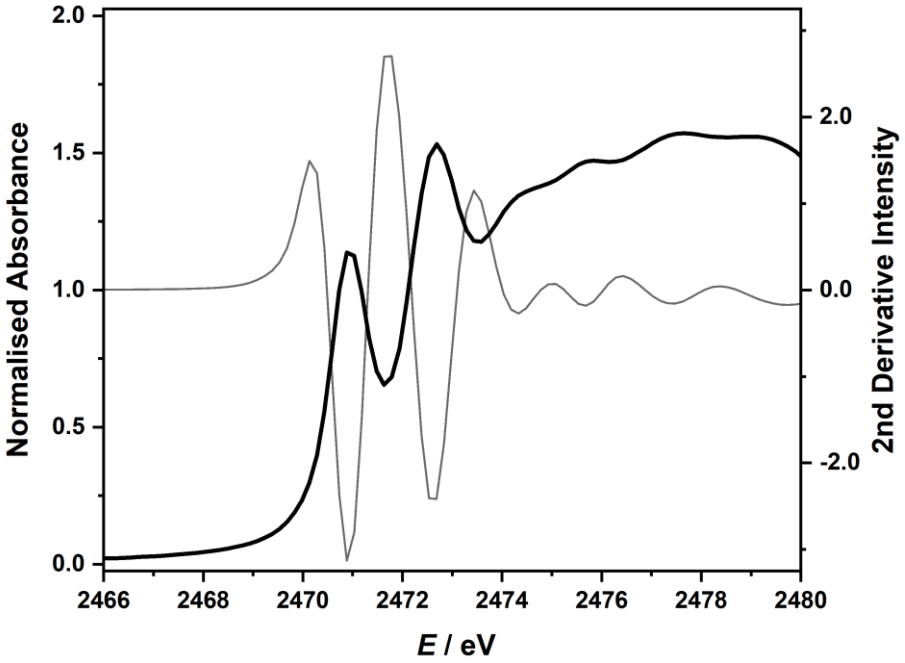

Figure 8.30 Normalised S K-edge spectrum and second derivative of K_2(*i*-mant).

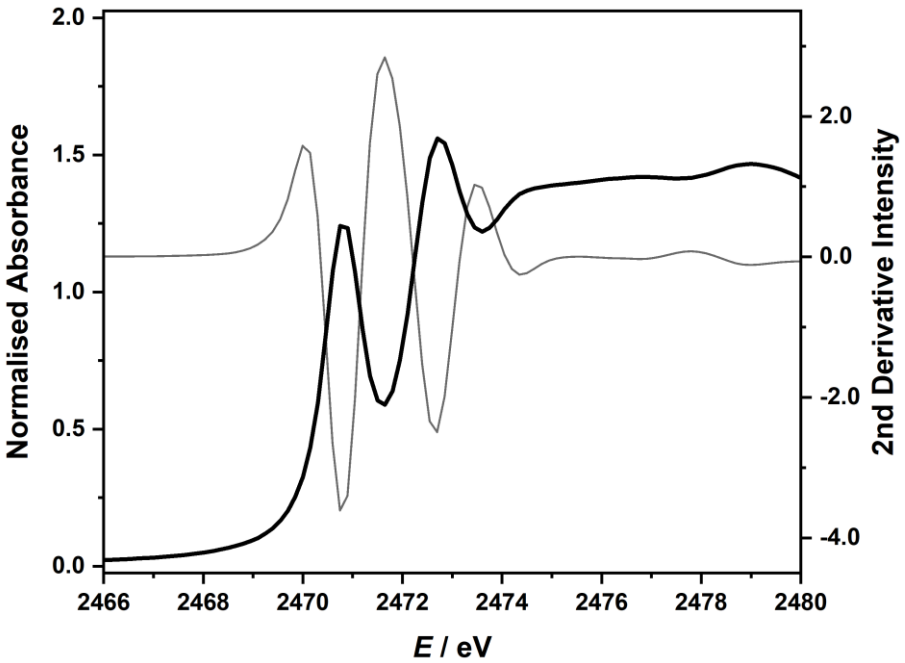

Figure 8.31 Normalised S K-edge spectrum and second derivative of K_2(*i*-ect).

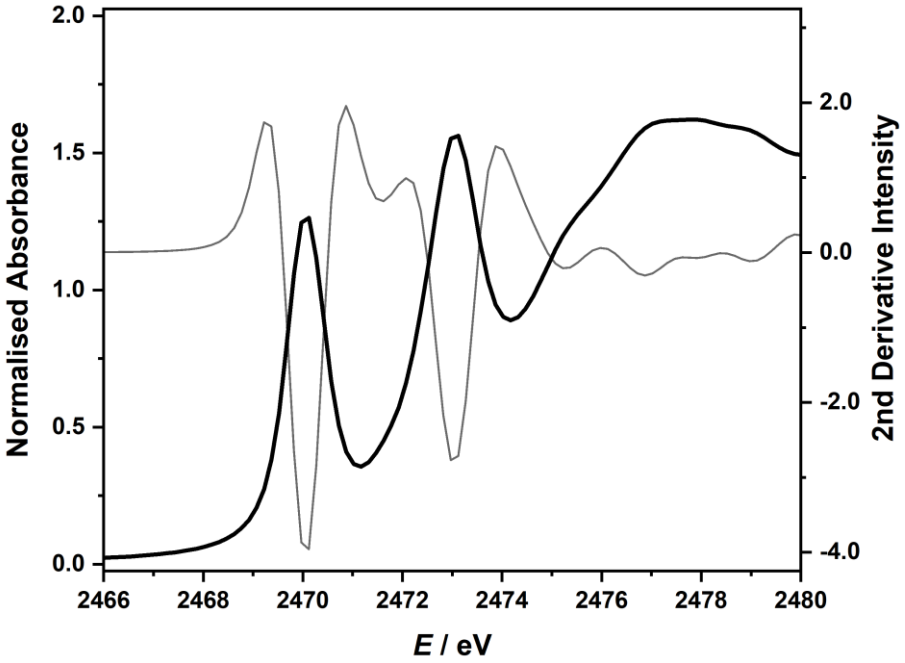

Figure 8.32 Normalised S K-edge spectrum and second derivative of K_2(nmt).

8.8 Co^{II} Complex Electronic Spectra

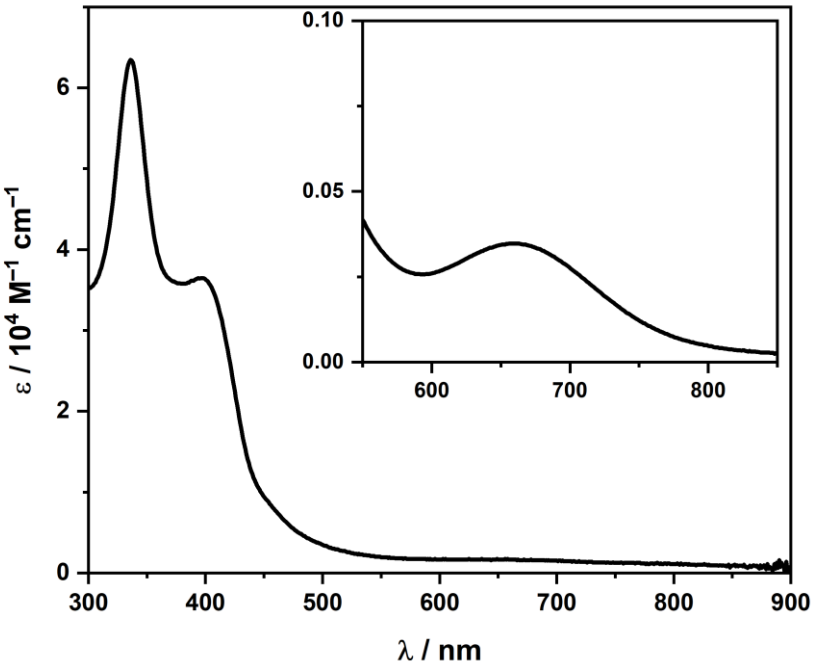

Figure 8.33 Electronic spectrum of $(PPh_4)_2[Co(i\text{-}mnt)_2]$ recorded in MeCN.

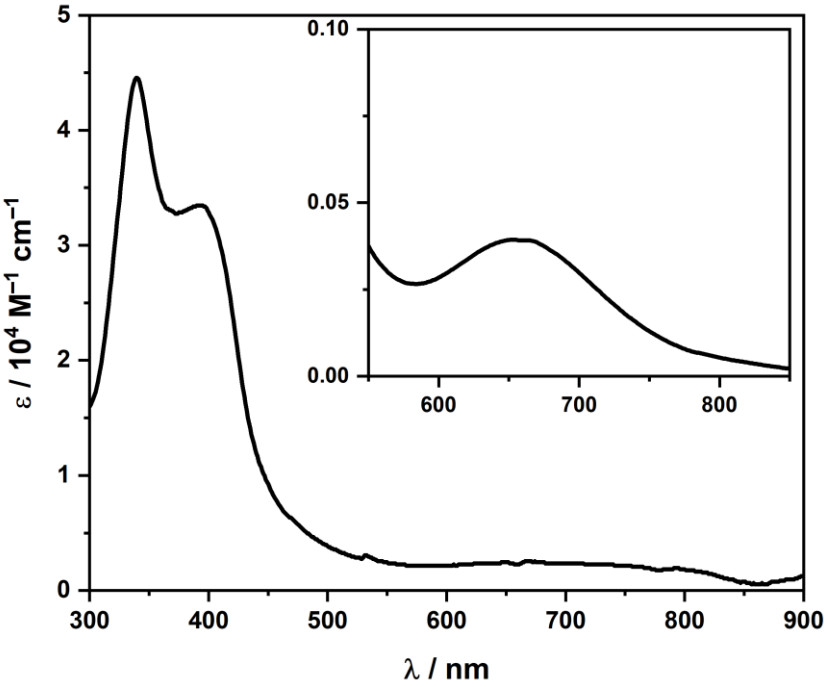

Figure 8.34 Electronic spectrum of $(PPh_4)_2[Co(i\text{-mant})_2]$ recorded in MeCN.

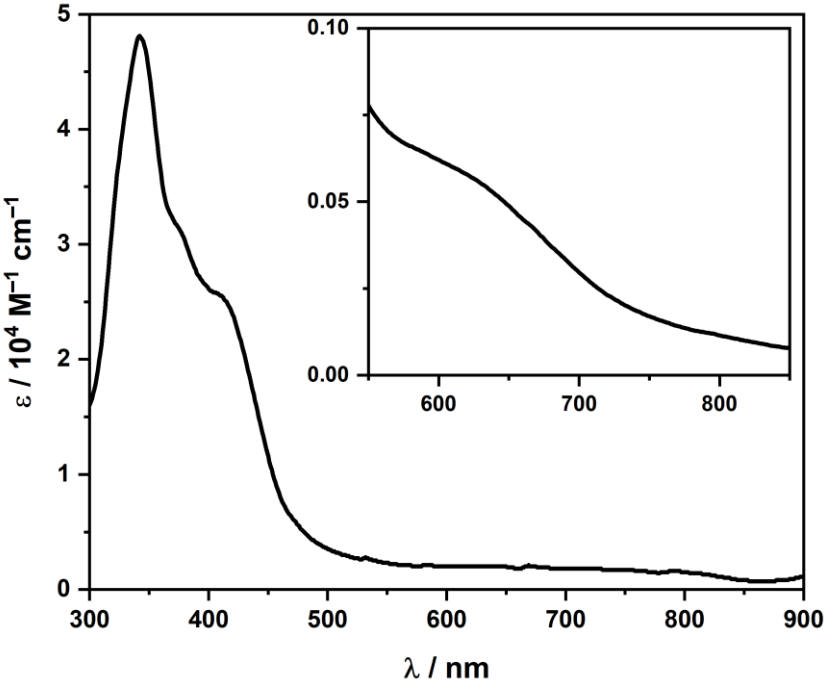

Figure 8.35 Electronic spectrum of $(PPh_4)_2[Co(i\text{-ect})_2]$ recorded in MeCN.

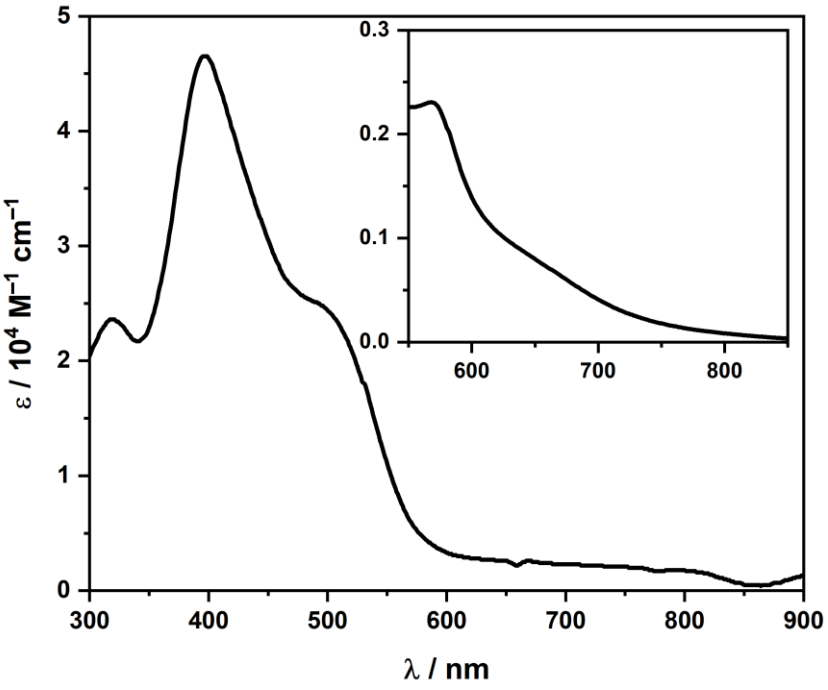

Figure 8.36 Electronic spectrum of $(PPh_4)_2[Co(nmt)_2]$ recorded in MeCN.

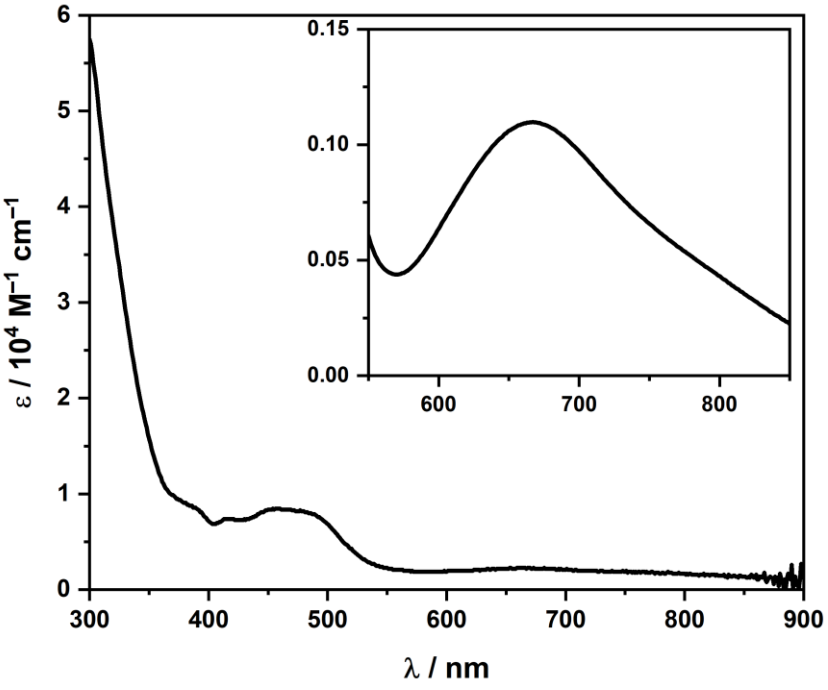

Figure 8.37 Electronic spectrum of $(PPh_4)_2[Co(mnt)_2]$ recorded in MeCN

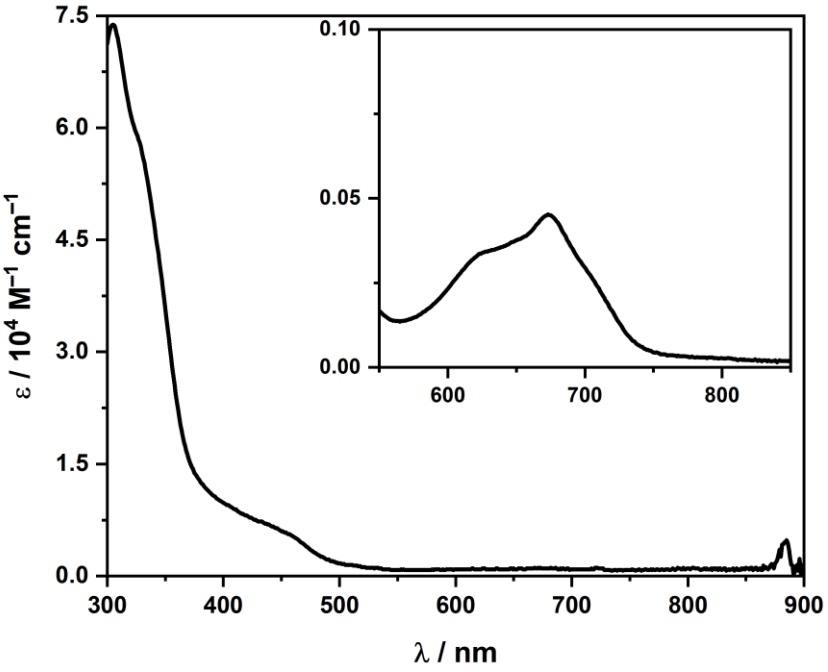

Figure 8.38 Electronic spectrum of $(PPh_4)_2[Co(dts)_2]$ recorded in MeCN

8.9 Co Complex Co K-edge Spectra

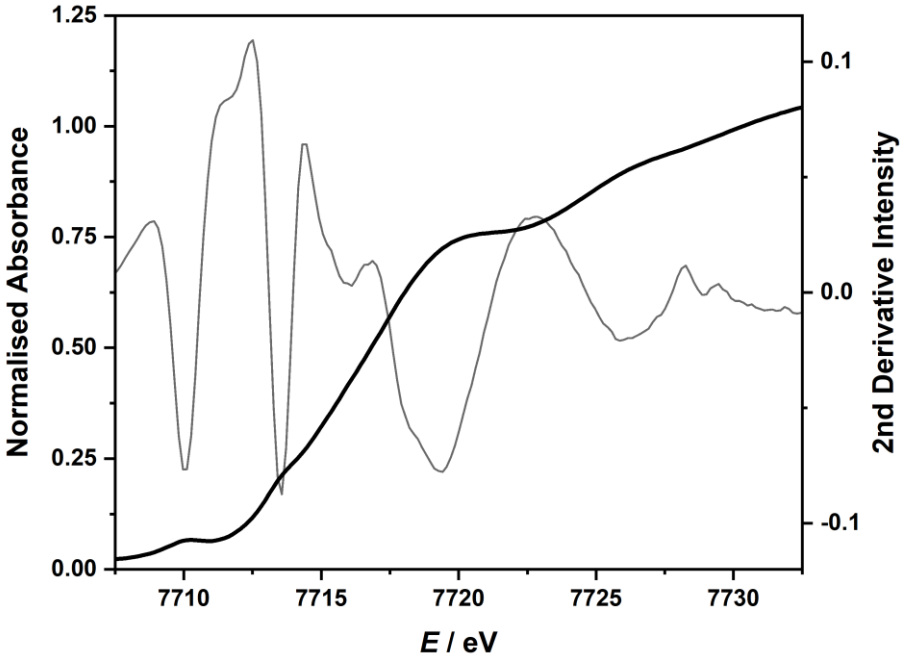

Figure 8.39 Normalised Co K-edge spectrum and second derivative of $(PPh_4)_2[Co(i\text{-}mnt)_2]$.

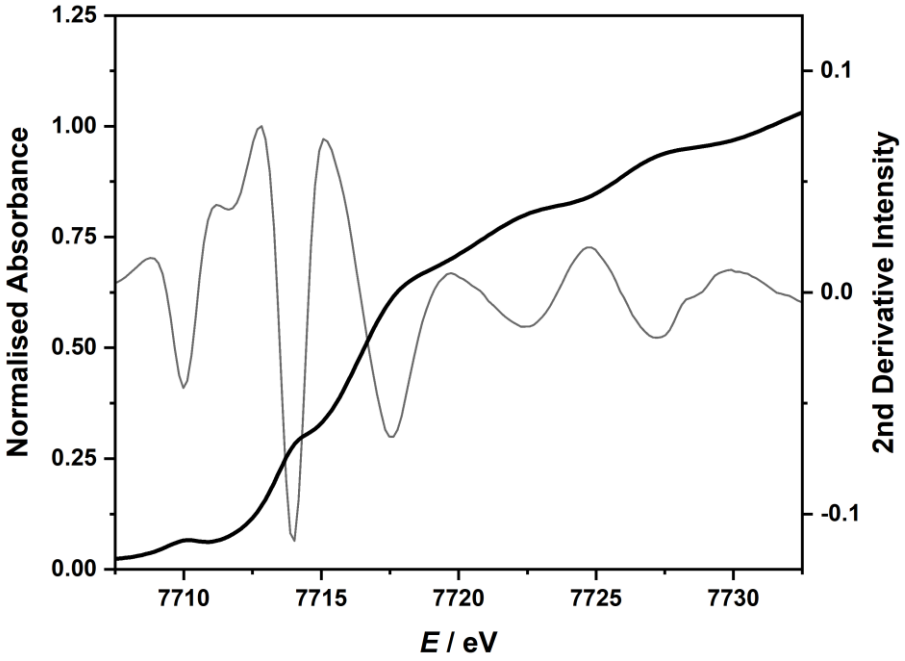

Figure 8.40 Normalised Co K-edge spectrum and second derivative of $(PPh_4)_2[Co(i\text{-mant})_2]$.

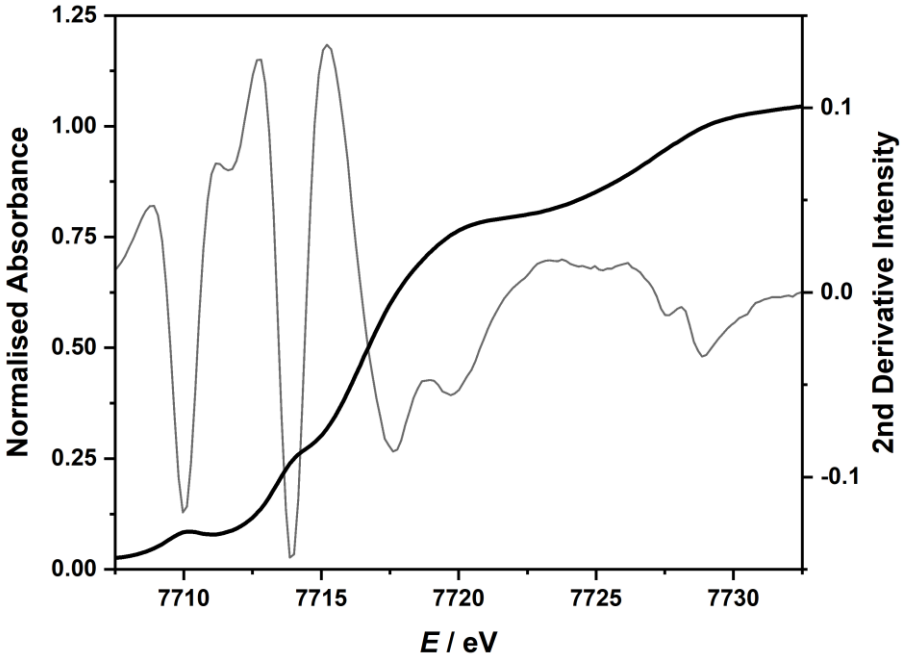

Figure 8.41 Normalised Co K-edge spectrum and second derivative of $(PPh_4)_2[Co(i\text{-ect})_2]$.

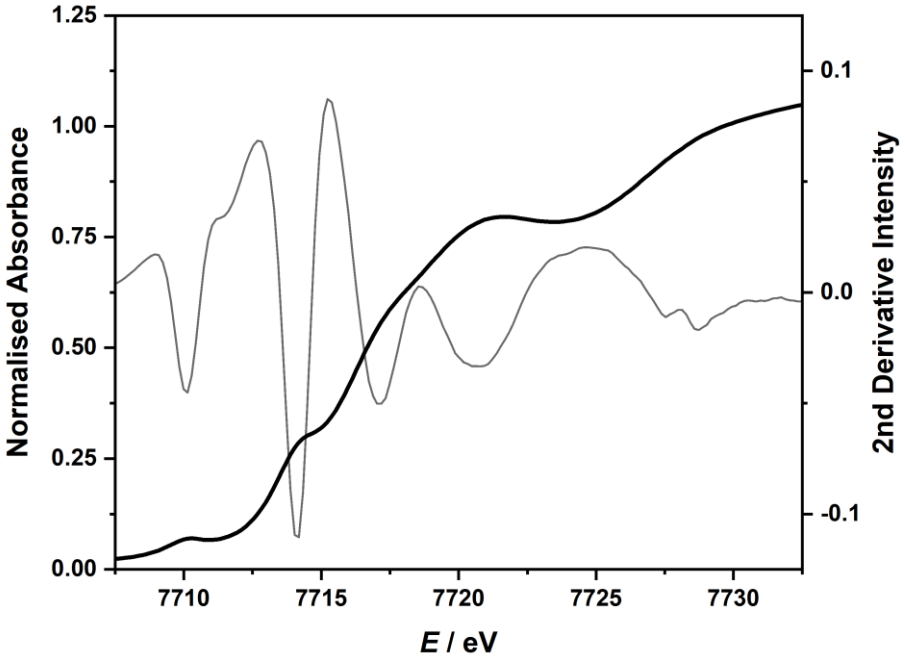

Figure 8.42 Normalised Co K-edge spectrum and second derivative of $(PPh_4)_2[Co(nmt)_2]$.

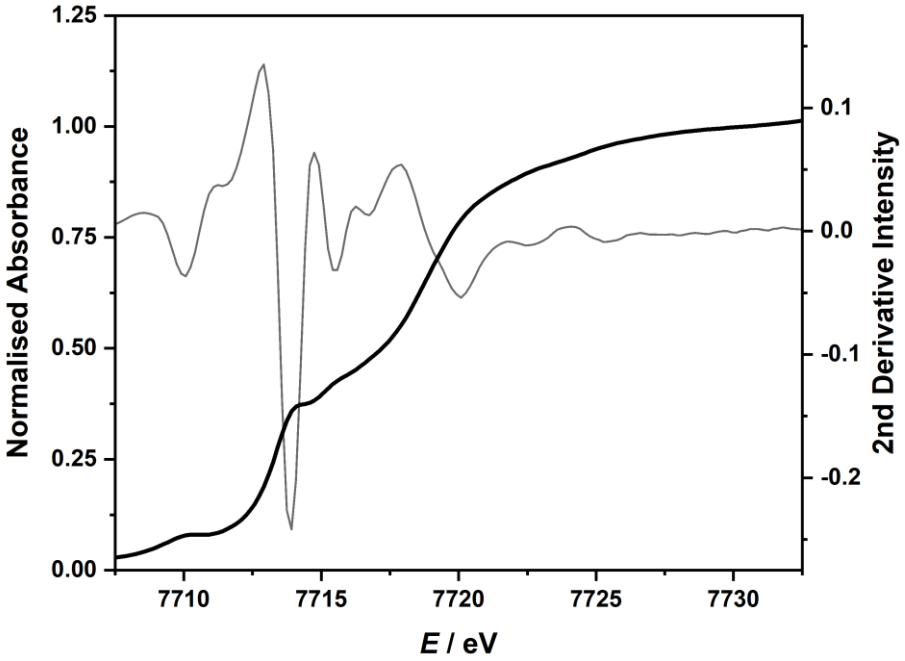

Figure 8.43 Normalised Co K-edge spectrum and second derivative of $(PPh_4)_2[Co(mnt)_2]$.

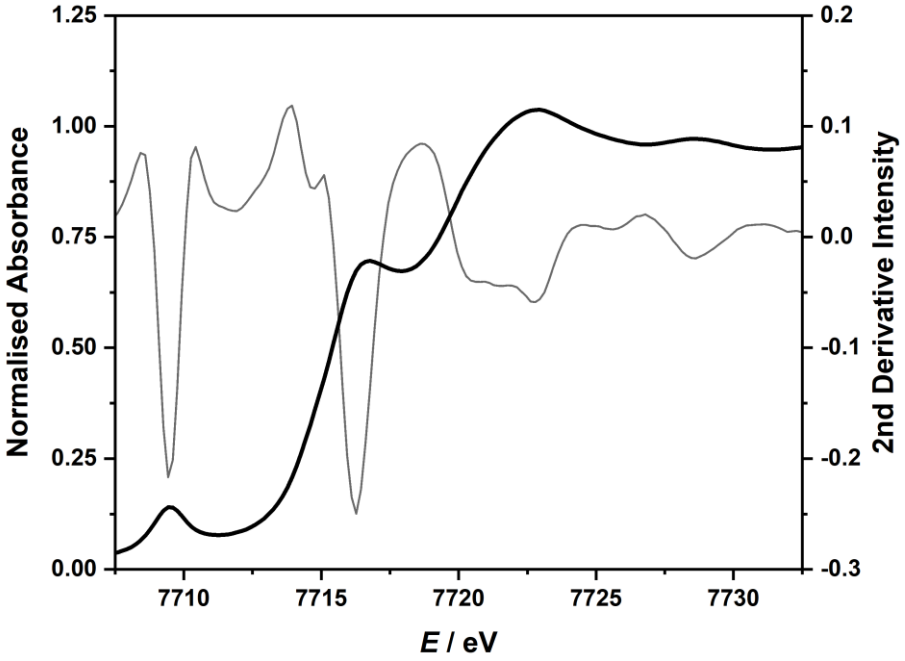

Figure 8.44 Normalised Co K-edge spectrum and second derivative of $(PPh_4)_2[Co(dts)_2]$.

8.10 Co Complex S K-edge Spectra

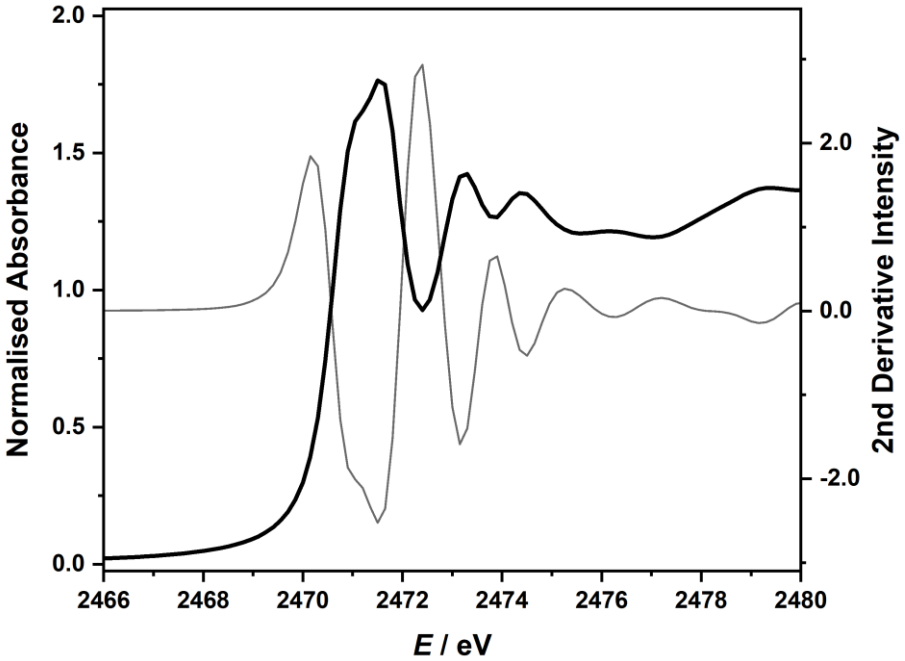

Figure 8.45 Normalised S K-edge spectrum and second derivative of $(PPh_4)_2[Co(i\text{-}mnt)_2]$.

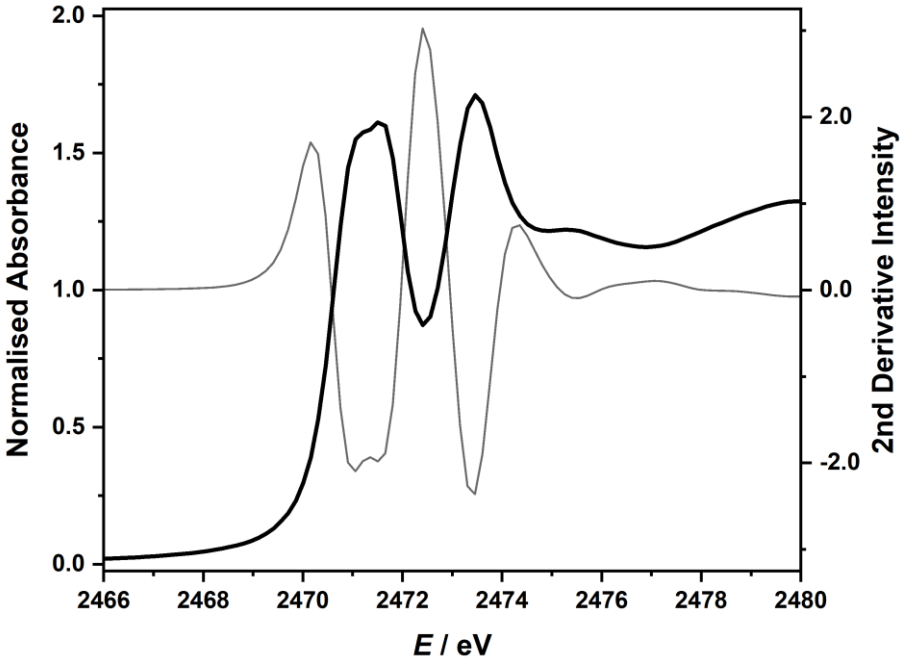

Figure 8.46 Normalised S K-edge spectrum and second derivative of $(PPh_4)_2[Co(i\text{-mant})_2]$.

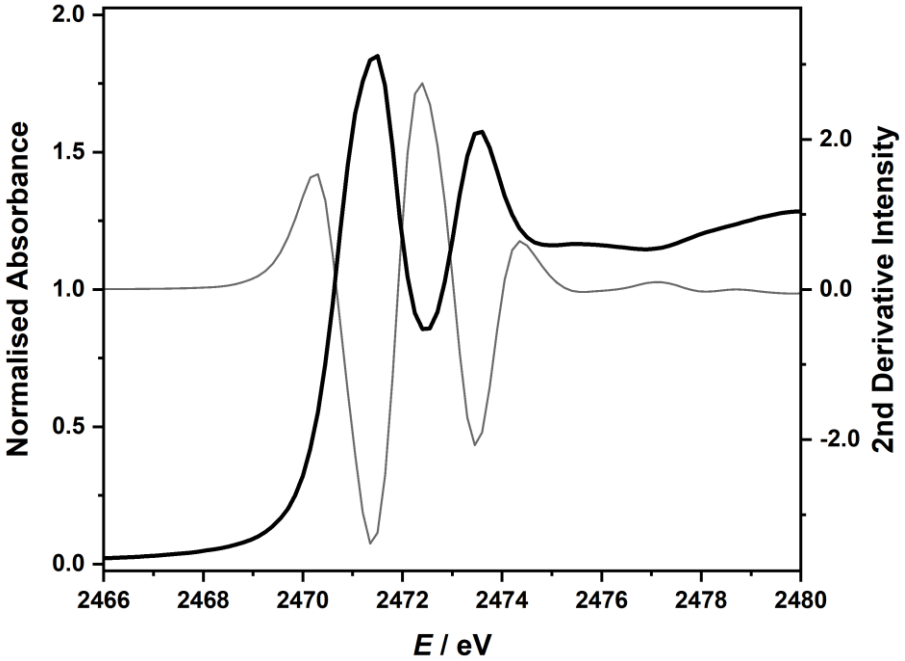

Figure 8.47 Normalised S K-edge spectrum and second derivative of $(PPh_4)_2[Co(i\text{-ect})_2]$.

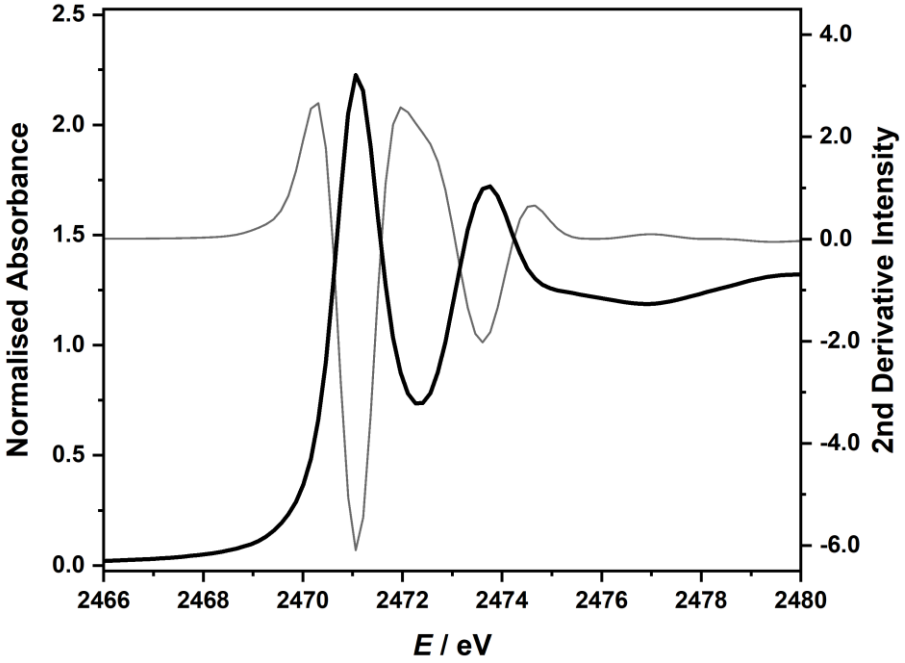

Figure 8.48 Normalised S K-edge spectrum and second derivative of $(PPh_4)_2[Co(nmt)_2]$.

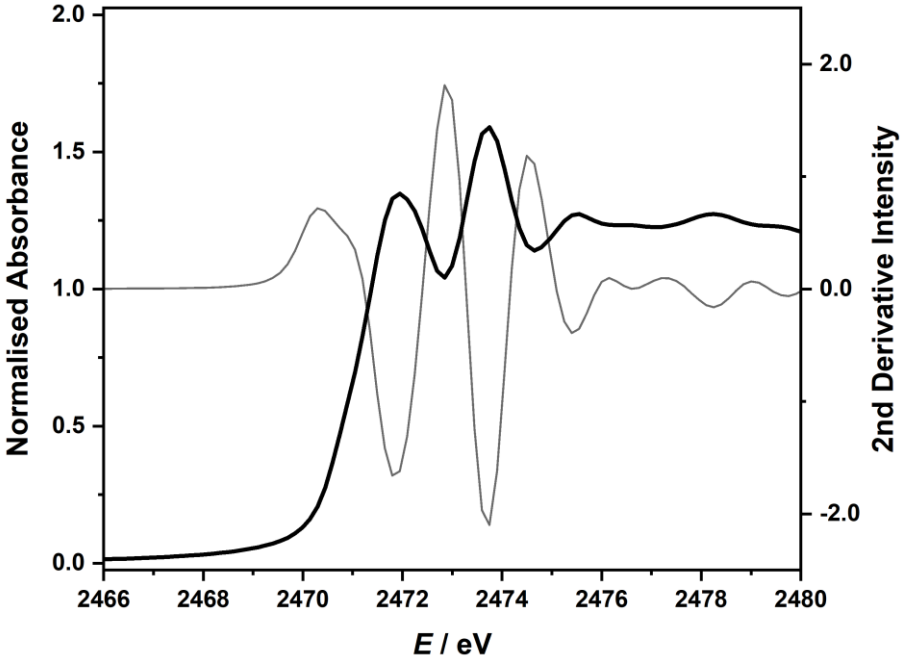

Figure 8.49 Normalised S K-edge spectrum and second derivative of $(PPh_4)_2[Co(mnt)_2]$.

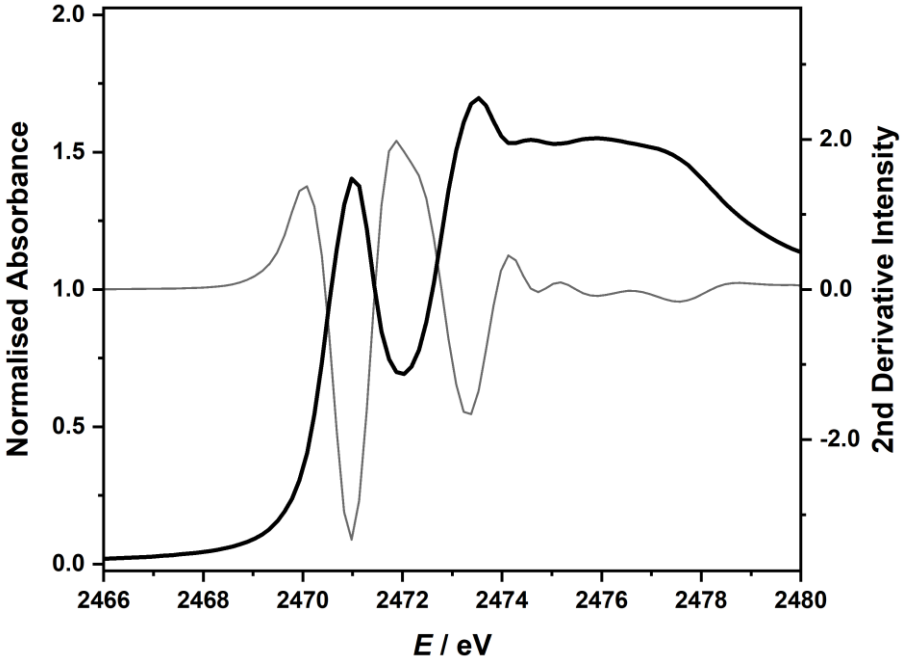

Figure 8.50 Normalised S K-edge spectrum and second derivative of $(PPh_4)_2[Co(dts)_2]$.

8.11 Tetrathiotungstate Complex Electronic Spectra

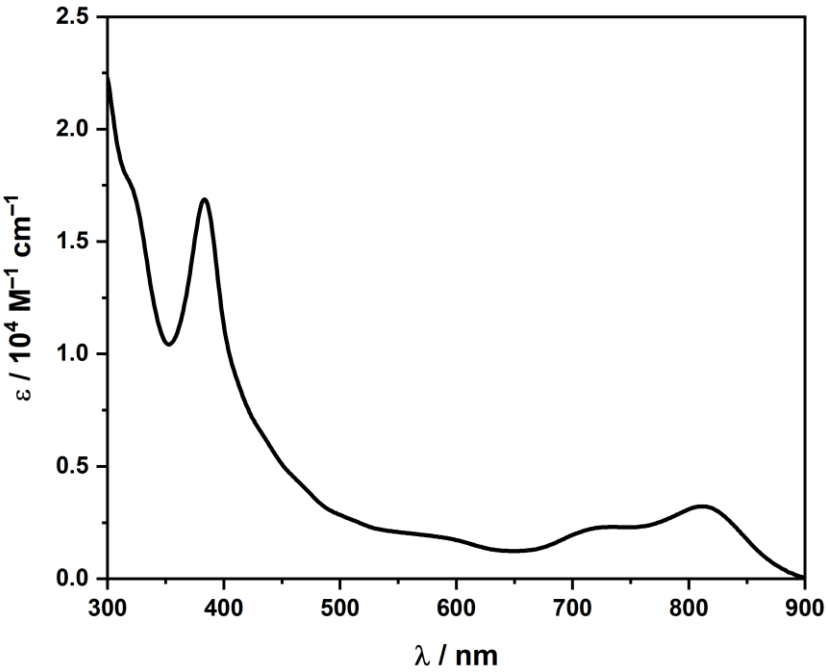

Figure 8.51 Electronic spectrum of $(PPh_4)_2[Co(WS_4)_2]$ recorded in CH_2Cl_2.

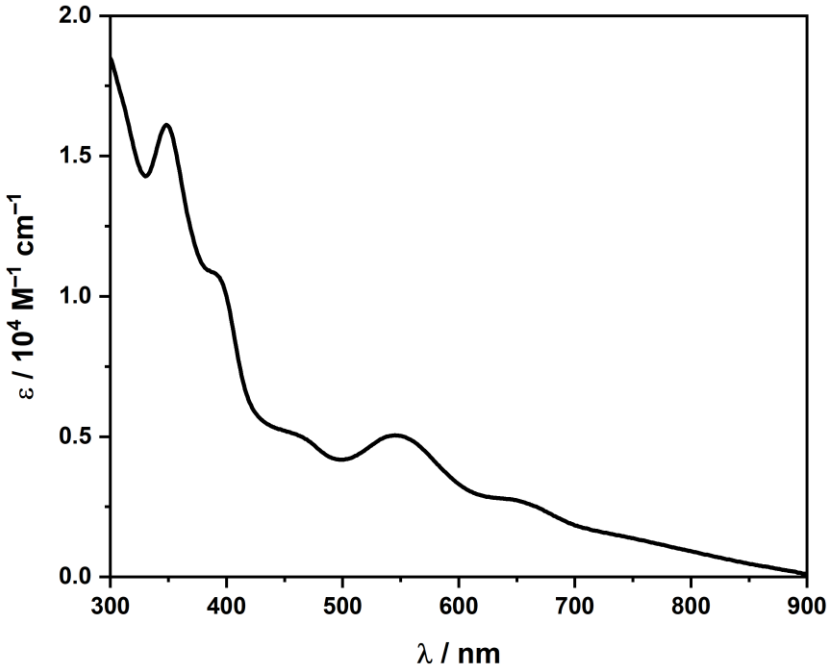

Figure 8.52 Electronic spectrum of $(PPh_4)_3[Co(WS_4)_2]$ recorded in CH_2Cl_2.

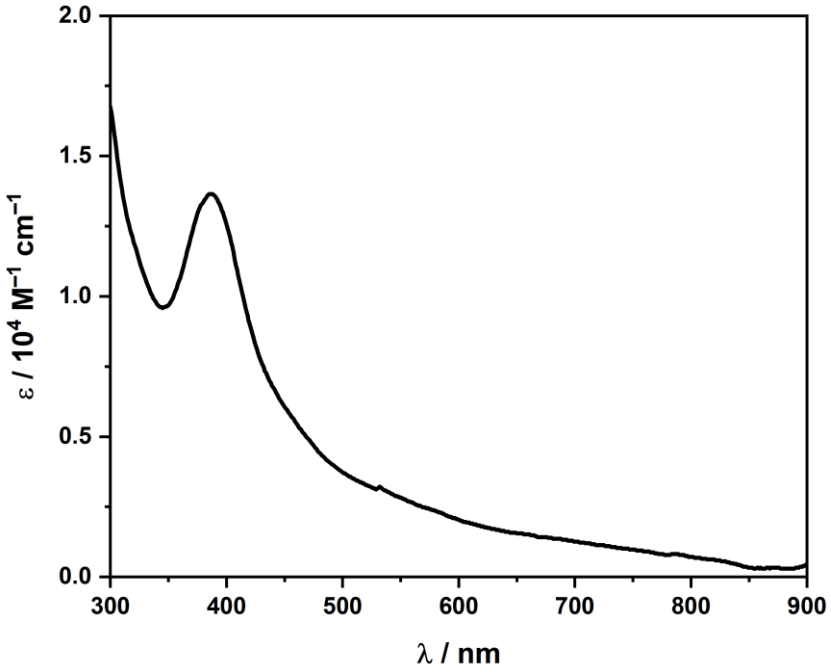

Figure 8.53 Electronic spectrum of $(PPh_4)[Cu(WS_4)_2]$ recorded in MeCN.

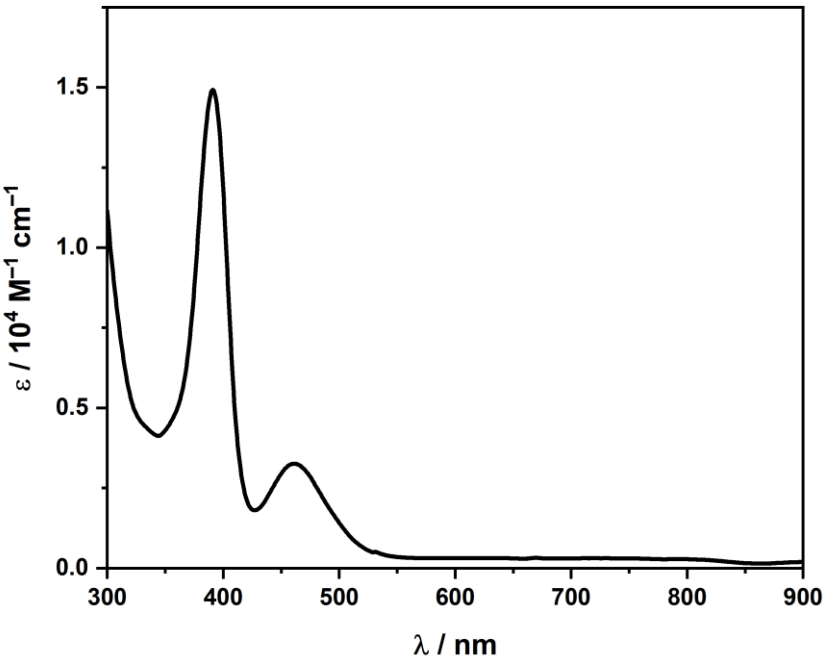

Figure 8.54 Electronic spectrum of $(PPh_4)_2[Zn(WS_4)_2]$ recorded in MeCN.

8.12 Co Tetrathiotungstate Co K-edge Spectra

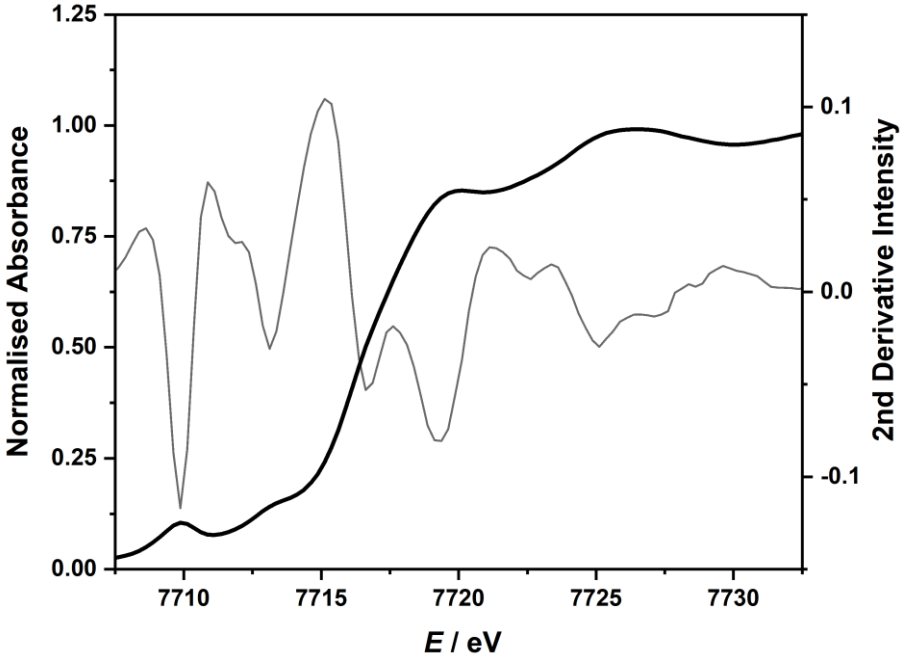

Figure 8.55 Normalised Co K-edge spectrum and second derivative of $(PPh_4)_2[Co(WS_4)_2]$.

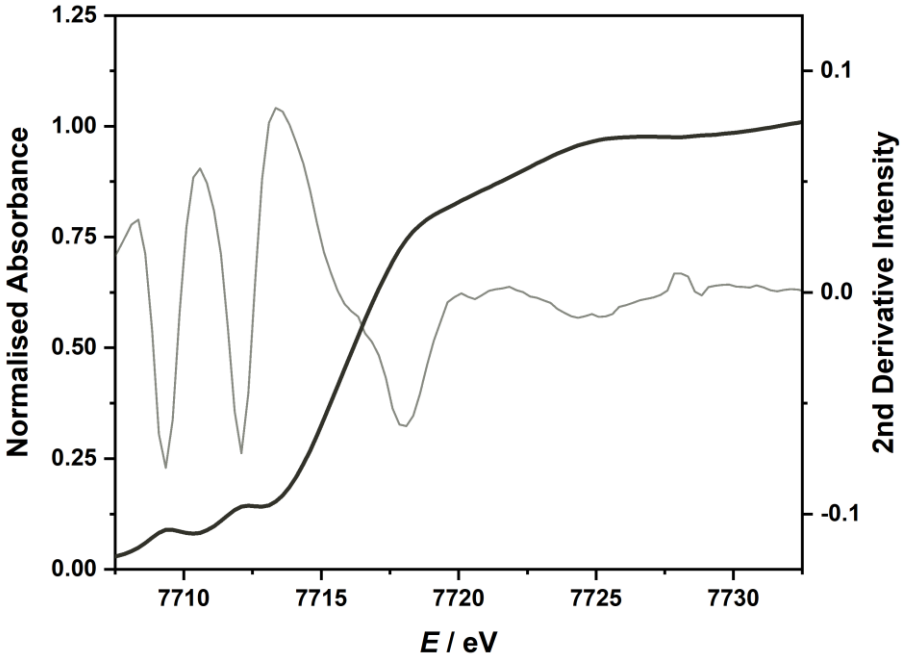

Figure 8.56 Normalised Co K-edge spectrum and second derivative of $(PPh_4)_3[Co(WS_4)_2]$.

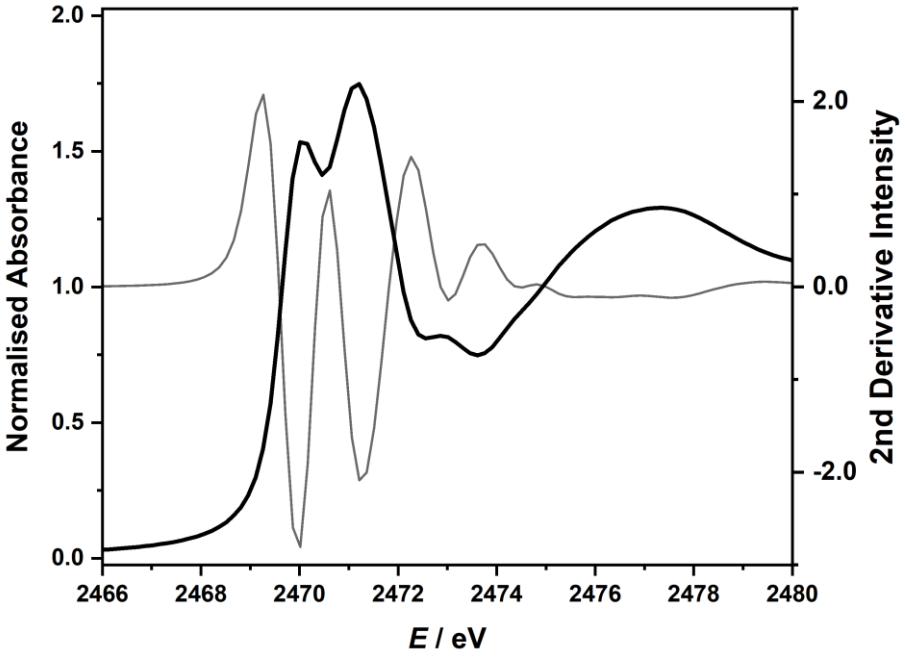

Figure 8.57 Normalised Co K-edge spectrum and second derivative of $(PPh_4)_2[Zn(WS_4)_2]$.

8.13 Tetrathiotungstate Complex S K-edge Spectra

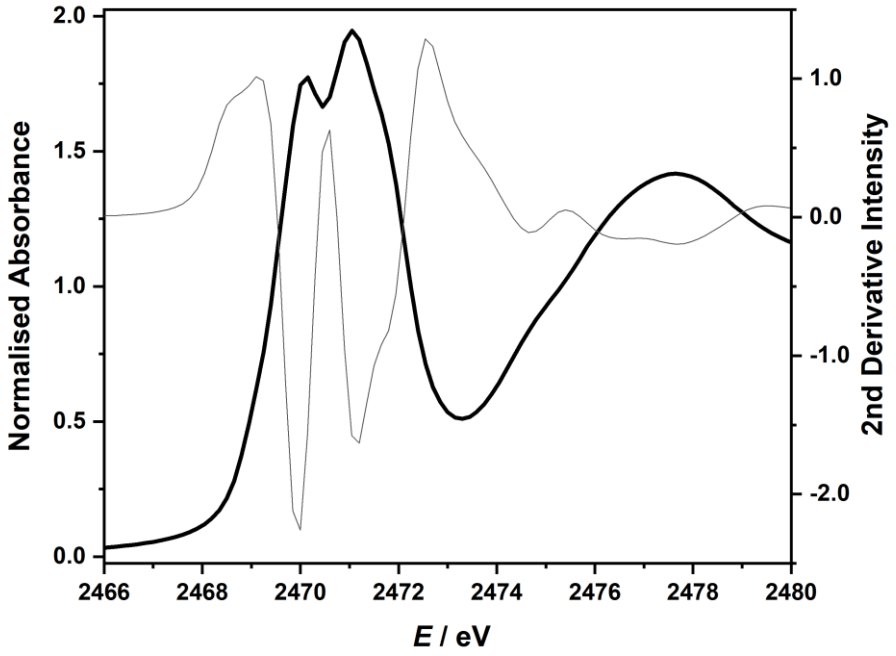

Figure 8.58 Normalised S K-edge spectrum and second derivative of $(PPh_4)_2[Co(WS_4)_2]$.

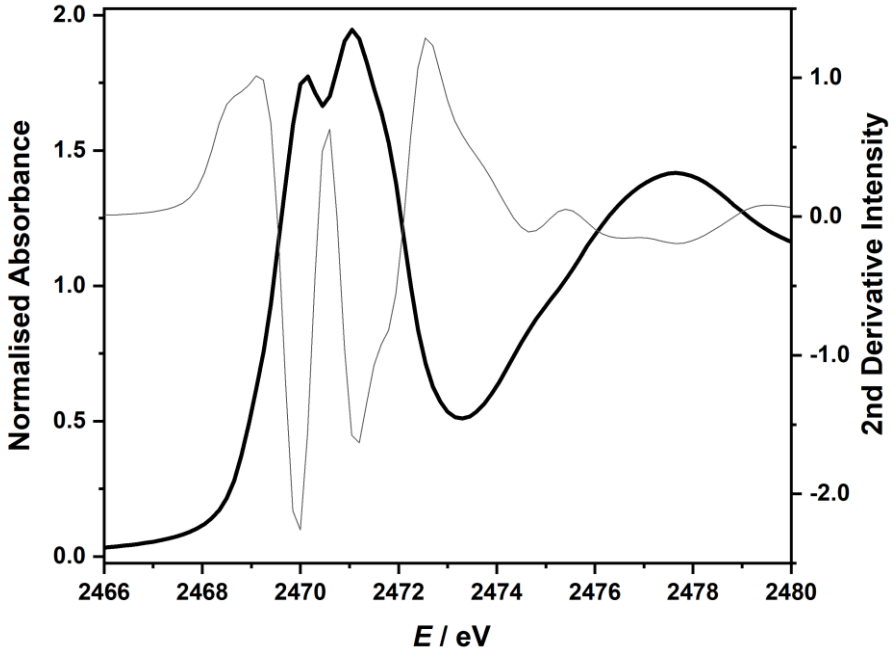

Figure 8.59 Normalised S K-edge spectrum and second derivative of $(PPh_4)_3[Co(WS_4)_2]$.

8.14 Cu 1,1-Dithiolate Electronic Spectra

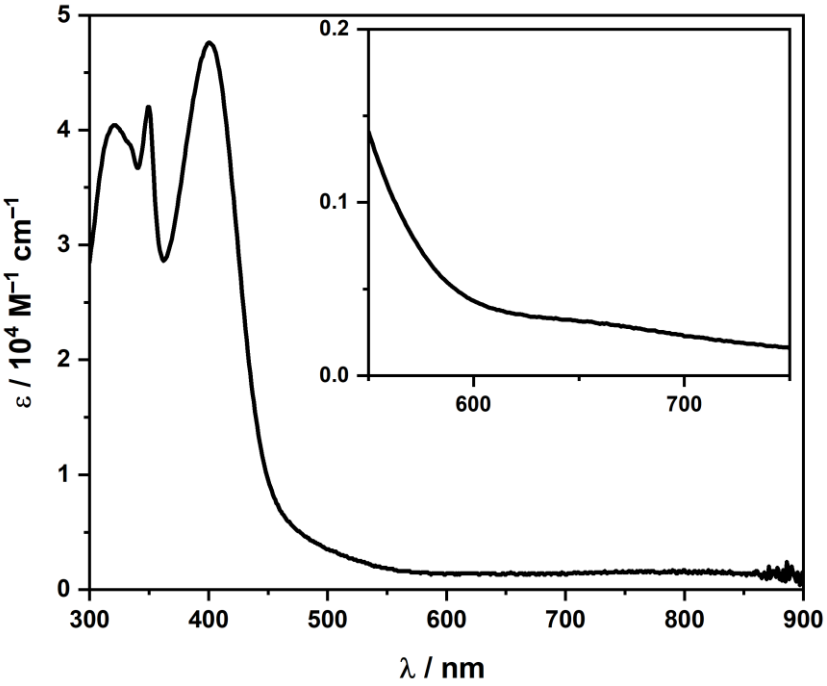

Figure 8.60 Electronic spectrum of $(NBu_4)_2[Cu(i\text{-}mnt)_2]$ recorded in MeCN.

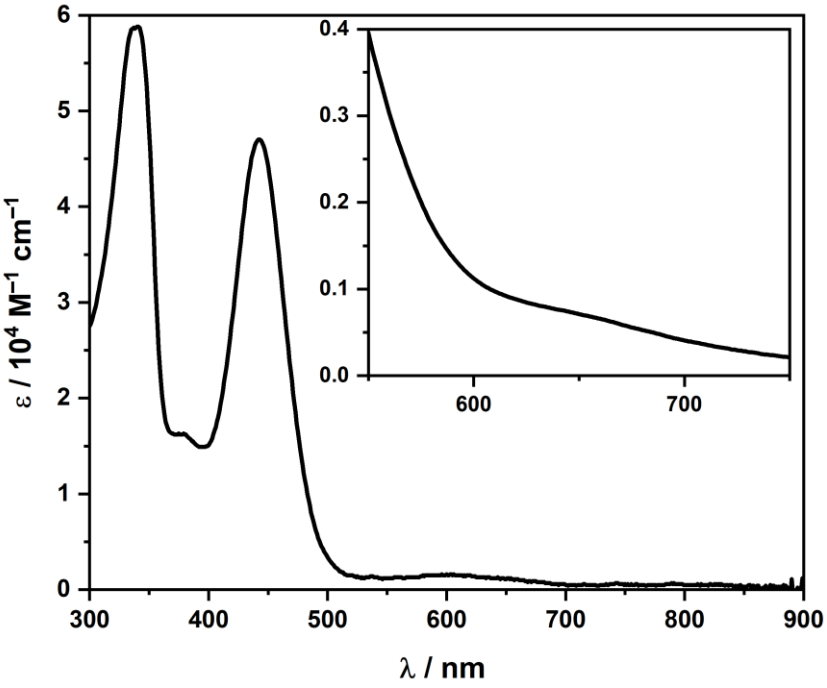

Figure 8.61 Electronic spectrum of $(NBu_4)_2[Cu(i\text{-}mant)_2]$ recorded in MeCN.

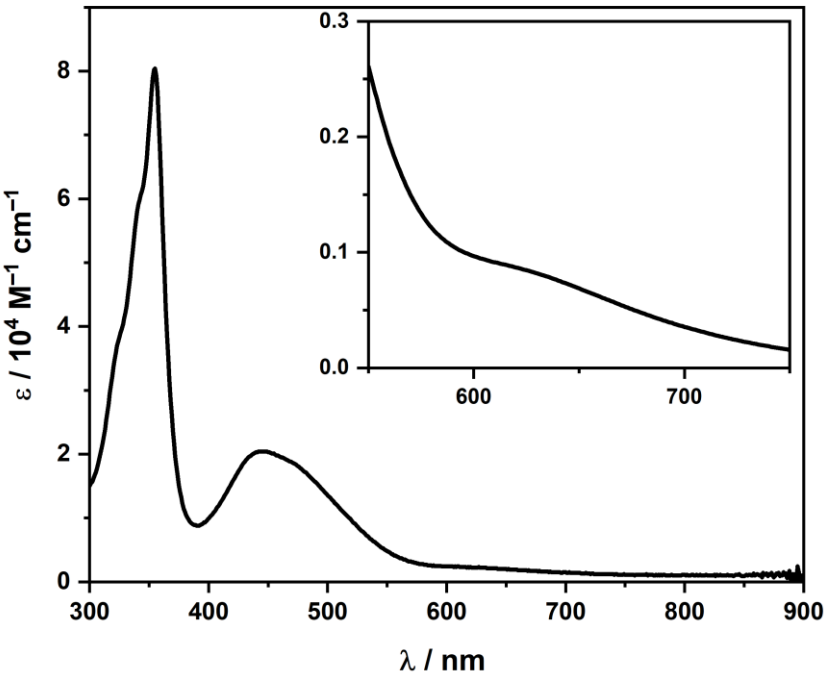

Figure 8.62 Electronic spectrum of $(NBu_4)_2[Cu(i\text{-}ect)_2]$ recorded in MeCN.

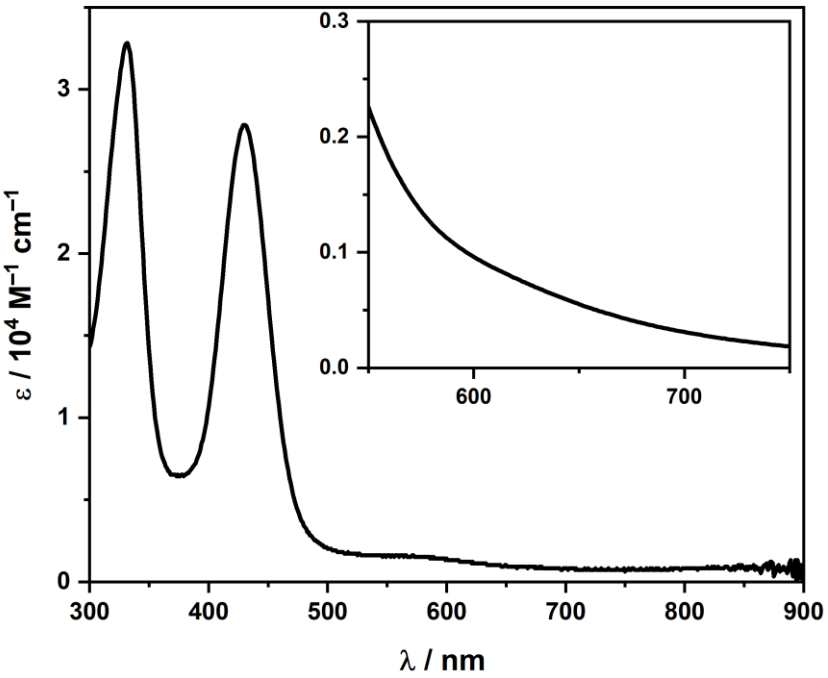

Figure 8.63 Electronic spectrum of $(PPh_4)_2[Cu(ded)_2]$ recorded in MeCN.

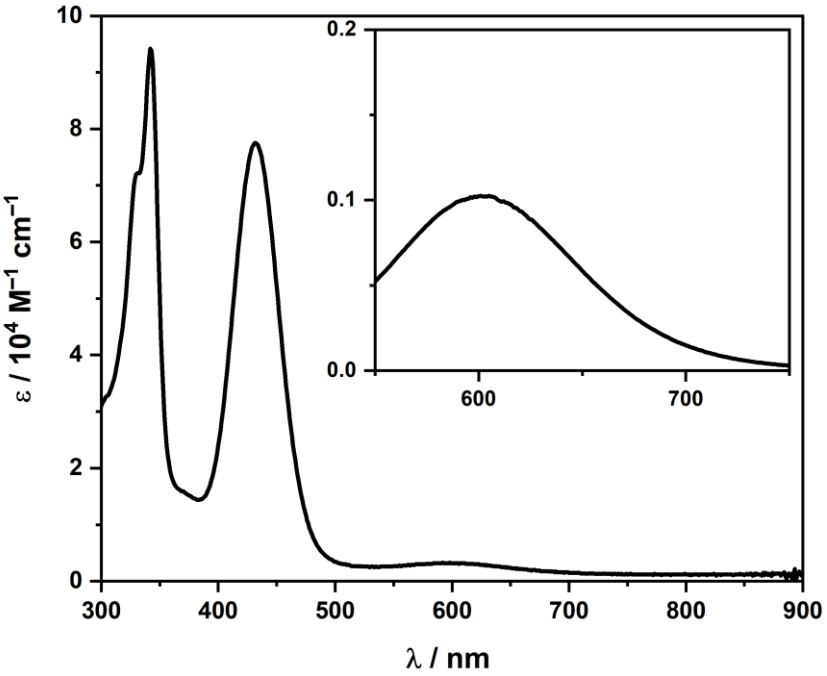

Figure 8.64 Electronic spectrum of $(NBu_4)_2[Cu(i\text{-}ect)_2]$ recorded in MeCN.

8.15 Fluid Solution EPR Data

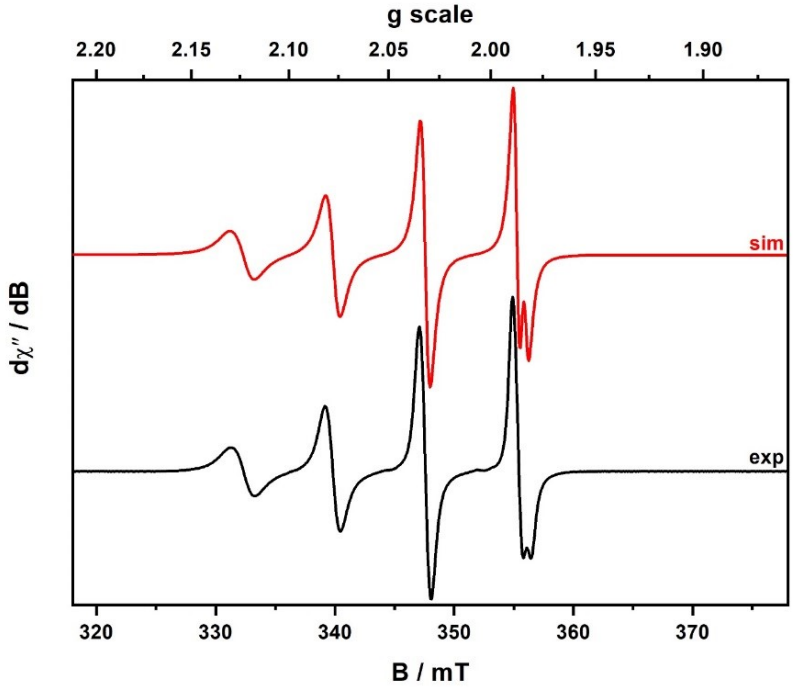

Figure 8.65 X-band EPR spectrum of $(NBu_4)_2[Cu(i\text{-}mnt)_2]$ recorded in acetone at 293 K (conditions: frequency, 9.8476 GHz; modulation, 1 mT; power, 0.02 mW). Experimental spectrum shown in black and simulation depicted by the red trace: g_{iso} = 2.0451; A_{iso} = 72.3 × 10^{-4} cm^{-1}.

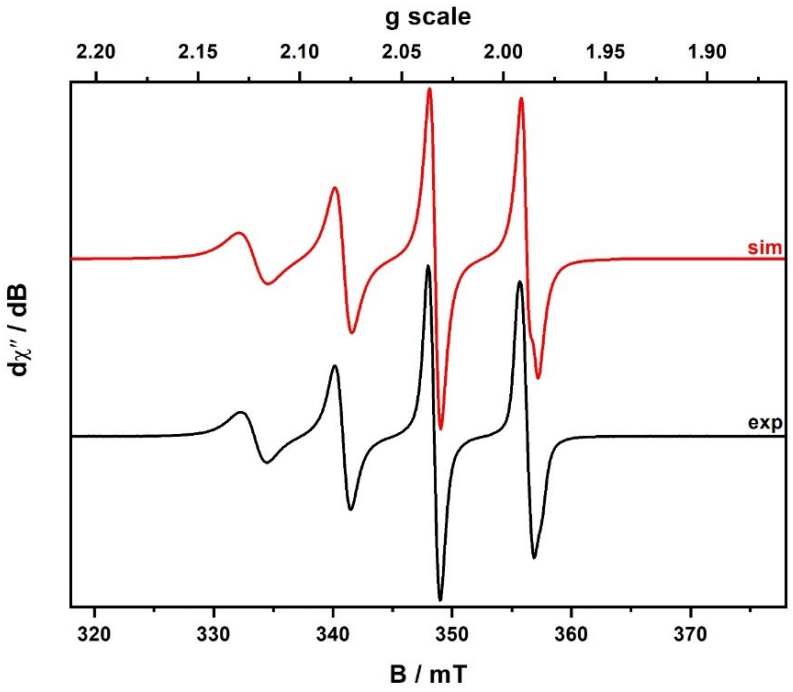

Figure 8.66 X-band EPR spectrum of $(NBu_4)_2[Cu(i\text{-mant})_2]$ recorded in acetone at 293 K (conditions: frequency, 9.8723 GHz; modulation, 1 mT; power, 0.2 mW). Experimental spectrum shown in black and simulation depicted by the red trace: g_{iso} = 2.0441; A_{iso} = 71.7 × 10^{-4} cm^{-1}.

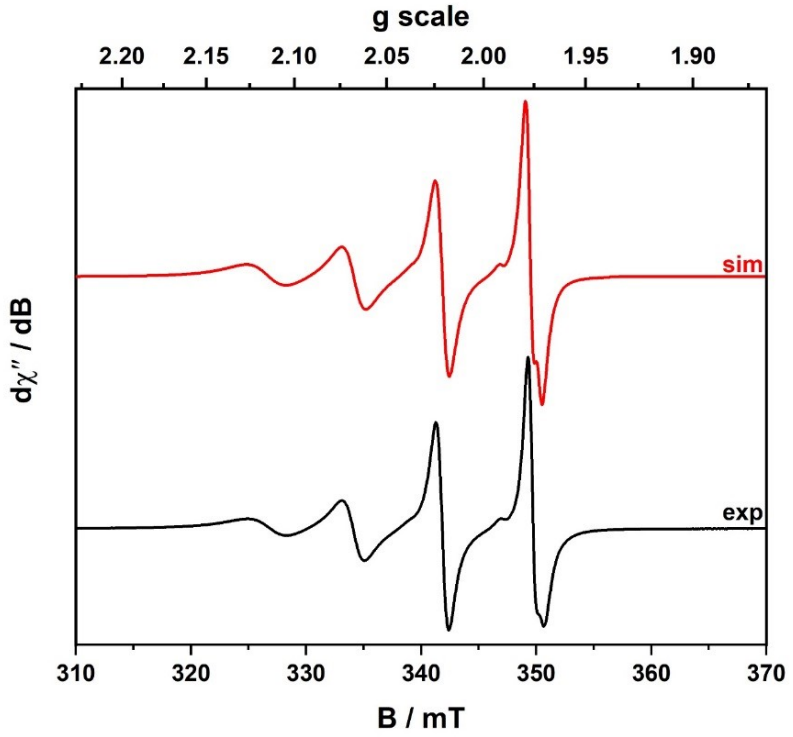

Figure 8.67 X-band EPR spectrum of $(NBu_4)_2[Cu(i\text{-ect})_2]$ recorded in $CHCl_3$ at 293 K (conditions: frequency, 9.6698 GHz; modulation, 0.5 mT; power, 0.63 mW). Experimental spectrum shown in black and simulation depicted by the red trace: g_{iso} = 2.0420; A_{iso} = 71.6 × 10^{-4} cm^{-1} (97%), g_{iso} = 2.0560; A_{iso} = 71.6 × 10^{-4} cm^{-1} (3%).

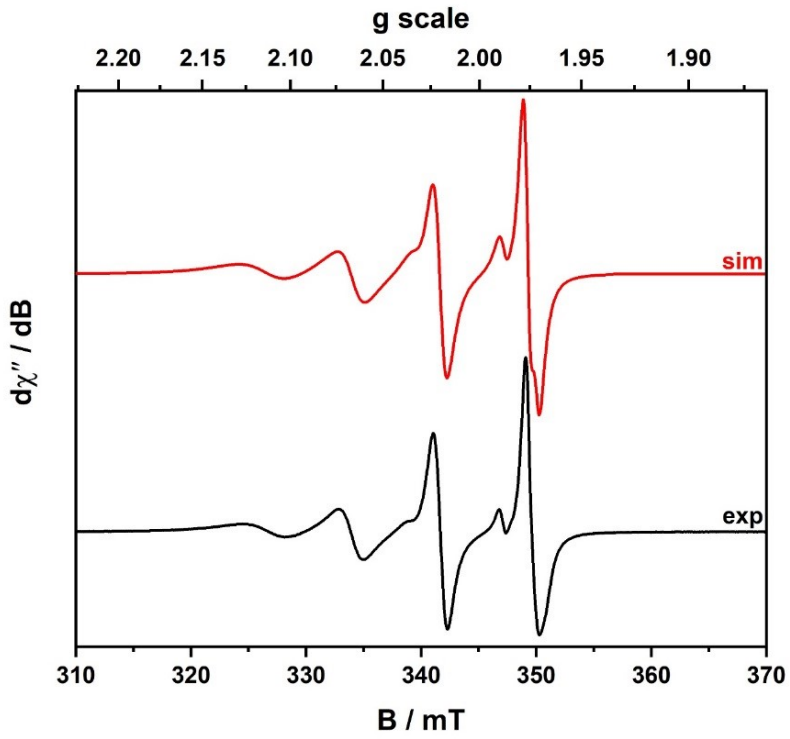

Figure 8.68 X-band EPR spectrum of $(NBu_4)_2[Cu(ded)_2]$ recorded in $CHCl_3$ at 293 K (conditions: frequency, 9.6596 GHz; modulation, 0.5 mT; power, 0.63 mW). xperimental spectrum shown in black and simulation depicted by the red trace: g_{iso} = 2.0410; A_{iso} = 71.4 × 10^{-4} cm^{-1} (87%), g_{iso} = 2.0530; A_{iso} = 71.4 × 10^{-4} cm^{-1} (13%).

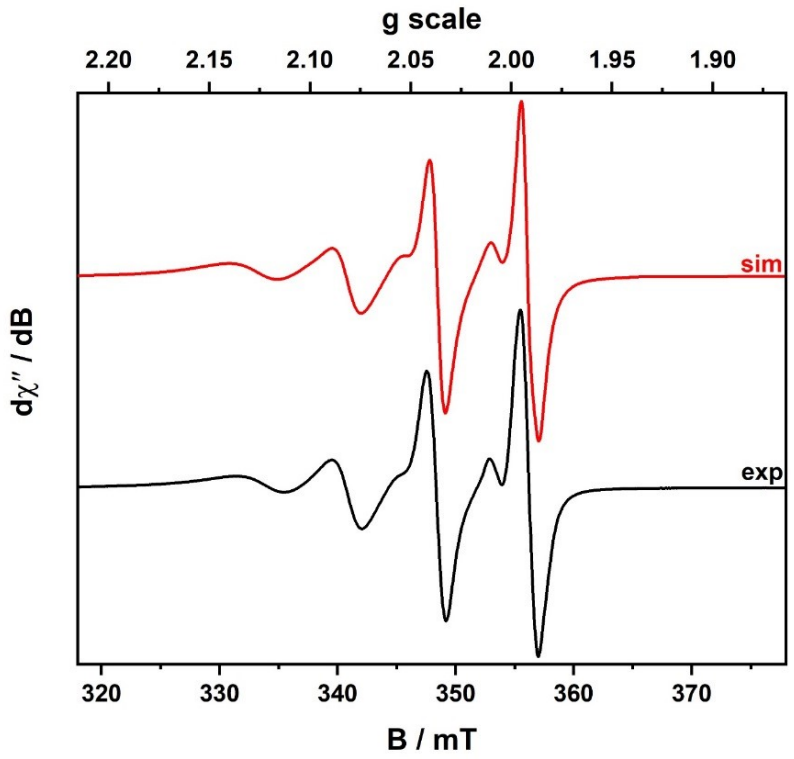

Figure 8.69 X-band EPR spectrum of $(PPh_4)_2[Cu(ded)_2]$ recorded in $CHCl_3$ at 293 K (conditions: frequency, 9.6596 GHz; modulation, 0.5 mT; power, 0.63 mW). Experimental spectrum shown in

black and simulation depicted by the red trace: g_{iso} = 2.0410; A_{iso} = 71.0 × 10^{-4} cm^{-1} (87%), g_{iso} = 2.0570; A_{iso} = 71.0 × 10^{-4} cm^{-1} (13%).

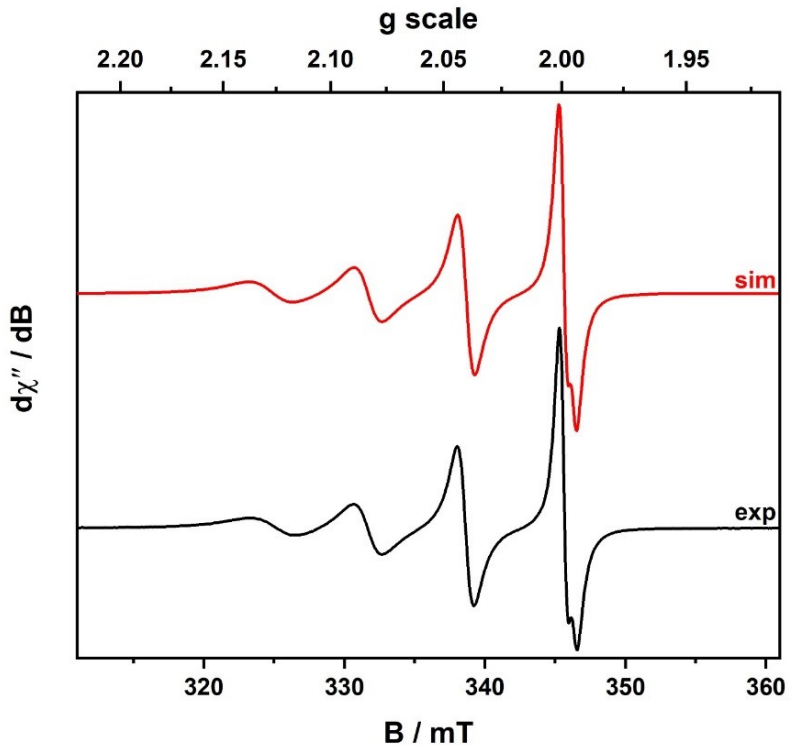

Figure 8.70 X-band EPR spectrum of $(PPh_4)_2[Cu(dts)_2]$ recorded in $CHCl_3$ at 293 K (conditions: frequency, 9.6706 GHz; modulation, 0.3 mT; power, 0.2 mW). Experimental spectrum shown in black and simulation depicted by the red trace: g_{iso} = 2.0595; A_{iso} = 65.7 × 10^{-4} cm^{-1}.

8.16 Frozen Solution EPR Data

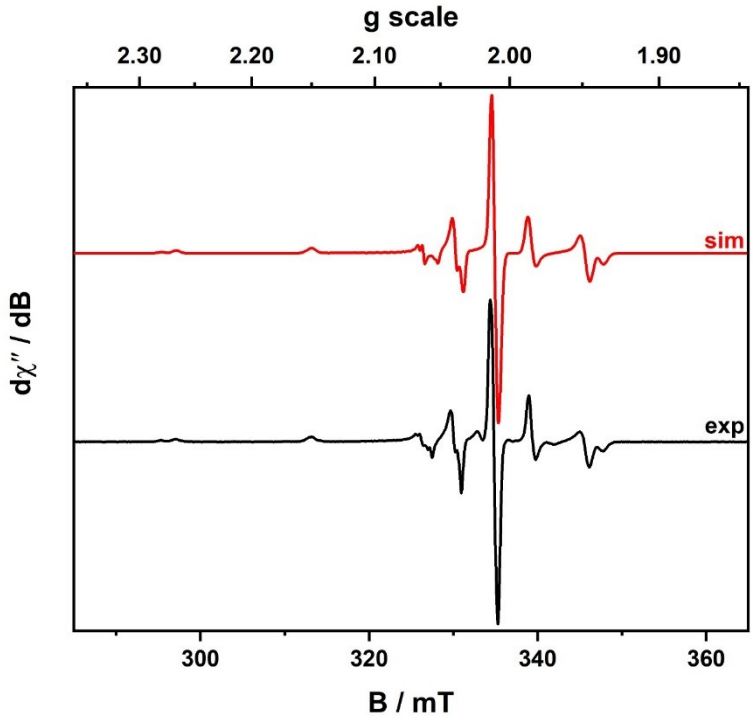

Figure 8.71 X-band EPR spectrum of $(NBu_4)_2[Cu(i\text{-}mnt)_2]$ recorded in CH_2Cl_2/DMF at 130 K (conditions: frequency, 9.4247 GHz; modulation, 0.1 mT; power, 0.063 mW). Experimental spectrum shown in black and simulation depicted by the red trace: g = (2.017, 2.021, 2.094); A = (33.0, 40.0, 155.8) × 10^{-4} cm^{-1}.

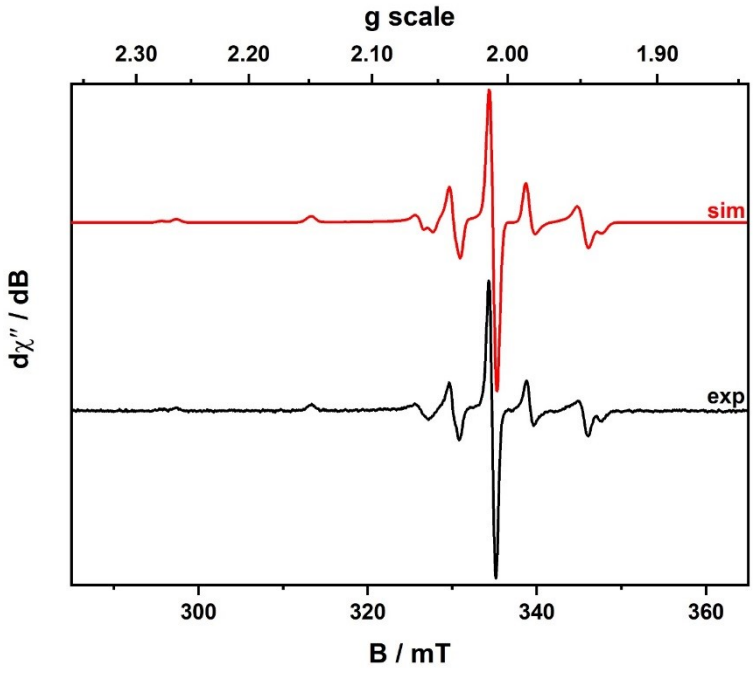

Figure 8.72 X-band EPR spectrum of $(NBu_4)_2[Cu(i\text{-}mant)_2]$ recorded in CH_2Cl_2/DMF at 130 K (conditions: frequency, 9.4207 GHz; modulation, 0.3 mT; power, 0.63 mW). Experimental spectrum shown in black and simulation depicted by the red trace: g = (2.018, 2.022, 2.0935); A = (34.0, 40.0, 157.5) × 10^{-4} cm^{-1}.

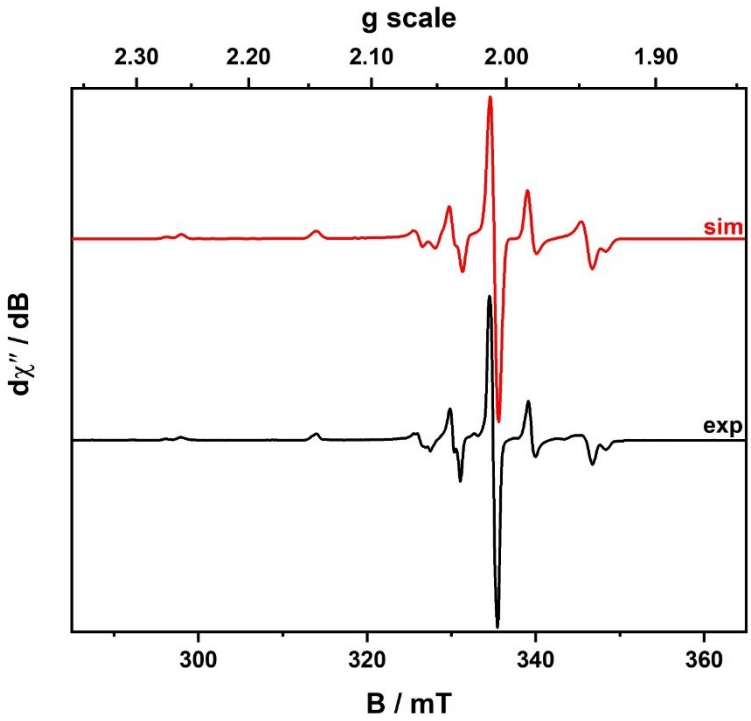

Figure 8.73 X-band EPR spectrum of $(NBu_4)_2[Cu(i\text{-}ect)_2]$ recorded in CH_2Cl_2/DMF at 130 K (conditions: frequency, 9.4210 GHz; modulation, 0.1 mT; power, 0.63 mW). Experimental spectrum shown in black and simulation depicted by the red trace: g = (2.0151, 2.021, 2.089); A = (34.0, 41.0, 157.5) × 10^{-4} cm^{-1}.

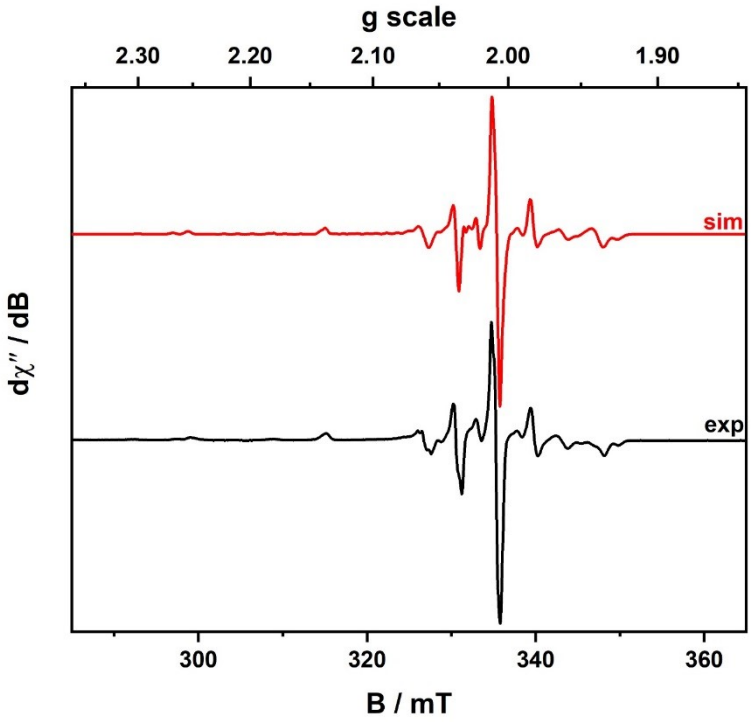

Figure 8.74 X-band EPR spectrum of $(PPh_4)_2[Cu(ded)_2]$ recorded in CH_2Cl_2/DMF at 130 K (conditions: frequency, 9.4264 GHz; modulation, 0.1 mT; power, 0.63 mW). Experimental spectrum shown in black and simulation depicted by the red trace is composed of two subspectra (a) g = (2.018, 2.018, 2.082); A = (37.5, 40.0, 159.0) × 10^{-4} cm^{-1} (87%); and (b) g = (2.009, 2.029, 2.123); A = (20, 20, 169) × 10^{-4} cm^{-1} (13%).

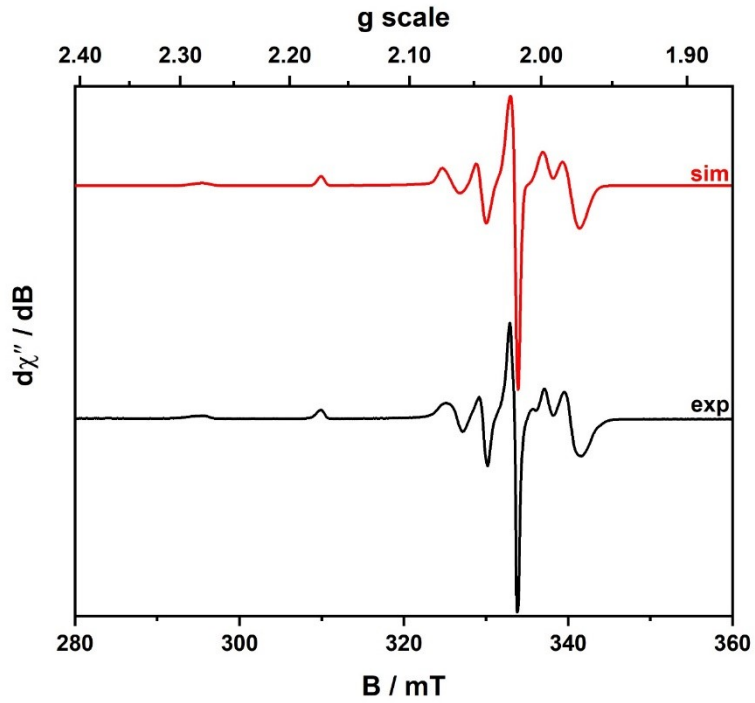

Figure 8.75 X-band EPR spectrum of $(PPh_4)_2[Cu(dts)_2]$ recorded in CH_2Cl_2/DMF at 130 K (conditions: frequency, 9.4246 GHz; modulation, 0.1 mT; power, 6.30 mW). Experimental spectrum shown in black and simulation depicted by the red trace: g = (2.029, 2.025, 2.1225); A = (33.0, 32.0, 143.0) × 10^{-4} cm^{-1}.

8.17 Cyclic Voltammograms of Cu^{II} 1,1-Dithiolates

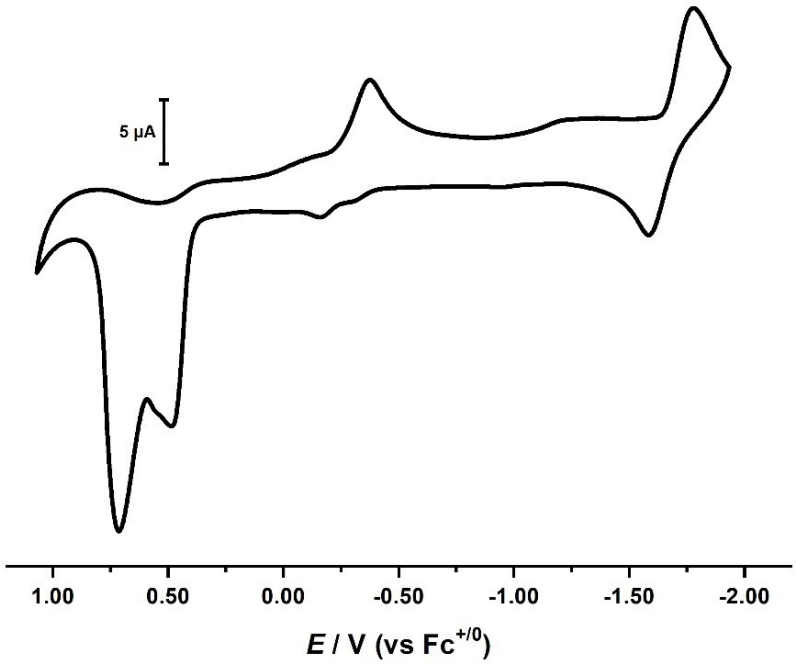

Figure 8.76 Full sweep cyclic voltammogram of $(NBu_4)_2[Cu(i\text{-}mnt)_2]$ in CH_2Cl_2 at room temperature; 0.10 M $(NBu_4)PF_6$; scan rate 100 mV s^{-1}; glassy carbon working electrode.

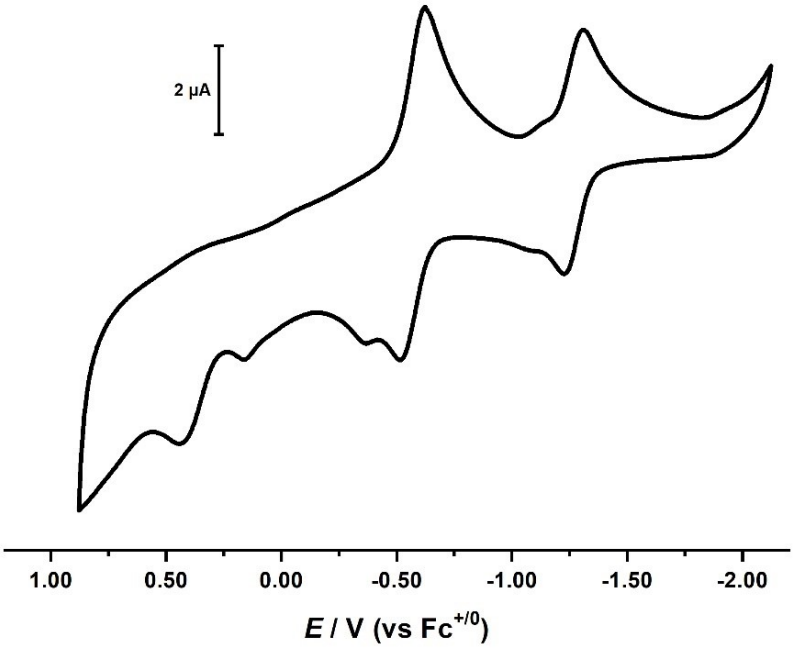

Figure 8.77 Full sweep cyclic voltammogram of $(NBu_4)_2[Cu(i\text{-mant})_2]$ in CH_2Cl_2 at room temperature; 0.10 M $(NBu_4)PF_6$; scan rate 100 mV s^{-1}; glassy carbon working electrode.

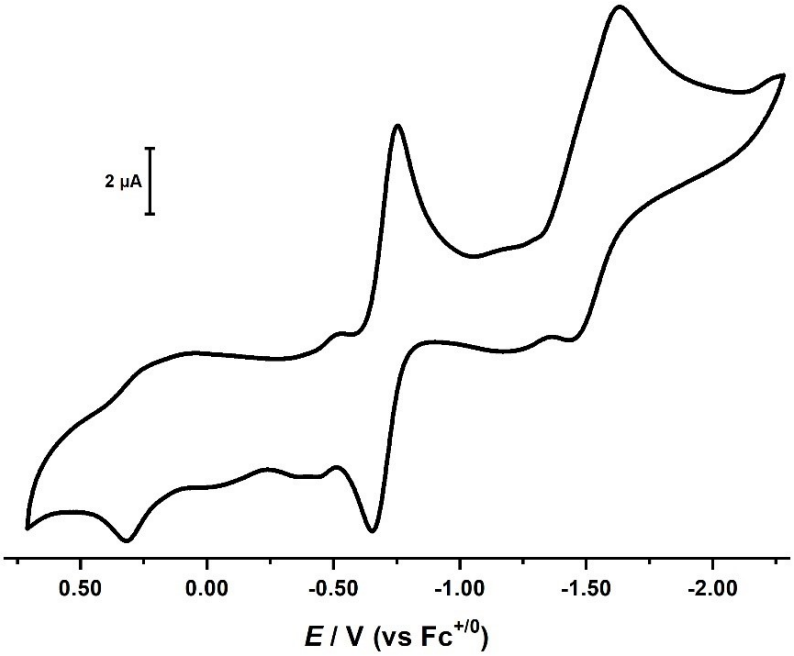

Figure 8.78 Full sweep cyclic voltammogram of $(NBu_4)_2[Cu(i\text{-ect})_2]$ in CH_2Cl_2 at room temperature; 0.10 M $(NBu_4)PF_6$; scan rate 100 mV s^{-1}; glassy carbon working electrode.

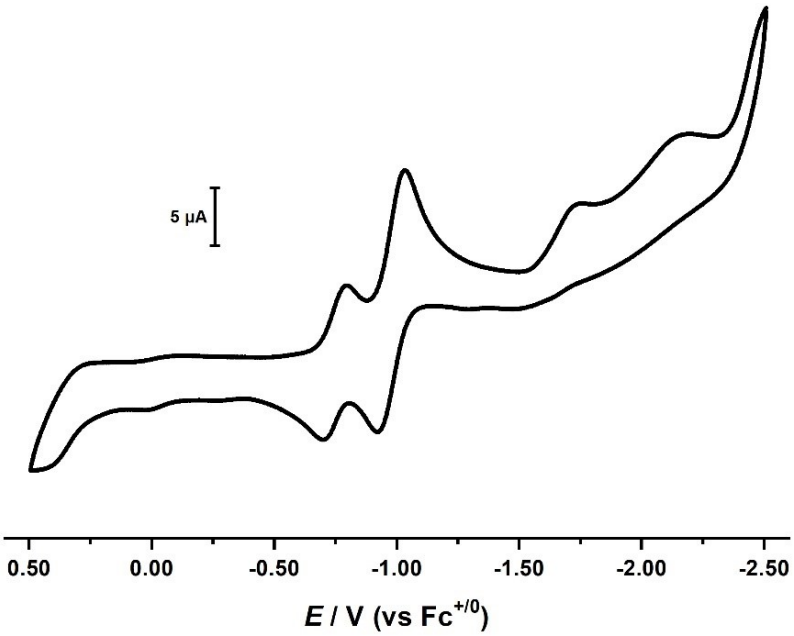

Figure 8.79 Full sweep cyclic voltammogram of $(PPh_4)_2[Cu(ded)_2]$ in CH_2Cl_2 at room temperature; 0.10 M $(NBu_4)PF_6$; scan rate 100 mV s^{-1}; glassy carbon working electrode.

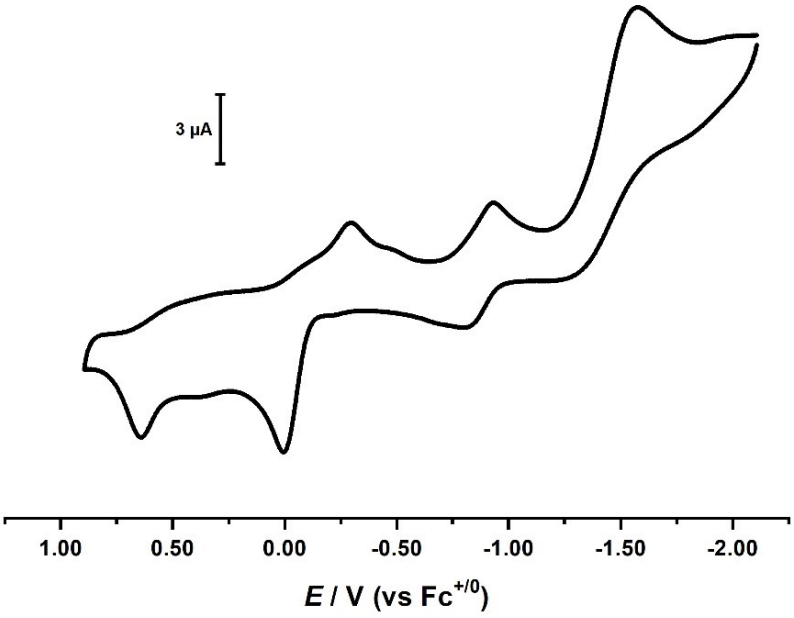

Figure 8.80 Full sweep cyclic voltammogram of $(PPh_4)_2[Cu(dts)_2]$ in CH_2Cl_2 at room temperature; 0.10 M $(NBu_4)PF_6$; scan rate 100 mV s^{-1}; glassy carbon working electrode.

8.18 Cu Redox Event Voltammogram Data

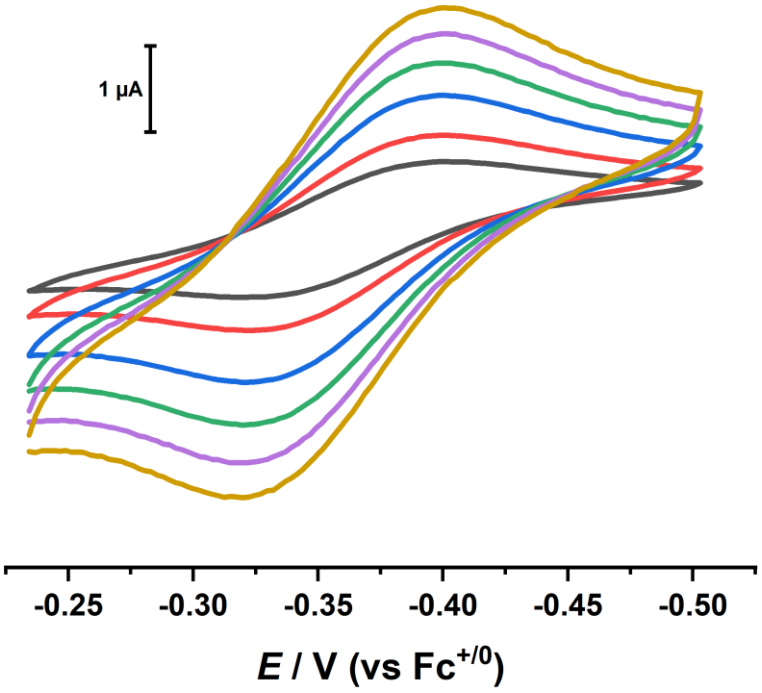

Figure 8.81 Cyclic voltammogram of the redox event at −0.36 V in $(NBu_4)_2[Cu(i\text{-}mnt)_2]$ in CH_2Cl_2 at room temperature; 0.10 M $(NBu_4)PF_6$; scan rates: 50 mV s^{-1}, charcoal; 100 mV s^{-1}, red; 200 mV s^{-1}, blue; 300 mV s^{-1}, olive; 400 mV s^{-1}, violet; 500 mV s^{-1}, mustard, glassy carbon working electrode.

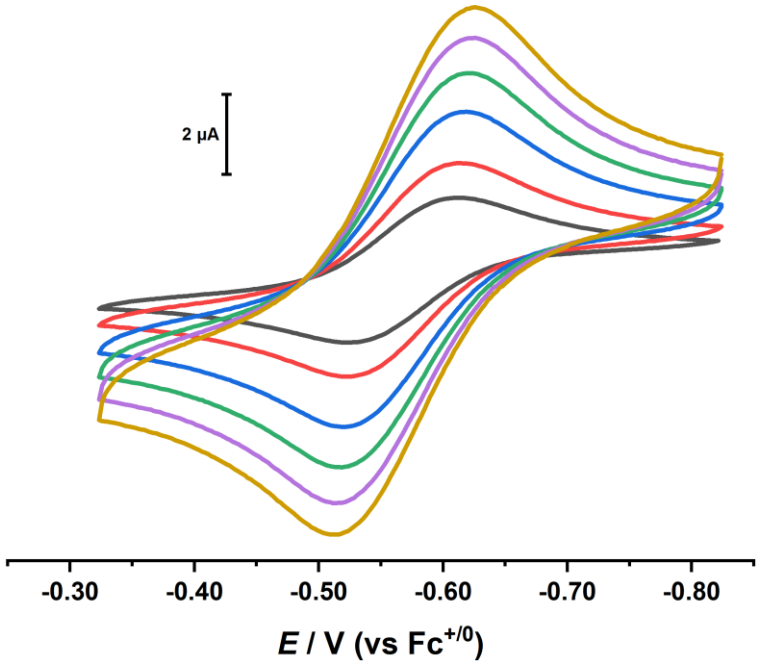

Figure 8.82 Cyclic voltammogram of the redox event at −0.57 V in $(NBu_4)_2[Cu(i\text{-}mant)_2]$ in CH_2Cl_2 at room temperature; 0.10 M $(NBu_4)PF_6$; scan rates: 50 mV s^{-1}, charcoal; 100 mV s^{-1}, red; 200 mV s^{-1}, blue; 300 mV s^{-1}, olive; 400 mV s^{-1}, violet; 500 mV s^{-1}, mustard, glassy carbon working electrode.

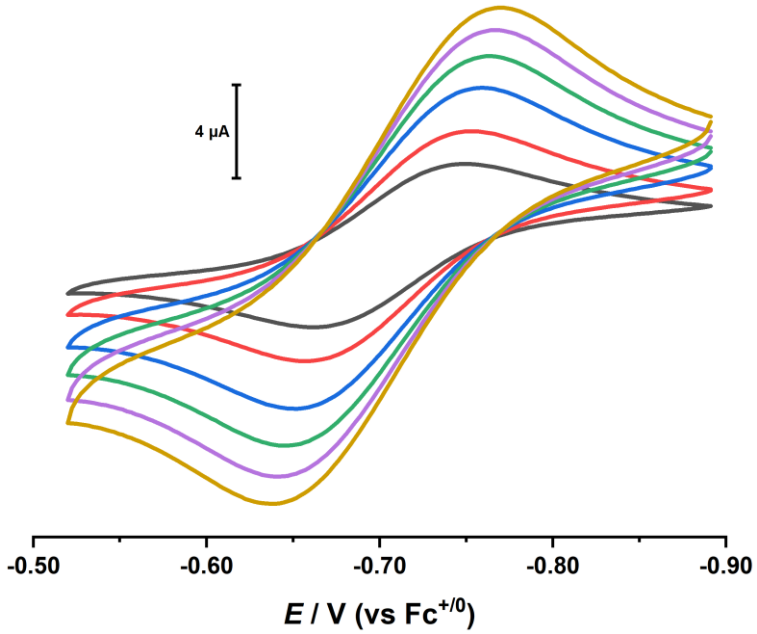

Figure 8.83 Cyclic voltammogram of the redox event at −0.71 V in $(NBu_4)_2[Cu(i\text{-}ect)_2]$ in CH_2Cl_2 at room temperature; 0.10 M $(NBu_4)PF_6$; scan rates: 50 mV s^{-1}, charcoal; 100 mV s^{-1}, red; 200 mV s^{-1}, blue; 300 mV s^{-1}, olive; 400 mV s^{-1}, violet; 500 mV s^{-1}, mustard, glassy carbon working electrode.

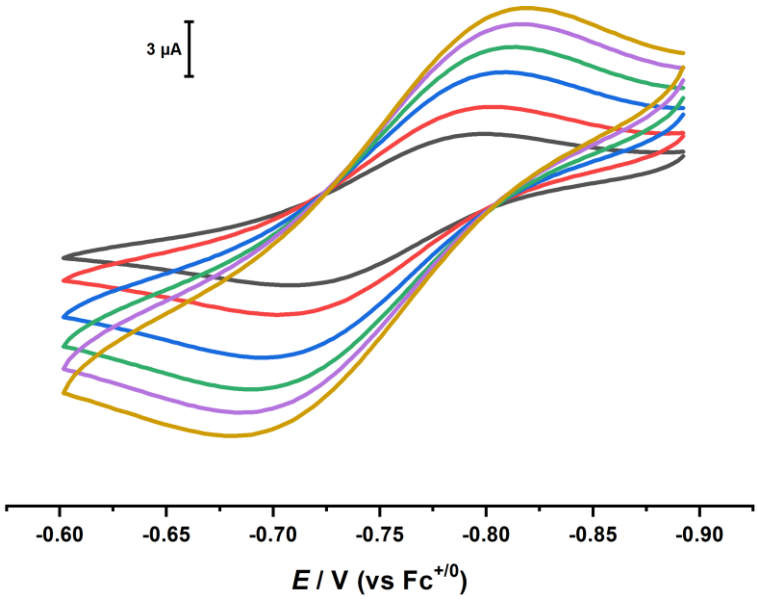

Figure 8.84 Cyclic voltammogram of the redox event at −0.75 V in $(PPh_4)_2[Cu(ded)_2]$ in CH_2Cl_2 at room temperature; 0.10 M $(NBu_4)PF_6$; scan rates: 50 mV s^{-1}, charcoal; 100 mV s^{-1}, red; 200 mV s^{-1}, blue; 300 mV s^{-1}, olive; 400 mV s^{-1}, violet; 500 mV s^{-1}, mustard, glassy carbon working electrode.

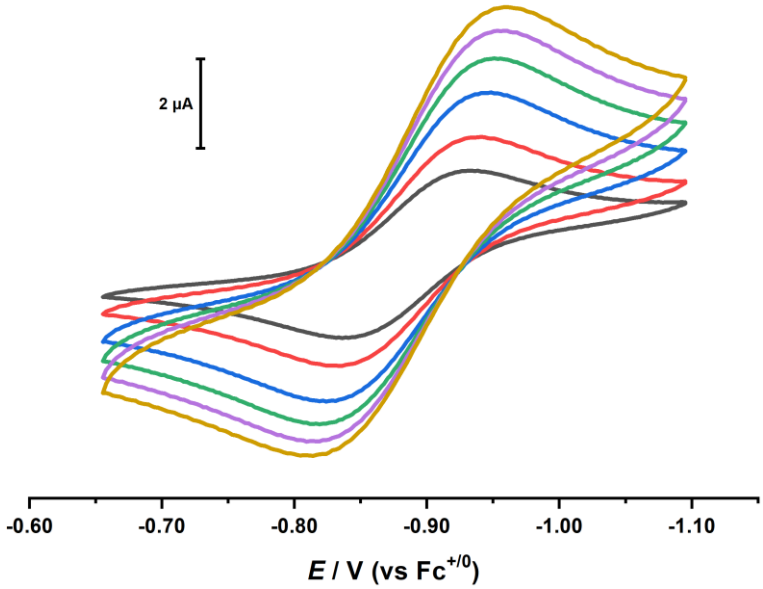

Figure 8.85 Cyclic voltammogram of the quasi-reversible redox event at −0.89 V in $(PPh_4)_2[Cu(dts)_2]$ in CH_2Cl_2 at room temperature; 0.10 M $(NBu_4)PF_6$; scan rates: 50 mV s^{-1}, charcoal; 100 mV s^{-1}, red; 200 mV s^{-1}, blue; 300 mV s^{-1}, olive; 400 mV s^{-1}, violet; 500 mV s^{-1}, mustard, glassy carbon working electrode.

Table 8.2 Variable Scan Rate Data for the Redox Event −0.36 V in $(NBu_4)_2[Cu(i\text{-}mnt)_2]$

Scan Rate	I_{pa}	I_{pc}	I_{pa}/I_{pc}	E_{pa}	E_{pc}	ΔE_{pp}	$E_{1/2}$	sqrt(scan rate)
50 mV s^{-1}	0.642	0.426	1.508	−0.403	−0.320	0.083	−0.361	0.2236
100 mV s^{-1}	0.824	0.608	1.355	−0.400	−0.322	0.078	−0.361	0.3162
200 mV s^{-1}	1.257	0.900	1.397	−0.403	−0.320	0.083	−0.361	0.4472
300 mV s^{-1}	1.500	1.077	1.393	−0.400	−0.320	0.081	−0.360	0.5477
400 mV s^{-1}	1.681	1.068	1.574	−0.400	−0.320	0.081	−0.360	0.6325
500 mV s^{-1}	1.763	1.263	1.396	−0.400	−0.320	0.081	−0.360	0.7071

Table 8.3 Variable Scan Rate Data for the Redox Event −0.57 V in $(NBu_4)_2[Cu(i\text{-}mant)_2]$

Scan Rate	I_{pa}	I_{pc}	I_{pa}/I_{pc}	E_{pa}	E_{pc}	ΔE_{pp}	$E_{1/2}$	sqrt(scan rate)
50 mV s^{-1}	1.844	1.594	1.157	−0.524	−0.612	0.088	−0.568	0.2236
100 mV s^{-1}	2.659	2.590	1.027	−0.519	−0.614	0.095	−0.566	0.3162
200 mV s^{-1}	3.300	3.180	1.038	−0.521	−0.619	0.098	−0.570	0.4472
300 mV s^{-1}	4.500	4.300	1.047	−0.519	−0.619	0.100	−0.569	0.5477
400 mV s^{-1}	5.350	5.100	1.049	−0.514	−0.626	0.112	−0.570	0.6325
500 mV s^{-1}	5.720	5.500	1.040	−0.514	−0.626	0.112	−0.570	0.7071

Table 8.4 Variable Scan Rate Data for the Redox Event −0.71 V in $(NBu_4)_2[Cu(i\text{-ect})_2]$

Scan Rate	I_{pa}	I_{pc}	I_{pa}/I_{pc}	E_{pa}	E_{pc}	ΔE_{pp}	$E_{1/2}$	sqrt(scan rate)
50 mV s^{-1}	3.563	3.313	1.075	−0.750	−0.662	0.088	−0.706	0.2236
100 mV s^{-1}	5.191	4.857	1.069	−0.754	−0.657	0.098	−0.706	0.3162
200 mV s^{-1}	6.600	6.300	1.048	−0.759	−0.652	0.107	−0.706	0.4472
300 mV s^{-1}	6.929	7.571	0.915	−0.764	−0.647	0.117	−0.706	0.5477
400 mV s^{-1}	8.647	8.294	1.043	−0.767	−0.640	0.127	−0.703	0.6325
500 mV s^{-1}	8.710	8.807	0.989	−0.769	−0.637	0.132	−0.703	0.7071

Table 8.5 Variable Scan Rate Data for the Redox Event −0.75 V in $(PPh_4)_2[Cu(ded)_2]$

Scan Rate	I_{pa}	I_{pc}	I_{pa}/I_{pc}	E_{pa}	E_{pc}	ΔE_{pp}	$E_{1/2}$	sqrt(scan rate)
50 mV s^{-1}	2.692	3.154	0.854	−0.709	−0.802	0.093	−0.756	0.2236
100 mV s^{-1}	3.463	4.000	0.866	−0.702	−0.802	0.100	−0.752	0.3162
200 mV s^{-1}	4.600	5.067	0.908	−0.697	−0.809	0.112	−0.753	0.4472
300 mV s^{-1}	5.291	5.732	0.923	−0.692	−0.814	0.122	−0.753	0.5477
400 mV s^{-1}	5.523	6.008	0.919	−0.685	−0.819	0.134	−0.752	0.6325
500 mV s^{-1}	5.694	5.797	0.982	−0.680	−0.819	0.139	−0.750	0.7071

Table 8.6 Variable Scan Rate Data for the Redox Event −0.89 V in $(PPh_4)_2[Cu(dts)_2]$

Scan Rate	I_{pa}	I_{pc}	I_{pa}/I_{pc}	E_{pa}	E_{pc}	ΔE_{pp}	$E_{1/2}$	sqrt(scan rate)
50 mV s^{-1}	1.594	1.953	0.816	−0.836	−0.934	0.098	−0.885	0.2236
100 mV s^{-1}	2.180	2.630	0.829	−0.834	−0.941	0.107	−0.887	0.3162
200 mV s^{-1}	2.720	3.480	0.782	−0.819	−0.948	0.129	−0.884	0.4472
300 mV s^{-1}	3.280	4.160	0.788	−0.819	−0.951	0.132	−0.885	0.5477
400 mV s^{-1}	3.125	4.300	0.727	−0.817	−0.958	0.142	−0.887	0.6325
500 mV s^{-1}	3.250	4.600	0.707	−0.814	−0.961	0.146	−0.887	0.7071

8.19 Ni^{II} 1,1-Dithiolates ^1H NMR Spectra

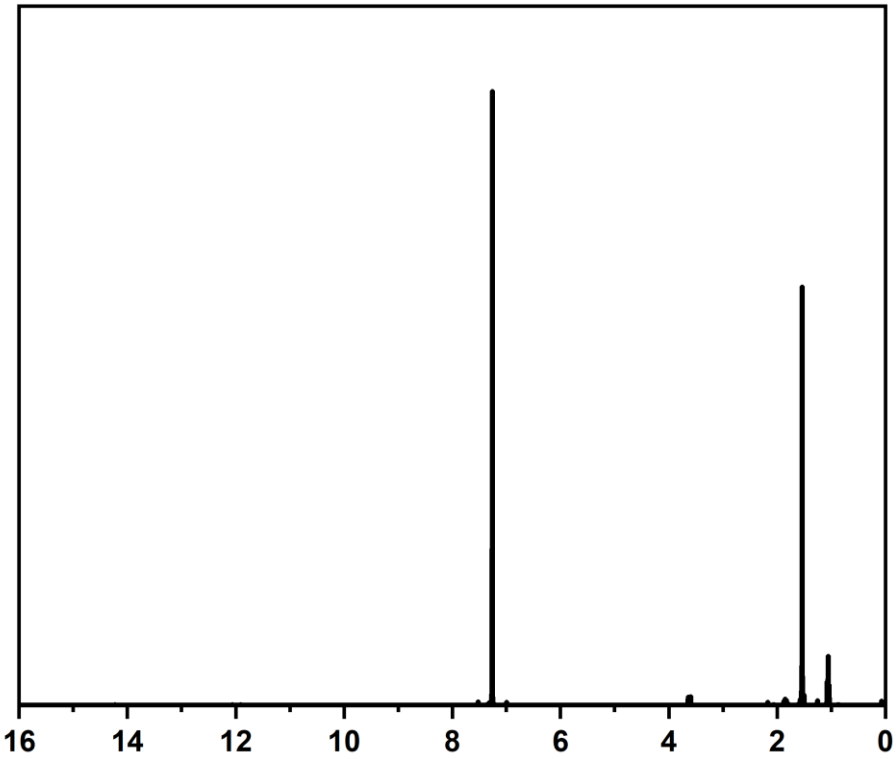

Figure 8.86 ^1H NMR Spectrum of $(NBu_4)_2[Ni(i\text{-}mnt)_2]$ in $CDCl_3$.

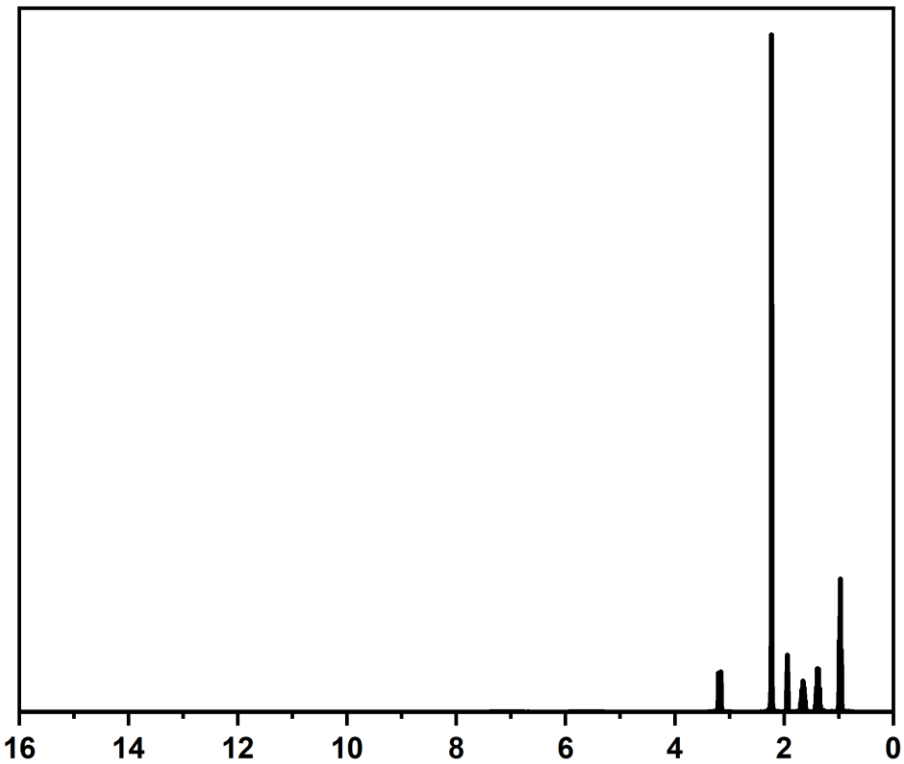

Figure 8.87 ^1H NMR Spectrum of $(NBu_4)_2[Ni(i\text{-}mant)_2]$ in CD_3CN.

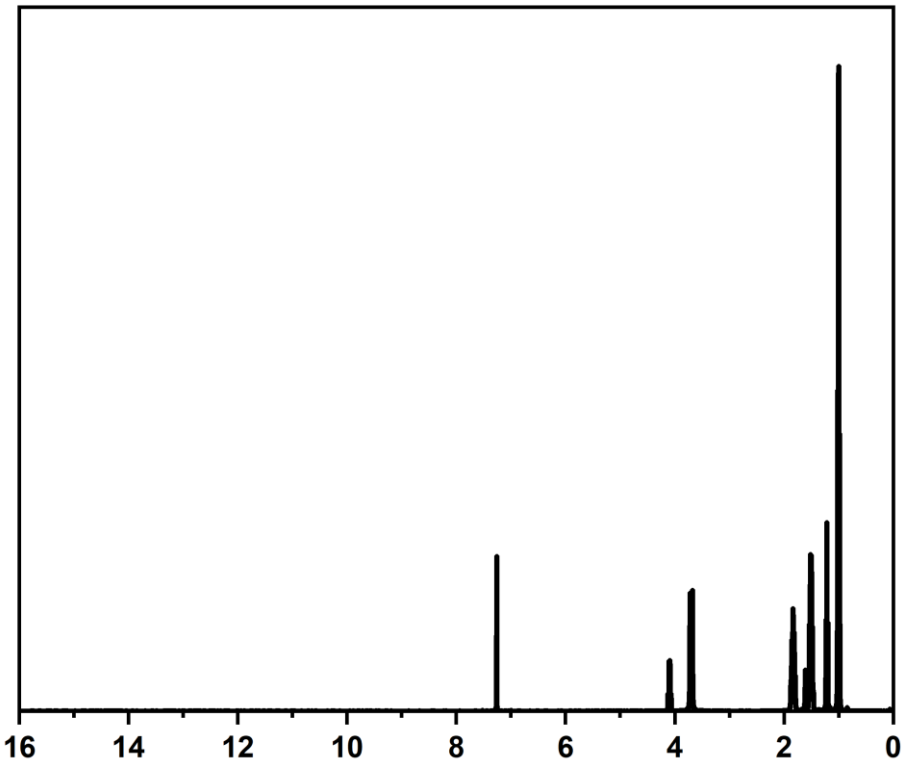

Figure 8.88 ^{1}H NMR Spectrum of $(NBu_4)_2[Ni(i\text{-}ect)_2]$ in $CDCl_3$.

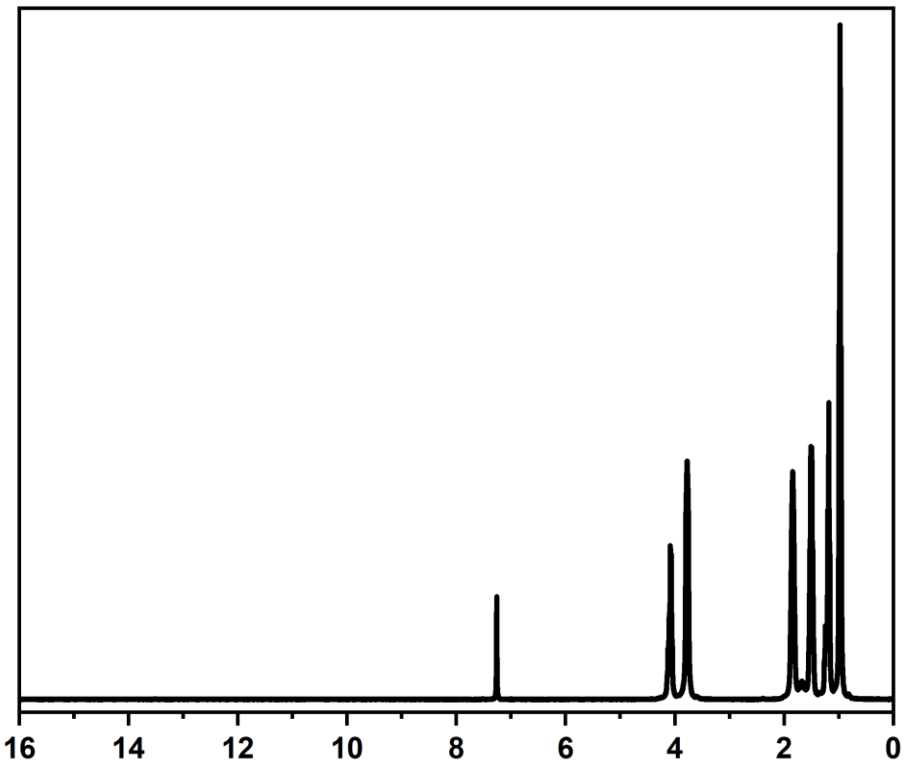

Figure 8.89 ^{1}H NMR Spectrum of $(NBu_4)_2[Ni(ded)_2]$ in $CDCl_3$.

8.20 Ni^{II} 1,1-Dithiolates ^{13}C NMR Spectra

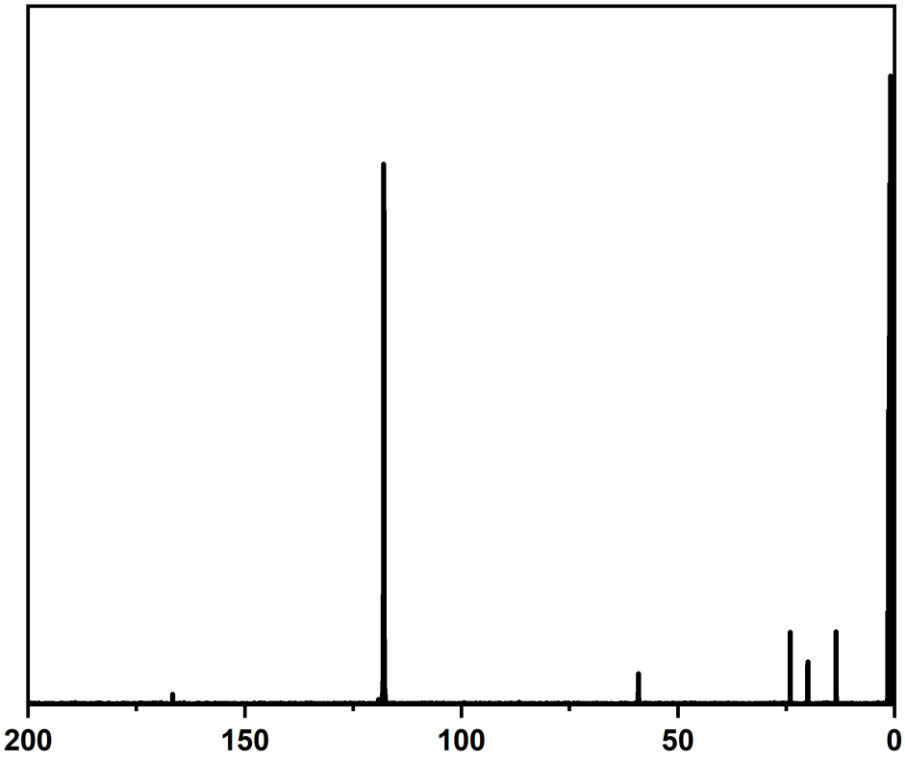

Figure 8.90 ^{13}C NMR Spectrum of $(NBu_4)_2[Ni(i\text{-mant})_2]$ in CD_3CN.

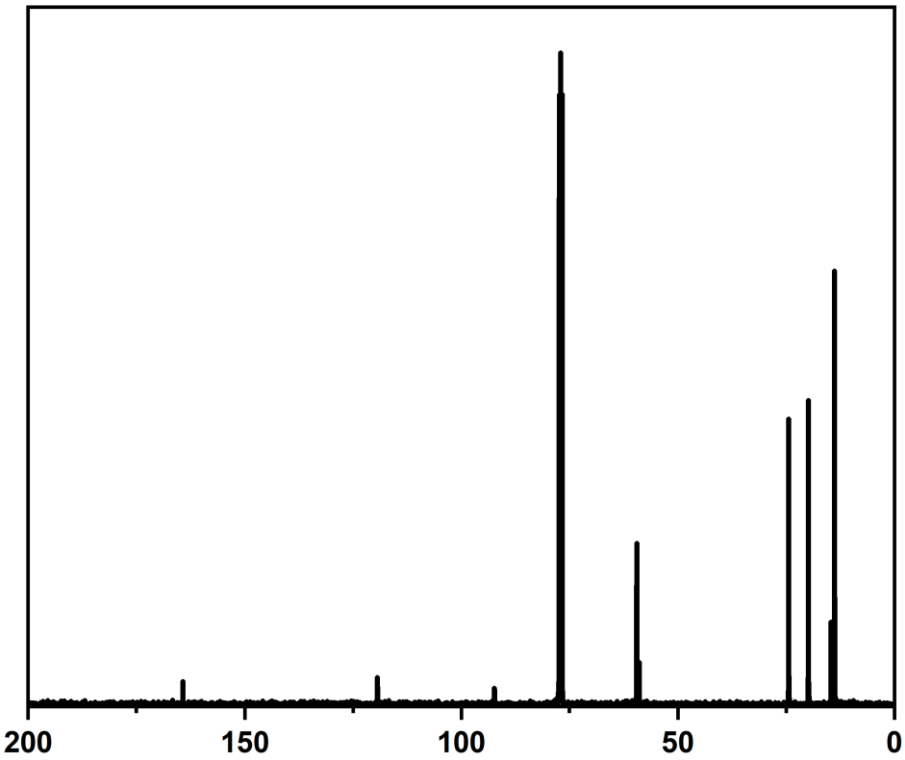

Figure 8.91 ^{13}C NMR Spectrum of $(NBu_4)_2[Ni(i\text{-ect})_2]$ in $CDCl_3$.

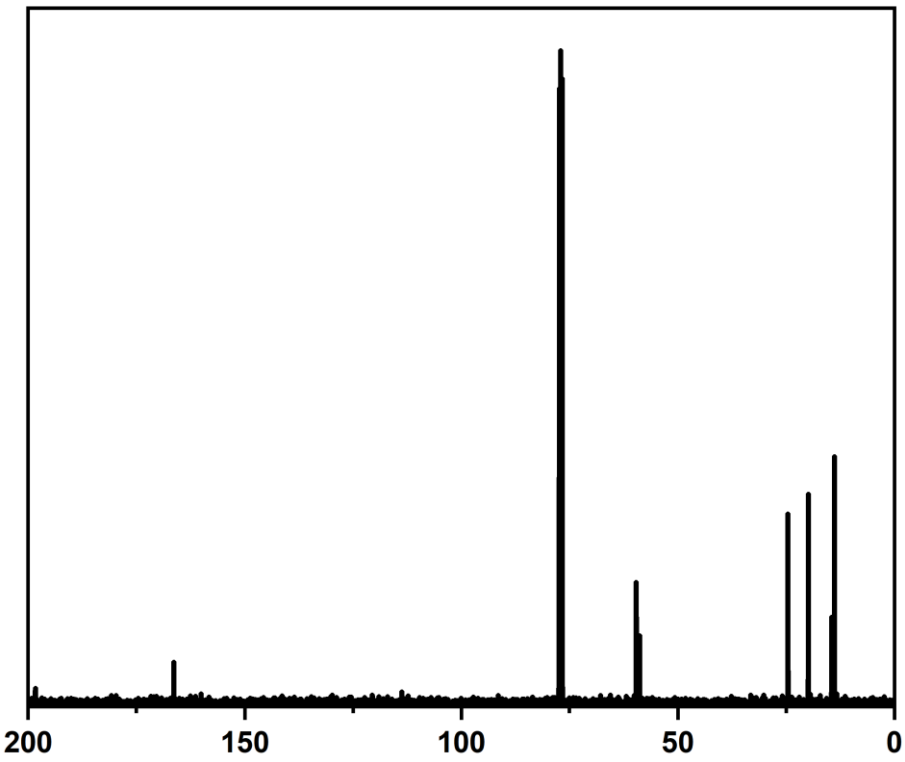

Figure 8.92 ^{13}C NMR Spectrum of $(NBu_4)_2[Ni(ded)_2]$ in $CDCl_3$.

8.21 Ni^{II} 1,1-Dithiolate Electronic Spectra

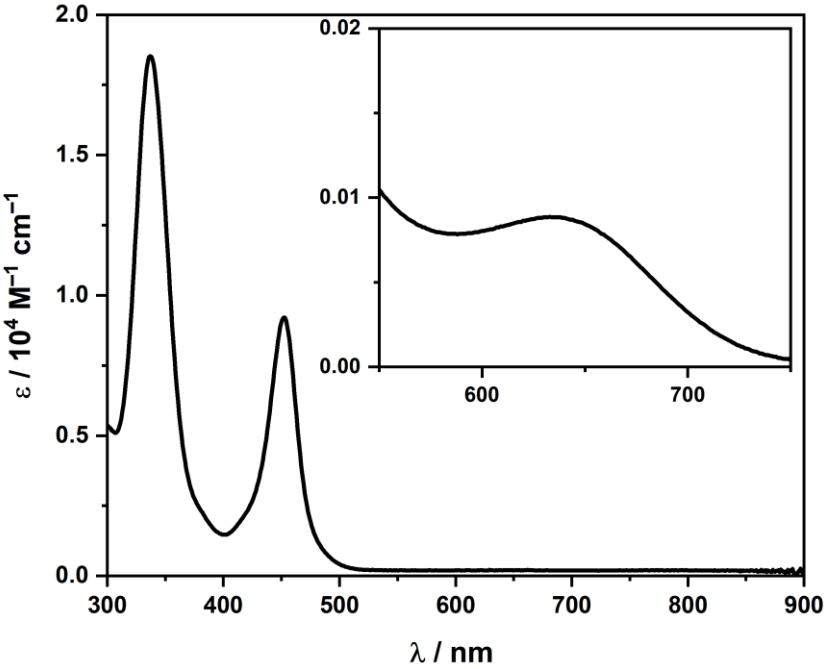

Figure 8.93 Electronic spectrum of $(NBu_4)_2[Ni(i\text{-}mnt)_2]$ recorded in MeCN.

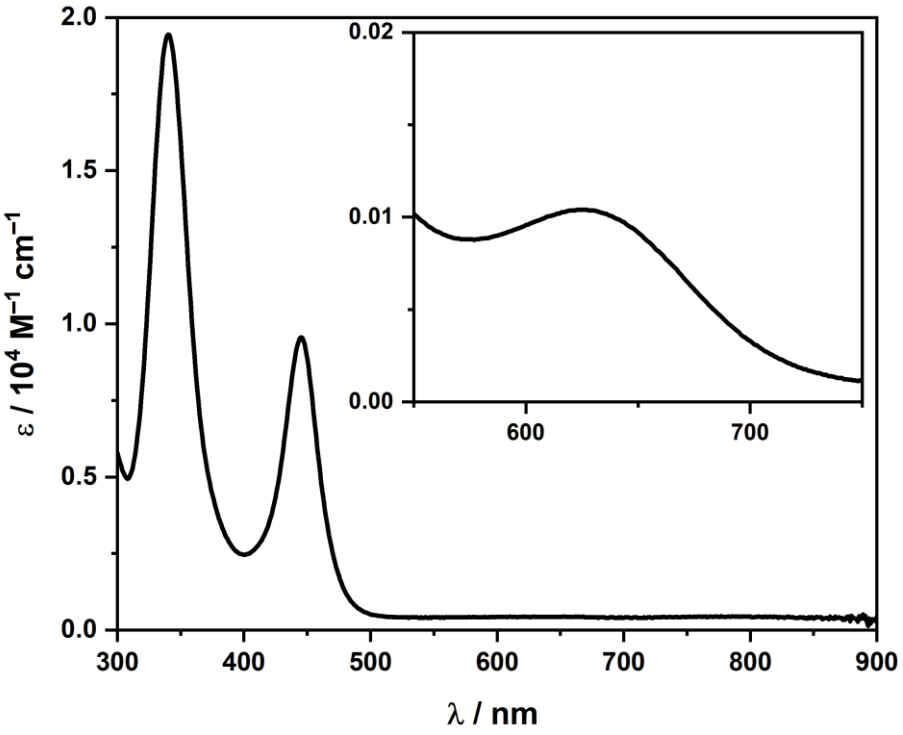

Figure 8.94 Electronic spectrum of $(NBu_4)_2[Ni(i\text{-mant})_2]$ recorded in MeCN.

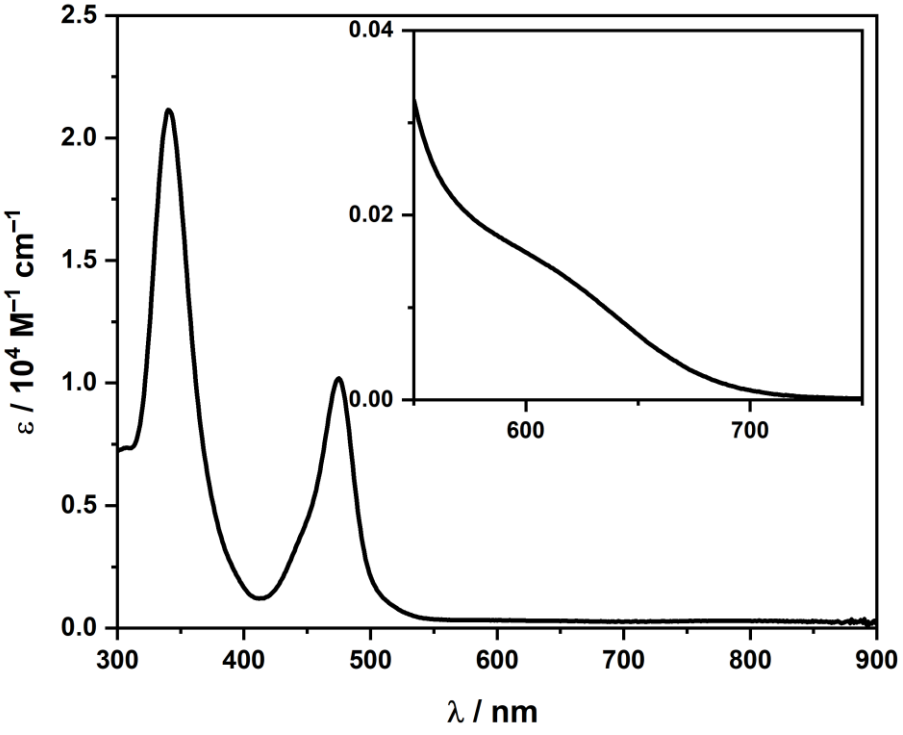

Figure 8.95 Electronic spectrum of $(NBu_4)_2[Ni(i\text{-ect})_2]$ recorded in MeCN.

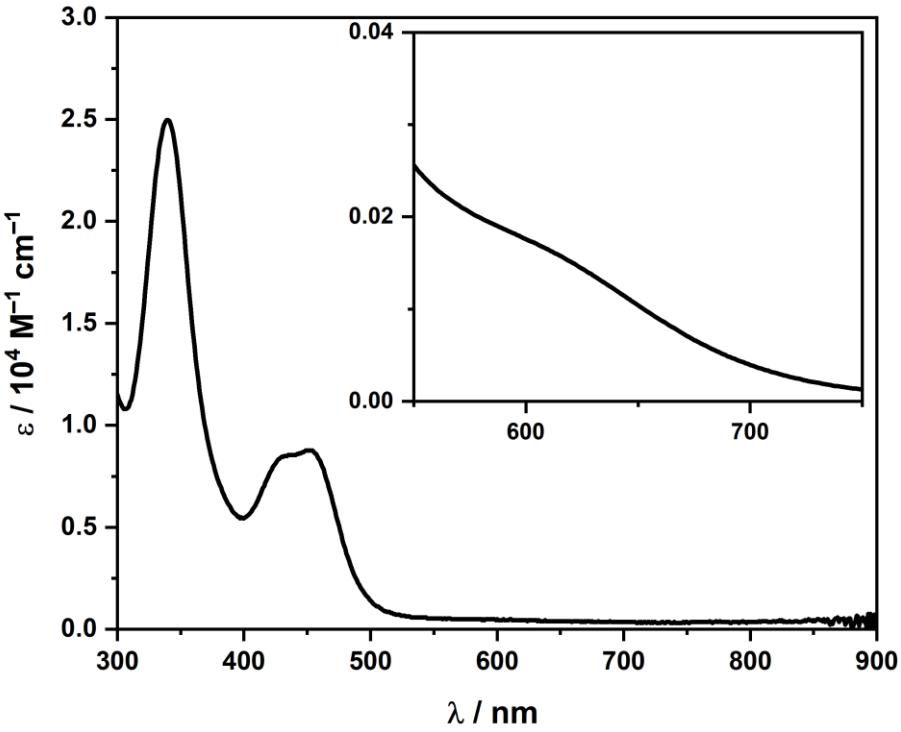

Figure 8.96 Electronic spectrum of $(NBu_4)_2[Ni(ded)_2]$ recorded in MeCN.

8.22 Cyclic Voltammograms of Ni^{II} 1,1-Dithiolates

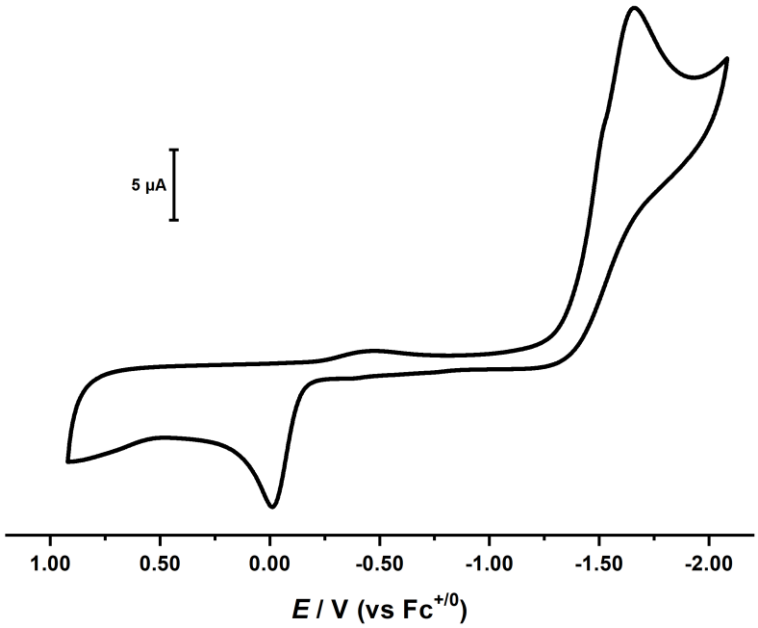

Figure 8.97 Full sweep cyclic voltammogram of $(NBu_4)_2[Ni(i\text{-}mnt)_2]$ in CH_2Cl_2 at room temperature; 0.10 M $(NBu_4)PF_6$; scan rate 100 mV s^{-1}; glassy carbon working electrode.

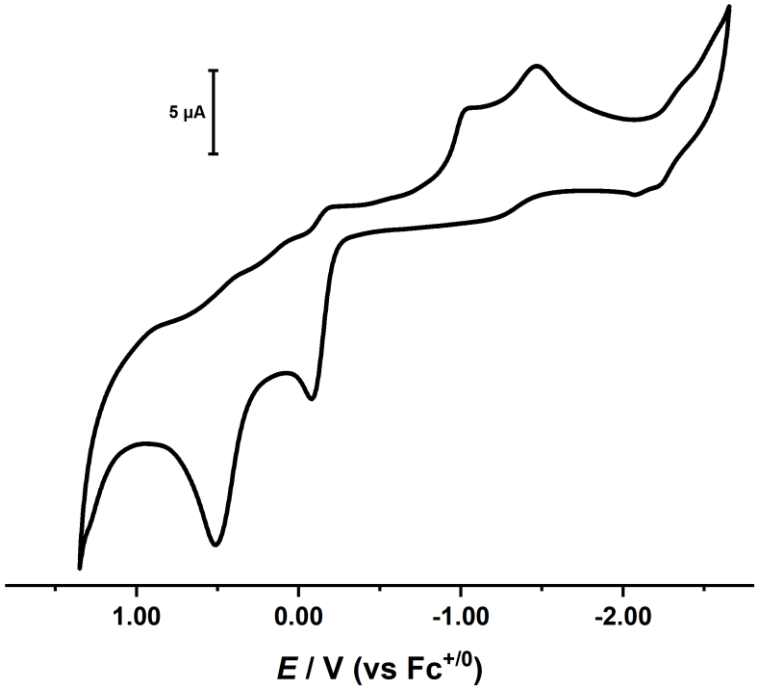

Figure 8.98 Full sweep cyclic voltammogram of $(NBu_4)_2[Ni(i\text{-mant})_2]$ in CH_2Cl_2 at room temperature; 0.10 M $(NBu_4)PF_6$; scan rate 100 mV s^{-1}; glassy carbon working electrode.

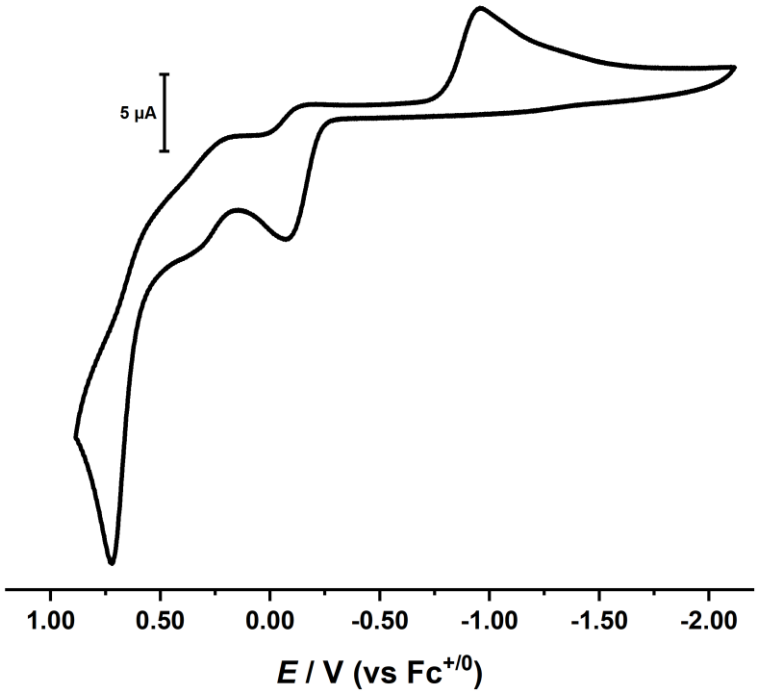

Figure 8.99 Full sweep cyclic voltammogram of $(NBu_4)_2[Ni(i\text{-ect})_2]$ in CH_2Cl_2 at room temperature; 0.10 M $(NBu_4)PF_6$; scan rate 100 mV s^{-1}; glassy carbon working electrode.

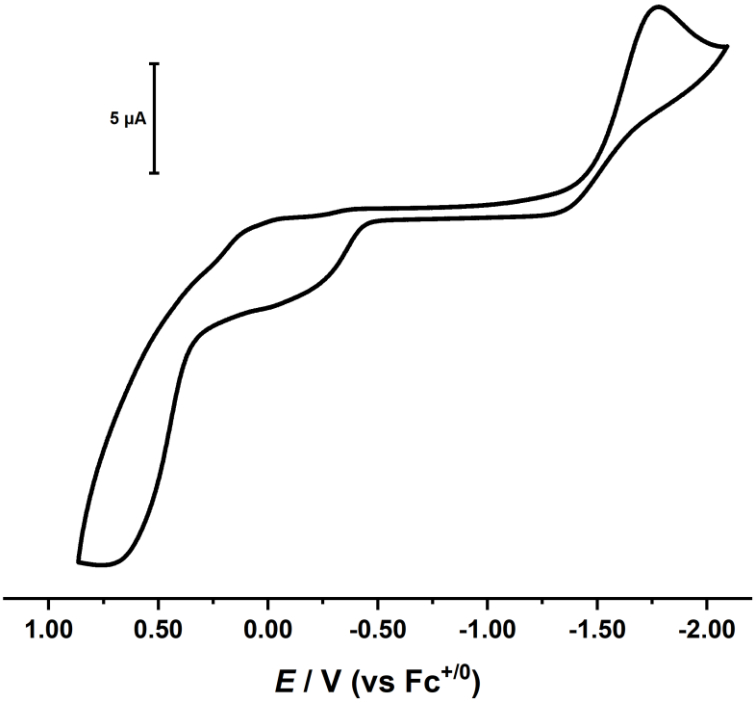

Figure 8.100 Full sweep cyclic voltammogram of $(NBu_4)_2[Ni(ded)_2]$ in CH_2Cl_2 at room temperature; 0.10 M $(NBu_4)PF_6$; scan rate 100 mV s^{-1}; glassy carbon working electrode.